Finite Element Modelling and Simulation of Metal Flow in Bulge Forming

by

Mahiuddin Ahmed, B Sc Eng , M Eng

Ph D 1997

Finite Element Modelling and Simulation of Metal Flow in Bulge Forming

by

Mahiuddin Ahmed, B.Sc.Eng, M Eng

This thesis is submitted to Dublin City University as the fulfilment of the
requirement for the award of the degree of

Doctor of Philosophy

Supervisor: Professor M S.J Hashmi, PhD, D Sc

School of Mechanical and Manufacturing Engineering
Dublin City University

September, 1997

DECLARATION

I hereby certify that this material, which I now submit for assessment on the programme of study leading to the award of *Doctor of Philosophy*, is entirely my own work and has not been taken from the work of others save and to the extent that such work has been cited and acknowledged within the text of my work.

Mahiuddin Ahmed

Signed ---------------------------- I D No 93700351

Date 9th September, 1997

বাবা এবং মার জন্য

To my parents who took all the troubles in the world with a smile for the advancement of their children's knowledge and to my son to inspire him in the pursuit of knowledge

Acknowledgement

I would like to express my sincere thanks and gratitude to Prof M S J Hashmi for his kind guidance and supervision in carrying out this work His teachings to the subject matter of the work sometimes formally and sometimes not so formally will always be thankfully remembered

I would like to thank the School of Mechanical and Manufacturing Engineering of Dublin City University for awarding me the scholarship for this work under the DCU-BUET linkage programme I would also like to thank BUET for granting me necessary study leave to carry out the work In this connection I would like to thank the BUET co-ordinator of the programme, Prof M Mizanur Rahman for selecting me for the award

I must thank Mr Liam Domican for his co-operation and assistance in developing one of the models in AutoCAD His services in the matters of procurement of computer hardware and software are also thankfully acknowledged I would also like to thank all the members of the staff in the school for their help and co-operation during the work

Times during the period of this work were never been even There were times of happiness, and there were times of distress My wife, Suraiya and myself shared the both She made life much better at the times of distress with her support and comfort I must thank her for her supportive role during the work I would also like to thank our families back home who always supported and comforted us through their letters during these long years

Finally, all praises to the God almighty for enabling me to complete this work

Mahiuddin Ahmed

FINITE ELEMENT MODELLING AND SIMULATION OF METAL FLOW IN BULGE FORMING

Contents

Finite Element Modelling and Simulation of Metal Flow In Bulge Forming

Mahiuddin Ahmed

ABSTRACT

The research and application of finite element methods in the area of material processing has increased rapidly in recent years Application of FEM is reported in the processing of most engineering materials including new materials like metal matrix composites In metal forming, FEM is mostly applied to conventional forming situations like forging and upsetting, extrusion, drawing, rolling, sheet metal forming, casting and moulding and machining Most of these forming operations are also well analysed by theories of plastic deformation like limit theorems, slip-line field theory etc In contrast, new and unconventional metal forming cases, which are often very complex, are relatively under-analysed either by the theoretical methods mentioned above or by numerical methods like finite element

This work is mainly devoted to computer simulation and study of one of the unconventional metal forming process called bulge forming There are various type of industrial products made by bulge forming process In some processes the main forming load is the hydrostaic pressure on the surface of the blank plate or shell While in others, an in-plane compressive load is also applied simultaneously with the pressure load Depending on the initial blank shape and final product shape, the simultaneous loading case becomes a complex forming situation This project has simulated the later category of bulge forming by finite element method

Number of such cases were simulated to cover initial blank shape viz flat circular plate, flat rectangular plate and initially curved shell In the latter category axisymmetric expansion of tubes, T-branch forming from straight cylindrical tubes and forming of box-sectioned elbow from cylindrical tubes were simulated In each case different loading and friction conditions were tried Distribution of stress and strain were studied for all the cases Comparison were made between comparable forming conditions Response of certain parameter with respect to the changes of different forming variables of the process were also studied for most of the simulated cases In case of the bulging of flat circular plate, optimum forming condition were identified for different objective criteria Taguchi parameter design method was applied to transform the above optimum values to practicable engineering values All the simulations were carried out using well known commercial finite element packages Both static frontal solvers and explicit dynamic solvers were used for the simulations

Chapter 1

INTRODUCTION

1.1 Rationale

The use of computer aided analysis and design of metal forming has increased considerably in recent years. If one takes the number of published papers as a measure of activity in any field then surely one would discover rapid growth in the use of computer in simulation of metal forming by finite element method (FEM). In a recent review paper[1] on application of FEM on material processing with more than 1100 listed references it was shown that during 1982-1992 period the number of published papers has grown more than three times. High computational speed and low cost of computers at desk top level are the main driving forces for much wider application. Besides, the development in computer graphics, new solution techniques and user friendly interactivity with computers have also contributed to more applications. The need for rapid product development has definitely provided a pull effect to the situation.

However, within the metal forming area, the application of computer in analysis and design is still mostly limited to common forming techniques. Authors of the review paper mentioned earlier have grouped the listed references according to different areas of metal forming. Figure 1-1 shows a pie chart of the groupings indicating the major application areas.

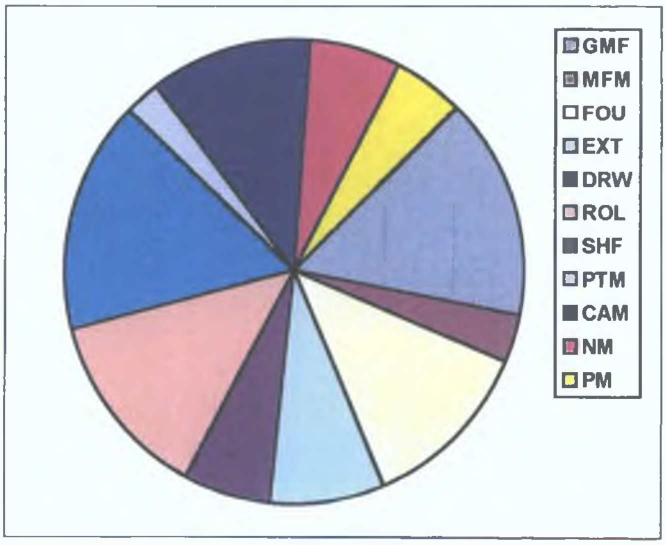

Legend:

GMF = General Metal Forming
MFM = Metal Forming and Meshing
FOU = Forging and Upsetting
EXT= Extrusion
DRW = Drawing,
ROL = Rolling
SHF = Sheet Metal Forming,
PTM = Pipe and Tube Manufacturing
CAM = Casting and Moulding
NM = Non-metal Forming
PM = Powder Metallurgy

Figure 1.1: Pie chart of FEM simulation studies in different metal forming areas

The papers in the first two groups are related to theoretical aspects of FEM Metal forming processes exhibited in other groups are common industrial processes Probably demand from the industry is one of the reasons that these processes are more simulated and studied than others Besides, most of these processes can be simulated in two dimensions Considering the computer resources required for three dimensional finite element analysis, more complex metal forming operations requiring 3D treatment were so far been less simulated However, very recently this constraint has eased and the simulation of three dimensional metal forming process has become practical

There are many different types of complex metal forming processes which require simulation in three dimensions Most of these processes are very promising and can produce near net shape products Because of the complexity involved in these processes, they are relatively less analysed either by established analytical methods or by numerical methods Considering the importance of these innovative processes of metal forming and the availability of computational power it has become essential that these processes be analysed by numerical methods to understand the effect of the product and process variables on the process This would be helpful in designing better processes and thereby better products

1.2 Bulge Forming

Bulge forming is an innovative metal forming process by which many near-net shaped industrial parts are manufactured Deep vessels, T-branches, X-branches and other tubular components, stepped hollow shafts, bicycle wheel hub, rear axle casing of cars, axles, nozzles, metal bellows etc are typical parts made by bulge forming processes The products are either axisymmetric or asymmetric However, the basic process for either type of product is the same

Bulge testing is the most simple case of bulge forming In this process the material is biaxially stretched at the bulge by application of hydraulic pressure More complex bulge forming processes involve application of additional forces other than the pressure to supply material in the areas of bulging from other areas of the blank This is ne to enhance the formability of the process There are different arrangement of die-fixture for bulge forming Figure 1 2 shows cross-sectional view of one of the possible

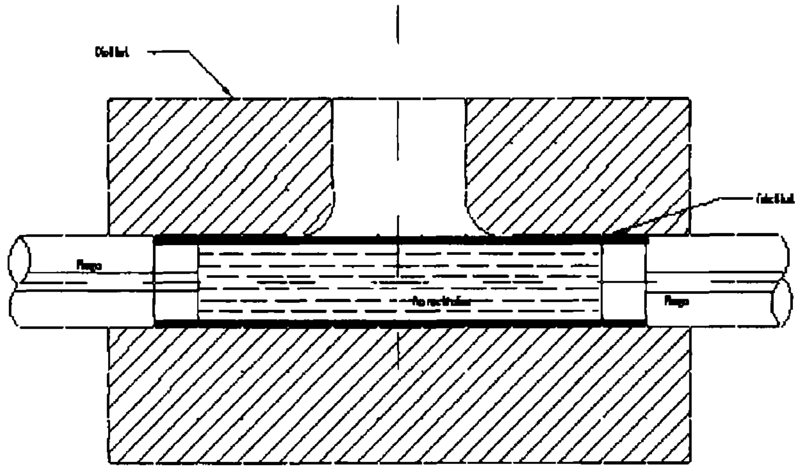

[illegible]

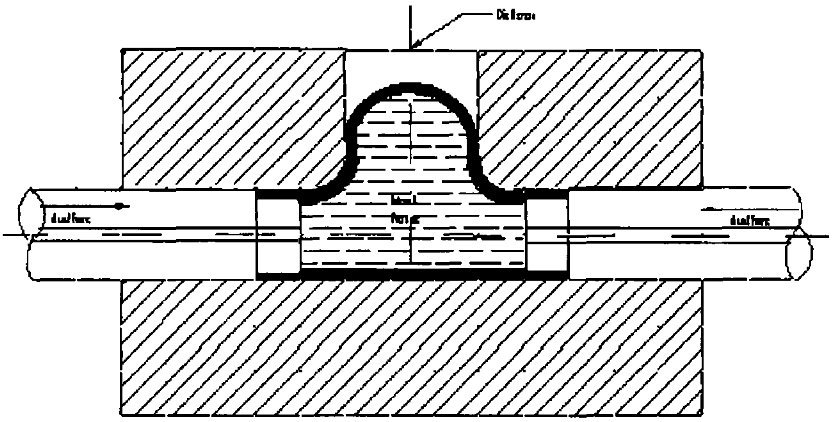

[illegible]

Figure 1 2 Diagram of bulge forming principle

arrangements for the manufacture of tubular components The tube blank is placed between two die halves and tube ends are held by two plungers the tips of which act as punch The hydraulic fluid is pumped through holes in the plunger and pressure builds up inside the tube The plungers are pushed inwards to provide the axial compressive load Due to pressure and the axial load the branch starts forming Simultaneous application of these loads help to obtain large deformation in the process Prominence of any one type of loading leads to instability and thereby defects

There are two main modes of defects from process instability of bulge forming One is the defect by rupture which occurs due to excessive thinning of the bulge area

This situation is the result of dominant pressure loading Defects by buckling usually occurs in non-bulged areas when the axial compressive loading is excessive Thus an optimum loading condition avoiding these instabilities would also enable higher deformation in the process But to tread that path requires a good understanding of the deformation process Theoretical methods for plastic deformation analysis of bulge forming have generated limited understanding of the process Numerical analysis by simulation could provide much deeper understanding on the process and thereby promise better design of process machineries and eventual products

Hydrostatic pressure applied in bulge forming can be applied by solid medium instead of liquid medium as described earlier Soft metal or elastomers may be used for this purpose However, with these solid media it is very difficult to control the pressure on the tube which is very important for the stability of the process But generally, the solid medium produces better product provided a stable process can be maintained Both solid and liquid media have other operational advantages and disadvantages

Researchers and practitioners have long been studying and experimenting on bulge forming A survey of the theoretical and experimental works done on bulge forming is presented in the next chapter

Chapter Two

LITERATURE SURVEY AND SCOPE OF WORK

2.1 Simple Bulge Forming

2.1.1. Analytical and Experimental Studies

The most common case of bulge forming is the hydraulic bulge testing, an experiment to determine biaxial stress-strain characteristics of ductile materials up to large plastic strains In this experiment a thin circular sheet is clamped along its periphery and a uniform pressure is applied on one side of the sheet Under ideal conditions this gives rise to a non-uniform strain distribution varying from in-plane plane strain at the edge to balanced biaxial tensions at the pole [2] There are many experimental and analytical works on bulge testing Pioneering works of Brown and Sachs[3], Gleyzal [4], Brown and Thompson[5], Hill[6], Swift [7] and Mellor [8] must be mentioned in this regard

Many studies have since been published considering various aspects of bulge testing such as different materials, directional properties of materials, geometry of the opening, geometry of the bulge etc References[9-13] may be mentioned as examples Most of these works on bulging concentrated on the pole region with much simplification of the process Little or no attention was given to the deformation behaviour at the periphery This was obvious due to the fact that the main objectives were either to characterise the stress strain behaviour of the material or to study the situation leading to instability at the polar region Even then the behaviour at the bulge forming periphery can not be ignored In this regard, the study by Atkinson [10] deserve special mention as it points out some issues related to bulging process itself In this paper the author questions the appropriateness of the usual assumptions that the bulge profile is circular and the pole area is uniformly strained According to Atkinson, due to the contribution of bulging, thinning and increasing strain gradation during bulging the relationships between different parameters of the process are rather complex

For practical applications these information are definitely useful Additional information with respect to the effects of the die geometry at the opening, bulging of thick sheet and simultaneous in-plane load on the sheet on bulge forming could be equally useful for industrial bulge forming Incorporating these aspects in simple bulge forming could practically be not feasible but simulation by numerical methods could be an alternative way to gain more insight of the process

2 1.2. Numerical Studies

A number of works have been reported on simulation analysis of simple bulge forming of sheet metals or bulge testing Numerical analysis of bulge forming of circular sheet by finite difference method was done by Woo [14], Yamada and Yokouchi [15], Wang and Shammamy[16] and subsequently by Ilahi et al [17] and Ilahi and Paul[11]

The first finite element solution of bulge testing was done by Iseki et al [18] They formulated the problem using elastic-plastic material law and updated Lagrangian formulation They compared their results with experimental values At the pole of the bulge both the simulated and the experimental results showed quite good match but they diverged at the periphery of the bulge Iseki et al [19] also analysed elliptical and rectangular metal diaphragms by the same formulation Comparison of experimental results with simulation shows similar trend

Kobayashi and Kim [20] formulated a finite element analysis technique using rigid-plastic material characteristics They verified their formulation by simulating bulge forming problem analysed by Iseki et al [18] and compared the results Kim and Yang [21] formulated a more general finite element solution method applicable to axisymmetric cases also using the same rigid-plastic material model They also compared their results with that from Iseki et al [18] Wifi [22] also analysed bulge forming by a generalised correction formulation of finite element method He also compared his findings with that of Iseki et al [18]

All the above simulations were carried by modelling a circular sheet clamped at the edge Although their illustrations show a die with some edge radius, the simulations did not consider this peripheral boundary conditions of the sheet with the die Keck et al [23] simulated the simple bulge forming problem using an elastic-plastic formulation and took the peripheral boundary condition into account They found that their simulation results agree very well with the experimental results of Iseki et al [18] According to Keek et al significant differences exist between this analysis and the simplified model that was used by Iseki et al [18] and Kim and Yang [21] Lange et al [24] of the same research group simulated bulging through elliptical dies with edge boundary conditions included in the model and got good agreement with experimental results

Recent finite element simulation work on bulge forming of sheets were reported by Li et al [25] and Cronin et al [26] In the former work , the authors observed from simulation the influences of various material parameters on bulge forming They obtained an empirical relation linking average limit thickness strain with material hardening and rate sensitivity parameters by regression fitting of the simulation results In the second work by Cronin et al a general purpose FE code, ABAQUS was used for simulation They studied the influence of varying mesh size and element type together with the variation of normal anisotropy of the material From the simulation results they found that (i) beyond certain mesh density the results are unaffected, (ii) the continuum elements predicted better results than the shell elements and (iii) normal anisotropy of the sheet induces more uniform strain distribution on bulging Predictions were verified by experimental results Both these works modelled the sheet to be clamped at the periphery thereby disregarding the contact and friction conditions between the sheet and the die

Practical bulge forming of a circular cup to a certain shape and height was simulated by Lee and Ma [27] The simulation result predicted shape and limiting height of the cup that can be formed from particular blank geometry without failure and the strain distribution Experimental verification showed good agreement with predicted results They considered all contact and interface boundaries in modelling the problem

In all of the above studies circular blanks of different diameter and thickness were used for bulging It is understandable because of the fact that the objectives of most of these studies were to evaluate finite element formulations Therefore, the focus was mostly on the deformation behaviour at the pole Bulging for some practical end product like deep vessels or cups could necessitate different blank geometry like rectangular or square sheet for operational reasons Unfortunately, no such effort was evident either from the academia or from industry For the same reason, perhaps, there was no effort to see what happens if blanks are pushed in towards the bulge while forming Obviously, this has merit when the objective is to maximise the bulge height This is very much in practice in bulge forming of tubular components like tee or cross branches or other industrial parts from straight tubular blanks

2.2 Bulge Forming of Industrial Parts and Components

2 2 1 Analytical and Experimental Studies

The first work on bulge forming applying pressure and axial load on tube blanks was reported as early as 1939 in a patent by Grey et al [28] The patented process was described as upsetting a copper tube blank of approximately tee shape with the application of internal hydraulic pressure and axial load at the blank ends Crawford [29] described an applied process wherein a soft metal was poured in copper tube blank and endwise pressure was applied to both the filler metal and tubing whilst they were restrained in the die An improved method of the process was patented by Stalter[30] to increase the productivity of the process and to remove the disadvantages caused by shrinking of the filler metal on pouring Remmerswall and Verkaik [31] successfully formed axisymmetric conical products from deep drawn cylindrical blanks Ogura and Ueda[32] reported procedures to form both axisymmetric and asymmetric components by simultaneous application of axial compressive load and hydraulic internal pressure Al-Qureshi et al [33] reported axisymmetric bulging of thin-walled metal tubes of widely different work hardening characteristics They used polyurethane rod to apply the internal pressure and the friction between the tube bore and the rod provided the axial load on the tube Al- Qureshi [34] presented experimental evidence showing the difference between axisymmetric bulge of thin-walled tubes using the rubber forming technique and hydraulic forming technique He found greater circumferential expansion and longitudinal drawing with rubber forming technique than by hydraulic forming technique

Woo [35] presented a numerical solution for tube bulging under axial compressive force and internal hydraulic pressure assuming that the whole length of the bulged tube was in tension Experiment results presented show reasonably good agreement with the numerical results

Limb et al [36, 37] reported their experimental works on hydraulic bulge forming of tubes using combined axial compressive load and internal hydraulic pressure Both axisymmetric and asymmetric components were formed from various blank material and geometry For axisymmetric bulging Limb et al [38] also developed a theoretical analysis method of the process and suggested the manner in which the internal pressure and the axial load must be varied during the process

Kandil [39] reported experimental works in which tubes of different material were bulge formed axisymmetrically under hydraulic pressure only The experimental results were used to derive empirical relationships between pressure, stress and the die and tube geometry

Sauer et al [40] published their theoretical and experimental work on axisymmetric bulging of tubes by internal pressure and axial load They assumed that a constant ratio of the meridional to circumferential stress in the tube wall is maintained during bulging They developed a computer program to determine the bulge shape when load increments are specified on a step by step basis Woo and Lua [41] extended their earlier theoretical work[35] by introducing anisotropy of tube material and considered bulge forming under internal pressure only

Woo[42] presented an experimental technique of bulge forming closed ended deep vessels from deep drawn tubular blanks which were formed out of circular sheet metal blanks Both hydraulic pressure and axial load were applied in the process Lukanov et al [43] reported an experimental technique of bulge forming of double tee-joints out of a single tubular blank by controlled internal hydraulic pressure

Super-plastic forming of tee-joints from tubular blanks was reported in reference [44] In this process pressurised hot air was used to bulge tubes of lead-tin alloy material Approximate analysis was also given to predict the wall thickness of the formed components The analysis was based on those applicable to simple bulge forming of circular diaphragm

Hashmi[45] put forward an analysis for the prediction of the wall thickness around the circumference of the bulge formed tee brunch The analysis is based on the geometrical consideration of the bulging surface Experimental results indicated that the analysis over-estimated the thinning of the wall Hashmi[46] also reported an analytical method to predict height and thickness distribution of both the axisymmetrically and asymmetrically bulged products The analysis is based on the geometry of the forming bulge and equilibrium conditions The analysis considered variation of the stress ratio at the bulge However, the key parameters like internal pressure, friction, corner radius of the die etc were not taken into consideration for the analysis Later, Hashmi and Crampton[47] presented comparison of experimental results with predictions by the analytical method in reference [46] They found that the theory generally overestimates the thickness of the formed components

Hutchinson et al [48, 49] studied the effect of plunger shape and size (Fig 1) , lubrication and blank material on bulge forming of tubular components using internal hydraulic pressure and axial compressive load They found that all of these factors have considerable effect on bulge shape and size as well as on the forming load

Ueda [50,51] reported a process of manufacturing differential gear casing for automobiles from a single tubular blank by the liquid bulge forming technique with sliding type dies The sliding die components compress the ends of the tube without any relative movement between the tube and the die components thereby reducing friction

Filho and Qureshi [52] developed and tested an experimental machine for the bulge forming of tee joints using elastomer rod They developed theoretical expressions for total forming load prediction and verified them with experimental forming loads with good agreement

Dohmann and Klass[53] reported axisymmetric bulging of tubes with sliding dies The sliding dies push the tube ends giving the axial compressive forming load without friction between die and tube They used hydraulic pressure inside the tube as other forming load

Murata et al [54] reported developing a new machine for axisymmetric tube bulging which initially puts a deflated rubber membrane into a work tube and while forming, the internal pressure is applied on the membrane which in turn presses the tube wall With this machine they experimentally examined the effects of tube end condition and tube length on the deformed shape and the strain distribution therein

Thiruvarudchelvan and Travis[55] reported axisymmetric bulging of copper tubes to bottle shaped products They used urethane rods of different hardness as pressure medium and applied different conditions of lubrication Thiruvarudchelvan with Lua [56] developed a machine for axisymmetric tube bulging that can apply axial compressive force proportional to the internal hydraulic pressure They experimented bulging of copper tubes with this machine and reported an optimum ratio of axial load to internal pressure for which maximum bulging was achieved

Dohmann and Hartl [57] presented a flexible die system for tube bulging to both axisymmetric and asymmetric products The die system with adjustable segments can expand, displace or reduce the tube blank resulting in various shapes of end products The same authors later presented the procedure and methods to develop process controls and the significance of the control for the quality of bulge forming products in reference [58]

Filho et al [59] have done theoretical analysis of the bulge forming of tee junction using elastomor rod The slab method was used to obtain equilibrium equation for different zones of deformation They solved the equations simultaneously by finite difference method to determine the axial compressive load required for the process

Thiruvarudchelvan [60] reported theoretical analysis of initial yield conditions for axisymmetric tube bulging with internal urethane rod He [61] also put forward an approximate theory for determining initial yield pressure and the final forming pressure needed on an internal urethane rod to bulge a tube

Sheng and Tonghai [62] reported experimental research result on forming asymmetric products by bulge forming In addition to internal pressure and axial load, they used counter pressure on the bulged part According to them, this method greatly improved the stress state and raised the forming limit An upper-bound analysis was done to estimate power requirements In the analysis they considered a uniform velocity of material around the whole circumference of the tube

Tirosh et al [63] reported an upper-bound analysis of axisymmetric bulging of tubes by internal pressure and axial compression Guided by their formulation they experimentally tried to find an optimum loading path that would give maximum bulging strain without early failure by buckling or necking

In bulge forming process of tubes, one area of concern is the instability In almost all experimental and analytical studies it was observed that excessive amount of either of the loads (pressure or axial) relative to one another causes instability of the process resulting in necking or bucking Many researchers worked in determining the instability of thin walled tubes Mellor [64] presented an analytical solution to determine the strain at instability of thin-walled tubes In his analysis he assumed that the circumferential to axial stress ratio remains constant and positive throughout the straining process Jones and Mellor [65] later experimentally showed that their theoretical solution in [64] was in satisfactory agreement with experimental values In the experiment they tried to maintain a constant axial load/pressure ratio (obtained from theoretical calculation) to achieve constant stress ratio but could not maintain the constant stress ratio when either the pressure or the axial load reached a maximum

Felgar[66] also analysed instability of pressure vessels subjected to internal pressure and tensile axial load He analysed both thin-walled and thick-walled vessels for constant circumferential and axial stress ratio From experimental results he found that his theoretical prediction of instability pressure is pretty accurate However, the prediction of instability strains were in gross disagreement with the experimental results

Weil[67] theoretically analysed tensile instability of thin-walled cylinders of finite length His analytical results showed that burst pressures increase progressively as the length/diameter ratio of the cylinders is reduced from infinity to lower values His analysis considered a constant ratio of the principal stresses during deformation

All of the above instability studies of cylinders and other similar studies found in secondary references considered a tensile axial loading of the cylinders In bulge forming by pressure and compressive axial load the forming regime is at a totally different strain quadrant Sauer et al [40] developed a theoretical necking criterion for axisymmetric bulging of thin shell tubes They found that the effective strain before necking depends on pre-strain in the material and circumferential stress/axial stress ratio at the point of necking They have concluded from their necking criterion that if the stress ratio could be maintained less than or equal to -1, infinitely large effective strain before necking may be attained Thiruvaraudchelvan and Lua [56], following similar assumptions and procedure, have also noted that when compressive meridional stress is equal to the tensile hoop stress, the instability condition will never be reached for work hardening material however high the strain is

Tirosh et al [63] experimentally tried to attain the so called “infinite strain” in axisymmetric bulge forming of thin-walled tubes From their experiments they could get products free of either buckling or bursting only in the stress ratio range from -1/5 to 0 The experience of Manabe et al [68] is almost similar However, Tirosh et al has not ruled out the possibility of getting closer to stress ratio of -1 to attain an infinite strain forming situation

Eldred et al [69] reported a different kind of tube manipulation system suitable for manufacturing complex tubular components for the automobile and other industries The process patented as “vari-form” uses internal hydraulic pressure to a pre-bent tube to create structural tubular components of varying cross section, complete with mounting holes

Apart for tube bulging, bulge forming technique has been utilised in forming spherical pressure vessels [70, 71] In this process an integral polyhedron is made by joining flat pentagonal and hexagonal blank sheets of metal in a specific pattern The polyhedron is then bulged by internal hydraulic pressure

2.2.2 Simulation Studies

Bulge forming of industrial components is usually a complex process involving multidirectional forming load The geometric shape of most products warrant three dimensional finite element analysis Until recently finite element analysis of metal forming in three dimension was very computer resource intensive But development of faster computer processors at lower prices and the availability of dynamic explicit finite element programs have made it a possibility to numerically analyse complex metal forming problems At present most applications of three dimensional FEA are in sheet metal forming sector- specially products related to automobile industry In comparison, analyses in other metal forming processes requiring three dimensional treatment are negligible In bulge forming it is even rare

Most finite element analysis of bulge forming processes are done for simple bulging of circular diaphragms Various studies of this nature have been presented in the previous section Lange et al [72] have presented a simulation study of axisymmetric bulging of tubes Taking advantage of axisymmetry, the analysis was done in two dimension using implicit codes of their own They have simulated the process for three different load characteristics defining the relation between the pressure load and the axial load For moderate axial load, the simulation results agreed quite well with experimental results However, for higher axial load, substantial difference between the simulated results and experimental results were observed

Bauer[73] reported finite element simulation of a process that bulge a hollow cam shaft from pipe The process, termed as interior high pressure process, involves forming of a pipe by very high internal pressure and simultaneous force in the axial direction In this process cams are fitted with the shafts and bearing surfaces are formed simultaneously Essentially a three dimensional simulation was done A commercial explicit FE code, LS-DYNA3D, was used for the purpose Two loading situations viz pressure load with axial compression and pressure load without any axial compression were simulated It was found that cams are better fit and bearing surfaces well developed by pressure load and axial compression Residual stress in the shaft and fitted components were also less for this loading Also, forming by pressure loading only reduces the thickness of the pipe wall thereby affecting the shaft strength Comparison of simulated displacements and stress results with those obtained by extensive measurements on formed cam shafts_showed that the agreement is generally very good

Michino et al [74] presented a 3D finite element analysis of forming elbows from straight tubes by internal pressure and axial loading They used commercial implicit code, MARC, for the analysis The process involves little bulging but the deformation induces large strains The prediction of the total load, distribution of strain and configuration of the elbow by FE simulation agreed well with the experimental findings

In available literature no other simulation study of tube bulging could be found However, a couple of simulation studies on bulging of a different kind i e , bulging of an integral polyhedron to a spherical vessel was reported Zhang and Wang [75] presented the 3D simulation of a part of 32- petal polyhedron taking advantage of the repeated pattern of the polyhedron An implicit finite element method was used The FE analysis results are reported to be in good agreement with those from experiments Hashemi and Zhang [76] presented a 3D finite element analysis of the full polyhedron using commercial code ABAQUS The simulation, according to the authors, helped understand the mechanics of the process in detail Also the simulation predicted the bulging pressure with reasonable accuracy and showed accurate patterns of stress distribution

2.2.3 Relevant Studies

Generally bulge forming is a large deformation and large strain forming process From this perspective, deep drawing of sheet metal is similar to bulge forming although the loading method and pattern is completely different Also, the initial blank is curved in bulge forming as opposed to flat sheet in deep drawing Large number of simulation studies in deep drawing available in literature Recent studies include asymmetric product analysis in three dimensions Most studies are done assuming thin shell behaviour of the sheet which is sharply in contrast with bulge forming of tubes However, for the sake of completeness of the survey, some recent 3D studies of deep drawing are presented in the following

Honecker and Mattiasson [77] evaluated the commercially available FE codes viz implicit ABAQUS and explicit DYNA3D by simulating deep drawing of automotive parts The authors concluded that explicit codes are primarily suitable for large scale 3D problems which could hardly be performed by implicit code Mattiasson et al [78] also simulated and evaluated deep drawing of cylindrical cups and rectangular boxes by using DYNA3D code They found that the agreement between the numerical and experimental results has been good and indicated that explicit dynamic code like DYNA3D offers an efficient and robust means to simulate forming of large scale 3D products

Rebelo et al [79] also simulated deep drawing of an oil pan by commercial FEA code, ABAQUS They used both implicit and explicit module of ABAQUS for comparison They also concluded that for practical large scale problems the explicit method offers considerably more potential than the implicit method Yoo et al [80] simulated deep drawing of cylindrical, elliptical and hemispherical cup and a clover type cup by using their own implicit FE code involving continuous contact treatment and membrane elements with bending effects Their computation results have been shown to be in good agreement with available experimental and analytical results

Teodosiu et al [81] simulated can-making process They treated the sheet as thick shell and used solid elements for analysis Using semi-implicit FE code of their own, the authors confirmed the good performance of solid elements in very accurate analysis of through- thickness stress

The above studies most of which were done using commercially available codes indicate that complex three dimensional problems can be simulated by these packages with satisfactory results Some of the complex bulge forming simulation studies cited in the previous section also showed the capability of the packages in obtaining good results

2 3 Optimisation Studies

Analysis of metal forming is a product as well as a process study Thus both the product and process variables affect the metal flow Naturally, a certain combination of these variables would result in a better performance measure of the product than other combinations The process of finding the best combination of variables is thus a logical pursuit Experimental studies to obtain better metal forming condition by varying variable values are common This study, however, concerns with analytical optimisation studies at design stage of metal forming analysis This is a relatively new area of study informally termed by some as computational design optimisation This involves integration of finite element simulation program with mathematical optimisation technique(s) in such a manner that a repeated sequence of 'simulation', 'evaluation' and 'variation' are carried out until an optimum condition is reached

There are three areas of computational design optimisation One is structural design optimisation where in the deformation is within the elastic limit of the material The other area is metal forming where the state of deformation is essentially in the plastic region And the third kind is the optimisation of the thermo- fluid and other problems in engineering design There are many studies on structural design optimisation Arora [82] and Cohn[83] in their review paper on design optimisation, have listed a representative collection of such studies Comparatively, few studies are done on design optimisation of metal forming No such work on bulge forming could be found in the literature However, optimisation studies in other metal forming processes are considered to be relevant and, therefore, presented in the following

Kusiak and Thompson [84] reported optimisation of extrusion die shape by minimising the ram force Becker and Kopp[85] presented an algorithm of optimisation and cited successful application to flat rolling and drop forging by minimising the power and strain gradient respectively Joun and Hwang [86-88] have presented an algorithm using a simulation module of penalty rigid-viscoplastic finite element method and optimisation module involving design sensitivity and gradient projection method They applied the algorithm to the optimal design of an extrusion die profile by minimising the forming energy Han et al [89] have presented design of intermediate die shapes for plane strain and axisymmetric forging Their approach is based on backward deformation finite element simulation and shape optimisation techniques Shu and Hung [90] presented optimisation of springback reduction in U-channel formed by double bend technique They used ABAQUS code for finite element simulation and MOST, an optimisation program The two programs are appropriately interfaced for the work The results are compared with experimental data in literature and found good agreement

Kusiak[91] described a non-gradient optimisation technique that can be coupled with commercial FE programs for metal forming He substantiated his algorithm by finding an optimum die shape for axisymmetric closed die forging where uniform distribution of the austenite grains in the material of the forged piece is chosen as the optimisation criterion

Fourment and Chenot [92] formulated a shape optimisation method for non-steady state metal forming process A finite element method with remeshing capability and unconstrained optimisation method were used in the formulation Fourment et al [93] applied this formulation to the shape optimisation of the pre-forming tools for forging

Roy et al [94, 95] formulated and used a genetic algorithm for optimisation Using that algorithm and a FE package, NIKE2D they optimised the process variables of multi-pass wire drawing , multi-pass cold drawing of a tubular profile and cold forging of an automotive outer race

Most of the design optimisation algorithms consider the design variables to be continuous in the design space But in practical engineering , the design variable values are discrete As such values obtained from a design optimisation exercise may have to be approximated to nearby discrete values This might result in loss of the optimality Park et al [96] has used Taguchi parameter design method to obtain discrete design variables by post processing a structural optimisation solution In metal forming no such exercise could be found

2.4 Summery of the Literature Survey and Possible Scope of Work

From the literature cited and described in the previous section, the following points may be noted

i Analysis of simple bulge forming mainly focused on the pole region ignoring the situation at the periphery But studies suggest that end behaviour influence the deformation at the pole

ii No experimental or analytical study was found for bulging of rectangular or square sheets to cylindrical bulging with compound loading

iii Most finite element simulations of simple bulge forming ignored the peripheral boundary conditions As a result poor agreement with experimental results were observed specially at the periphery Some studies that included proper boundary condition provided better simulation results

iv Many experimental studies were done on both axisymmetric and asymmetric bulging of tubular blanks These studies covered a wide variety of process variables such as different material, tube size, pressure medium and also different die configurations

v Also quite a good number of analytical studies were done on axisymmetric bulging of tubes Studies were done for both hydraulic or solid pressure media The studies enabled prediction of bulging deformation and forming loads

vi Comparatively, very few analytical studies were done on asymmetric bulging of tubes Few studies that were done predicted deformation, thickness and forming load These analyses were done based on the study of the geometry of the deformed configurations Process parameters like internal pressure or the material characteristics were not considered in these analyses vii Instability in a tube undergoing bulging by internal pressure and axial tensile load (by keeping the ends fixed) was analysed and verified experimentally Analytical study of bulging of tubes with internal pressure and axial compressive load suggest that if the compressive axial stress could be maintained equal to the tensile hoop stress in the bulge, then infinitely large effective strain could be attained in the bulge However, no experimental exercise could achieve that stress ratio, let alone maintain that The reason for this is not yet known from the literature

viii Very few finite element simulation studies were found on bulge forming of tubular components One or two studies were done on axisymmetric bulge forming Asymmetric bulge forming of tubular components which are more complex and need 3D treatment were not simulated so far Finite element simulation of this type of problems could be immensely helpful in understanding the stress and strain patterns in the products as well as in the design of dies and determination of failure free operating parameters for a variety of blank materials and geometry

ix New manufacturing processes are developing based on bulge forming principle These new processes are used for manufacturing parts and components for important industrial sectors like automobile These new processes may be simulated for better product and process design

xi Computational design optimisation is a new area of research which demand extensive computer resources Good number of studies were reported in the areas of structural optimisation Comparatively, optimisation of metal forming is far less explored Studies that were reported dealt optimisation of two dimensional axisymmetric cases like extrusion and forging Optimisation of axisymmetric bulge forming cases are worth exploring

2 5 Objectives of this Work

Various scopes of work identified in the previous section mainly defined the objectives of this project Generally, the work was on the finite element simulation and analysis of different bulge forming processes Different forming conditions varying the loading ratio, blank size, blank material, friction condition etc were simulated Besides, some forming situations were simulated using two different solution procedure Pattern of metal flow, nature of deformation, stress and strain distribution, changes of thickness, development of stress or strain in any particular area of the formed product etc were the general focus of attention Specific cases of simulation that were undertaken in this project are

i Simulation of the bulge forming of a circular plates using pressure and in-plane compressive load with or without restraining load on the forming bulge
ii Optimisation of the bulge forming of a circular plate using pressure and in-plane compressive load
iii Simulation of bulging a rectangular plate in the middle
iv Simulation of axisymmetric bulging of a cylindrical tube using internal liquid pressure and axial compressive load
v Optimisation of axisymmetric bulging of a cylindrical tube
vi Simulation of asymmetric bulging of a cylindrical tube to a T-branch by using internal liquid pressure and axial compressive load
vii Simulation of the failure T-branch forming process
viii Simulation of the forming of a box-shaped elbow from a circular tube

Simulation of these cases has been carried out using two commercial FE packages viz ANSYS and LS-DYNA3D Some of the simulation results have been verified with experimental results available in the literature to establish the acceptability of the simulation results

2 6 Brief Description of the Project

The work of the project started with a 486 PC with 16MB of memory and 480MB hard disk space Relatively simpler and computationally less intensive modelling and simulation of axisymmetric bulge forming of circular plates was taken up with this computer ANSYS package licensed for limited model size was used for this work Soon it was realised that this computer would not be suitable for modelling and analysis in three dimension Therefore, a pentium PC with 64MB memory and 2GB hard disk space was bought and the limited version of ANSYS was installed for further work Three dimensional analysis of bulging rectangular plate and forming of T-branch from tube were carried out with this configuration But these analyses could not be carried out with intended full load because of the limitation on model size imposed by the analysis package, ANSYS Also the computation time for the solution of even a limited model of these problems was unusually high, for the simulation of T-branch forming it took several weeks At this point of the project the need for a faster solver was felt Going through the literature it was found that direct and implicit solvers like ANSYS are good for relatively smaller size problems Most large size problems are analysed by explicit solvers So, an explicit solver, LS-DYNA3D for PC was procured This package was installed in another pentium of 32MB memory and 1GB hard disk space DYNA3D is a public domain software and LS-DYNA3D is a commercial version of it Although it is widely used FEA package, the PC version of it is relatively new The pre-processor coming with this version is not very well developed to build complex finite element models It is also very poor in post-processing, very basic features are available at the moment Nevertheless, modelling and simulation of the failure of T-branch forming and bulge forming of an elbow were done with this package These simulations were done using shell elements as applying pressure load to brick elements was a difficulty mainly because of its poor pre-processing capability These simulations provided good learning opportunity to this package which later proved to be very useful

In the mean time ANSYS was in the process of incorporating LS-DYNA3D solver in its package as an add-on Towards the end of the project this add-on facility was procured and installed in the 64MB memory pentium used earlier for ANSYS This could be used with the existing ANSYS pre and post processor This coupled with the experience obtained earlier on LS-DYNA3D solver enabled simulation of the aimed complex cases fairly quickly The simulations of axisymmetric bulging of tubes and T-branch forming at different forming conditions were carried out in this newly installed configuration The hard disk space (2GB) of the computer run out of space very quickly Another 5GB of space was added to the computer

Looking back to the project some points may be jotted down

i when the project started in 1993 the pentium PCs were not available in the market,

ii also, the explicit solvers were not available at the PC level,

iii there was limitation on financial resource to procure workstations and the softwares

iv the computing capacity at PC level was growing very fast,

v computation intensive engineering analysis packages were adapting to the growing computing power at the PC level

Given this constraints and opportunities it was probably better to develop as the need arises specially for computational engineering research projects like this It is reckoned that the project was done with much less cost than investing on higher end computers at the beginning

Chapter Three

FINITE ELEMENT METHOD - THEORETICAL BACKGROUNDS

3 1 Finite Element Method

Finite element method is quite an involved subject both in terms of mathematical theory and in terms of application in engineering analysis This section does not delve into the details of finite element method Instead, a basic theoretical outline of the method will be presented drawing mostly from references[97, 98]

The basic steps in the finite element method are

1 Discretise the region of interest . Divide the problem domain into a number of finite subdomains each of simple geometry Each subdomain called element has a number of nodal points, the locations in space of which are given in co-ordinates relative to a set of global axes The shape of each element is defined in terms of these co-ordinates by interpolation or shape functions

2 Assume a variation of the unknown An interpolation function is proposed for the variation of the unknown (e g displacement, temperature) inside each element in terms of values at the nodes These interpolation functions in many cases are the same as the shape functions used to describe the element shape

3 Find element response matrices For each element, coefficient matrices which describe the response characteristics of the element are determined In solid mechanics applications, for example, a matrix of stiffness coefficients is computed In order to determine the stiffness matrix the material behaviour has to be defined

4 Assemble the element matrices . To find the stiffness matrix of the whole problem domain, the stiffness matrices of the individual elements are combined This forms a matrix equation expressing the behaviour of the entire solution region

5 Solve the system of equations : In most problems the number of equations is large, thus special solution techniques are employed After solution the values of the dependant variables at all the nodes of the domain are known

6 Determine other variables Using the nodal values and interpolation functions, other parameters such as strain, stress etc inside each element may be determined

3.1 1 General Theory

The governing differential equations of equilibrium for finite element method can be derived directly by equilibrium considerations on differential elements of the body or by using the stationary condition of the total potential of the body An equivalent approach to express the equilibrium of the body is to use the principle of virtual displacements This principle state that the equilibrium of the body requires that for any compatible, small virtual displacements which satisfy the essential boundary conditions imposed onto the body, the total internal virtual work is equal to the total external virtual work That is, for a general three-dimensional body with body forces $\mathbf{f}^B$, surface traction $\mathbf{f}^S$ and concentrated forces $\mathbf{F}^i$ resulting in virtual displacements **U**, virtual strain ε and stress τ,

$$\int_V \{\bar{\varepsilon}\}^T \{\tau\} dV = \int_V \{\bar{U}\}^T \{f^B\} dV + \int_S \{\bar{U}^S\}^T \{f^S\} dS + \sum_i \{\bar{U}^i\}^T F^i \qquad (1)$$

where,

$\{\bar{\varepsilon}\}^T = [\bar{\varepsilon}_{XX}\ \bar{\varepsilon}_{YY}\ \bar{\varepsilon}_{ZZ}\ \bar{\gamma}_{XY}\ \bar{\gamma}_{YZ}\ \bar{\gamma}_{ZX}]$

$\{\tau\}^T = [\tau_{XX}\ \tau_{YY}\ \tau_{ZZ}\ \tau_{XY}\ \tau_{YZ}\ \tau_{ZX}]$

$\{\bar{U}\}^T = [\bar{U}\ \ \bar{V}\ \ \bar{W}]$ $\bar{U}$, $\bar{V}$ and $\bar{W}$ are displacement in global directions

$\{f^B\}^T = [f_x^B\ f_y^B\ f_z^B]$

$\{f^S\}^T = [f_x^S\ f_y^S\ f_z^S]$ superscript S indicates surface

$\{F^i\} = [F_x^i\ F_y^i\ F_z^i]$ superscript i indicates points

The internal virtual work is given on the left side of (1) and is equal to actual stresses $\{\tau\}$ going through the virtual strains $\{\varepsilon\}$ The external work is given on the right side of (1) and is equal to the actual forces $\{f^B\}$, $\{f^S\}$ and $\{F^i\}$ going through the virtual displacement $\{\bar{U}\}$ In the above, the displacements considered should be continuous and compatible and should satisfy the displacement boundary conditions, and the stress should be evaluated from the strains using the appropriate constitutive relations Although Equation 1 is *written* in the global co-ordinate system X, Y, Z of the body, it is equally valid in any other system of co-ordinates

In finite element analysis the problem domain is approximated as an assemblage of discrete finite elements with the elements being interconnected at nodal points on the element boundaries The displacements measured in a local co-ordinate system x, y, z within each element are assumed to be a function of the displacements at the N finite element nodal points Therefore, for element m

$$u^{(m)}(x,y,z) = H^{(m)}(x,y,z)\hat{U} \qquad (2)$$

where $H^{(m)}$ is the displacement interpolation matrix or shape function, the superscript m denotes element m and $\hat{U}$ is a vector of three global displacement components U_i, V_i and W_i at all nodal points, including those at the supports of the element assemblage, i e , $\hat{U}$ is a vector of dimension 3N, and is expressed more generally as,

$$\hat{U}^T = [U_1 U_2 U_3 \qquad U_N] \qquad (3)$$

where it is understood that U_i may correspond to a displacement in any direction, which may not even be aligned with a global co-ordinate axis, and U_i may also signify a rotation when beams, plates or shells are considered

Although all nodal points displacements are listed in $\hat{U}$, it should be realised that for a given element only the displacements at the nodes of the element affect the displacement and strain distributions within the element With the assumption on the displacements in (2) corresponding element strains can now be evaluated as,

$$\varepsilon^{(m)}(x,y,z) = B^{(m)}(x,y,z)\hat{U} \qquad (4)$$

where, $\mathbf{B}^{(m)}$ is the strain-displacement matrix, the rows of $\mathbf{B}^{(m)}$ are obtained by appropriately differentiating and combining rows of the matrix $\mathbf{H}^{(m)}$ By using (2) and (4), the assemblage process of the element matrices to the whole structure matrices, refereed to as the direct stiffness method is automatically performed in the finite element application of the principle of virtual displacements

The stress within a finite element are related to the element strains and the element initial stresses by

$$\tau^{(m)} = C^{(m)}\varepsilon^{(m)} + \tau^{I(m)} \qquad (5)$$

where $\mathbf{C}^{(m)}$ is the matrix relating strain to stress of element m and $\tau^{I(m)}$ are element initial stresses The material law specified in $\mathbf{C}^{(m)}$ for each element can be that of an isotropic or anisotropic material and can vary from element to element

Using the assumption on the displacements within each finite element, as expressed in (2), equilibrium equations that correspond to the nodal point displacements of the assemblage of finite elements can now be derived Equation 1 can be rewritten as a sum of integrations over the volume and areas of all finite elements, i e ,

$$\sum_m \int_{V(m)} \bar{\varepsilon}^{(m)T} \tau^{(m)} dV^{(m)} = \sum_m \int_{V(m)} \bar{U}^{(m)T} f^{B(m)} dV^{(m)} + \sum_m \int_{S(m)} \bar{U}^{s(m)T} f^{s(m)} dS^{(m)} + \sum_i \bar{U}^{iT} F^{i} \qquad (6)$$

where m = 1, 2, k , k = number of elements

It is important to note that the integrations in (6) are performed over the element volumes and surfaces, and that for convenience different element co-ordinate systems may be used in the calculations Substituting (2)-(5) into (6) for the element displacements, strains and stresses,

$$\bar{U}^T\left[\sum_m \int_{V(m)} B^{(m)T} C^{(m)} B^{(m)} dV^{(m)}\right]\hat{U} = \hat{U}^T\left[\begin{array}{l}\left\{\sum_m \int_{V(m)} H^{(m)T} f^{B(m)} dV^{(m)}\right\} + \\ \left\{\sum_m \int_{S(m)} H^{S(m)T} f^{S(m)} dS^{(m)}\right\} - \\ \left\{\sum_m \int_{V(m)} B^{(m)T} \tau^{I(m)} dV^{m}\right\} + F\end{array}\right] \qquad (7)$$

where the surface displacement interpolation matrices $\mathbf{H}^{s(m)}$ are obtained from the volume displacement interpolation matrices $\mathbf{H}^{(m)}$ in (2) by substituting the element surface co-ordinates and **F** is a vector of the externally applied forces to the nodes of the element assemblage It may be noted that i_{th} component in **F** is the concentrated nodal force, which corresponds to i_{th} displacement component in $\hat{U}$ In (7) the nodal point displacement vector $\hat{U}$ of the element assemblage is independent of the element considered and is therefore taken out of the summation signs

To obtain from (7) the equations for the unknown nodal point displacements, virtual displacement theorem can be used by imposing unit virtual displacements in turn at all displacement components In this way $\hat{U}^{T} = \mathbf{I}$ (identity matrix) , and denoting nodal point displacements by **U**, i e , letting $\hat{U} \equiv \mathbf{U}$, the equilibrium equation of the element assemblage corresponding to the nodal point displacements are

$$K \; U = R \tag{8}$$

where $\mathbf{R} = \mathbf{R}_B + \mathbf{R}_S - \mathbf{R}_I + \mathbf{R}_C$

The matrix **K** is the stiffness matrix of the element assemblage ,

$$K = \sum_{m} \int_{V(m)} B^{(m)T} C^{(m)} B^{(m)} d V^{(m)} \tag{9}$$

The load vector R includes the effect of the element body forces ,

$$R_B = \sum_{m} \int_{V(m)} H^{(m)T} f^{B(m)} d V^{(m)} \tag{10}$$

the effect of the element surface forces

$$R_S = \sum_{m} \int_{S(m)} H^{S(m)T} f^{S(m)} d S^{(m)} \tag{11}$$

the effect of element initial stresses,

$$R_I = \sum_{m} \int_{V(m)} B^{(m)T} \tau^{I(m)} d V^{m} \tag{12}$$

and the concentrated loads, $\mathbf{R}_C = \mathbf{F}$

It may be noted that the summation of the element volume integrals in (9) expresses the direct addition of the element stiffness matrices $\mathbf{K}^{(m)}$ to obtain the stiffness matrix of the total element assemblage In the same way, assemblage body force vector $\mathbf{R_B}$ is calculated by directly adding the element body force vectors, $\mathbf{R_B}^{(m)}$ $\mathbf{R_S}$, $\mathbf{R_I}$ and $\mathbf{R_C}$ are obtained in similar manner

Equation (8) is a statement of the static equilibrium of the element assemblage In these equilibrium considerations, the applied forces may vary with time, in which case the displacements also vary with time and (8) is thus a statement of equilibrium for any specific point in time However, if in actuality the loads are applied rapidly, inertia forces need to be considered , i e , a truly dynamic problem need to be solved Using d Alembert s principle, the element inertia forces may simply be included as part of the body forces Assuming that the element accelerations are approximated in the same way as the element displacement (2), the contribution from the total body forces to the load vector **R** is

$$R_B = \sum_m \int_{V(m)} H^{(m)T} \left[f^{B(m)} - \rho^{(m)} H^{(m)} U \right] dV^{(m)} \qquad (13)$$

where $\mathbf{f}^{B(m)}$ no longer includes inertial forces, U lists the nodal point accelerations, and $\rho^{(m)}$ is the mass density of the element m The equilibrium equations are, in this case,

$$M \quad U + K \; U \; = \; R \qquad (14)$$

where **R** and **U** are time dependent The matrix **M** is the mass matrix of the structure,

$$M = \sum_m \int_{V(m)} \rho^{(m)} H^{(m)T} H^{(m)} dV^{(m)} \qquad (15)$$

In actually measured dynamic response of structures it is observed that energy is dissipated during vibration, which, in vibration analysis is usually taken account of by introducing velocity- dependent damping forces Introducing the damping forces as additional contributions to the body forces as additional contributions to the body forces are,

$$R_B = \sum_m \int_{V(m)} H^{(m)T} \left[f^{B(m)} - \rho^{(m)} H^{(m)} U - \kappa^{(m)} H^{(m)} U \right] dV^{(m)} \qquad (16)$$

where U is a vector of the nodal point velocities and K $^{(m)}$ is the damping property parameter of element m The equilibrium equations then take the shape of,

$$M \quad U + C \quad U + K \; U \; = \; R \qquad (17)$$

where **C** is the damping matrix of the structure and

$$C = \sum_{m} \int_{V^{(m)}} \kappa^{(m)} H^{(m)T} H^{(m)} dV^{(m)} \tag{18}$$

In the above formulation it is assumed that the displacement of the finite element assemblage are infinitesimally small and that the material is linearly elastic Also it is assumed that the nature of the boundary conditions remains unchanged during the application of the loads on the finite element assemblage

The above assumptions have entered the equilibrium equation in the following forms

1 the fact that the displacement must be small has entered into the evaluation of the matrix **K** and load vector **R**, because all integrations have been performed over the original volume of the finite elements,

2 the strain - displacement matrix **B** of each element was assumed to be constant and independent of element displacements,

3. the assumption of a linear elastic material is implied in the use of a constant stress-strain matrix **C**

4 the unchanged boundary conditions is implied by keeping constant constraint relations for the complete response

The above observations point to different kind of non-linearity that may arise in finite element analysis They are categorised as

i Material non-linearity

ii Non-linearity due to large displacements, large rotations, but small strains

iii Non-linearity due to large displacements, large rotations and large strains

iv Non-linearity due to contact

3.1.2 Solution Methodology

The solution procedure for non-linear problems depends on the type of non-linearity and is part of the complete modelling process The basic problem in a general non-linear analysis is to find the state of equilibrium of a body corresponding to applied loads Assuming that the externally applied loads are described as a function of time, the equilibrium conditions of a system of finite element representing the loading under consideration can be expressed as

$$ {}^{t}R - {}^{t}F = 0 \qquad (19) $$

where ${}^{t}R$ lists the externally applied nodal point forces in the configuration at time t and the vector ${}^{t}F$ lists the nodal point forces correspond to the element stresses at the same configuration ${}^{t}R$ and ${}^{t}F$ may respectively be expressed as,

$$ {}^{t}R = {}^{t}R_{B} + {}^{t}R_{S} + {}^{t}R_{C} \qquad (20) $$

and

$$ {}^{t}F = \sum_{m} \int_{{}^{t}V^{(m)}} {}^{t}B^{(m)T}\, {}^{t}\tau^{(m)}\, {}^{t}dV^{(m)} \qquad (21) $$

where in a general large deformation analysis the stress as well as the volume of the body at time t are unknown

Equation (19) must express the equilibrium of the system in the current deformed geometry taking due account of all non-linearity Also in a dynamic analysis, the vector ${}^{t}R$ would include the inertial and damping forces

Considering the solution of the non-linear response, it is recognised that (19) must be satisfied throughout the complete history of load application Three basic choices need to be made for the solution of the large deformation problems They are,

i the type of the mesh

ii the kinematics description, i e , how the deformation is measured

iii the kinetic description, i e , how the stresses are measured

Once these choices are made the solution process is effectively carried out using a step by step incremental analysis The basic approach in an incremental step by step solution is to assume that the solution for the discrete time t is known, and that the solution for the discrete time t+Δt is required, where Δt is a suitably chosen time increment Hence, at time t+Δt (19) can be rewritten as

$$ {}^{t+\Delta t}R - {}^{t+\Delta t}F = 0 \qquad (22) $$

Since the solution is known at time t, it can be written that

$$ {}^{t+\Delta t}F = {}^{t}F + F \qquad (23) $$

where, F is the increment in nodal point forces corresponding to the increment of element displacements and stresses from time to time t to time (t + Δ t) This vector can be approximated using a tangent stiffness matrix, ${}^{t}K$, which corresponds to the geometric and material condition at time t,

$$ F \cong {}^{t}K \; U \qquad (24) $$

where **U** is the vector of incremental nodal point displacements Substituting (24) and (23) in (22),

$$ {}^{t}K \; U = {}^{t+\Delta t}R - {}^{t}F \qquad (25) $$

and solving for **U**, an approximation to the displacements at time t+Δt can be calculated,

$$ {}^{t+\Delta t}U \cong {}^{t}U + U \qquad (26) $$

The exact displacement at time t+Δt are those that corresponds to the applied loads ${}^{t+\Delta t}R$ Only an approximate displacement is calculated by (25)

Having evaluated an approximation to the displacements corresponding to time t+Δt, an approximation for stresses and corresponding nodal point forces at time t+Δt can be obtained, and could then be proceeded to the next time increment calculations However, because of the approximation expressed in (25) such a solution may be subject to very significant errors and, depending on the time or load step sizes used, may indeed be unstable In practice, it is therefore frequently necessary to iterate until the solution of (22) is obtained to sufficient accuracy

Depending on the type of problem, different solution procedure is adopted for the solution of (25) For static non-linear problems Newton-Raphson iterative procedure along with Gauss elimination method or other suitable method for the solution of the system of equations are employed For non-linear dynamic problems also the same incremental formulation of finite elements and the same iterative solution procedure are used along with either explicit or implicit time integration method In this work the explicit time integration method was used for simulation of large problems Therefore, this method is briefly outlined bellow

The most common explicit time integration operator used in non-linear dynamic analysis is probably the central difference operator The equilibrium of the finite element system is considered at time t in order to calculate the displacements at time t+Δt Solution is sought for each discrete time step for the equilibrium equation neglecting the effect of damping which may be expressed as,

$$M \; {}^{t}U = {}^{t}R - {}^{t}F \tag{27}$$

where the nodal point force vector ${}^{t}F$ is evaluated on the basis of the ways how the material and the geometric non-linearities are formulated This involves the choice of element type, kinematics and kinetic descriptions which are problem dependent The solution for the nodal point displacements at time t+Δt is obtained using the central difference approximation for the accelerations In this approximation it is assumed that

$${}^{t}U = \frac{1}{\Delta t^{2}}\left\{ {}^{t-\Delta t}U - 2\,{}^{t}U + {}^{t+\Delta t}U \right\} \tag{28}$$

Substituting (28) in (27),

$$\frac{M}{\Delta t^{2}}\left\{ {}^{t+\Delta t}U \right\} = {}^{t}R - {}^{t}F - \frac{M}{\Delta t^{2}}\left\{ {}^{t-\Delta t}U - 2\,{}^{t}U \right\} \tag{29}$$

Thus, if ${}^{t-\Delta t}U$ and ${}^{t}U$ are known ${}^{t+\Delta t}U$ can be calculated from (29) The shortcoming in the use of the central difference method lies in the severe time step restriction for stability, the time step size Δt must be smaller than a critical time step, Δt_{cr} , which is equal to T_n/π, where T_n is the smallest period in the finite element system

In the present work two commercial finite element analysis packages, viz ANSYS and LS-DYNA3D were used ANSYS was used for the simulation of relatively simple static non-linear problems While LS-DYNA3D was used for complex three dimensional problems In the next two sections theoretical aspects of these packages with respect to element formulations and solution procedures and techniques will be presented

3.2 ANSYS Theoretical Methods

ANSYS is a general purpose finite element analysis package It can simulate problems in area of structural mechanics, electromagnetic, heat transfer, fluid dynamics, acoustics and coupled problems In structural analysis it has the capability to analyse static or dynamic linear and non-linear problems In addition, ANSYS has a design optimisation module based on non-linear optimisation theories which in conjunction with finite element procedure can be utilised for the optimisation of structural linear or non-linear problems The simulations carried out in this work are non-linear in nature Therefore, the theoretical procedures presented henceforth relates to non-linear problems only The theoretical methods described in the following sub-sections are taken from the manuals of ANSYS [99]

3.2.1 Solution Procedures

In ANSYS Newton-Raphson procedure is used for iterative solution of the equilibrium equations presented in 3 1 Wavefront solvers or conjugate gradient solvers are used for the solution of the system of equation at each iteration

In Newton-Raphson procedure an iterative solution is sought for the equation (22) by defining an out-of-balance load vector $\Delta\mathbf{R}_{(i-1)}$ as

$$\Delta\mathbf{R}_{(i-1)} = \{\mathbf{F}^a\} - \{\mathbf{F}_i^{nr}\} \tag{30}$$

where $\{\mathbf{F}^a\}$ is the vector of applied loads and $\{\mathbf{F}_i^{nr}\}$ is the vector of restoring loads corresponding to the element internal loads By the virtual displacement principle $\Delta\mathbf{R}_{(i-1)}$ is related as

$$[\mathbf{K}_i^T]\,\{\Delta\mathbf{u}_i\} = \Delta\mathbf{R}_{(i-1)} = \{\mathbf{F}^a\} - \{\mathbf{F}_i^{nr}\} \tag{31}$$

and

$$\{\mathbf{u}_{i+1}\} = \{\mathbf{u}_i\} + \{\Delta\mathbf{u}_i\} \tag{32}$$

Both $[\mathbf{K}_i^T]$ and $\{\mathbf{F}_i^{nr}\}$ are evaluated based on the values given by $\{\mathbf{u}_i\}$ The subscripts in the above equations refer to iteration numbers The final converged solution would be in equilibrium , such that the restoring load vector $\{\mathbf{F}_i^{nr}\}$ would equal to the applied load vector $\{\mathbf{F}^d\}$ or at least to within some tolerance If the analysis involves path dependent non-linearity such as plasticity, then the solution process requires that some intermediate steps be in equilibrium in order to correctly follow the load path This is accomplished effectively by specifying a step by step incremental analysis, i e , the final load vector $\{\mathbf{F}^a\}$ is reached by applying the load in increments and performing the Newton-Raphson iterations at each step

The incremental time is automatically determined by number of factors such as number of equilibrium iteration needed, time point at which element will have change of status allowable plastic strain increment etc Depending on the problem, different analysis tools such as adaptive descent and line search method is used to overcome convergence difficulties Convergence's is assumed when vector norm

$$\|\{R\}\| < \varepsilon_R R_{ref} \tag{33}$$

where {R} is the residual vector and

$$\{R\} = \{F^a\} - \{F^{nr}\} \tag{34}$$

ε_R is tolerance (default = 0 001) and R_{ref} is reference values which is $[[\{F_a\}]]$ by default The vector norm used in the analysis is the square root of the sum of the squares value of the terms expressed as,

$$\|\{R\}\| = \left(\sum R_i^2\right)^{\frac{1}{2}} \tag{35}$$

3.2 2 Large Strain Theory

Large strain theory of ANSYS is used for elastic-plastic elements Let a body has a position vector {X} and {x} at its undeformed state and deformed state respectively Then the displacement vector {u} would be

$$\{u\} = \{x\} - \{X\} \tag{36}$$

The deformation gradient defined as $[F] = \dfrac{d\{x\}}{d\{X\}}$ applied to (36) would give,

$$[F] = [I] + \frac{d\{u\}}{d\{X\}} \tag{37}$$

where the symbol [] stand for matrix and [I] is the identity matrix

The deformation gradient [F] includes the volume change, the rotation and the shape change of the deforming body [F] can be separated into a rotation and the shape change matrix using the right polar decomposition theorem

$$[F] = [R][U] \tag{38}$$

where $[\mathbf{R}]$ = rotation matrix

$[\mathbf{U}]$ = right stretch (shape change) matrix

Once $[\mathbf{U}]$ is known, then the logarithmic strain measure can be obtained as

$$[F] = \ln[U] \tag{39}$$

Computationally, the evaluation of (39) is performed by one of the two methods using incremental approximation

$$[\varepsilon] = \int d[\varepsilon] \cong \sum [\Delta \varepsilon_n] \tag{40}$$

with

$$[\Delta \varepsilon_n] = \ln[\Delta U_n] \tag{41}$$

where n refers to current time step and $[\Delta \mathbf{U}_n]$ is the incremental stretch matrix computed from the incremental deformation gradient,

$$[\Delta F_n] = [\Delta R_n][\Delta U_n] \tag{42}$$

where $[\Delta F_n]$ is

$$[\Delta F_n] = [F_n][F_{n-1}]^{-1} \tag{43}$$

where $[F_n]$ is the deformation gradient at the current time step and $[F_{n-1}]$ is at the previous time step

Method 1 for evaluating (41) is

$$[\Delta \varepsilon_n] = \sum_{i=1}^{3} \ln(\lambda_i)\{e_i\}\{e_i\}^T \tag{44}$$

where, λ_i and $\{e_i\}$ are the eigen value and eigen vector for the i_{th} principal stretch increment of the incremental stretch matrix $[\Delta U_n]$ This method is used for large strain solid elements For standard solid and shell elements an approximate method is used by evaluating the deformation gradient at the midpoint configuration

$$[\Delta \varepsilon_n] = [R_{1/2}]^T \Delta \bar{\varepsilon}_n] R_{1/2}] \tag{45}$$

and

$$[\Delta \bar{\varepsilon}_n] = [B_{1/2}]\{\Delta u_n\} \tag{46}$$

where, $[\Delta u_n]$ is the displacement increment over the time step and $[B_{1/2}]$ is the strain displacement matrix evaluated at the midpoint geometry

The computed strain increment $\{\Delta\varepsilon_n\}$ is then added to the previous strain $\{\Delta\varepsilon_{n-1}\}$ to obtain the current total logarithmic strain

$$[\Delta \varepsilon_n] = \{\varepsilon_{n-1}\} + \{\Delta \varepsilon_n\} \qquad (47)$$

The strain is then used in the stress updating procedure in stress-strain relationship matrix

The element matrices and load vectors are derived using an updated Lagrangian formulation The equilibrium equation of this form is

$$[K_i]\Delta u_i = \{F^{app}\} - \{F_i^{nr}\} \qquad (48)$$

where $\{F^{app}\}$ is the is the applied force vector and $\{F^{nr}\}$is the force obtained from Newton-Raphson current trial solution

The tangent matrix [**k**$_i$] has the form

$$[K_i] = \int [B_i]^T [D_i][B_i]dV \qquad (49)$$

integrated over the element volume [**B**$_i$] is the strain displacement matrix in terms of current geometry and [Di] is the current stress-strain matrix

The Newton -Raphson restoring force,

$$F_i^{nr} = \int [B_i]^T \{\sigma_i\} dV \qquad (50)$$

where, $\{\sigma_i\}$ is the current Cauchi stress

There are different material models in ANSYS In the present work only isotropic hardening model was used This model uses the von-Mises yield criteria and associated flow rule The equivalent stress is given as

$$\sigma_e = [\tfrac{3}{2}\{S\}^T\{S\}]^{1/2} \qquad (51)$$

where {S} is the derivative stress When σ_e is the equal to the current stress σ_k then the material is assumed to yield The yield criterion is,

$$F = [\tfrac{3}{2}\{S\}^T\{S\}]^{1/2} - \sigma_k = 0 \qquad (52)$$

For work hardening, σ_k is a function of the amount of plastic work done For isotropic hardening, σ_k is the equivalent stress corresponding to the equivalent plastic strain in uniaxial stress-strain curve

3 2 3 Element Formulation

From the ANSYS element library two types of elements were used in the present analysis works These are two dimensional and three dimensional large strain viscoplastic elements In these elements the Newton-Raphson restoring force (equation 50) is modified by assuming a decomposition of the Cauchi stress into the deviatoric part plus the pressure part The pressure is separately interpolated to conveniently allow for enforcement of the incompressibility constraint associated with large plastic strains The total Cauchi stress is calculated by finding the deviatoric part from the constitutive equations using the strains calculated from nodal displacements and subtracting the separately interpolated pressure

2-D elements have two integration points in each direction with standard shape functions for linear interpolation Similarly 3-D elements also have linear shape functions and two integration points in each direction Gauss quadrature rule for numerical integration procedure is used to evaluate matrix integration required in finite element calculations

3 2.4. Contact Algorithm

For the ANSYS analyses in the present work, 2D point to surface and 3D point to surface contact elements were used These are imaginary spring line elements Kinematics of both of these elements are similar and based on pinball algorithm Therefore, the kinematics of 2D point to surface contact elements are presented Figure 3 1 shows several positions of a contact node with respect to a circle centred on the target surface (nodes I and J) The circle is referred to as "a pinball" When a contact node (k) is outside the pinball an "open" contact condition is assumed, irrespective of whether or not the contact node is above or below the target Contact or penetration can only occur if the contact node is inside the pinball The radius of the pinball is internally fixed to be 50% greater than the distance between the target nodes

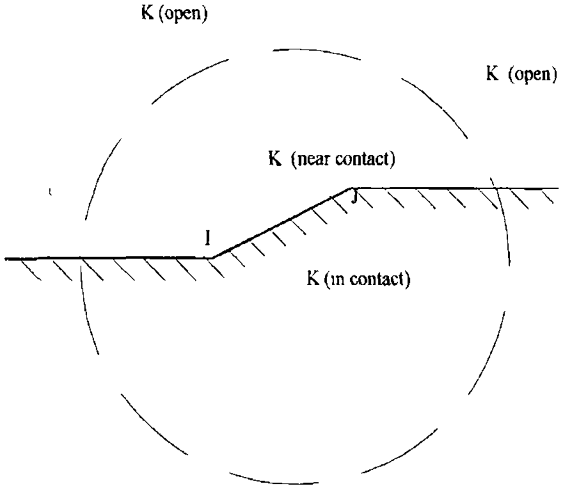

Figure 3 1 Principle of Pinball Algorithm

The contact node k may be near to several target elements From Figure 3 2 it can be seen that node k may belong to either element If a clear distinction is not made, it is possible that contact overlaps or voids may appear To remove this potential difficulty, solid "pseudoelements" are formed that surround each target The elements are temporarily formed for each equilibrium iteration and provide a continuous mapping for each contact node that is in or nearly in contact with target As can be

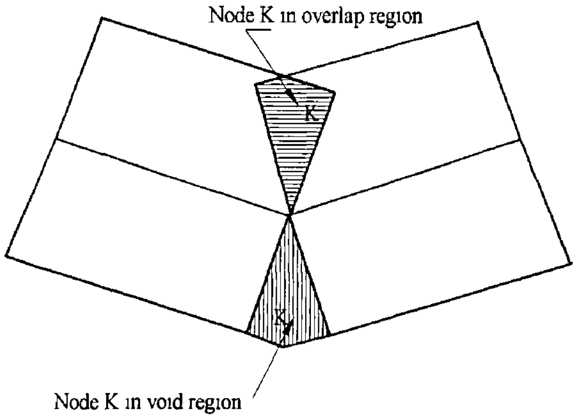

Figure 3 2 Potential voids or overlaps at contact intersection

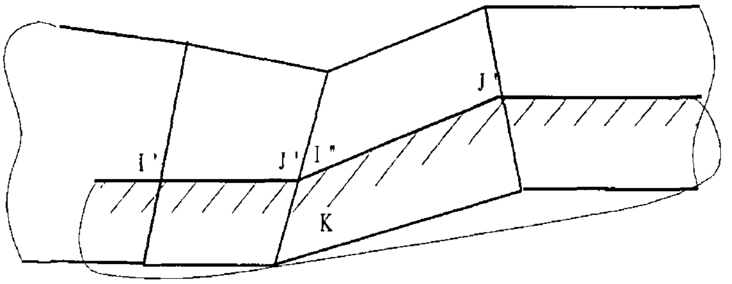

Figure 3-3 Pseudo element of a target surface

seen from Figure 3 3 , the pseudo element mapping indicates that node k is uniquely assigned to the target element I -J'

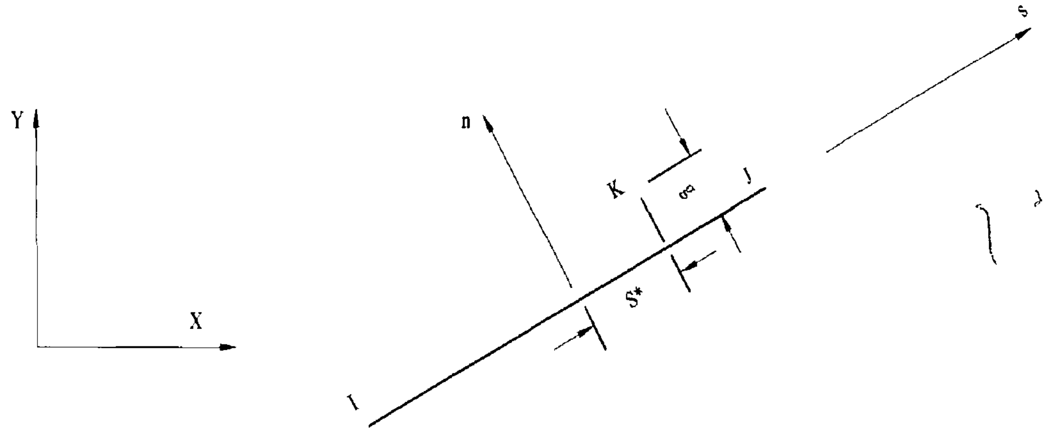

Figure 3 4 Location of contact node in local contact co-ordinates

Figure 3 4 shows an element co-ordinate system The gap, g and projection point S* , defined in local s-n co-ordinates are

$$g = (\{X_k\} - \{X_I\})^T \{n\} \tag{53}$$

$$S^* = -1 + 2[(\{X_k\} - \{X_I\})^T \{s\}] / L \tag{54}$$

where $\{X_k\}$ = position vector of node k

$\{X_I\}$ = position vector of node I

$\{n\}$= unit normal vector to target element I-J

$\{S\}$= unit tangent vector to target element I-J

L= length of the target element I-J

Contact penetration is assumed to occur if the value of g is negative and an open condition is assumed when g is positive

A penalty or a combined penalty plus Lagrange multiplier method is used for contact force calculation Penalty method is used for the analysis in this work for which the contact force f_n is given as

$$f_n = \begin{cases} k_n & \text{if } g \leq 0 \\ 0 & \text{if } g > 0 \end{cases} \qquad (55)$$

where k_n is the stiffness of the contact element k_n is chosen by the user on the basis of material properties of the contacting surfaces and requires several trials to get good contact condition

Tangential forces are due to friction that arises as the contact node meets and moves along the target The algorithm allows three friction models frictionless, elastic Coulomb friction and rigid Coulomb friction Elastic Coulomb friction condition is assumed in all analyses by ANSYS The tangential force for this friction condition is given as

$$f_s = k_t u^e_s < F \bar{f}_s \quad \text{if sticking} \qquad (56)$$

$$= \bar{f}_s \quad \text{if sliding}$$

where k_t = sticking stiffness, , u^e_s = elastic tangential deformation , F = static/dynamic friction factor and $\bar{f}_s$ = sticking force limit = $-\mu f_n$, μ = coefficient of sliding friction

3.2 5 Design Optimisation

The design optimisation module is an integral part of the ANSYS analysis program The optimisation process is a nesting process where in the analysis switches between finite element analysis and optimisation algorithm Figure 3 5 shows the process in schematic format

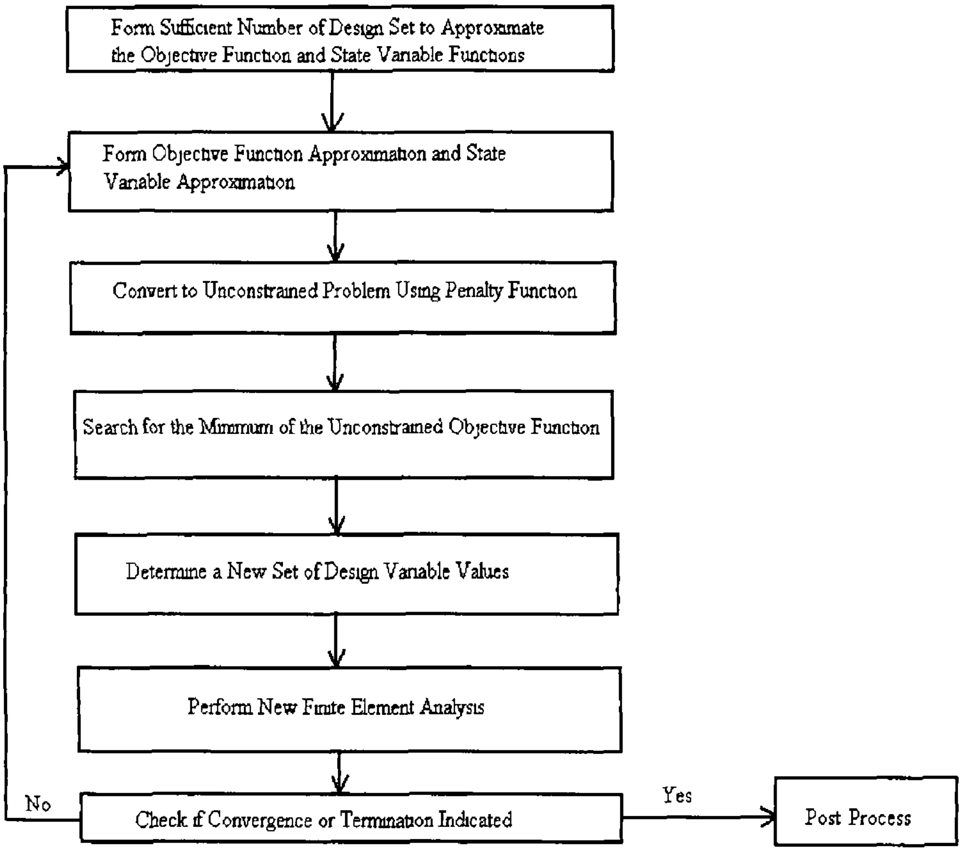

Figure 3 5 Optimisation analysis process flow

A typical optimisation problem deals with three types of variables design variables, state variables and an objective function These variables are represented by scalar parameters in ANSYS parametric design language Design variables are the independent variable of the problem The vector of the design variables is indicated by

$$\mathbf{X} = [\ X_1 \quad X_2 \quad X_3 \qquad\qquad X_n\ ] \tag{57}$$

where n is the number of design variables

Each design variable is subject to a constraint bound by its upper and lower limit, that is,

$$\text{lower limit, } \underline{X}_i \le X_i \le \text{ upper limit, } \bar{X}_i \tag{58}$$

The problems then can be defined as,

minimise, $f = f(\mathbf{X})$

subject to,

$$g_i(X) \le \bar{g}_i \quad (i = 1, 2, 3, \quad m_1) \tag{59}$$

$$h_i(X) \ge \underline{h}_i \quad (i = 1, 2, 3, \quad m_2) \tag{60}$$

$$\underline{w}_i \le w_i(X) \le \bar{w}_i \quad (i = 1, 2, 3, \quad m_3) \tag{61}$$

and

$$\underline{X}_i \le X_i \le \bar{X}_i \quad (i = 1, 2, 3, \quad n) \tag{62}$$

where f is the objective function

g_i, h_i, and w_i = state variables containing the design, with underbar and overbar representing the lower and upper bounds respectively

m_1, m_2, m_3 = number of state variables of different nature of limit

As illustrated in Figure 3 5, certain minimum number of design sets are to be generated either by the designer or randomly by the computer to figure out the approximate functions of the objective variable and state variables by fitting curve to the data from the generated design sets Approximation of objective function and state variable functions are done by method of least square regression method using normalised design variable values Linear or quadratic or quadratic plus cross terms options are available for describe the approximated curves The quality of data fitting is assessed by weighted multiple regression coefficient

The minimisation problem stated earlier is now defined by the approximate functions The approximate problem may be expressed as,

minimise, $f' = f'(\mathbf{X})$

subject to,

$$g_i(X) \le \bar{g}_i + \alpha_i \quad (i = 1, 2, 3, \quad m_1) \tag{63}$$

$$h_i(X) \ge \underline{h}_i - \beta_i \quad (i = 1, 2, 3, \quad m_2) \tag{64}$$

$$\underline{w} - \gamma_i \le w\ (X) \le \bar{w}_i + \gamma_i \quad (i = 1, 2, 3, \quad m_3) \tag{65}$$

and

$$\underline{X}_i \le X_i \le \bar{X}_i \quad (i = 1, 2, 3, \quad n) \tag{66}$$

This constrained problem is then transformed to an unconstrained problem by adding penalty functions to the objective function leading to the following statement, minimise,

$$F(X,p_k) = f + f_0 p_k \left[\sum_{i=1}^{n} P(X_i) + \sum_{i=1}^{m_1} G(g_i) + \sum_{i=1}^{m_2} H(h_i) + \sum_{i=1}^{m_3} W(w_i) \right] \qquad (67)$$

in which P is the penalty function used to enforce design variable constraints, and G, H, W are penalty functions for state variable constraints The reference objective function value, f_0 , is introduced in order to achieve consistent units Sequential unconstrained minimisation technique (SUMT) algorithm is employed to reach the minimum of the above approximate objective function The subscript k in the equation refers to the use of sub-iterations performed during the solution whereby the response surface parameter p_k is increased in value ($p_1 < p_2 < p_3$ etc) in order to achieve accurate converged results The design vector that provide the minimum response function is then input for next finite element analysis The process continues until a convergence is reached or any termination condition is attained Convergence is assumed when either the present design set, X^j, or the previous design set, X^{j-1}, or the best design set, X^b, is feasible, and one of the following conditions is satisfied

$$\left| f^{j} - f^{(j-1)} \right| \le \tau \qquad (68)$$

$$\left| f^{j} - f^{b} \right| \le \tau \qquad (69)$$

$$\left| X_i^{j} - X_i^{j-1} \right| \le \rho_i \quad (i = 1, 2, 3, \quad n) \qquad (70)$$

$$\left| X_i^{j} - X_i^{b} \right| \le \rho_i \quad (i = 1, 2, 3, \quad n) \qquad (71)$$

where τ and ρ_i are objective function and design variable tolerances If neither of the above are realised, then termination can occur if either the number of iterations has reached the pre-set maximum or the number of infeasible designs has reached the pre-set maximum number of sequential infeasible designs

In the optimisation process, the design variables are considered to be continuous But in practice the design variables have discrete values Thus optimum design values obtained by non-linear optimisation technique are difficult to put in practice Although other optimisation techniques exist that give solutions with discrete values, they are not well suited for structural design optimisation[96]

However, non-linear optimisation technique provides a good solution around which practical design can be sought Taguchi parameter design method is one such method to seek optimal solution with discrete design variable values This method was utilised for optimisation of certain simulation works of this project by post-processing the ANSYS optimisation results This is not a part of ANSYS package

The method identifies the optimum level of design variables that give minimal variation of the objective figure of merit Each design variable is given different desirable values around the optimum solution obtained by non-linear optimisation Each value is a level for that design variable A number of design factor-level combinations based on orthogonal design of experiment theory is adopted for trial runs The objective figure of merit values for the trial runs are analysed for optimum factor level combination A brief description of Taguchi method is presented in the Appendix

3 3 LS-DYNA3D Theoretical Methods

LS-DYNA3D is basically a vectorized, explicit three dimensional finite element code for analysing large deformation dynamic response of inelastic solids Metal forming is a quasi-state process Therefore, dynamic analysis process can be used for the simulation of metal forming process if the kinetic energy during the process does not become high compared to the internal energy This section presents the relevant theoretical methods for LS-DYNA3D analysis which are extracted from reference [100]

The equilibrium equation governing a dynamic problem and the solution process by central difference method was given in (27), (28) and (29) As mentioned, the time step size Δt is very important and must be smaller than a critical time step, Δt_{cr} for stability This smallest time step ensures that the minimum time required for a shock wave to cross the smallest element is within this time In LS-DYNA3D, Δt is calculated from

$$\Delta t = \frac{l}{C} \tag{72}$$

where l is the characteristics length of the smallest element and C is the sonic wave propagation velocity through the element material For reasons of stability a scale factor of 0 9 is used to decrease the time step in (72) The time step used in the program , therefore, is

$$\Delta t = 0.9 \frac{l}{C} \tag{73}$$

For different elements l and C values are calculated differently For solid elements l is the smallest distance between two neighbouring nodes of the smallest element in the model For shell elements the value of l depends on the shape of the smallest element for regular rectangular elements, the value of l is the length of the shortest side of the element For irregular shaped elements the value of l is determined by dividing the area of the element either by its longest side or by its longest diagonal The sound wave propagation speed is determined as bellow

For solid elements, $C = \sqrt{\dfrac{E(1-\nu)}{(1+\nu)(1-2\nu)\rho}}$ (74)

For shell elements, $C = \sqrt{\dfrac{E}{(1-\nu^2)\rho}}$ (75)

3.3.1 Element Formulation

In simulation within this work two types of elements are used from LS-DYNA3D element library They are 8-node hexahedron solid elements and Belytschko-Lin-Tsay shell elements Volume integration of the elements is done using Gaussian quadrature principle Both reduced (one point) and full integration procedure was used for the solid elements Shell elements are formulated for reduced integration procedure

The biggest disadvantage to one-point integration is the need to control the zero energy modes, called hourglassing modes that arise due to the reduced integration Undesirable hourglass modes tend to have periods that are typically much shorter than the periods of the structural response, and they are often observed to be oscillatory The zero energy or hourglass deformation mode in a two dimensional element is shown in Figure 3 5 The figure also illustrates a propagated hourglass mode The origin and the consequent computational implication of this mode is described in simple form by Hallquist and Benson [99] Adding illustration to their description the "hourglass" or "zero energy" mode of deformation would be if the nodes 1 and 3 of the element in Figure 3 5 are given a velocity of +1 and the nodes 2 and 4 are given a velocity of -1 in either X_1 or X_2 direction, then the velocity gradient of the element would be zero If the velocity gradient is zero, the element does not develop any stresses to oppose the velocities and the element may continue to deform in this mode without resistance These velocity distributions are referred to as "hourglass" or "zero energy modes"

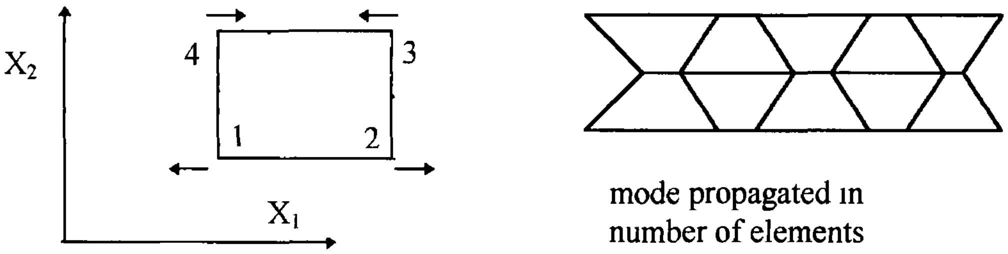

mode propagated in number of elements

Figure 3 5 "Hourglass" or "zero energy" deformation mode

One way of resisting the undesirable hourglassing is with a viscous damping or small elastic stiffness capable of stopping the formation of the anomalous modes but having a negligible effect on the stable global nodes The hourglass resisting force for a particular node in a particular co-ordinate direction is linked to the nodal velocity in that direction The resisting force in solid elements is defined as

$$f_{i\alpha}^{k} = a_h h_{i\alpha} \Gamma_{\alpha k} \tag{76}$$

where,

$$a_h = Q_{hg} \rho v_e^{2/3} \frac{c}{4} \tag{77}$$

$$h_{i\alpha} = \sum_{k=1}^{8} x_i^{k} \Gamma_{\alpha k} \tag{78}$$

in which α = number of hourglass mode $\Gamma_{\alpha k}$ = hourglass shape vectors

x_i^k = velocity of node k in i-direction

v_e = element volume , c = material sound speed and Q_{hg} is a constant usually set between 0 05 to 0 15

The hourglassing in shell elements is suppressed by adding hourglass viscosity stress to the physical stress at the local element level

3.3 3 Material Model

All models that were simulated used bilinear isotropic hardening plasticity with no strain rate dependence The yield stress σ_y is defined as [100]

$$\sigma_y = (\sigma_0 + E_p \varepsilon_p^{eff}) \qquad (79)$$

where σ_o = initial yield stress

E_p = plastic hardening modulus = $(E_{tan}E)/(E-E_{tan})$

$\varepsilon^{eff}{}_p$ = effective plastic strain

E_{tan} = tangent modulus

E = Young s modulus

3.3 3 Contact Algorithm

All models simulated using LS-DYNA3D employed surface to surface contact option The algorithm is based on penalty method as in ANSYS However, this algorithm uses different approach for contact searching as well as contact stiffness or interface stiffness The interface stiffness is chosen to be approximately the same order of magnitude as the stiffness of the interface element normal to the interface

Contact searching in LS-DYNA3D is done in two steps global and local search In global search the contact domain is subdivided into buckets, then the search is limited to the bucket where the contacting node is located The segment based search uses a total of minimum (NSN,5000) buckets with NSN being the number of nodes in the contact surfaces The search loop runs over the segments and for each segment over the buckets containing the segment Buck searchers are performed every five to fifteen cycles After the global search has located possible contact candidates, the local search checks for interpenetrating A node-to-segment algorithm is used to find the interpenetration

When a slave node penetrates a master surface, a restoring force, f, proportional to the penetration depth, l, acts to restore the node to the contact surface in the normal direction , n The restoring force may be expressed as,

$$f = - k\, l\, n \tag{80}$$

where k is the master surface stiffness which is independently calculated for each contact surface segment from the bulk modulus, K, and the volume and surface area of the element, V and A, respectively The stiffness is expressed as

$$k = s\, KA^2/V \tag{81}$$

where s is a scale factor the default value is 0 1, but it may be reset to higher values to increase the stiffness Higher values of stiffness might cause instability due to large point load from the contact elements

When the penetrator stays in contact with the target, it may either stick to the surface or slip along the surface In LS-DYNA3D friction is provided for stick-slip situations by an algorithm tailored after the radial return method in plasticity The relative slip between the master and slave surfaces is calculated by keeping track of the isoparametric co-ordinates and master segment number for every slave node that is in contact with the master surface Any distance moved by the slave node is treated as a measure of strain and the radial return algorithm is used to return the tangential force to the yield surface The elastic modulus is the same as the master surface stiffness used for the normal force calculation in penalty method in equation (80)

LS-DYNA3D implements the penalty method in a *symmetric manner* When the mesh grading varies along the contact surfaces, or the surfaces are subject to large distortions, the best choice of master surface may vary along the contact surfaces The symmetry greatly increases the robustness of the contact algorithm by allowing each surface to act as both the master and slave surfaces

Chapter 4

SIMULATION AND ANALYSIS

One of the important steps in finite element simulation of deformation is the idealisation and modelling of the deforming body A good idealisation and modelling of the deforming body is paramount to obtain good solution Although the simulation cases undertaken in this work are generically bulge forming with pressure and compressive end load, each case is different in terms of die geometry, blank geometry, contact, loading and discretisation Therefore, modelling for each simulation case is presented separately However, all cases are modelled using either ANSYS or LS-DYNA3D pre-processors In the case of complex geometrical models, AutoCAD, a computer aided design package was used with appropriate data exchange mechanism

4 1 Bulge forming from Circular Sheets

As outlined in chapter two a number of finite element simulations of simple bulge forming have been reported in the literature where only pressure load is applied to circular sheets clamped at the periphery No consideration to the modelling of the die and contact area was given In the following three subsections simulations of the bulge forming of circular sheets of different thickness, diameter and friction condition are presented Both pressure and in-plane compressive load are applied to all models In one model some restraining load on the top of the forming bulge is applied in addition to the pressure and in-plane compressive load Finally an optimisation analysis of one of the simulation cases is presented

4 1 1 Pressure and In-plane Compressive load.

Modelling

Basically circular blanks of two diametrical sizes were simulated for different thickness, friction conditions and loading patterns The die opening size and die corner radius are same for all the cases Figure 4 1 shows the schematic of the forming situation showing the discretised sheet and loading Some node numbers are shown in the figure for discussion of results later Because of circular symmetry an axisymmetric model is developed

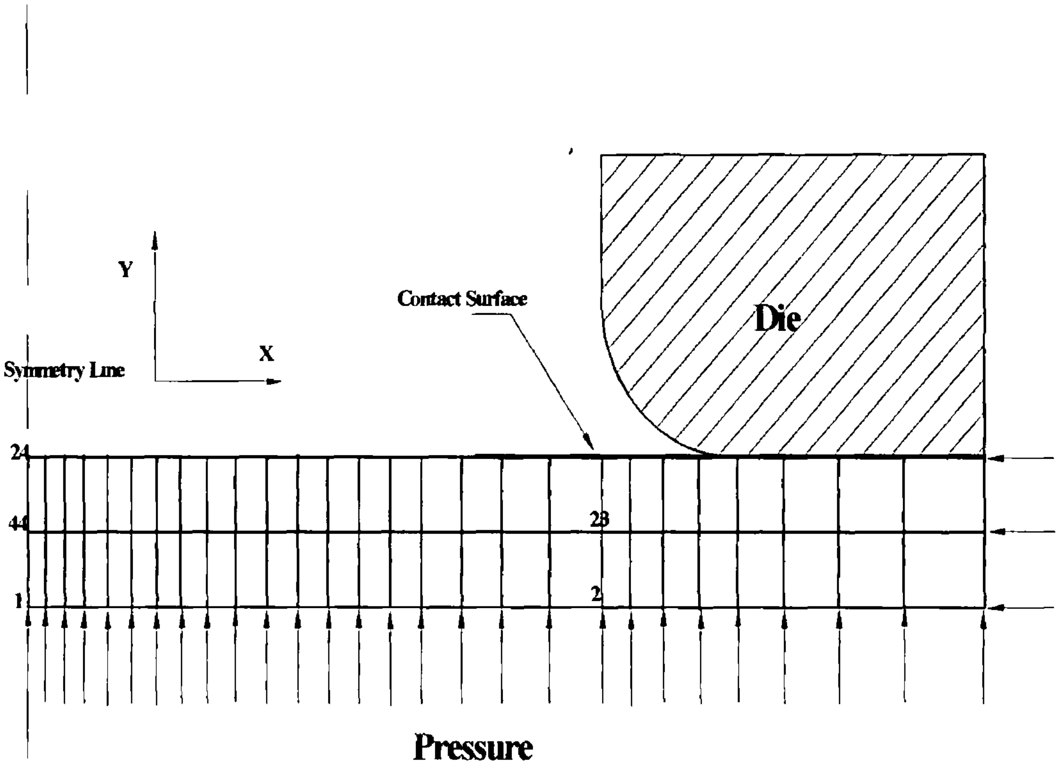

Figure 4 1 Axisymmetric finite element model of bulge forming of circular sheet

Two dimensional 4-noded axisymmetric solid elements are used for finite element discretisation of both the sheet and the die These elements are suitable for large strain and highly non-linear deformation behaviour Number of preliminary trials were done to locate high deformation and stress areas on the deformed sheet Based on the observations from these trials, the sheet was discretised in such a manner so that the mesh density is higher where there is more stretching and lower where the sheet is expected to experience less stretching

The trial solutions were also necessary to decide on the contact stiffness value A higher value poses convergence difficulties while a lower value allows easy penetration of contacting pairs Two dimensional point to surface contact elements were generated between the inner surface of the die and likely top surface of the sheet The contact zone is indicated by thick lines in Figure 4 1 Both the die and sheet surfaces behaved as master and slave surfaces so that a symmetrical contact was developed The principle of penalty function was assigned for the prevention of penetration An elastic Coulomb friction law was assumed Elastic Coulomb behaviour allows both sticking and sliding conditions The sticking zone is treated as an elastic zone with a sticking stiffness, k_s The tangential force is determined by multiplying the stiffness value with the elastic tangential deformation value As soon as the tangential force reaches the limiting value the contact node slides along the contact surface

The sheet was assigned bi-linear isotropic plastic material model Different parameters for the material are as below

Young s Modules = 207 GPa Yield strength = 280 MPa
Tangent Modulus = 920 MPa Poisson s ratio = 0 30
Friction factor = 0 15 Contact Stiffness = 243 kN/mm

The contact stiffness value was determined by trial solutions Different values based on the guidelines provided by the user's manual [99] were tried The contact gaps or penetrations were checked for each solution The value for which the penetrations were negligible was chosen as the desired contact stiffness

The die was assigned an elastic material model All the nodes of the die were fully constrained to simulate as a rigid body Because of axisymmetry the nodes at the centreline of the sheet were fixed radially The nodes at the periphery of the sheet were constrained in Y-direction and prescribed displacement was administered in negative X-direction (inwards)

Results and Discussions

A total of 8 simulations were carried out to take different parameters into consideration Table 4 1 presents a summary of physical parameters of different simulation cases

Effect of In-Plane Compressive Load

Simulation case II identifies the difference in deformation behaviour that a circular sheet experiences when in-plane compressive load is applied simultaneously with the pressure load as against Simulation I where a similar sheet was deformed with pressure load only Table 4 2 presents the main features of these two simulation results

Table 4 1 Parameters of different simulation cases

Simulation Case	Blank radius (mm)	Blank thickness (mm)	Die corner radius (mm)	Cumulative pressure at load steps (MPa)				Cumulative displacement of periphery at load steps (mm)			
				1	2	3	4	1	2	3	4
I	15 0	1 5	1 5	50	100	145 7	-	0 0	0 0	0 0	-
II	15 0	1 5	1 5	50	100	150	158 17	1 0	2 0	3 0	3 0
III	15 0	1 0	1 5	50	97 88	-	-	1 0	1 95	-	-
IV	15 0	1 0	1 5	50	99 90	-	-	2 0	2 99	-	-
V	20 0	1 0	1 5	50	100	103 28	-	4 0	8 0	-	-
VI	20 0	1 0	1 5	50	100	-	-	4 0	8 0	-	-
VII	20 0	1 0	1 5	50	100	103 94	-	6 0	6 0	6 157	-
VIII	20 0	1 0	1 5	5	50	100	104 05	6 0	6 0	7 0	7 081

Table 4 2 Results summary of simulation cases I and II

Simulation	After load step	Bulge height/ bulge dia	Max Eqv Stress (MPa)		Thickness at (% of original)	
			Value	Location	bulge crest	under die
I	1	0 162	471 34	around die	90 33	100 00
II	1	0 257	469 12	around die	97 50	106 98
I	2	0 309	680 36	around die	73 19	100 0
II	2	0 392	626 45	around die	88 95	106 56
I	3	0 561	1252 0	crest	35 09	100 0
II	3	0 608	838 83	crest	55 12	102 0
I	4	-	-	-	-	-
II	4	0 679	1099 0	crest	42 33	96 53

After the first load step where the pressure loads are equal in both cases but case II has 1 mm of peripheral inward displacement, the bulge height attained in case II was 5 14 mm as against 3 24 mm in case I The stress and strain developed in cases I and II are not very different The change in sheet thickness was apparent at this stage The bulge in case I has thinned by 2 5% Also, the sheet has thickened under the die in case II

After the load step 2, the difference in bulge height has narrowed down to 1 66 mm from 1 90 mm although case II was loaded with equal pressure to that of case I plus 2 mm of peripheral inward movement At this stage of loading, the stress and strain difference between cases I and II has just started to show Bulge crest thickness in case I is now down to 73% compared to 89% in case II These differences have become more pronounced in the next and final load step

The maximum pressure load that could be applied in loading case I in the last load step was 145 72 MPa Beyond this the sheet experienced a sharp rise in stress indicating the on onset of instability Figure 4 2 shows the development of principal strains in a node (node 44 in Figure 4 1) at the centre of the sheet in case I during the whole loading process Figure 4 3 shows the principal strains in the same node in case II where a maximum pressure load of 158 17 MPa could be applied It can be seen that the strain path followed by the node in case II is different from that in case I Sheet in case II thus had a different yield point thereby allowing more deformation

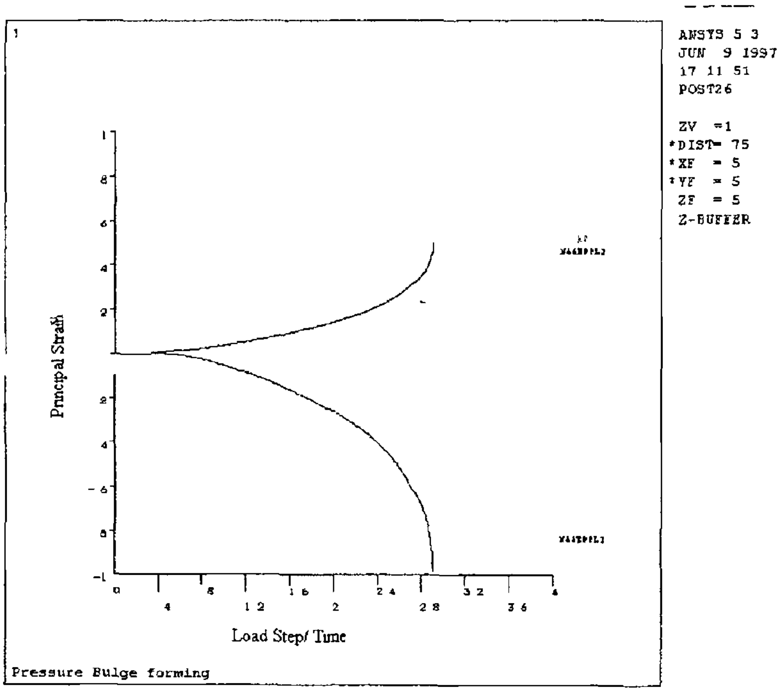

Figure 4 2 Development of principal strains in a central node of the bulge in case I during the load steps

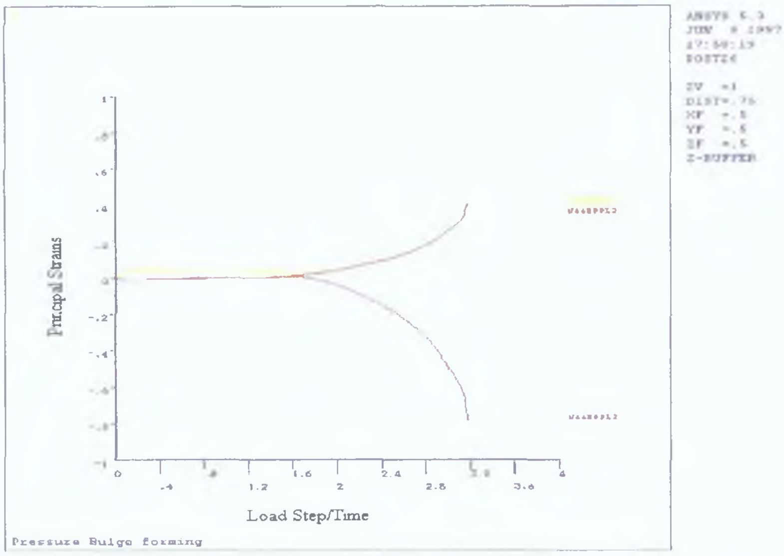

Figure 4.3: Development of principal strains in a central node of the bulge in case II during the load steps.

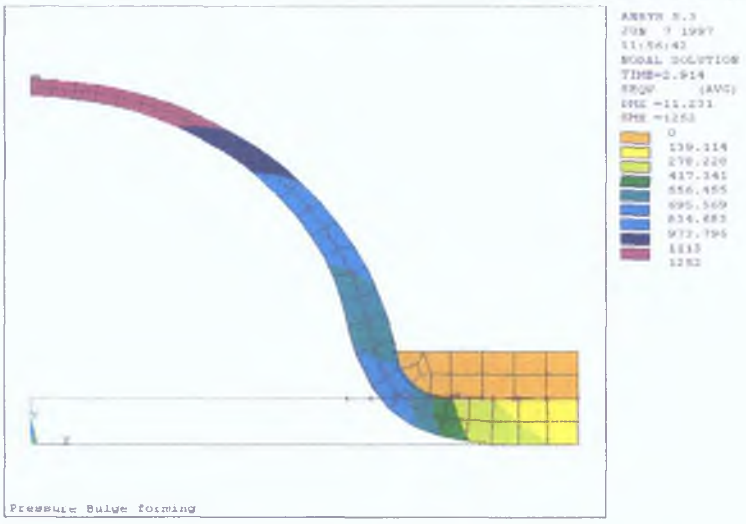

Figure 4.4: Distribution of von-Mises stress in case I

Figure 4.4 illustrates the distribution of von-Mises stress in case I just before instability. Maximum bulge height attained at this stage is 11.23 mm. Figure 4.5 shows the distribution of plastic strain in thickness direction in case I at the same stage of deformation as for Figures 4.4. From Figure 4.4 it can be seen that the crest region of the bulge has the maximum stress. Also the minimum thickness strain occurs at the same region. However, considerable thinning is also evident at the bend around the die. The crest of the bulge has on the average thinned down to about 35% of the original thickness of 1.5 mm.

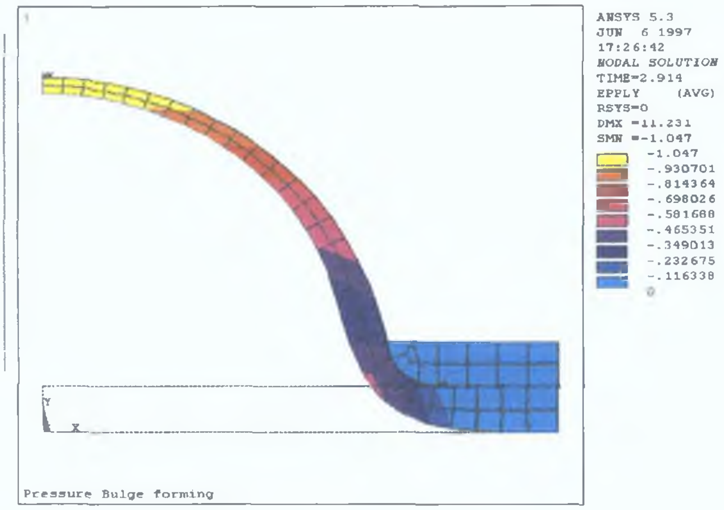

Figure 4.5: Distribution of strain in the thickness direction of the sheet in case I

Figure 4.6 illustrates the distribution of von-Mises equivalent stress in case II just before instability. Maximum bulge height attained in case II at this deformation stage was 13.59 mm.

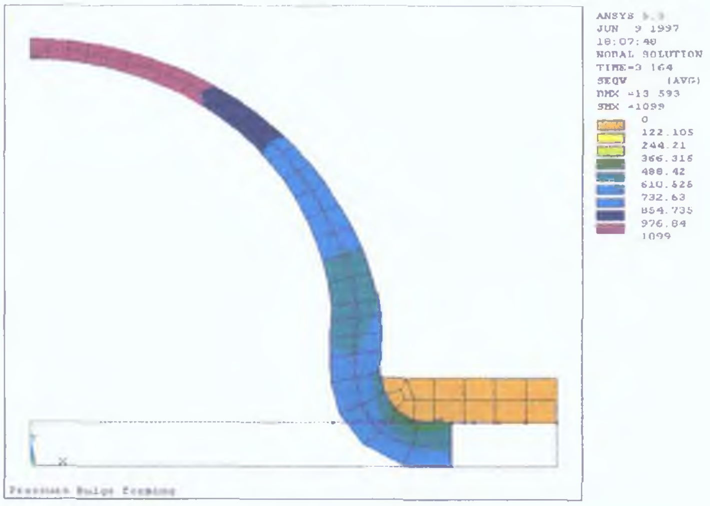

Figure 4.6: Distribution of von-Mises stress in case II

Figure 4.7 shows the thickness strain in case II at this stage. It is seen that the maximum stress is in the crest area of the bulge as in case I. However, the magnitude of stress is much less in case II than that in case I. From Figure 4.7 it is evident that the maximum thinning has occurred at the crest as in case I but the intensity of thinning is much less. The average thinning at the crest in case II is about 55% of the original thickness. The bend around the die has not thinned, rather it has slightly thickened.

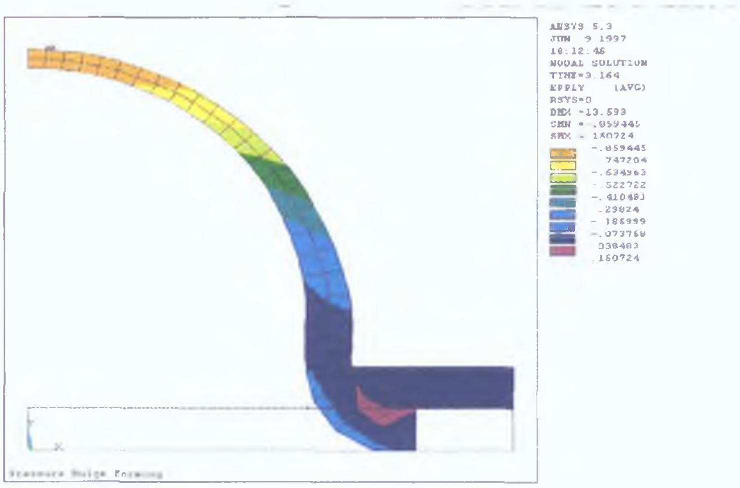

Figure 4.7: Distribution of strain in the thickness direction of the sheet in case II

From the above observations it could be seen that bulge forming of a circular sheet by pressure and in-plane compressive load gives higher bulge height, lower stress and strain and less thinning compared to bulging by pressure load only. Most of the differences appeared during the initial period of bulging. This is apparent from Figures 4.2 and 4.3 where differences in strain path has disappeared within the first load step. Also the difference in bulge height has minimised over the load steps although the periphery was pushed inwards right to the end of the loading in case II. Figure 4.8 shows the bulge height gain in case II over case I for the inward displacement of the periphery. It may be mentioned that pressure loading was equal for both.

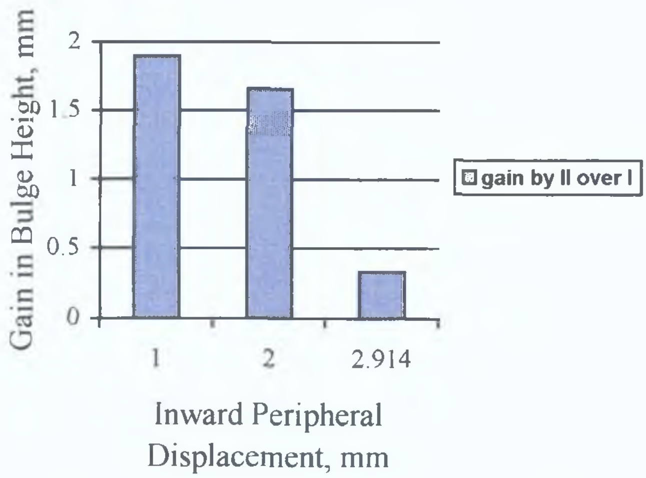

Figure 4.8: Trend of bulge height gain against peripheral inward push

Although it appears from Figure 4 8 that the gain is lost very quickly but it masks the fact that due to the peripheral movement, the same sheet in case II has thinned less and was able to take more pressure load and eventually form a bulge of 13 59 mm which is about 2 72 mm more than that formed in case I

Effect of Blank Thickness

Simulation case III deals with the same die-sheet configuration except that the sheet thickness is only 1 0 mm The loading pattern is same as in case II Table 4 3 shows the comparative summary results of simulation cases II, III and IV Simulation cases III and IV are same except that case IV was given enhanced inward push at the periphery

Table 4 3 Results summary of simulation cases II, III and IV

Simulation	Pressure (MPa)	Peripheral Displ (mm)	Bulge ht /Bulge dia	Maxm Eqv Stress (MPa) Value	Maxm Eqv Stress (MPa) Location	Thickness at (% of original) Bulge crest	Thickness at (% of original) Under die
II	50 0	1 0	0 257	469 12	around die	90 33	100 0
III	50 0	1 0	0 286	508 28	around die		
IV	50 0	2 0	0 349	552 021	around die	94 69	112 34
II	100 0	2 0	0 3927	626 45	around die	88 95	106 56
III	97 885	2 0	0 618	1116 0	bulge crest	40 6	100 0
IV	99 9	3 0	0 660	1106 0	bulge crest	41 24	111 02
II	150	3 0	0 608	838 83	bulge crest + around die	55 12	102 0

Because of the smaller initial thickness, the sheet in case III could only be loaded up to about 98 MPa before instability was reached However, the deformation was quite high compared to case II for similar loading The bulge height attained in case III was 12 36 mm at 98 MPa pressure and 1 96 mm inward peripheral displacement It was only 7 7 mm in case II at this state of loading Figure 4 9 illustrates the von-Mises stress in case III The stress developed in case III is high compared to that developed in case II (Figure 4 6) before it was unstable However, it should be pointed out that the sheet periphery in case III could not be pushed as much inward as it was possible in case II because of early instability. A different loading pattern was used to the same model which is described in the next paragraph. Figure 4.10 shows the thickness strain developed in case III. The sheet has thinned most at the bulge crest area. The average thickness reduction in this region is about 40% of the original thickness.

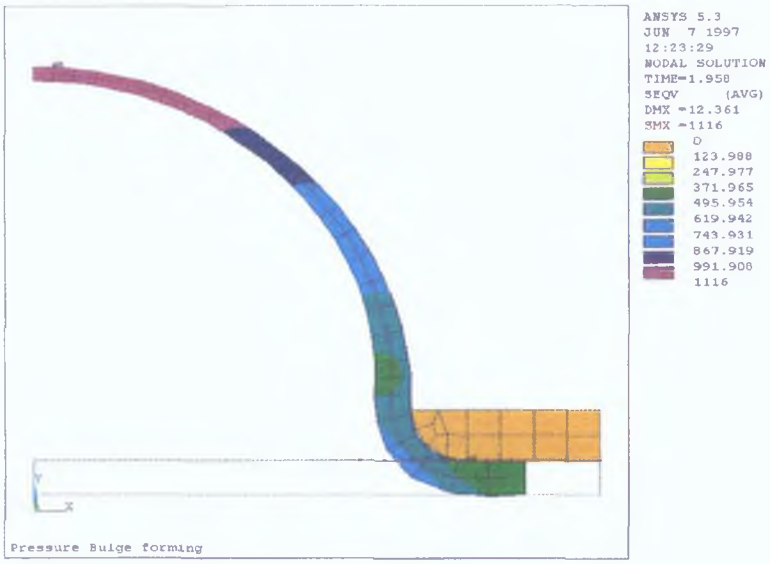

Figure 4.9: Distribution of von-Mises stress in case III

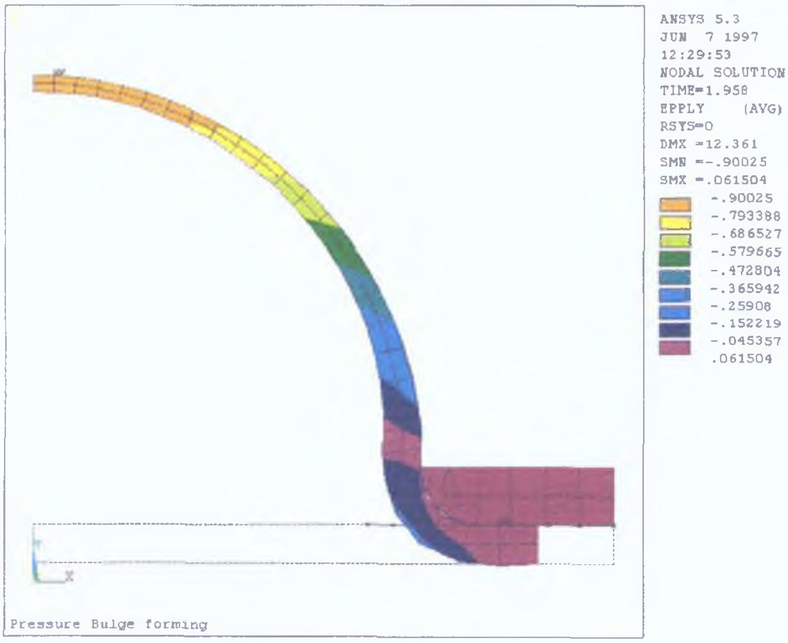

Figure 4.10: Distribution of strain in thickness direction of the sheet in case III

As mentioned earlier, the periphery of the sheet in case III could not be pushed inward sufficiently because of the dominant pressure loading which resulted in an early instability An enhanced peripheral displacement loading was given to the model of case III in simulation case IV The enhanced in-plane loading delayed the onset of instability slightly thereby affording more deformation Figure 4 11 shows the loading profile for cases III and IV The bulge height attained in case IV due to the enhanced displacement loading was 13 21 mm compared to 12 36 mm obtained in case III

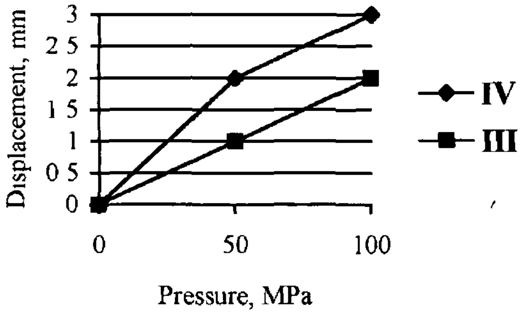

Figure 4 11 Loading profile for simulation cases III and IV

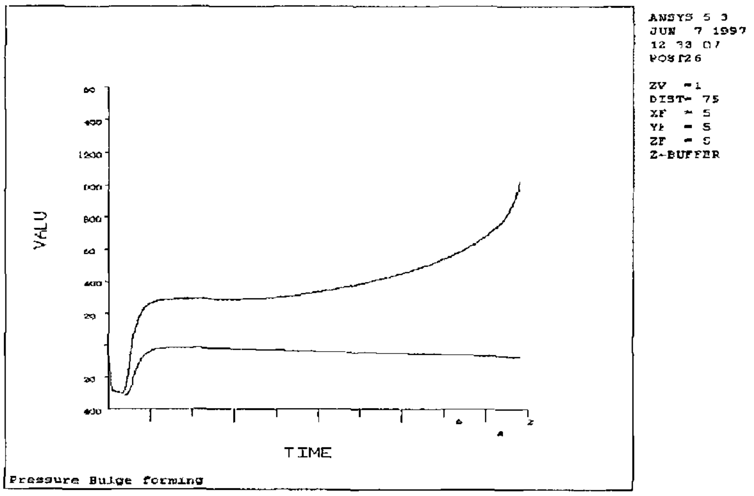

Figure 4 12 History of stress in the central node in case III during loading

Figures 4 12 and 4 13 respectively show how the central node(44) in cases III and IV was stressed due to their different loading profile From these two figures it can be seen that the node experienced considerably different stressing pattern for initial 20% of the first load step Subsequently the rate of stressing in case IV was less than that in case III although the former experienced more forming load

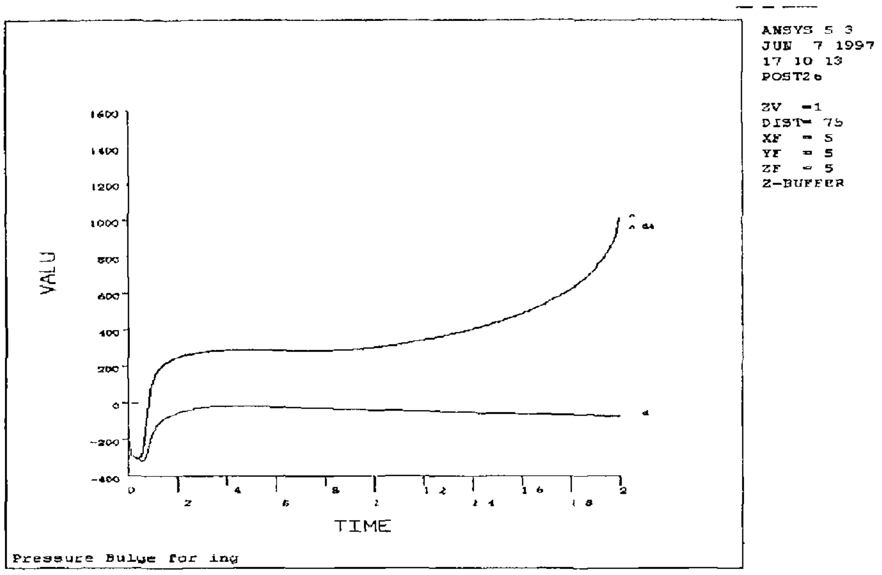

Figure 4 13 History of stress in the central node in case IV during loading

Effect of Friction

In simulation cases V and VI the sheet radius was increased to 20 mm The die was modified accordingly to cover the sheet surface in the axisymmetric model as before Frictionless contact was simulated in case V while case VI was simulated for elastic Coulomb friction law The coefficient of friction was 0 15 Both of them were loaded identically as was presented in Table 4 1 before Table 4 4 presents the main features of the simulation result at different load steps

Table 4 4 Results summary of simulations cases V and VI

Simulation	After pressure (MPa)/Disp (mm)	Bulge ht /Bulge dia (mm)	Maxm Eqv Stress (MPa)		Thickness at (% of original)	
			Value	Location	bulge crest	under die
V(no friction)	50/4	0 466	666 29	around die	97 0	127 20
VI (friction)	50/4	0 460	655 39	around die	96 8	129 13
V(no friction)	100/8	0 863	965 86	around die + bulge crest	57 51	154 35
VI(friction)	100/8	0 862	966 37	around die + bulge crest	54 49	160 28

From the summary of results in Table 4.4 it is seen that two simulation cases show not much differences. The bulge height, stress and strain are nearly equal for both simulation cases after each load step. The bulge height attained in cases V and VI after 100 MPa pressure and 8 mm inward push of the periphery was 17.26 mm and 17.24 mm respectively. Figures 4.14 and 4.15 respectively show the von-Mises stress in cases V and VI after equal loading. Figures 4.16 and 4.17 respectively show the thickness strain distribution in cases V and VI at the same stage of loading. Although most stress in Figures 4.14 and 4.15 is in the bend region, the bulge crest region has

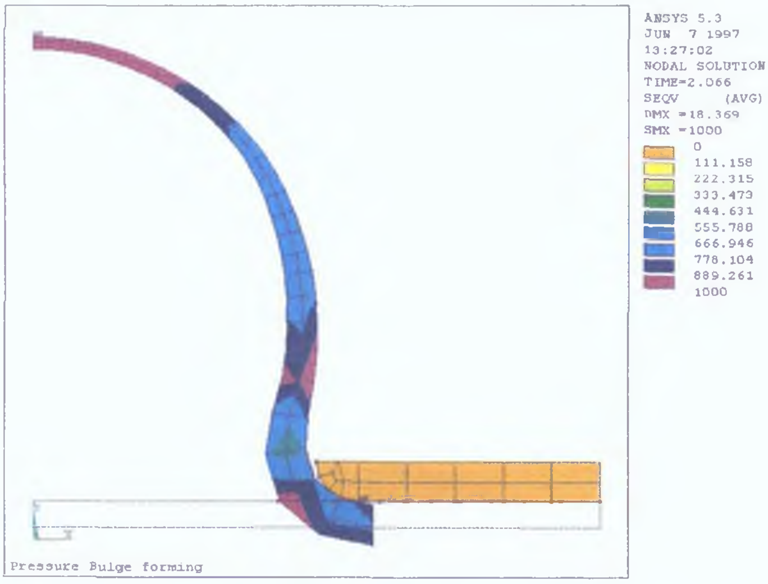

Figure 4.14: von-Mises stress in case V after full load.

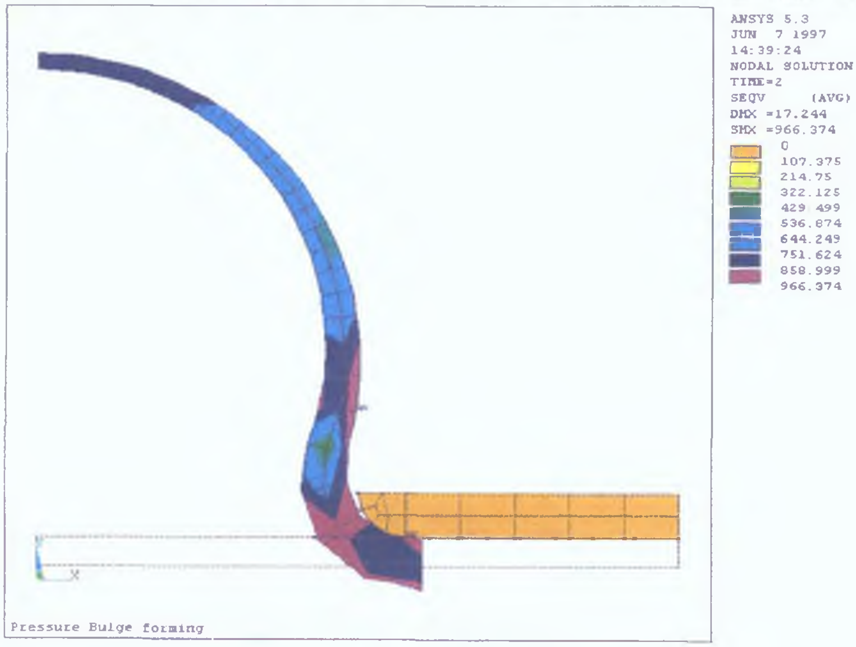

Figure 4.15: von-Mises stress in case VI after full load.

stressed quite intensely at this stage. . Also, a larger area of the crest in case VI has stressed more compared to that in case V. From figures 4.16 and 4.17 it is apparent that the thinning pattern of these simulations are not significantly different. It is also evident that the thinning of the bulge crest and thickening under the die was little more in case VI than that in case V.

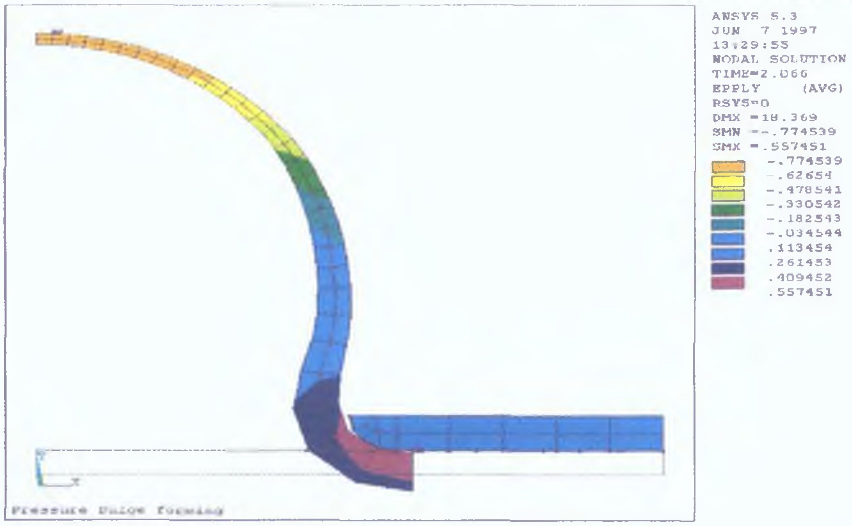

Figure 4.16: Distribution of strain in the thickness direction of sheet in case V.

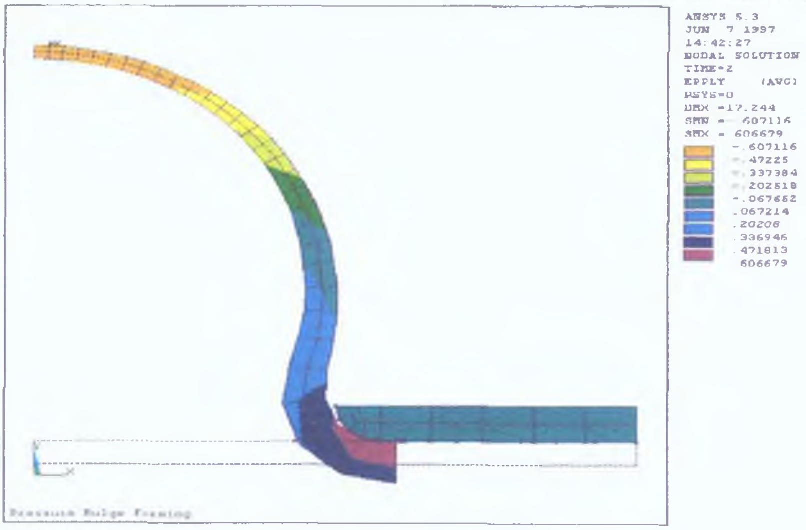

Figure 4.17: Distribution of strain in the thickness direction of sheet in case VI.

In both these simulation cases the periphery was moved inward by prescribed displacement irrespective of friction. Therefore, the effect of friction was not reflected much in the above results. The main effect of friction is expected in the reaction loads at the peripheral nodes Total reaction load from the nodes at the periphery in case VI in X-direction was 38 52 kN after load step 2 On the other hand, for the same loading condition the total reaction load of the peripheral nodes in case V in X-direction was 32 63 kN As expected, the reaction load at the peripheral nodes in X-direction was higher for the case with friction than that without friction

Effect of Blank Diameter

Simulation cases IV and V were similar models except that the blank diameter was different The sheet diameter in case IV was 30mm while that in case V was 40 mm Because of the higher diameter of the sheet in case V its periphery could be given more displacement Table 4 5 presents the comparative results of these two simulations

Table 4 1 5 Results summary of simulations IV and V

Simulation	Pressure (MPa)	Peripheral Displ (mm)	Bulge ht /Bulge dia	Maxm Eqv Stress (MPa)		Thickness at (% of original)	
				Value	Location	bulge crest	under die
IV	50 0	2 0	0 349	552 20	around die	94 69	112 34
V	50 0	4 0	0 416	666 29	around die	97 0	127 20
IV	99 9	3 0	0 66	1106 0	bulge crest	41 24	111 02
V	100 0	8 0	0 863	965 86	around die + bulge crest	57 50	154 35
V	103 28	8 0	0 918	1000 0	bulge crest	46 09	150 5

It can be seen from the table that significant gain in bulge height could be attained due to the additional peripheral push of the sheet In fact the gain was little over 5 0 mm which was incidentally the additional peripheral displacement given in case V over case IV Pushing of more material in the bulge area has resulted in less stress and thinning at the bulge crest At the same time, there was considerable thickening of the bulge base under the die due to the extra radial displacement

Effect of Loading

From the previous simulations it was observed that the loading pattern has marked influence on the deformation behaviour of the sheets. Simulation cases VII and VIII were designed to try two significantly different loading pattern on the same model. Simulation case V is also included in the subsequent discussion to have more variety in loading profile. All three simulations deal with sheets of equal diameter i.e. 40 mm. Figure 4.18 shows pressure versus peripheral displacement loading for the three cases. Both pressure and displacement loads were increased uniformly at a particular step in loading. Most variation in loading was tried during the first 50 MPa pressure loading. This was done mainly due to the limited peripheral displacement that was available in the models. Also, it was thought that in-plane displacement at lower pressure would enable movement of more material to the bulging area from the periphery.

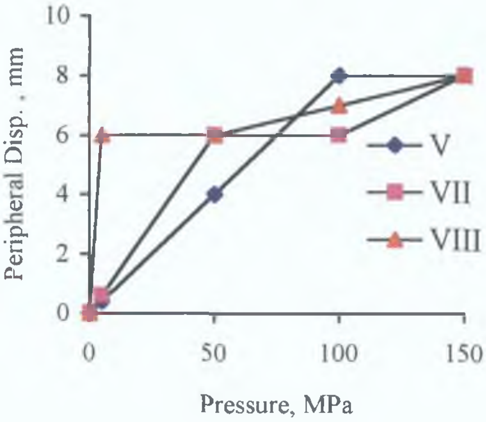

Figure 4.18: Loading pattern of simulation cases V, VII and VIII

Table 4.6 presents the major findings from these three simulation cases. From the table it is evident that after the completion of loading, the maximum bulge height along with minimum stress and strain were obtained in case V compared to the other two. A uniform displacement to pressure ratio was maintained in the loading in case V. This loading resulted in slightly less thinning of the crest before rupture. However, within the pressure step of 50 Mpa the deformation outcome was in favour of

Table 4 6 Results summary of simulations V, VII and VIII

Simulation	Pressure (MPa)	Bulge ht / Bulge dia	Maxm Eqv Stress (MPa)		Thickness at (% of original)	
			Value	Location	bulge crest	under die
VIII	5 0	0 465	819 9	around die	95 56	156 50
V	50 0	0 466	666 29	around die	97 0	127 20
VII	50 0	0 574	789 81	around die	99 22	150 90
VIII	50 0	0 479	776 8	around die	96 52	145 63
V	100 0	0 863	965 86	around die	57 50	154 35
VII	100 0	0 709	806 87	around die + crest	61 93	152 06
VIII	100 0	0 723	956 647	around die + crest	58 71	166 28
V	103 3	0 918	1000 0	crest	46 09	150 59
VII	103 95	0 809	1050 0	crest	43 81	150 4
VIII	104 05	0 803	1059 0	crest	43 82	162 05

simulation case VII in terms of bulge height In this step, case V had displacement pressure ratio of 0 08, case VII had 0 12 and case VIII had 1 2 up to 5 MPa pressure and then slowly decreased to 0 12 Figure 4 19 presents the ratio of bulge height, maximum equivalent stress, and bulge crest thickness with respect to simulation case V values after the 50 MPa pressure step for all three simulation cases From Figure 4 19 it can be seen that simulation case VII attained most bulge height although at the expense of slightly higher stressing However, it retained most of its thickness as can be seen from Table 4 6 Because of the dimensional limit of the models, the same ratio of loading could not be continued in the subsequent load steps The sheets in all three models eventually failed by rupture at a pressure of about 104 MPa It appears from the above that the pressure at which the bulge ruptures is the same irrespective of the loading profile Therefore the key to obtain a higher bulge is to push the ends keeping the pressure as low as possible so that no buckling occurs at the bulge root or bulge base The pressure on the sheet surface and the strain in the plane of the sheet at any instant seem to have influence on the buckling

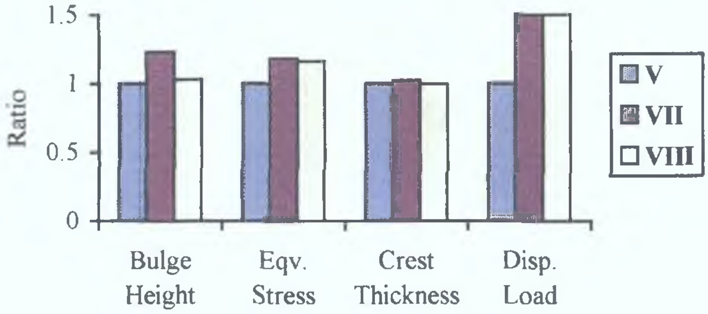

Figure 4.19: Ratio of bulge height, equivalent stress and crest thickness of simulation cases VII and VIII with respect V for different loading pattern.

A very low pressure-displacement ratio loading (as was done in case VIII) pushes the bulge away from the die wall. Figure 4.20 shows the situation for that kind of loading. Subsequent pressure loading, of course, brought much of the bulge back to the die wall, but by this time the bulge crest has reached the instability. This simulation also shows that enhanced in-plane displacement without adequate pressure does not give any better bulge deformation.

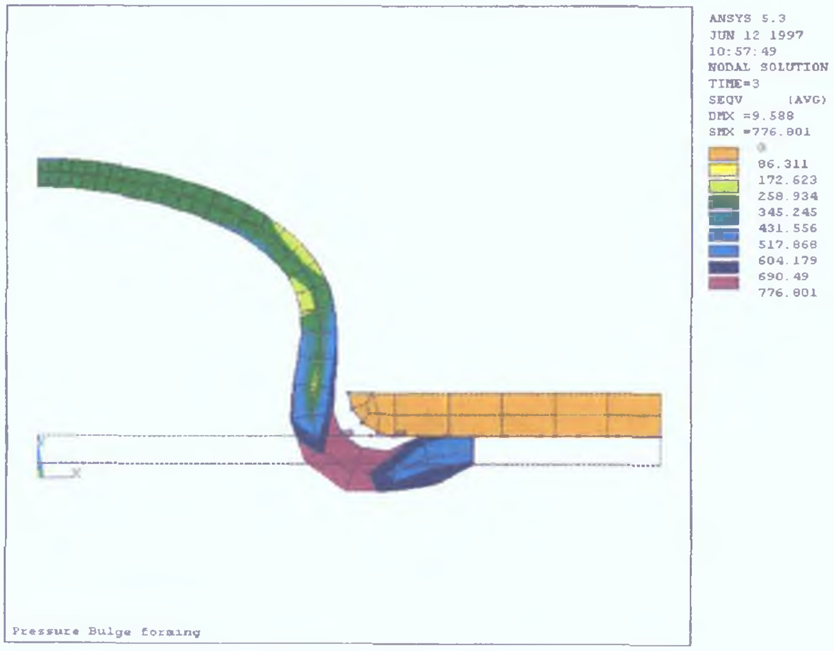

Figure 4.20: Deformation of an enhanced peripheral displacement case

Figure 4.21 shows the development of principal stresses in the central node of the bulge in case VII and Figures 4.22 and 4.23 show the same in the bulge of VIII and V respectively. It appears from these figures that the differences between the 1st and the 2nd principal stresses vanishes quickly at the early part of the first pressure load step in cases V and VII Although the difference continues in case VIII up to the end of the first pressure load step, but it was seen that the deformation behaviour in this was not favourable compared to others The third principal stress maintained negative value throughout the deformation period for all three simulation cases Both the 2nd and 3rd principal stresses in all the cases were strongly compressive at the start and then the compression eased out very quickly

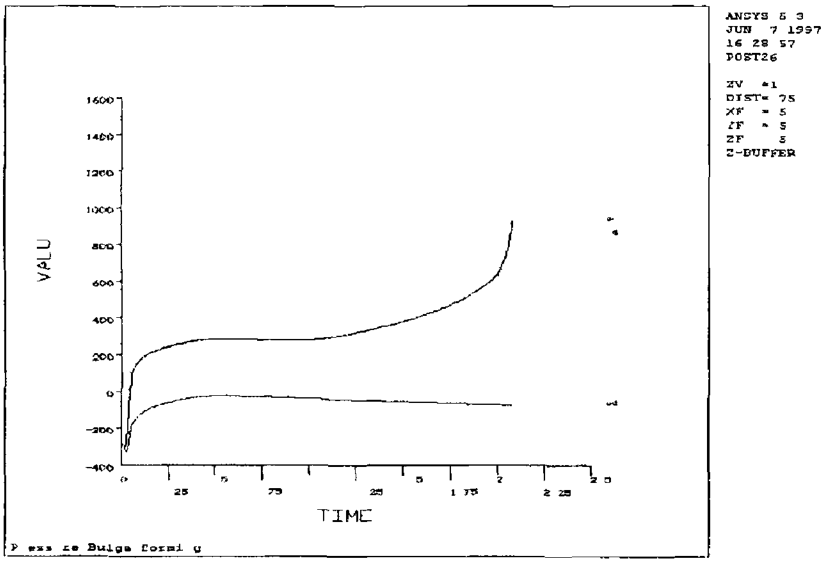

Figure 4 21 Development of principal stresses in the central node of the bulge in case VII

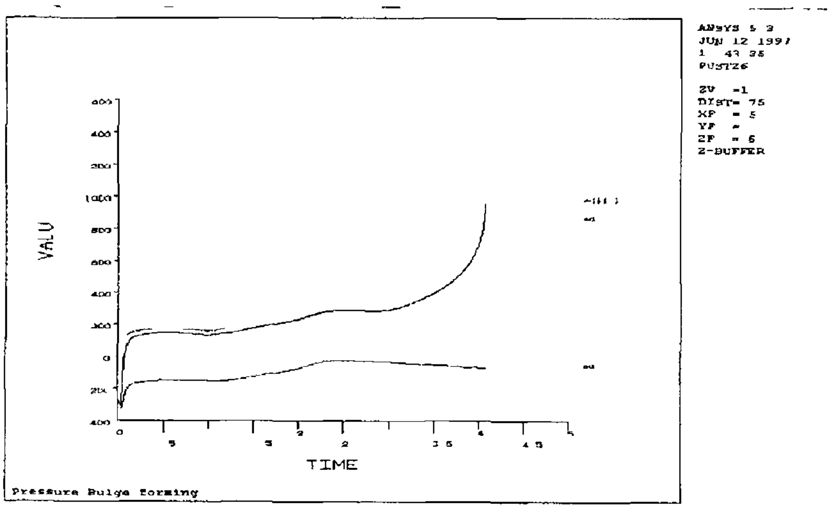

Figure 4 22 Development of principal stresses in the central node of the bulge in case VIII

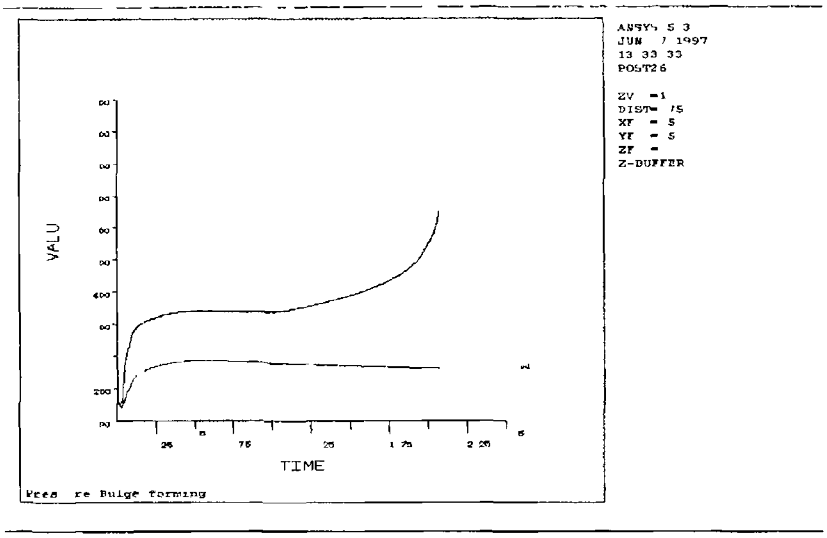

Figure 4 23 Development of principal stresses in the central node of the bulge in case V

General observations

The development of stress and strain in the bulge crest as observed by the history of a central node in the bulge appears to be similar for all the cases with pressure and peripheral displacement loading Slight difference was observed presumably due to the intensity of peripheral displacement loading during the first load step With pressure load beyond 50 Mpa the stress development was identical for all cases although peripheral displacement loading were not similar However, because of model constraint, significantly different displacement loading could not be imparted at that stage Development of stress and strain in the bulge crest in case I where only pressure load was applied is slightly different from the cases with pressure and peripheral displacement loading

The history of the development of principal stresses in a node at the bulge crest suggests that the bulge crest experiences equal biaxial stresses from very early stage of loading This state of stress seems to reach when the pressure loading is about 10% of the critical pressure, a pressure at which there is onset of instability (rupture) in the bulge crest Only exception to this general trend is found to be in the case of simulation VIII where the equal biaxial stress state was reached at about 17% of the critical pressure This is the case where in-plane compressive load was very high compared to the pressure load. But it was seen that this loading did not result in good deformation behaviour.

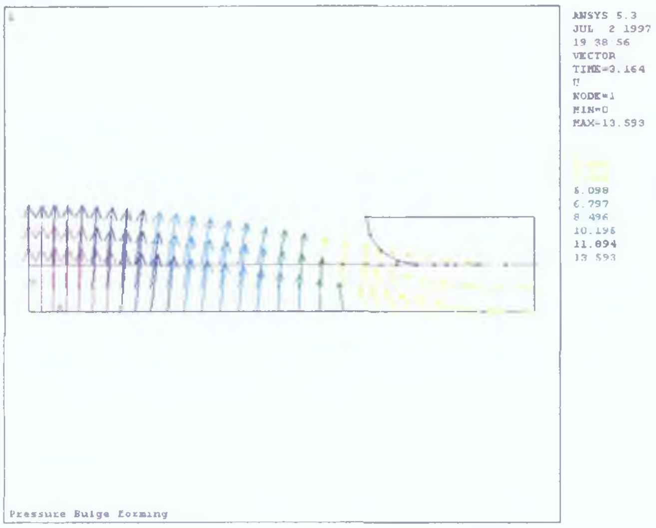

Figure 4.24: Vector plot of total displacement of nodes of a circular sheet with peripheral displacement loading

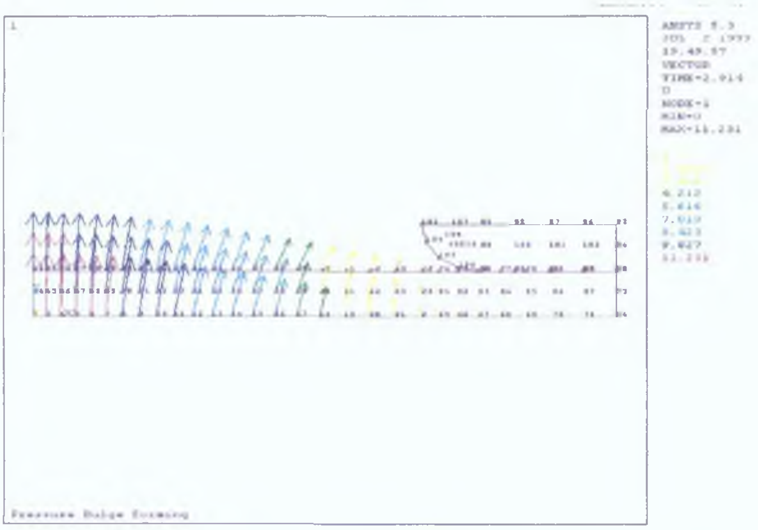

Figure 4.25: Vector plot of total displacement of nodes of a circular sheet without peripheral displacement loading

The absolute displacement of the nodes in all the simulation cases with in-plane compressive load show similar pattern. Figure 4.24 illustrates the vector plot of absolute displacement of the nodes for one such simulation. It is seen that the nodes at the centre have moved the most. The in-plane inward push has induced some material movement towards the centre. This is evident when compared with Figure 4.25 where no in-plane inward displacement was applied. The slope of nodal displacement vectors near the die in Figure 4.24 is higher compared to that on Figure 4.25 indicating a push towards the centre.

Since the sheets were pushed inwards it was obvious that there will be compressive circumferential strain in the bulge root specially under the die. Figure 4.26 shows the plastic strain in circumferential direction. All simulations involving in-plane compressive loading resulted in similar straining. It is seen from the figure that considerable compressive strain developed in the circumferential direction. The elements have been compressed circumferentially between 70-85% around the die bend. In reality this may or may not result in wrinkling at the bulge base since considerable thickening is also observed in this areas.

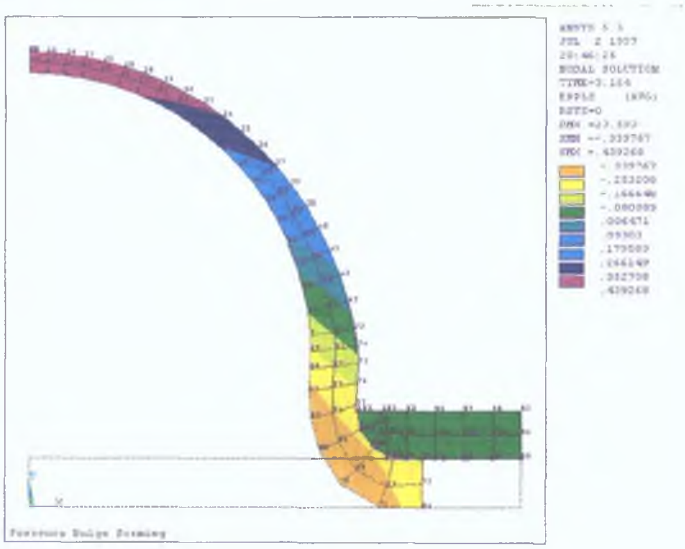

Figure 4.26: Distribution of circumferential strain in a peripherally displaced bulge.

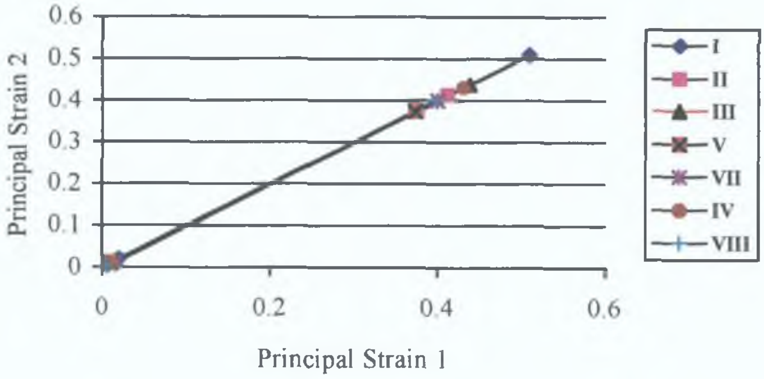

Figure 4.27: Plot of principal strains for different cases of simulation.

The plot of principal strains for different simulation cases at two stages of loading is presented in Figure 4.1.26. One is at a very early stage of loading and the other is at a stage just before instability in the bulge. It can be seen from the figure that although the strains at an early stage of the simulation cases differ very marginally, the instability in them starts at widely different state of straining It can be observed from the figure that more the peripheral displacement less the extent of straining that could be achieved in principal directions It is also evident from the figure that although the sheets in different simulation cases rupture at different strain values, the ratio between the principal strains are almost same as all the points appear to be on the same line

In all the above simulations, the die and the sheet maintained their interfaces as desired, i e , no penetration of the sheet or the die was observed Convergence was smooth for all the simulation cases This is also evident from the smooth development of stress and strain in the central node illustrated in the relevant figures for all the simulation cases

Summary Observations

From the various simulation cases of bulging a circular sheet by simultaneous pressure and in-plane compressive load the main observations may be summarised as below

i) the bulge formation by simultaneous application of pressure and in-plane compressive load produces more height, less stress and strain, and the bulge crest thins less compared to the one formed by pressure load only

ii) thinner sheets may be formed to comparable height with less pressure load But for same blank size, and bulge diameter, thicker sheets can be bulged to more height before instability is reached

iii) Bulging of same blank size and same bulge diameter by same loading pattern but different friction condition (frictionless and with friction) gives comparable bulge height and gives rise to comparable stress But strains in the bulges are different for changes in friction conditions Forming with friction induces more thickening at the bulge root and more thinning at the bulge crest compared to frictionless forming Also larger surface area of the bulge formed with friction has higher stress

iv) Bulging from a sheet of larger blank diameter but same thickness allows more bulging as more peripheral displacement is available It is seen that the gain in the bulge height is nearly equal to the additional peripheral displacement This also gives a thicker bulge

v) The ratio of pressure load to displacement load has marked influence on the bulge forming process Enhanced peripheral displacement without sufficient pressure pushes the bulge root away from the die rather than material to the bulge centre

vi) Direction of absolute displacement of the sheets nodes indicate that the nodes have deviated from the direction that they would have taken in case there were no in-plane compressive load on the sheet The deviation indicates a movement towards the bulge centre

vii) The sheet undergoes considerable circumferential compressive strain at the bulge root and base area At the same time these regions of the bulge have also thickened The net effect of straining in these regions is difficult to predict without simulating the problem in three dimensions

viii) The bulge crest reaches equal biaxial stress when the pressure loading is about 10% of the critical pressure For very accelerated in-plane compressive loading this state of stress in the bulge crest reaches at little higher pressure But if buckling at the bulge root area results for the enhanced compression, then the deformation behaviour is no better

ix) The instability in the bulge occurs at different state of strain for different loading condition It is seen that bulges that are formed with more peripheral displacement fails at lower state of biaxial strain

4.1 2 Bulge Forming of Circular Sheet With Restrained Loading

In the previous simulations the circular sheet was bulged with pressure and in-plane compressive load at the periphery keeping the sheet top free to bulge It was observed that the bulge formed by the combined load has higher height, has more uniform thickness and has less stress and strain It is expected that if the bulge is restrained at the top rather than allowing to form free, it might result in a bulge with longer cylindrical part which is more desirable from manufacturing point of view This section presents the results of the simulations where the cap of the forming bulge is restrained in some form while applying pressure at the under surface and compressive load at the periphery of the sheet Results from the case without any restraining load are also presented as comparison All simulations in this section were modelled and solved using ANSYS

Finite Element Model

Simulation was carried out on the similar model as in Section 4 1 1 The basic outline of the model is presented in Figure 4 28 In this model an adjustable restraining load is placed on the top surface of the forming bulge The restraining load is applied as a pressure proportional to the main bulging pressure applied at the under-surface of the sheet In the finite element model the restraining load is put on some central elements as illustrated in the figure A rigid form of restraint on the forming bulge may be imposed by physically obstructing the bulge after certain height is achieved Figure 4 29 shows a model with such an arrangement The sheet diameter and thickness in these models are 40 mm and 1 5 mm respectively The die opening is smoothed by a 2 0 mm corner radius The advantage of symmetry was availed in modelling Discretisation of the sheet and the die was done utilising the knowledge from the previous analysis

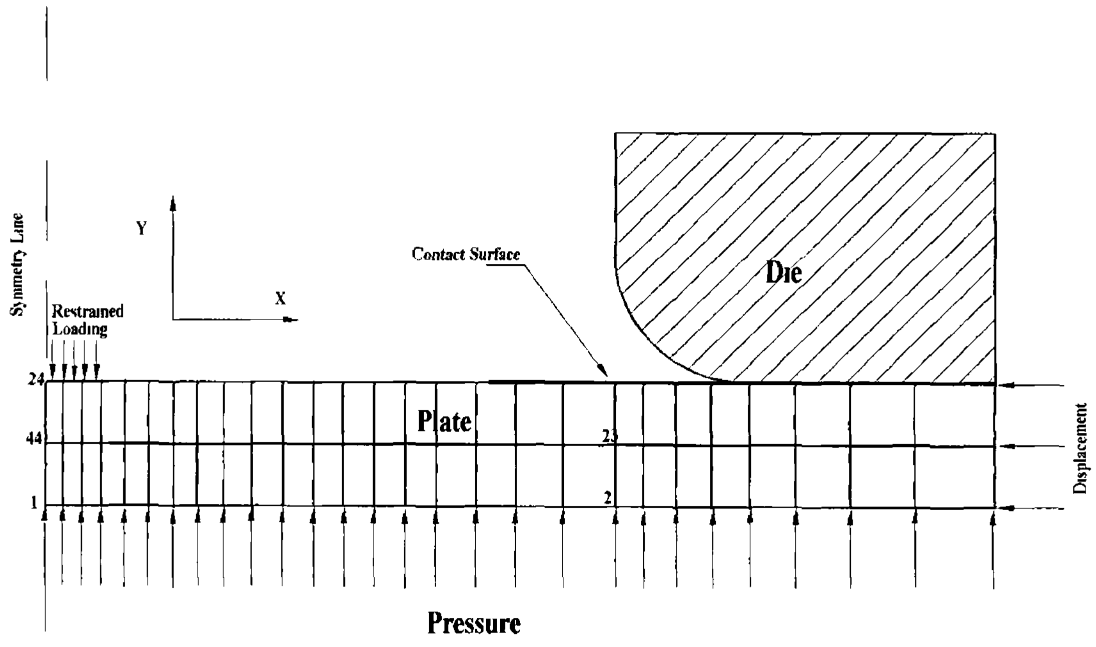

Figure 4 28 Schematic of restrained bulge forming model

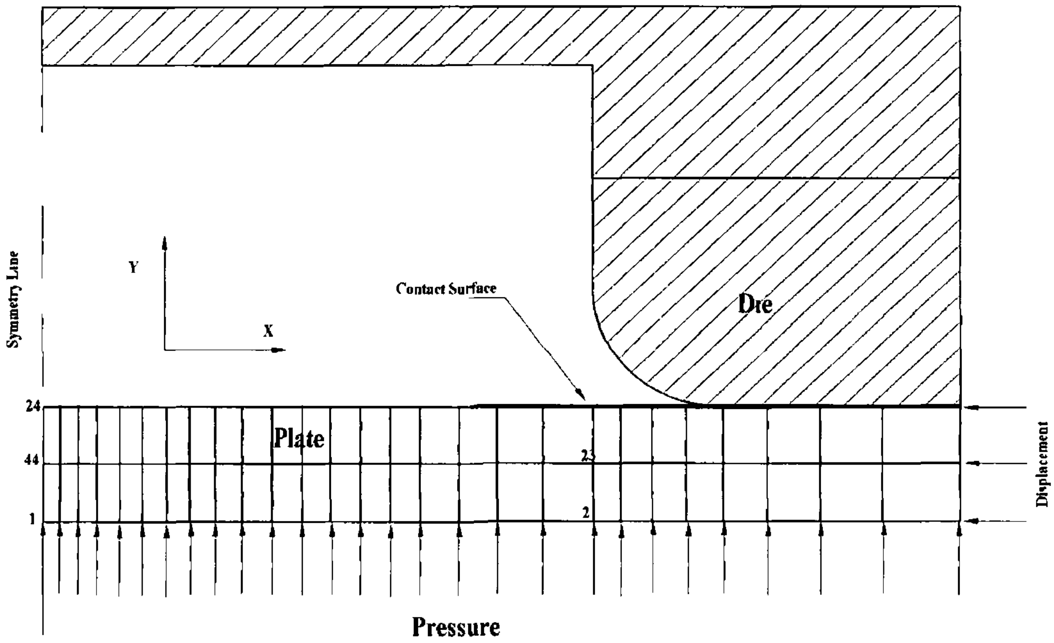

Figure 4 29 Schematic of bulge forming by rigid restraint

A bilinear isotropic elasto-plastic material model approximating the characteristics of an annealed mild steel was adopted as sheet material The characteristics parameters of the assumed material are

Young's Modulus = 207 GPa Yield strength = 280 MPa

Tangent Modulus = 920 MPa Poisson's ratio = 0 3

The die material was assumed to an elastic material with an identical Young's Modulus as the sheet material

The sheet and the die were modelled with 2-dimensional 4-node quadrilateral large strain solid elements This element is slightly different from the elements used in modelling the simulations in Section 4 1 1 However, this is also suitable for simulation of cases involving large deformation, large strain and plastic deformation The interface between the die and the sheet was modelled with general contact elements This is a 2-dimensional 3-node point to surface type element Penalty function method was adopted to determine the contact forces An elastic Coulomb friction behaviour was assumed between the contacting surfaces The coefficient of friction between the die and the sheet was taken to be 0 25

Loading and Solution

Because of axisymmetric modelling, the nodes at the central axis were restricted in X-direction Prescribed displacement was applied to the nodes at the periphery of the sheet Essentially, all the die nodes were totally fixed Pressure load was applied at the bottom surface of the sheet Adjustable pressure load was applied on the face of the three central elements at the top surface of the sheet as restraining load The magnitudes of the restraining pressure load varying between 10% and 25% of the under-surface pressure load were used and a number of models were tried with different ratios However, models with very close ratio of restraining load showed very similar deformation pattern Cumulative load histories of both restrained forming and free forming cases is presented in table 4 7 At each load step, the full load is applied in very small substeps Two loading conditions of adjustable restrained load forming will be referred to as model RFI and RFII respectively The rigidly restrained forming model will be referred to as RFIII The model without any restraint loading will be referred to as FF

Table 4 7 Cumulative load history for free and restrained bulge forming

Load Step	Load			
	Free Forming (FF)	Restrained Forming (RFI)	Restrained Forming (RFII)	Restrained Forming (RFIII)
1	Pressure = 50 MPa Inward Displ = 1mm	Pressure = 50 MPa Inward Displ = 1mm Restraint Load = 5 MPa	Pressure = 50 MPa Inward Displ = 1mm Restraint Load = 12 5 MPa	Pressure = 50 MPa Inward Displ = 1mm
2	Pressure = 100 MPa Inward Displ = 2mm	Pressure = 100 MPa Inward Displ = 2mm Restraint Load = 10 MPa	Pressure = 100MPa Inward Displ = 2mm Restraint Load = 25 MPa	Pressure = 100 MPa Inward Displ = 2mm
3	Pressure = 150 MPa Inward Displ = 3mm	Pressure = 150 MPa Inward Displ = 3mm Restraint Load = 15 MPa	Pressure = 150 MPa Inward Displ = 3mm Restraint Load = 37 5 MPa	Pressure = 150 MPa Inward Displ = 3mm (restraint active)
4	Pressure = 200 MPa (instability)	Pressure = 200 MPa (instability)	Pressure = 200 MPa (instability)	Pressure = 200 MPa
5	-	-	-	Pressure = 250 MPa
6	-	-	-	Pressure = 300 MPa

All the simulation models except the case of RFIII became unstable at 4th load step. By the end of the 3rd load step the periphery of the models were pushed to possible maximum. In subsequent load steps only pressure was applied. The maximum pressure that could be applied to the cases of FF, RFI, and RFII were 155.85 MPa, 157.0 MPa and 157.85 MPa respectively which are quite close. Since the bulge in the case of RFIII reached the obstruction by the end of the 3rd load step, it was possible to pressurise it without the onset of instability. However, after application of the pressure in the last step from 250 to 300 MPa, no additional inflation of the bulge was noticed.

The shape of the bulges in the cases of FF, RFI and RFII just before the instability can be seen in Figures 4.30, 4.31 and 4.32 respectively. These figures also display the von-Mises stress in the bulges. It can be seen from the figures that the shapes of the bulges are not very different. The bulge height obtained at this stage in the cases of FF, RFI and RFII were 13.11 mm, 13.37 mm and 12.62 mm respectively. The pattern of stress distribution in the bulges is also very similar although the surface area for each stress range is slightly different. The maximum stress in the bulges are different; 1016 MPa for the case of FF, 1085 MPa for the case of RFI and 974.6 MPa for the case of RFII.

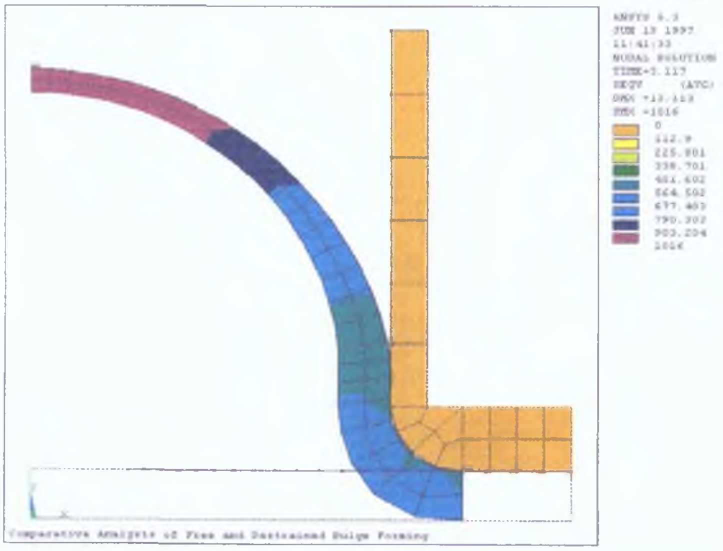

Figure 4.30: von-Mises stress in the bulge for the case of FF.

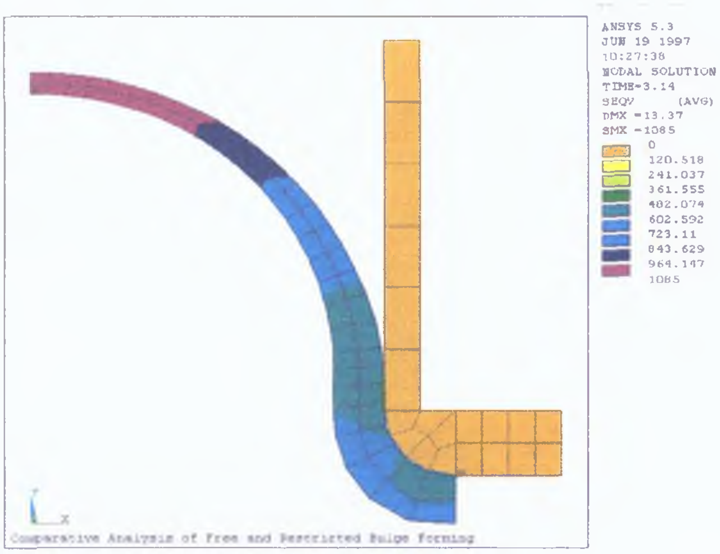

Figure 4.31: von-Mises stress in the bulge for the case of RFI.

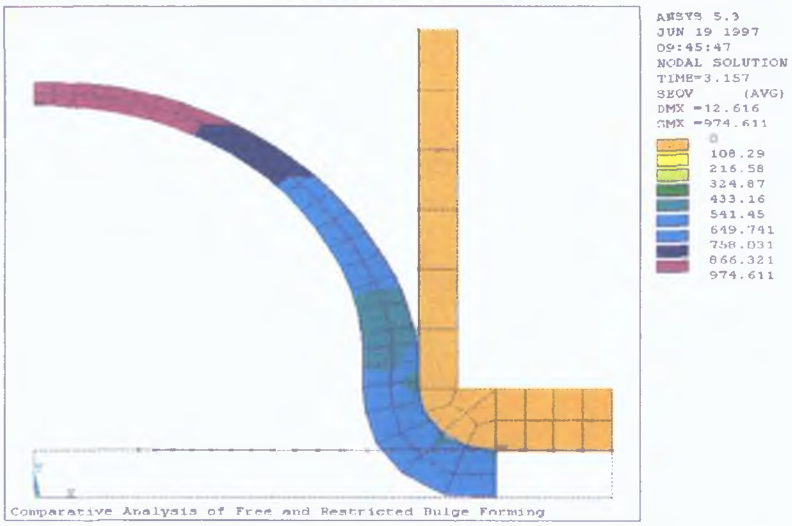

Figure 4.32: von-Mises stress in the bulge for the case of RFII.

The bulge in the case of RFIII had reached the rigid obstruction at the top during the 3rd load step. Therefore, the deformation behaviour in this case is supposed to be different from the others as the restraining load here will be in increasing ratio of the applied pressure load. Figure 4.33 shows the von-Mises stress in the case of RFIII after 3rd load step. The bulge shape is also apparent from the figure. Naturally, the bulge took a flatter shape. It can be seen from the figure that the top surface of the bulge touching the obstruction is being relieved of the stress because of the compression there. The stress concentration has moved towards the bulge root area as opposed to the crest area in other models. The root area now has a strong stress gradient.

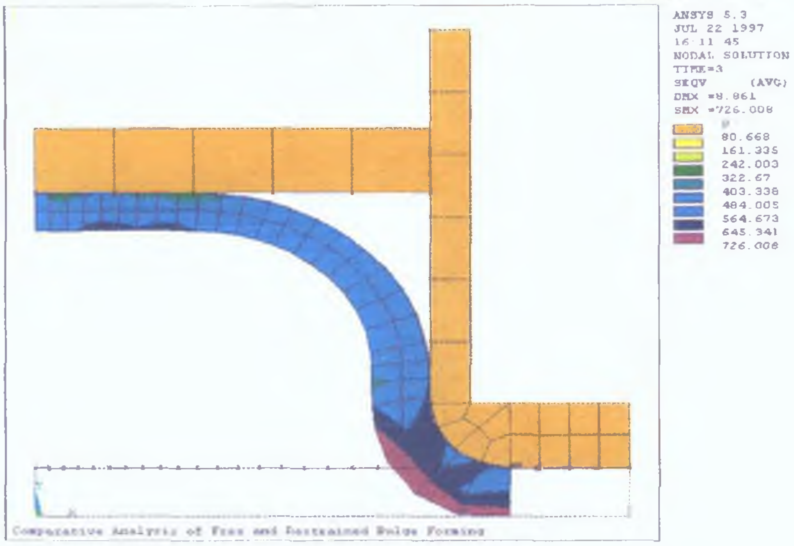

Figure 4.33: von-Mises stress in the case of RFIII after load step 3.

Thickness of the bulges can be ascertained from the strain in the thickness direction of the sheet. Figures 4.34, 4.35 and 4.36 show the distribution of the strain in the bulges for the cases of FF, RFI and RFII respectively just before instability. Again the pattern of distribution is very similar. However, the extent of thinning in the crest area is different. The crest in the case of FF has on the average thinned down to 48% of the original thickness of 1.5 mm. The corresponding figures for the cases of RFI and RFII are 45% and 50% respectively.

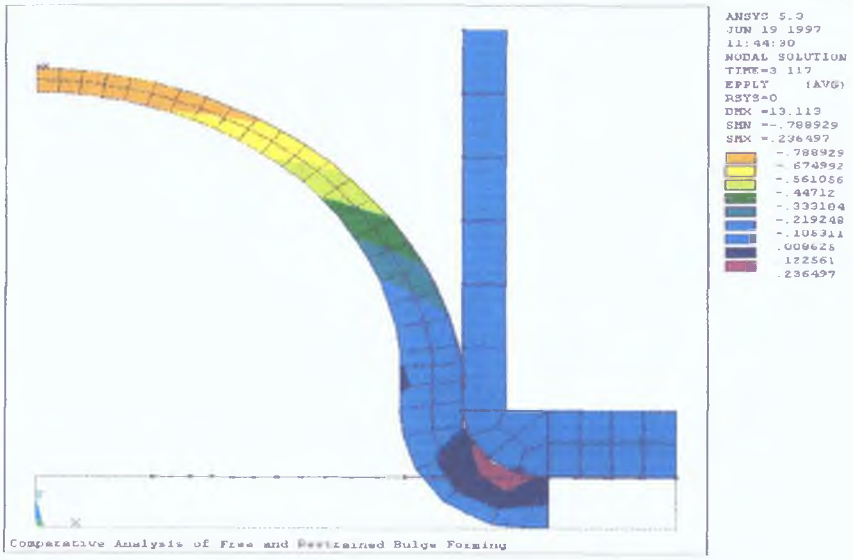

Figure 4.34: Distribution of strain in thickness direction of the sheet in the case of FF.

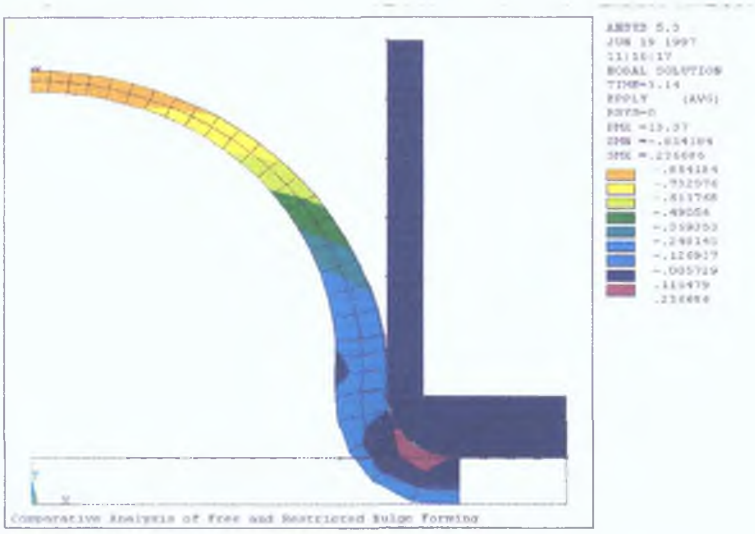

Figure 4.35: Distribution of strain in thickness direction of the sheet in the case of RFI.

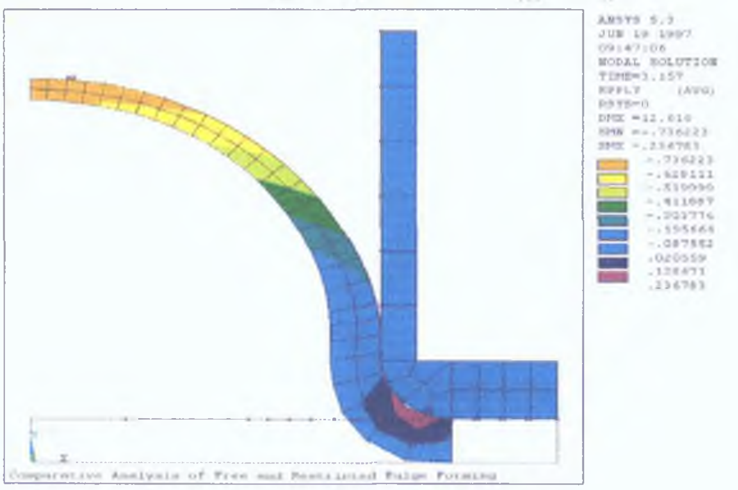

Figure 4.36: Distribution of strain in thickness direction of the sheet in the case of RFII.

It appears from the above that the effect of the adjustable restraining load in pressure form is not very distinctly apparent. In the case of RFII, however, a smaller bulge height is obtained, the stress has reduced and the thinning process slowed down compared to the cases of FF and RFI. Although the loading case of RFI has a restraining load, it seems that it does not put any appreciable counter load on the bulge. The effect of the counter load can be best observed from the deformation in the case of RFIII. The effect was evident in the shape and stress pattern in Figure 4.33. The effect can be further observed in Figure 4.37 which shows the strain in thickness direction for the RFIII loading case. The average thickness in the crest area is 77% of the original thickness. The best thickness obtained from adjustable restraining load was 50% for the case of RFII.

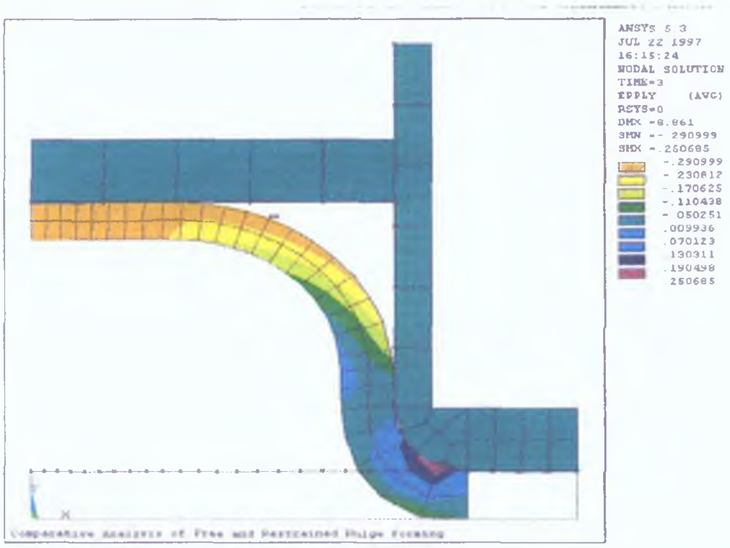

Figure 4.37: Distribution of strain in the thickness direction of the sheet in the case of RFIII.

The development pattern of strain in the central node of the bulges (node 44) for the loading cases of FF, RFI and RFII are not very different. Figure 4.38, for example, shows the development of principal strains in node 44 for the case of RFII. On the contrary the principal strain in the same node has developed very differently in the case of RFIII when the bulge faced the restraint. Figure 4.39 shows the strain history for this case. After the bulge touches the restraint, the strain in the node becomes steady during the 4th load step despite further increase in the pressure load. It seems that during this period the bulge crest was both stretched by the pressure and compressed by the restraint resulting in steady strain state. The balance was lost on further pressure loading when stretching took over the compression.

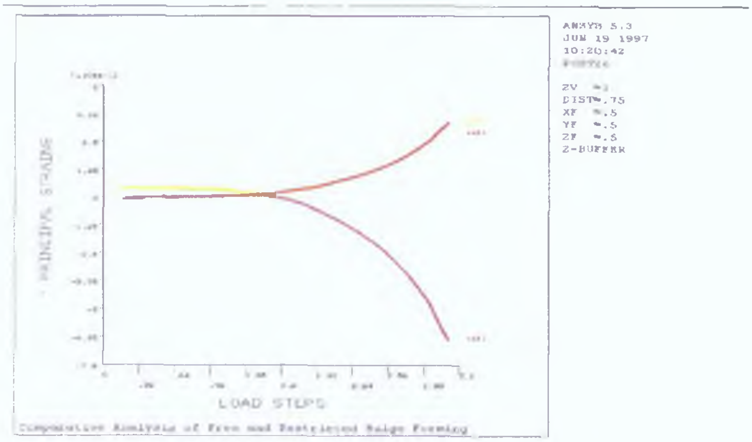

Figure 4.38: Development of principal strains in node 44 in the case of RFII loading period.

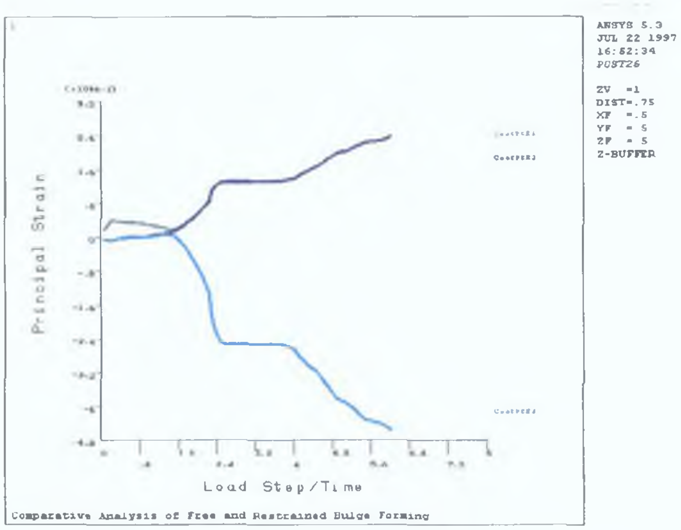

Figure 4.39: Development of principal strains in node 44 in the case of RFIII.

The development of stress in the central node for the RFIII loading case is interesting specially after the bulge has touched the restraint. Figure 4.40 shows the stress history over the load steps. It can be seen that the node has undergone an unsteady state of stress when the bulge touched the restraint. This could be due to the contact and resulting impact on the bulge which stabilised quickly on further pressure loading. The bulge crest then continued to be stressed due to the stretching.

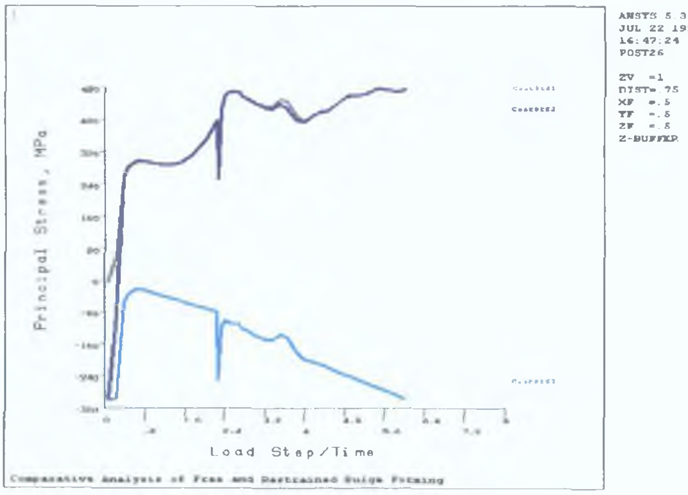

Figure 4.40: Development of stress in node 44 in the case of RFIII.

The bulge in the case RFIII could be further pressurised as there was no possibility of instability at the crest. It can be seen from figure 4.40 that the stress in main two directions in the crest seems to have become steady although the stress in the third direction (through-the-thickness) is getting compressive at an uniform rate. This indicates that the pressure load is just compressing the bulge without much stretching. This is also evident from figure 4.39 where it can be seen that the rate of increase of strains in main principal directions are much less than that in the thickness direction.

The shape of the bulge taken in the case of RFIII is nearly the shape of a cup. The peripheral displacement of the sheet has an important effect on the shape of the bulge. This observation is apparent when compared to the findings of Lee and Ma [27] on similar simulation. In their simulation they did not push the periphery. The shape of the bulge they got did not have any true vertical surface. The bulge did not touch the die recess wall while in the case of RFIII a good part of the bulge trunk has touched the die recess wall. In their simulation the maximum strain in the bulge were found to occur near the edge of the contact area between the sheet and the obstruction. Figure 4.41 shows the equivalent plastic strain distribution in the bulge in the case of RFIII. It can be seen from the figure that the maximum straining is at the same region as found by Lee and Ma. This is also conceivable given the fact that the bulge is now supported at the crest and the most likely area of straining and eventual failure is the unsupported region between the die vertical and horizontal walls.

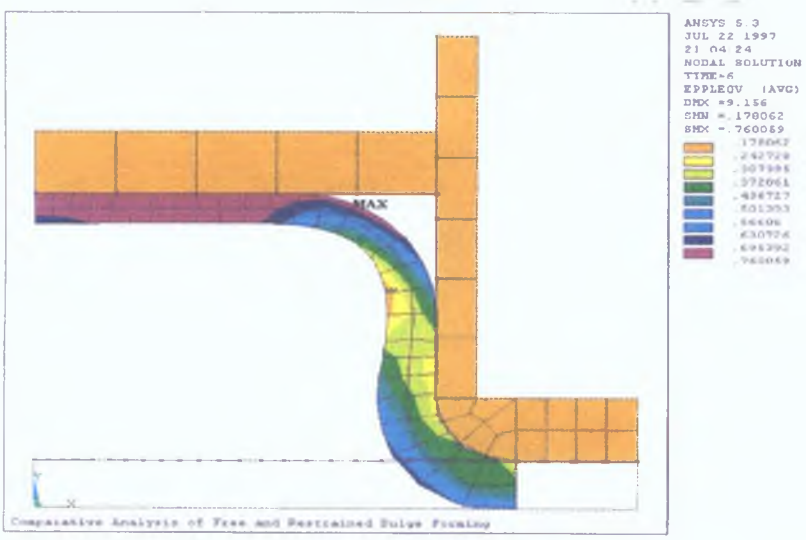

Figure 4.41: Distribution of equivalent plastic strain in the bulge of RFIII loading case after 6th load step.

4.1.3 Optimisation of bulge forming of circular sheet

So far the results of the simulation of bulge forming of circular sheets for different forming conditions have been presented. It was seen that bulge forming of such a component applying combined pressure and axial compressive load involves a number of variables. From the simulation analyses it was apparent that the variables influence the forming process differently. In the forming process, therefore, there is scope to vary different forming parameters and thereby improve certain characteristics of the bulge. Following that line of investigation two optimisation exercises were carried out on bulge forming of a circular sheet applying pressure and in-plane compressive load. This section presents the results from these exercises. Firstly, it was tried to maximise the bulge height with pressure (PRESS), in-plane compressive load in displacement form (DISP) and die corner radius (RAD) as design variables and constraining the problem by specifying the maximum equivalent stress (STRSMAX) in the bulge within certain limit values. Secondly, the same problem was tried for the minimisation of stress differential in the bulge with same design variables and additionally constrained by limiting the bulge height.

Modelling

The problem under consideration was bulge forming of the same 30mm diameter plane sheet of 1.5 mm thickness as in Simulation case II in section 4.1.1. The circular sheet was placed under a circular die with a 20 mm diameter opening. The die opening is smoothed with a corner radius. Advantage of axisymmetry of the structure was availed for the modelling. Meshing of the model was done based on the knowledge from the simulation in the previous section The model was developed parametrically using ANSYS parametric design language. Figure 4.42 exhibits the meshed model identifying the variables of the problem. These variables viz. RAD, PRESS and DISP are the parametric variables in the model.

A bilinear isotropic elasto-plastic material model approximating the characteristics of an annealed mild steel was adopted for the analysis. The characteristic parameters of the assumed material are - Young's Modulus = $207X10^3$ MPa , Yield Stress = 280 MPa and Tangent Modulus = 920MPa.

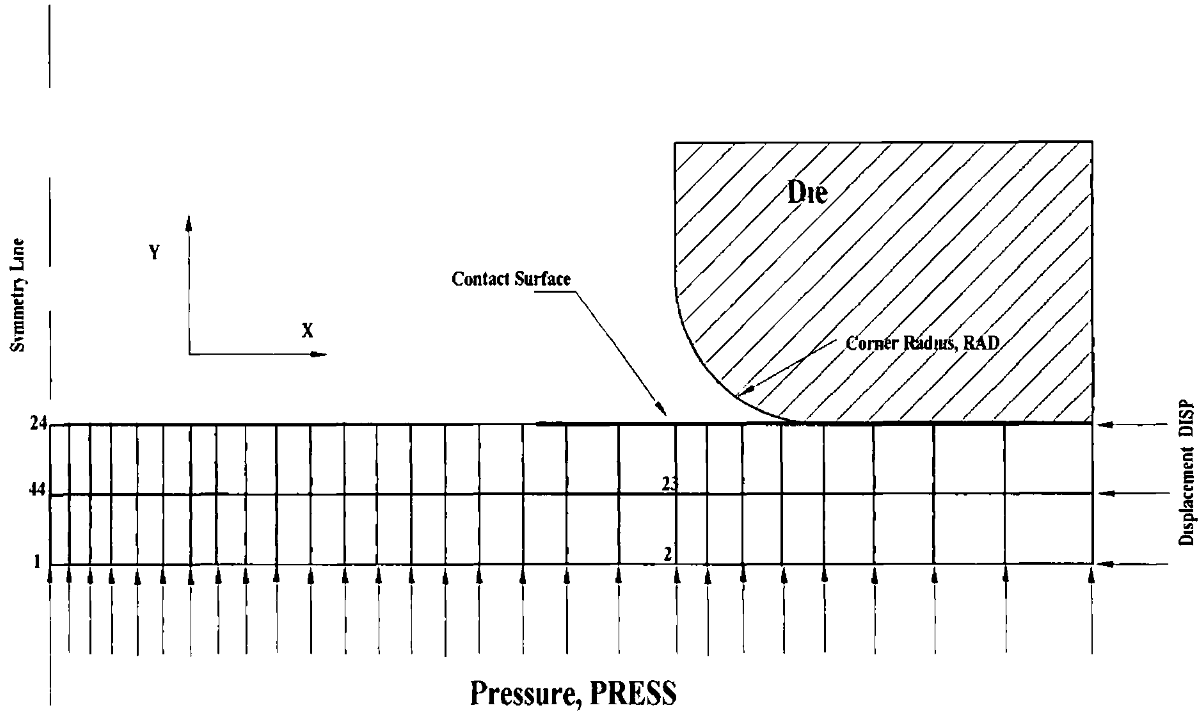

Figure 4 42 The forming model identifying the design variables

The sheet and the die were modelled with 2D four noded quadrilateral This element is suitable for large deformation and large strain analysis It is also designed for plasticity analysis Probable contact surfaces between the die and sheet were modelled with 3 - noded point to surface elements suitable for general contact analysis Penalty method of contact compatibility was adopted for the analysis The contact stiffness value of 2 43X10^3 kN/mm was taken from the previous analyses An elastic Coulomb friction condition was assumed and the value of the coefficient of friction taken was 0 2 Symmetric contact modelling was done making both the die and sheet interfacing surfaces as contact as well as target surfaces

Because of axisymmetric modelling of the structure the nodes at the central axis were restrained in X-direction All die nodes are restricted for all degree of freedom Pressure load was applied on the bottom surface of the sheet and in-plane compressive load was applied at the outer edge in the form of displacement Both types of loads were defined parametrically and applied in four equal sub-steps Depending on the iteration strategy the trial load could vary from 0 2% to 2% of the sub-step load Full Newton - Raphson method was adopted along with line search technique for the solution of the finite element analysis

The optimisation problem

An optimisation problem has to be defined by defining the objective function that relates a certain figure of merit with other relevant variables of the problem In ANSYS this relationship and that between state variables and design variables are determined by regression analysis In defining the optimisation problem one has to decide on the design variables, state variables and objective figure of merit that adequately define the design problem One must keep in mind that all these variables can be handled in the finite element analysis

A metal forming problem may be optimised with respect to more than one aspect In bulge forming one of the prime objective is to attain as maximum bulge height as possible The other objectives could be the minimisation of the unevenness of stress or strain distribution in the bulge or minimising the in-plane compressive load etc The present problem was optimised on two aspects viz maximising the bulge height and minimising the difference between the maximum and minimum equivalent stress in the bulge Table 4 8 presents different variables of the above two optimisation problems Intermediate variables were not active variables of the problem but they defined some active variables Limit values of the variables and their tolerances are also presented in the table

Table 4 8 Variables of the optimisation problems

	Problem 1 (maximising the bulge height)	Problem 2 (minimising stress differential)
Objective variable	**BLGHT** = 50 - **DEFL** tolerance = 0 01X initial value	**STRSDIF** = **STRSMAX** -**STRSMIN** tolerance = 0 01X initial value
Design variables	**RAD**, die corner radius limit, 1 5mm - 3 0mm tolerance, 0 01X limit range **DISP**, displacement of outer edge limit, 0 0 - 3 5mm tolerance, 0 01X limit range **PRESS**, pressure load limit, 50 - 150 N/mm^2 tolerance, 0 01X limit range	**RAD**, die corner radius limit, 1 5mm - 3 0mm tolerance, 0 01X limit range **DISP**, displacement of outer edge limit, 0 0 - 3 5mm tolerance, 0 01X limit range **PRESS**, pressure load limit, 50 - 150 N/mm^2 tolerance, 0 01X limit range
State variables	**STRSMAX**, maximum equivalent stress limit, 400 - 1000 N/mm^2 tolerance, 0 01X limit range	**STRSMAXM**, maximum equivalent stress limit, 600 - 1100 N/mm^2 tolerance, 0 01X limit range **DEFL**,Y-displacement of node 44 limit, 11 5 - 12 5 mm tolerance 0 01X limit range
Inter variable	**DEFL**,Y-displacement of node 44	**STRSMINM**, minimum equivalent stress in the bulge

The tolerances were used for the determination of feasibility and convergence of the solution The constants in the tolerance values were chosen by judging the reasonableness and acceptability of the minimum variation of the variables The limit values for problem 1 were taken from the knowledge of the previous analysis and those of problem 2 were adopted based on the results of problem 1

Quadratic plus cross term regression fit was opted for the approximation of both the objective and state variable function The weightage to each design vector for the error function was based on their distance from the best design, difference of their objective function value from best value and their feasibility The options related to the determination of trial design vector for the next loop of the process (Figure 3 5) were left with the default choices as they would provide a bias towards best design vector

Results And Discussion

The problem was first analysed for maximising the deflection of node 44 (DEFL) which is the through-thickness midpoint node of the bulge crest as shown in Figure 4 42 Since ANSYS optimisation process only minimises the objective function the maximisation objective was modified to a minimisation problem by bringing in the BLGHT as can be seen in Table 4 8 The analysis converged after 12 loops based on the objective function value tolerance between best and final design set Four initial loops were run interactively with chosen design variable values to create data across the design space Subsequent loops were run with computer chosen variables within limit Results of the optimum design set, design sensitivities, and correlation coefficients are presented in Table 4 9

Table 4 9 Summary results of the solution of problem 1

	Sensitivity of obj function BLGHT=50-DEFL	Sensitivity of state variable, STRSMAX	Optimum solution	Multiple correlation coefficient
DEFL	-	-	12 12	
STRSMAX	-	-	833 06	0 99786
BLGHT	-	-	37 88	0 99999
Design variable DISP	-1 237	-570 8	3 4924	-
Design variable, PRESS	-0 05155	18 06	149 77	-
Design variable, RAD	-1 699	-102 1	2 9956	-

It appears from the correlation coefficient values in the table above that a good fit to a quadratic plus cross term surface achieved for both objective and state variable function. Design sensitivities, derivative of the approximate function with respect to each design variable at the solution point, of the objective function are all negative as can be seen in Table 4.9 indicating that DEFL value would increase for positive change in any design variable. Die corner radius, RAD is most sensitive followed by DISP, displacement of the outer edge of the sheet. Naturally, the values of the design variables were pushed to the upper limit for optimality. Sensitivity values of state variables in the table suggest that STRSMAX, the maximum equivalent stress in the bulge will increase for increase in PRESS but will decrease for a larger RAD or DISP.

. Figures 4.43 and 4.44 show how the values of different variables changed during the analysis. It can be seen that the design variables reached about their maximum limit and stabilised fairly quickly half-way through the looping process. DEFL and STRSMAX stabilised after 10th loop and converged thereafter.

From the results presented above it is apparent that optimality of the solution is not conclusive. However, the analysis provided a maximum achievable bulge height value that can be incorporated in some form while optimising from some other point of view. In fact in the second analysis of this presentation, DEFL was taken as a state variable with limits close to the value obtained in the first.

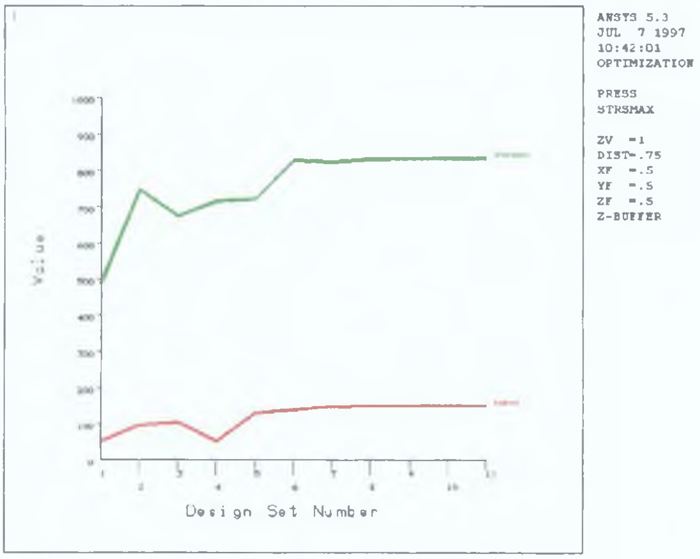

Figure 4.43: Behaviour of STRSMAX and PRESS during the height maximisation analysis

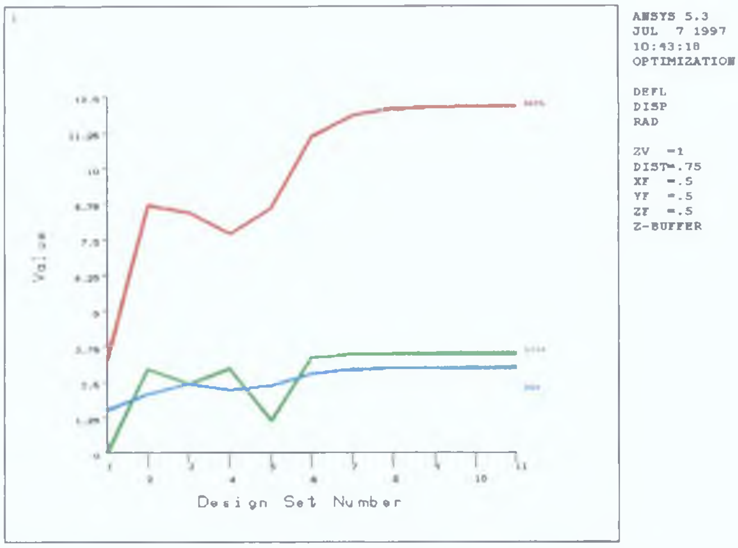

Figure 4.44: Behaviour of DEFL, DISP, RAD during the height maximisation analysis

The objective of the second analysis was to minimise the difference between the maximum and minimum equivalent stress in the bulge. The design variables remain the same as the first one. Table 4.8 presented earlier shows the variables and their limits and tolerances.

As in the first analysis, design variable values for four initial loops were provided manually to create data across the design space. The solution converged after 27 loops based on design variable tolerance between best and final design. Results of the optimum solution and sensitivity and coefficients of the approximate functions are presented in Table 4.10.

Table 4.1.10: Summary results of the second optimisation problem

	Sensitivity of Objective Function, STRSDIF= STRSMAXM - STRSMINM	Sensitivity of State Variables		Optimum Solution	Multiple Correlation Coefficient
		DEFL	STRSMAXM		
STRSDIF	-	-	-	464.81	0.93788
DEFL	-	-	-	11.501	0.99634
STRSMAXM	-	-	-	834.33	0.98116
DISP	138.1	1.062	-263.0	3.3412	-
PRESS	12.40	0.08351	-2.285	145.12	-
RAD	-249.40	-.4921	383.30	2.9969	-

It appears from the table above that the approximate function of quadratic plus cross term form are well fitted to the data points. Two design variables viz. inward displacement of the periphery and die corner radius have reached close to their upper limit values. As to the sensitivity, it can be seen that die corner radius is again the most sensitive variable for stress differential and second most for bulge height. Both the stress differential and bulge height will decrease for positive change of die corner radius. Stress differential will increase if the periphery of the sheet is pushed further inward. The sensitivity value of DEFL shows that positive changes in DISP and PRESS would increase the bulge height.

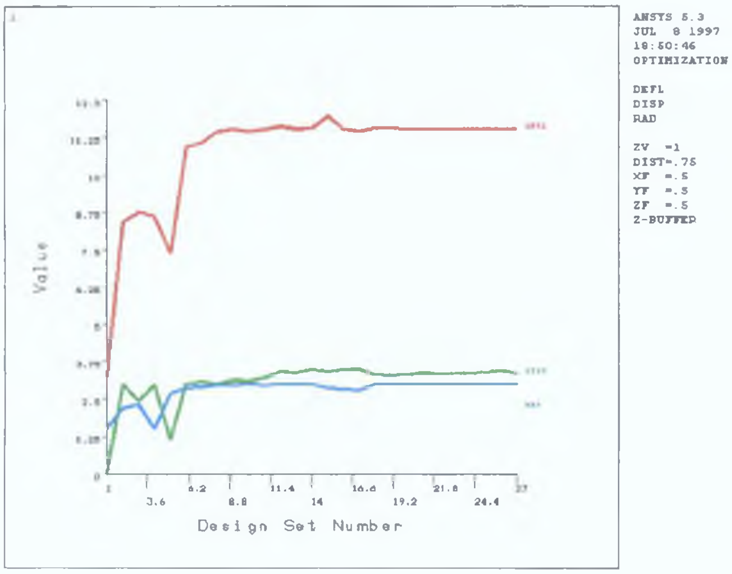

Figure 4.45: Changes in DEFL, DISP and RAD during the stress differential minimisation

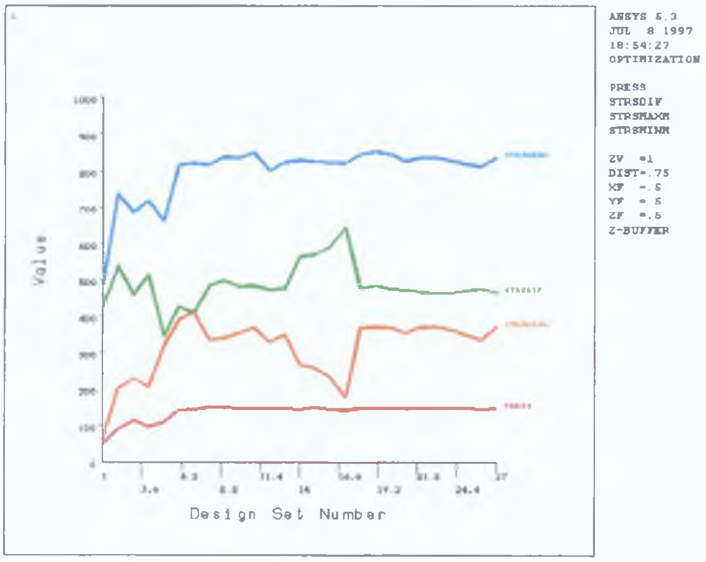

Figure 4.46: Changes in STRSDIF, STRSMAXM, STRSMINM and PRESS during the stress differential minimisation analysis

Changes in the values of different variables can be seen in Figures 4.45 and 4.46. All the variable values except pressure were unstable until 19th loop. After 17th loop the minimum equivalent stress in the bulge has increased significantly thereby decreasing the stress differential very sharply. In fact the solution encouraged development of compressive stress in the structure. This has increased the overall stress in the bulge. Figure 4.47 shows the distribution of equivalent stress in the bulge for the above optimum solution. Figure 4.48 shows the distribution of equivalent stress in an equivalent bulge where the pressure load applied was 150MPa and the peripheral displacement was 3.0mm. Comparing these two figures it is evident that the range of stress in the bulge is not very different, but the pattern of stress distribution is significantly different. In the optimised bulge the crest and the body are less stressed and the distribution is also more even compared to the non-optimised bulge.

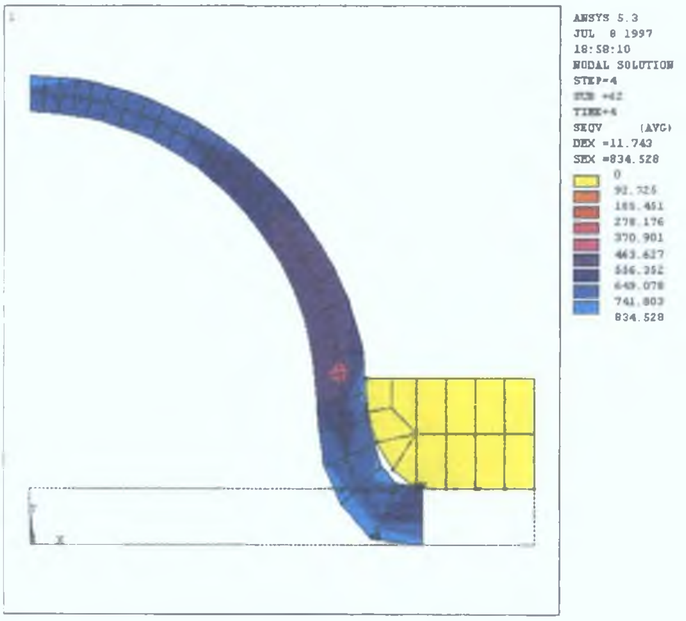

Figure 4.47: Distribution of equivalent stress in the optimised bulge

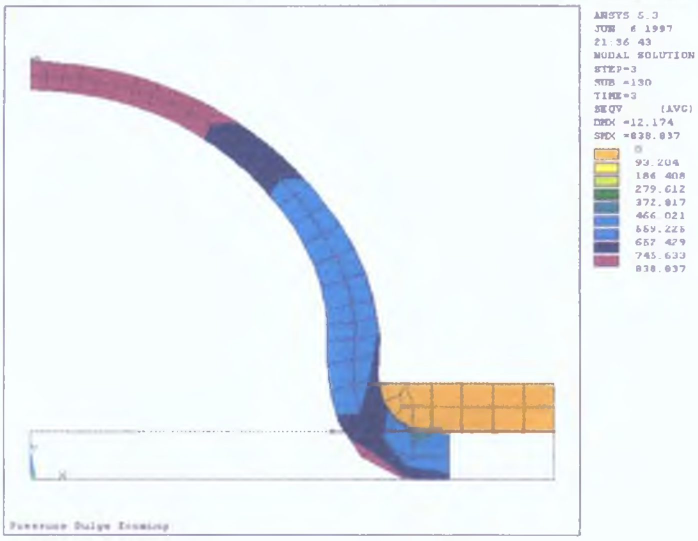

Figure 4.48: Distribution of equivalent stress in an equivalently loaded non-optimised bulge

The difference is more apparent from the distribution of equivalent strain in the bulges. Figures 4.49 and 4.50 show the distribution in optimised and non-optimised bulge respectively. From the figures it can be seen that the optimised bulge as a whole has strained less by about 10% from the non-optimised bulge. Also, the distribution is much even in the optimised bulge. Of course, the bulge has a height less by about 3% from that attained in the non-optimised bulge. However, the better stress and strain condition in the optimised bulge are worthy of consideration.

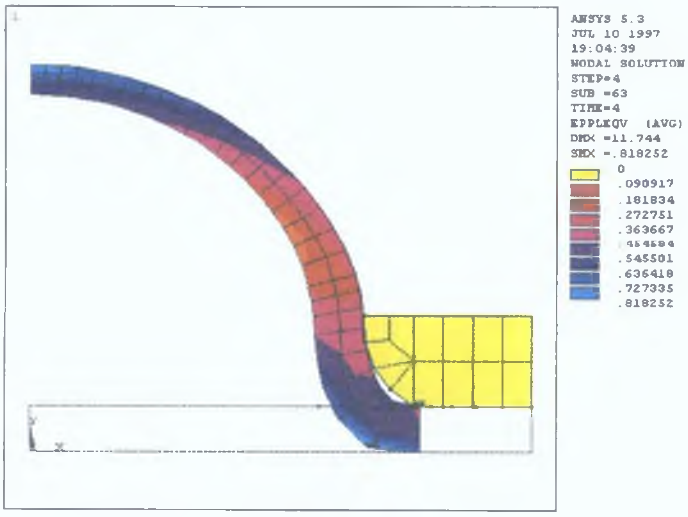

Figure 4.49: Distribution of equivalent plastic strain in the optimised bulge

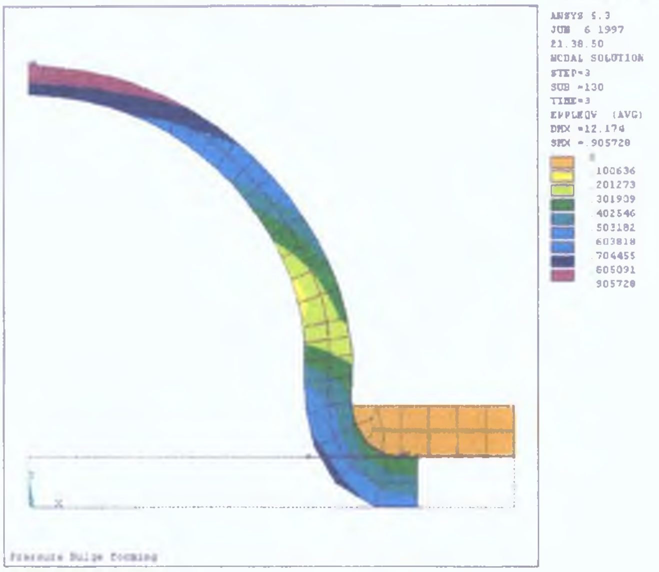

Figure 4.50: Distribution of equivalent plastic strain in an equivalent non-optimised bulge

As mentioned before, most of the design variable limits were chosen based on the analysis done on this structure earlier so that instability does not arise during the course of finite element analysis. It was found from the results that thickness ratio at the bulge crest, likely region of most thinning, was 0.593 for the second analysis. The bulge can thin up to a ratio of about 0.425 before the onset of instability as was observed before. From the above it appears that the bulge has not reached instability and further deformation is possible by changing the limit of suitable design variables based on the sensitivity values available from these analyses.

The mesh in the structure can not be modified although the geometry is changing from solution to solution. However, the changes in geometry is limited to the die in these analyses. The mesh density in the die region has changed but considering the limit of the corner radius it is expected that the analyses would give fairly reliable result. The results were checked for reliability by checking the load-displacement and stress-strain behaviour of the structure during deformation. It was found that these relationships were smooth throughout the deformation process.

Discrete Optimum by Taguchi Method

Looking at the optimum solutions in Table 4 9 and Table 4 10 it can be seen that the design variable values are precise up to 4 decimal places From engineering implementation point of view the values are either difficult or impractical to manufacture or control For ease of manufacture or control, discrete values of design variables are always desirable Table 4 11 was developed with probable discrete values to the design variables close to their optimum solution values keeping the manufacturing concerns in mind and satisfying the simulation model constraints The sensitivities of the objective function and the state variable with respect to each design variable in Table 4 9 and Table 4 10 were considered for respective cases and in possible cases taken care of to choose the discrete values The values were chosen close to the optimal values so that the probability of missing any local behaviour of the design space is minimal

Table 4 11 Chosen values of design variables at two levels

Design variable	Bulge height maximisation		Stress differential minimisation	
	level 1	level 2	level 1	level 2
RAD , mm	2 75	3 0	2 75	3 0
DISP, mm	3 25	3 5	3 25	3 5
PRESS, MPa	149 0	150 0	144 0	145 0

Three factor-two level orthogonal array from Wu and Taguchi[102] was adopted for the design of the trial runs Table 4 12 presents the factor-level combination for the four trials runs to be simulated and analysed in this sub-section Each trial run was simulated by putting the corresponding design variable values as input to the design optimisation algorithm Result from each run would give different performance characteristic values of the process

Table 4 12 Factor level combinations for the trial runs

Trial Run / Factor	Factor levels		
	RAD	PRESS	DISP
1	1	1	1
2	1	2	2
3	2	1	2
4	2	2	1

Results of Bulge Height Maximisation

As outlined in the Appendix on Taguchi's method, the S/N ratio was calculated from the responses of the objective criterion for respective trial runs For the objective criterion of bulge height maximisation, Equation A-3 of the Appendix was used to calculate the S/N ratio Table 4 13 shows the bulge height and S/N ratio of different runs Table 4 14 presents the level-wise average bulge height and S/N ratio for each factor Figure 4 51 graphically shows the trend of average bulge height and S/N ratio due to change in the level of different factors

Table 4 13 Bulge height and corresponding S/N ratio for the trial runs

Run/Factor	Factor values			Bulge height,mm	S/N ratio
	RAD, mm	PRESS, MPa	DISP, mm		
1	2 75	149 0	3 25	11 8	21 43
2	2 75	150 0	3 5	12 15	21 69
3	3 0	149 0	3 5	12 041	21 61
4	3 0	150 0	3 25	11 855	21 47

Table 4 14 Level-wise average bulge height and S/N ratio for different factors

Factors	Average bulge height		Average S/N ratio	
	level 1	level 2	level 1	level 2
RAD, mm	11 975	11 948	21 56	21 54
PRESS, MPa	11 920	12 002	21 52	21 58
DISP, mm	11 827	12 095	21 45	21 65

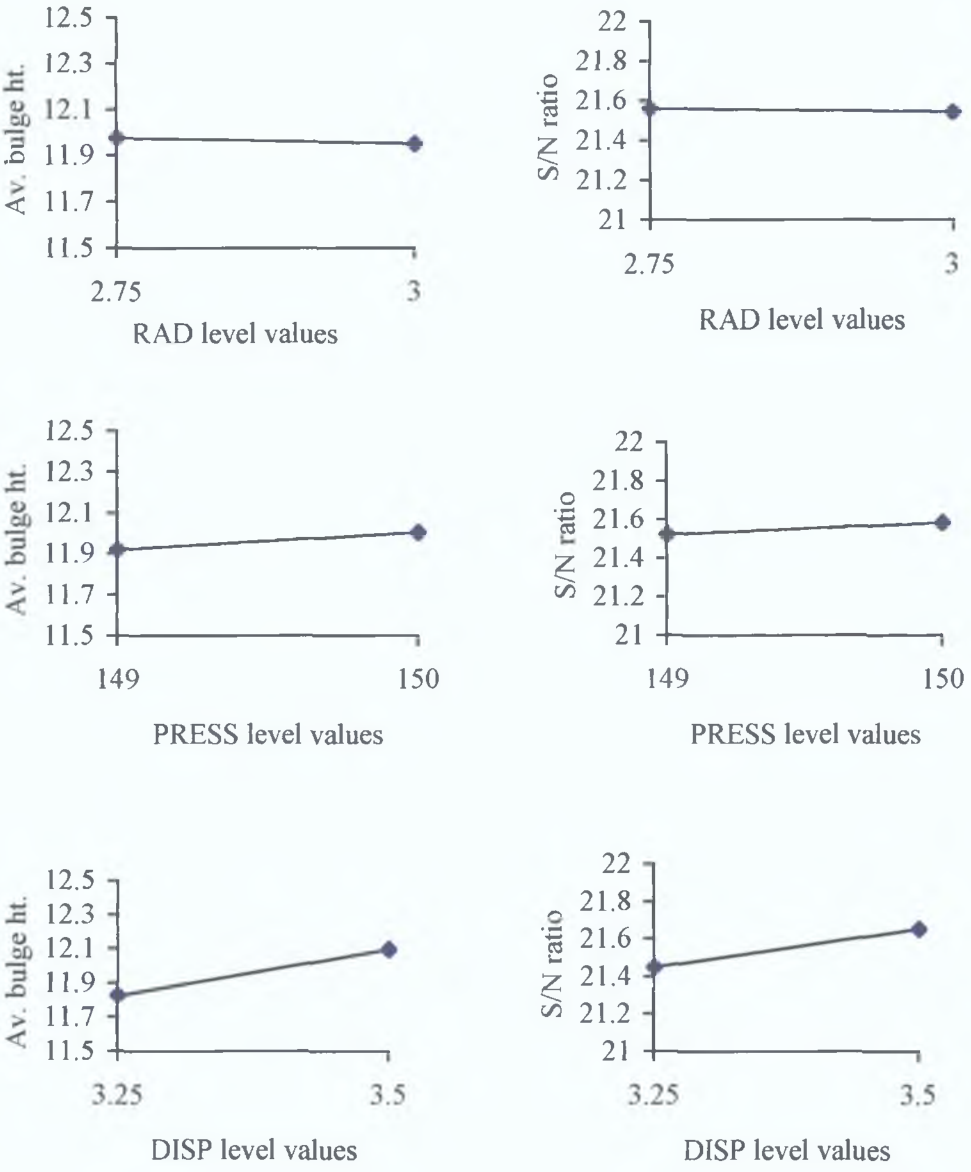

Figure 4.51: Trend of average bulge height and S/N ratio against factor levels

From Table 4.14 and Figure 51 it can be seen that the corner radius (RAD) value at level 1 gives slightly higher bulge height and S/N ratio. Pressure load (PRESS) at level 2 also gives slightly higher bulge height and S/N ratio than that at level 1. Inward peripheral displacement (DISP) at level 2 gives higher bulge height and S/N ratio compared to that at level 1. The trend of change of bulge height is more significant in case of change in DISP level than those for the other factors viz. RAD and PRESS. Selecting the levels that give higher bulge height and higher S/N ratio as suggested by

Taguchi method, the optimal combination that would give bulge height with minimal variability could be corner radius of 2 75 mm, 150 0 MPa pressure and 3 5 mm inward displacement of the sheet periphery

The solution set obtained by Taguchi method may be compared with that from the original optimum solution by ANSYS Table 4 15 presents both solution sets It can be seen from the table that the discrete solution gives almost equal bulge height to that of the ANSYS continuous solution Discrete design variable values except the corner radius are very close to the original solution The maximum stress in the bulge has almost remained the same

Table 4 15 ANSYS solution and *solution by Taguchi method*

Objective criterion/Factor	ANSYS continuous solution	Taguchi method solution
Bulge height, mm	12 12	12 15
Maximum stress, MPa	833 6	835 55
Corner radius, mm	2 9956	2 75
Pressure load, MPa	149 77	150 0
Inward disp, mm	3 4924	3 5

Results of Stress Differential Minimisation

For the above objective criterion, Equation A-2 of the Appendix was used to calculate the S/N ratio from the stress differential values obtained in the four simulation runs Table 4 16 presents the stress differential values and corresponding S/N ratio for each run Level-wise average stress differential and average S/N ratio is shown in Table 4 17 Figure 4 52 shows the trend of average stress differential and average S/N ratio for changes in the level of each factor

From Table 4 17 and Figure 4 52 it is apparent that corner radius at level 2, pressure at level 2 and inward displacement at level 1 give lower stress differential and higher S/N ratio According to Taguchi method this factor-level combination would give stress differential in the bulge with least variability

Table 4.16: Stress differential and corresponding S/N ratio of the trial runs

Run/ Factor	Factor values			Stress differential, MPa	S/N ratio
	RAD, mm	DISP, mm	PRESS, MPa		
1	2.75	3.25	144.0	502.45	-54.02
2	2.75	3.5	145.0	543.86	-54.70
3	3.0	3.25	145.0	451.00	-53.08
4	3.0	3.5	144.0	546.89	-54.75

Table 4.17: Level-wise average stress differential and average S/N ratio for the factors

Factor	Stress differential, MPa		S/N ratio	
	level 1	level 2	level 1	level 2
RAD, mm	523.15	498.94	-54.36	-53.91
PRESS, MPa	524.67	497.43	-54.38	-53.89
DISP, mm	476.72	545.37	-53.55	-54.72

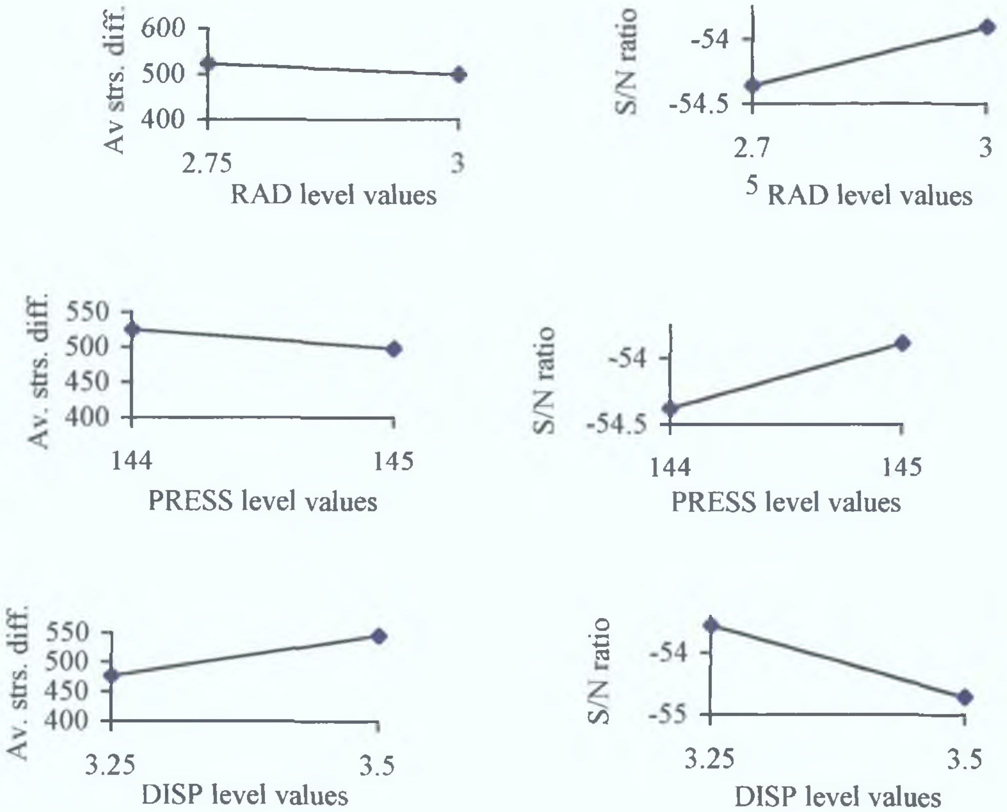

Figure 4.52: Trend of average stress differential and S/N ratio against the factor levels

The solutions by ANSYS and Taguchi method for stress differential minimisation case are presented in Table 4 18 for comparison The Taguchi optimum solution is not very different from the ANSYS solution but the former gives discrete design variable values Also, the stress differential in the bulge has slightly reduced keeping the bulge height almost close to the ANSYS solution value

Both ANSYS optimum solutions are almost at the edge of the design space As a result there was limited scope to consider sensitivity aspects in choosing the discrete values of the design variables For example, in bulge height maximisation case none of the chosen discrete values satisfy the direction as suggested by the sensitivity of the objective criterion but some conform to the sensitivity of the maximum stress In stress differential minimisation case the pressure values and displacement values conform to the sensitivity of the objective criterion and most conform to sensitivity of the maximum stress As a result, an equally optimal solution was obtained for bulge height and somewhat better solution was obtained for stress differential

The two analyses are actually the design of the same forming process but optimised for two different objectives However, the two approaches have resulted in two slightly different solution sets with respect to the pressure value

Table 4 1 18 ANSYS solution and solution by Taguchi method

Objective function/ Factor	ANSYS solution	Taguchi method solution
Stress differential, MPa	464 81	451 00
Maximum stress, MPa	834 33	852 19
Bulge height, mm	11 501	11 415
Corner radius, mm	2 9969	3 0
Pressure load, MPa	145 12	145 0
Inward displacement, mm	3 3412	3 25

The design factors were assigned values at two levels in this work In normal design of experiment, two level experiments actually reveal limited behaviour of the process compared to experiment with more levels However, considering the fact that the design space has already been searched by another algorithm, the main purpose of the Taguchi method is to find a combination of discrete factor levels very close to the already found saddle point In this sense, two levels within a narrow range does not contradict the purpose

4.2 Bulging a Rectangular Plate in the Middle by Pressure and In-Plane Compressive Load

Simulation of bulging of a circular sheet with pressure and in-plane compressive load has shown that appropriate application of in-plane compressive load gives higher bulge height, lower stress and strain compared to forming by pressure load only However, in real forming the application of peripheral push on the sheet could be difficult More realistic forming situation would be to bulge a rectangular or square plate In such a case application of in-plane compressive load is much simpler This section presents the simulation of forming a rectangular plate ANSYS finite element package was used for the simulation

Modelling

The plate size to model was (107 X 75 77 X1 37)mm The bulge diameter that had to be formed was 24 mm Since the bulge was formed at the middle of the plate, the model required a three dimensional treatment One quarter of the whole problem was modelled taking advantage of quarter symmetry The finite element package used for the work had a limited node assignment facility The model size had to be limited to keep the wavefront size of the solver within limit This put a major constraint on the modelling of the problem The die covering the whole of the plate quadrant would increase the number of elements beyond the allowable limit So, modelling was planned considering the probable deformation the plate might undergo

It was planned that the in-plane compressive load would be given by pushing the longer side of the plate It was conceived that by keeping the end movement within certain limit, certain portions of the plate would not move into the bulge region This would enable to model the die covering a limited part of the plate With the above forming condition in mind the plate was modelled in four parts so that each part could be constrained independently Figure 4 53 shows the plate identifying the four parts as volumes The die was built on the top of volume 1 only A projection of the die is drawn on the plate in Figure 4 53 identifying the bulging region Volume 1 was so

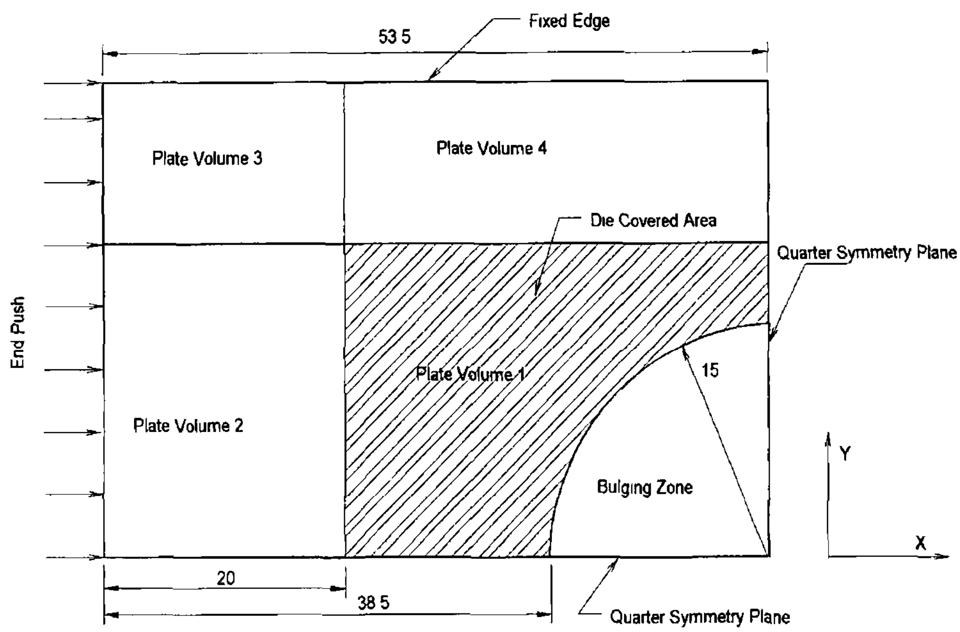

Figure 4 53 Schematic of the model in X-Y plane

approximated that the nodes at the surface between volume 1 and volume 2 would move at most by the amount the plate end would be pushed This would ensure that the nodes of volume 2 would not move into the bulging region which is a certain distance away from the interface of volume 1 and volume 2 Since the plate will be pushed at the end of volumes 2 and 3, it is almost unlikely that the nodes in volumes 3 and 4 would move in the bulging region

To keep the number of elements in the model low, a skinned volume of the die was built instead of a solid die block The die was built in five volumes mainly to facilitate contact modelling and to take care of the curvilinear part of the die The curvilinear part of the die consists of double curvature surfaces described by coons patches The die fillet radius was 3 mm

Both the plate and the die were discretised with 8 node brick elements with two integration points in each co-ordinate direction The plate was discretised with two elements across the thickness in order to have better deformation result in thickness direction Figure 4 54 shows the discretised plate and die Given the limitation on number of elements, the discretisation is rather coarse However, volume 1 of plate where most deformation is likely and the curvilinear part of the die were relatively densely meshed A total of 7512 elements were generated in the model These include the contact elements also The number nodes in the model was 564 Some mid-plane nodes of the plate are indicated in the figure for discussion of results. Nodes 3 and 4 are the nodes in volume 1 which would go to the bulging zone before any nodes in volume 2 would go. Node 236 is the corner node on volume 1 which is likely crest point of the bulge.

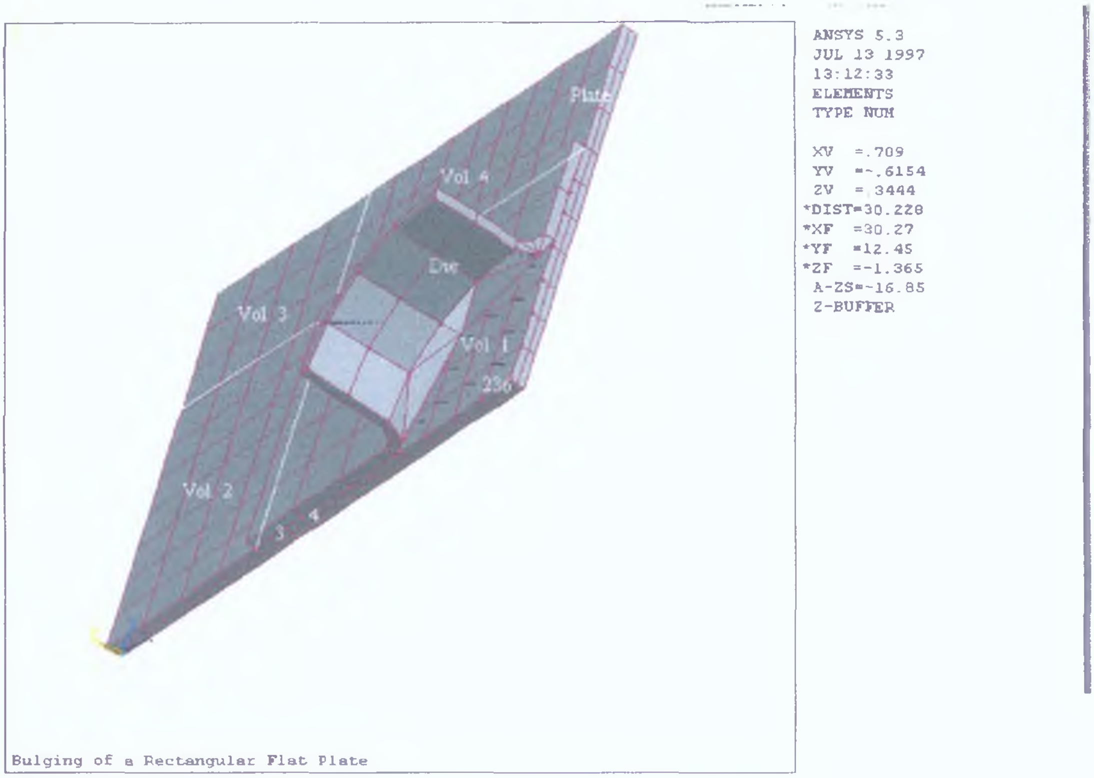

Figure 4.54: Discretised die and plate.

The plate is modelled with multilinear isotropic material model. Different parameters describing the material behaviour are:

Young`s Modulus: $3.60\times10^3$ Mpa Poisson`s ratio: 0.3

Strain	Stress(MPa)
0.005	18.3
0.50	220.0
2.0	465.0

The die was modelled with an elastic material of Young`s Modulus of 2.07×10^5 Mpa. The die was treated as rigid body by fixing its all degrees of freedom.

Three dimensional point-to-surface contact elements were used to model contact between the die and the plate. Selective surfaces of the plate and the die were used to define contact interface elements. All the under surfaces of the die and top surface of the volume 1 of plate were used to define the contact situation. Elastic Coulomb friction model was assigned with a friction factor of 0 3 Symmetric contact elements were generated so that both the die and the plate become contact and target at the same time The stiffness of the contact elements was 9 15 kN/mm which was established after several trial runs when the penetration of contacting nodes at the interface were negligible

Loading and Solution

As mentioned, modelling of the problem was done with certain loading conditions that would compensate the absence of die on certain surfaces of the plate This was done by constraining the top surfaces of volume 2, 3 and 4 of the plate in their normal direction This is exactly what the die would do had it been in place The other nodes in those plate volumes were left free so that the interior material is free to deform in thickness direction

Other constraints put in the plate were the constraints for quadrant symmetry and constraints on the edge Planes of symmetry of the plate have been labelled in Figure 4 53 All die nodes were totally fixed Displacement loading was given to the outer edge of the plate volumes 2 and 3 This loading was kept limited so that nodes in the plate volumes 2,3 and 4 do not move to the bulging region Pressure load was applied to all the under-surfaces of the plate Two simulations were done for the same model with different loading profile Figure 4 55 shows the loading profiles It can be seen from the figures that in both profiles displacement loading was same up to an intermediate pressure Displacement loading was continued in loading profile II along with pressure load while only pressure was built up in loading profile I Further displacement loading in loading profile I was given at a higher pressure

Displacement loading was given to only one free edge of the plate for a secondary objective Bulging a rectangular plate in the middle with this loading condition is nearly equivalent to bulging a tube to T-branch by pressure and end -push Since one of the component of this work is to simulate the bulge forming of T branch from tube, it was expected that the deformation behaviour in this model would provide some insight in to the situation of T-branch forming

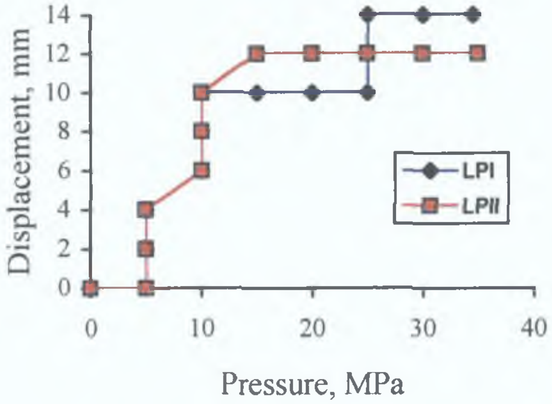

Figure 4.55: Two loading profiles in plate bulging

Newton-Raphson solution procedure with frontal solver was adopted with the control that load at each step could be divided into a maximum of 1000 substeps. This was done to ensure that load change can adequately cope with the non-linearities arising in the deformation process. This is also necessary to avoid any convergence difficulties during the solution.

Results

Figures 4.56 and 4.57 respectively show the deformed plate for loading profiles I and II. The contour shows the total resultant displacement of the nodes. Loading profile I produced a bulge of height 18.6 mm while that developed by loading profile II was 21.4 mm. It may be pointed out here that the maximum pressure that could be applied by loading profile I before instability (rupture) at the bulge was 34.17 MPa. The end displacement applied at that stage was 14.0 mm. Corresponding values by loading profile II was 34.36 MPa and 12.0 mm. It is evident that a higher bulge could be attained by loading profile II than by loading profile I for a comparable pressure and smaller end displacement. However, it is also evident from the deformed figure that the bulge root by loading profile II has depressed down even though the end push was different. It is thought that this might have resulted from the enhanced push at the end while the pressure was lower than what was required.

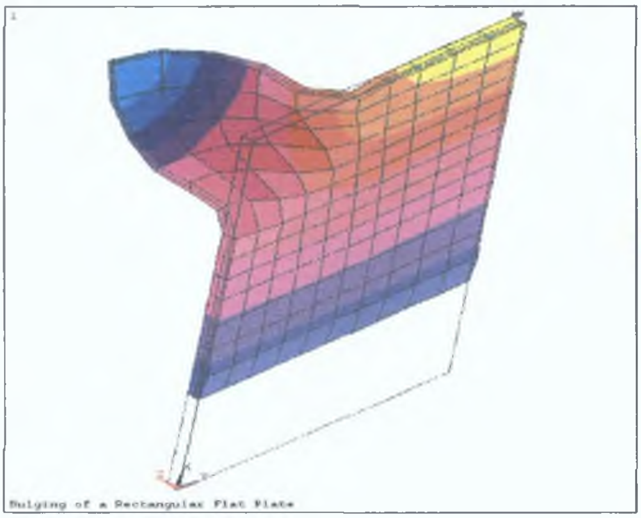

Figure 4.56: Deformed shape by loading profile I

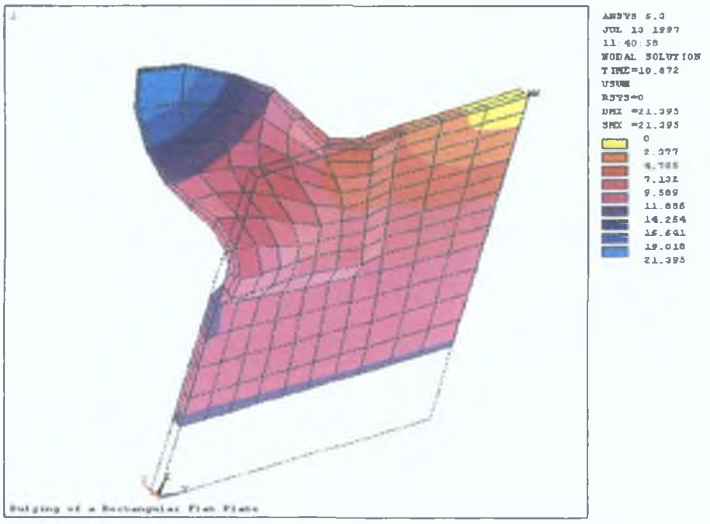

Figure 4.57: Deformed shape by loading profile II

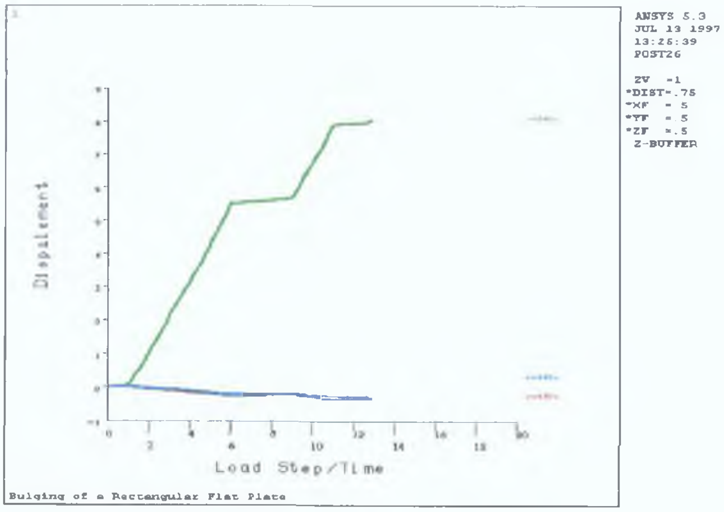

Figure 4.58: Displacement of nodes 3 and 4 by loading profile I.

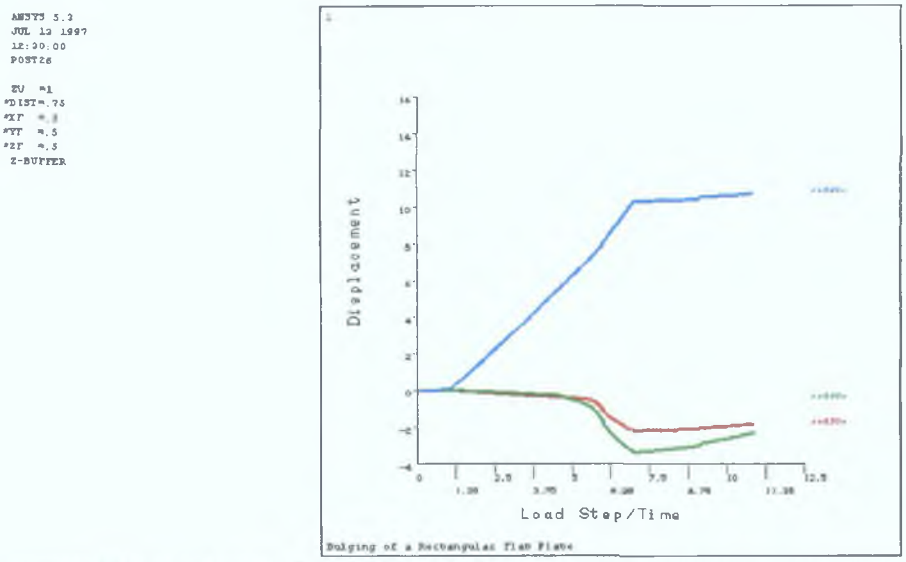

Figure 4.59: Displacement of nodes 3 and 4 by loading profile II.

Figures 4.58 and 4.59 show the displacement of nodes 3 and 4 in Z-direction of the model for loading profiles I and II respectively. Positions of node 3 and 4 was indicated in Figure 4.54. It is seen from Figure 4.59 for loading profile II that node 3 was moving down when the pressure was building to 15 Mpa while the plate end was pushed by 12.0 mm. During the same period, the end push was maintained at 10.0 mm in I and pressure was building . Subsequent pressure in loading profile II was pulling up the plate but could not level it.

One of the concern from modelling was that the nodes in plate volumes 2,3 or 4 must not enter the bulging region. Nodes 3 and 4 belong to plate volume 1. Node 3 is the nearest point to volume 2. Node 4 is one element-length away. Node 4 was originally about 14 mm away from the bulging zone. It can be seen from Figures 4.58 and 4.59 that node 4 has moved about 8.0 mm and 12 mm in X-direction respectively. This means that the nodes in volume 2 of the plate for loading profile I are still at least 6 mm away from the bulging zone. For loading profile II, they are at least 2 mm away from the bulging zone.

Figures 4.60 and 4.61 show the vector plot of total displacement of nodes. The vectors are proportional to their resultant displacement. It is evident from the figures that nodes in volume 2 and 3 have moved about equally. Therefore, nodes in volume 3 also have not moved in the bulging region. Nodes in volume 4 have least movement. The nearest nodes in volume 4 from bulging zone were 10 mm away before deformation. Those nodes have maximum movement of 7 mm in loading profile II which implies they are still 3 mm away from the bulging zone. In loading profile I nodes in the above location had even less movement.

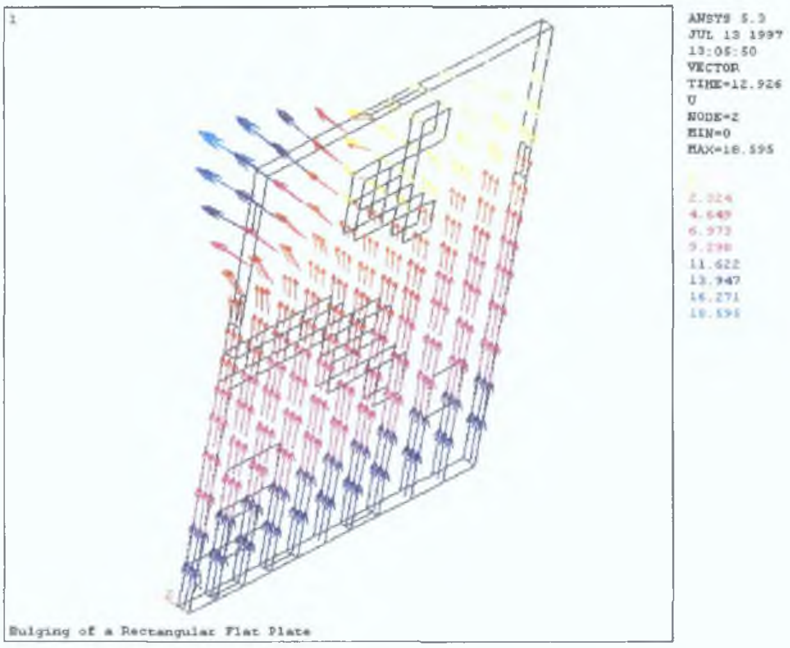

Figure 4.60: Vector plot of resultant displacement of nodes in the plate by I.

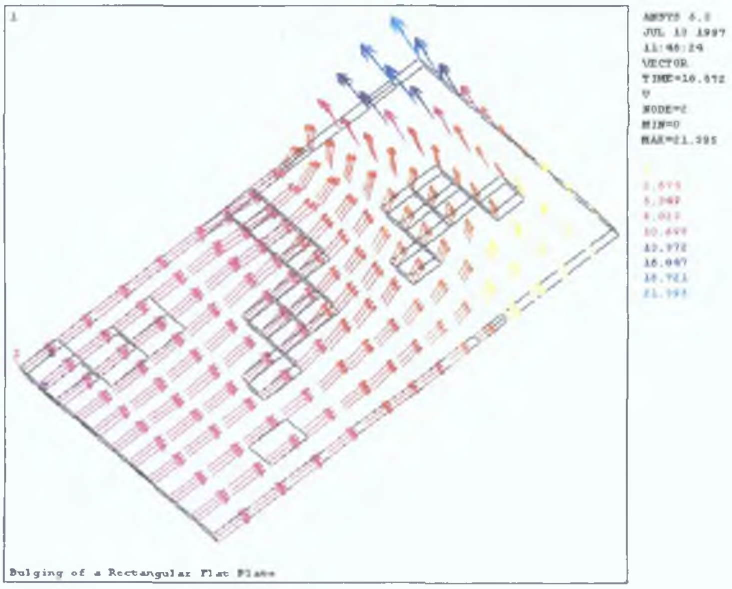

Figure 4.61: Vector plot of resultant displacement of nodes in the plate by II.

It is also evident from Figures 4.56., 4.57, 4.60 and 4.61 that there is a dead zone in the plate. This zone is limited to the plate volume 4 for obvious reason. However, the area of the region found to be different for the two loading profiles. The area developed by loading profile II is approximately half the area developed by loading profile I.

Loading profile II induces more movement of materials from volume 4 towards the bulging region than that by loading profile I as evident from Figures 4.60 and 4.61.

It was seen that the nodes in plate volumes 2, 3 and 4 have not moved to the bulging zone. However, they experienced a pull effect due to the bulging in plate volume 1. The regions of the plate where the pull effect has reached are expected to thin while other regions are expected to thicken due to the compression from the end. Figures 4.62 and 4.63 show the plastic strain in the thickness direction of the plate for loading profiles I and II respectively. These figures, in fact, all contour figures in three dimensions, can not clearly display the contours because of the directional light used in the computer graphics. Changing the view point only move the shade from one area to another.

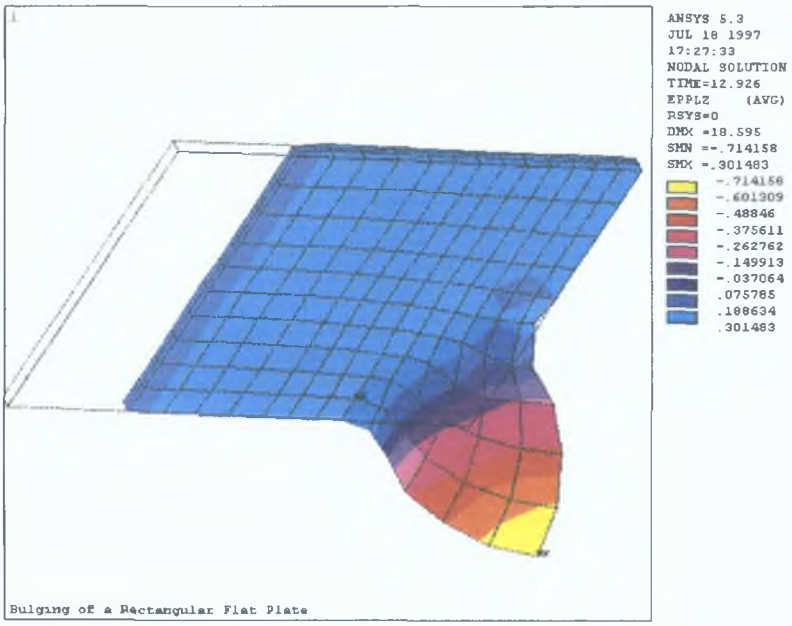

Figure 4.62: Distribution of strain in thickness direction of the deformed plate by loading profile I.

From Figures 4.62 and 4.63 it can be seen that the flat part of the plate has largely thickened (positive strain) and the bulge body and crest has thinned (negatively strain). The transition region is at and around the bulge base where change in thickness is minimal. The maximum thickening in the flat area by loading profile I is about 135% of the original thickness. The bulge crest is thinned to about 49% of its thickness by loading profile I.

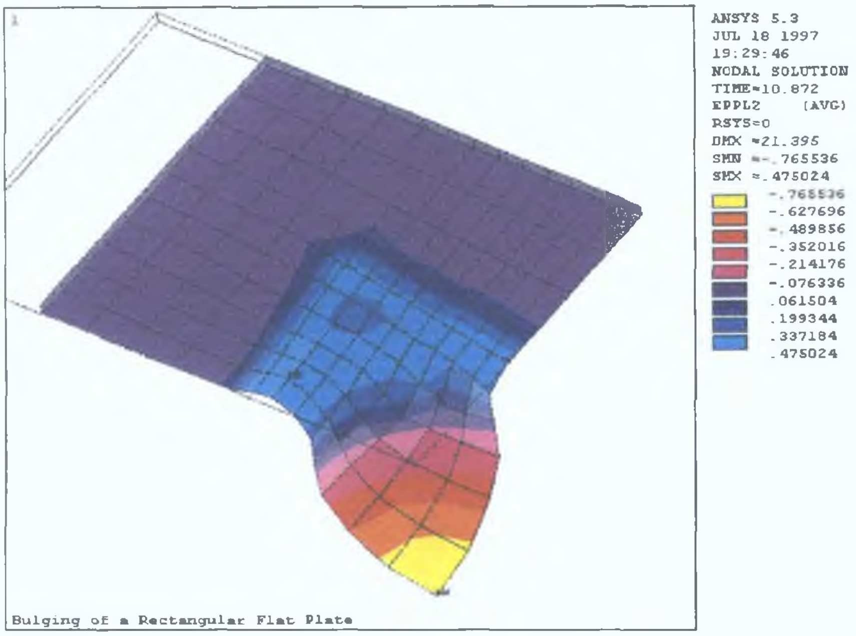

Figure 4.63: Distribution of strain in thickness direction of the deformed plate by loading profile II.

The flat part of the plate has thickened more by loading profile II. The maximum thickening is about 160% of the original thickness. The bulge crest, on the other hand, has thinned to about 46% of its original value by this loading profile. It seems that enhanced pushing in loading profile II has thickened the flat part of the plate as the depression (buckle) developed at the bulge base has prevented material to move inside bulging zone. The flat part of the plate has undergone considerable compression in its width direction as the side edges were fixed. In spite of this compression, the plate has not wrinkled longitudinally. The thickening has largely compensated the compression eliminating the possibility of wrinkling.

The ripple of the enhanced push has, however, reached the bulging area and has given rise to a different strain situation in the bulge which permitted more straining of the bulge by loading profile II and thereby more thinning and bulge height compared to loading profile I. Figures 4.64 and 4.65 show the history of principal strain of a node in bulge crest (node 236) for loading profiles I and II respectively. It can be seen from the figures that the node was strained differently in principal directions by the loading profiles. Sharp rise in strain values toward the end of loading indicates instability by both loading profiles. Figure 4.66 shows the development of strain in the same node in principal strain plot for loading profiles I and II. It can be seen that up to certain loading both had same strain path. After that they deviated and then maintained an approximate parallel path and eventually failed at different strain conditions. The bulge by loading profile I has failed at lower strain condition than that by loading profile II although more end displacement was given by loading profile I. This phenomenon was also observed in the cases of bulging circular plate by pressure and in-plane compressive load in Section 4.1.1.

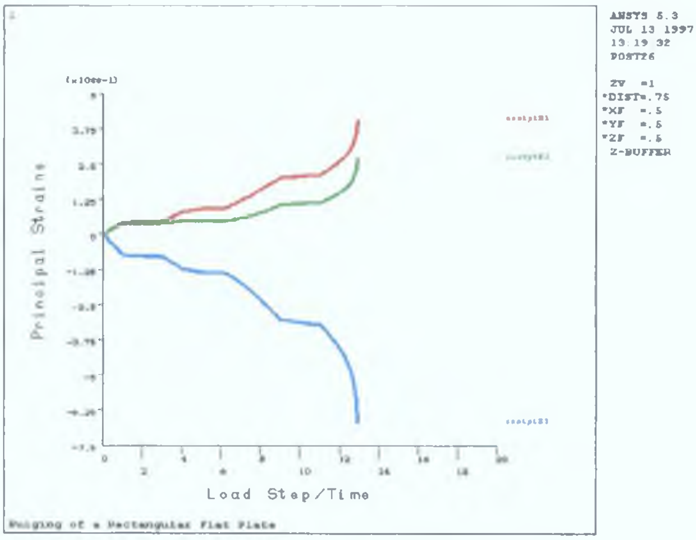

Figure 4.64: Development of principal strains in node 236 by loading profile I.

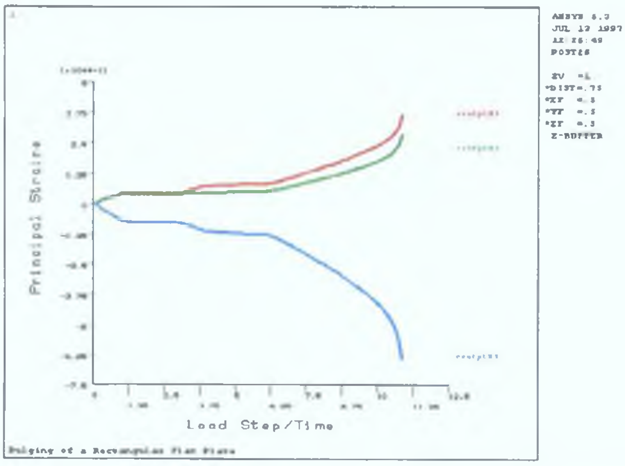

Figure 4.65: Development of principal strains in node 236 by loading profile II.

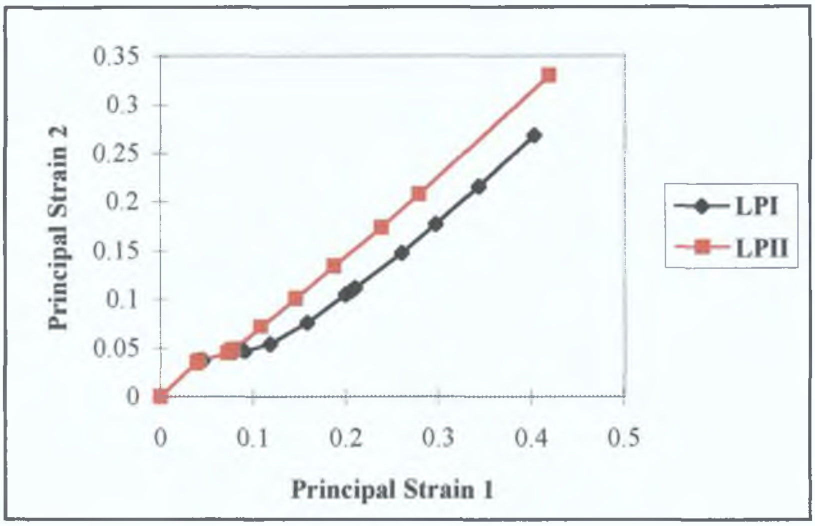

Figure 4.66: Strain path of node 236(in bulge crest) by loading profiles I and II on principal strain plane

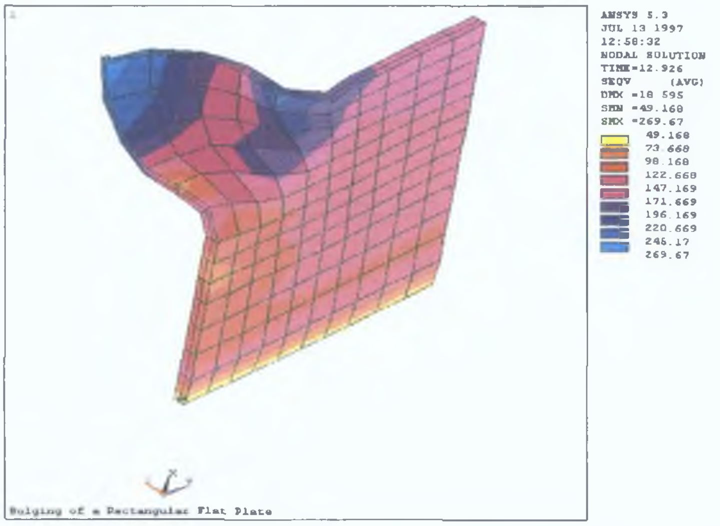

Figure 4.67: von-Mises stress in the deformed bulge by loading profile I.

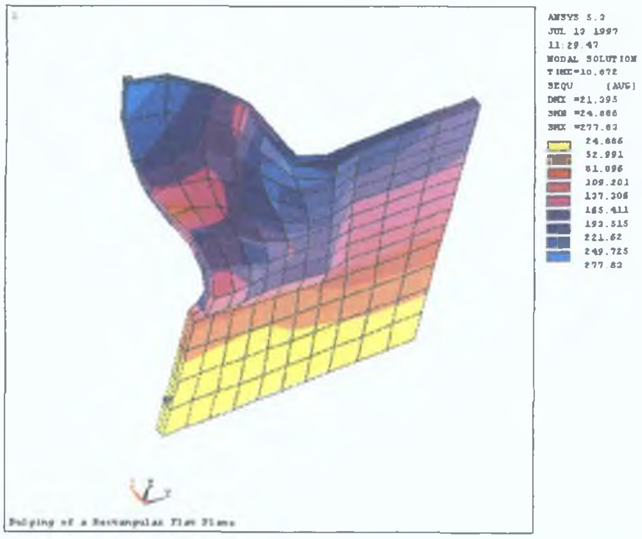

Figure 4.68: von-Mises stress in the deformed bulge by loading profile II.

Figures 4.67 and 4.68 show the von-Mises stress distribution in the bulged plate by loading profiles I and II respectively. The crest of the bulge has stressed most in both cases and the magnitude of stress is also very close. Apart from the crest, some stress concentration may be noticed in the bulge base area near the symmetry edge across breadth of the plate . This phenomenon is common for both loading profile. However, in the plate loaded by loading profile II the stress concentration is spread over more area than the other one. The flat part of the bulged plate by loading profile I is more or less uniformly stressed while that by loading profile II has a quite considerable stress gradient. The stress gradient developed at the flat part by loading profile II is thought to be due to the buckling at the bulge base.

The critical pressure that ruptures the bulge is the same for both loading profile as was observed in the case of bulging circular plates. Although loading profile II gave a higher bulge, the buckling resulting from the loading is undesirable. The probable situation leading to buckling in the flat part is when the stress in the direction of compression in the flat part is not tensile enough to counter the compressive strain in that direction. The pressure applied for bulging affects the stress mentioned above as is evident from Figure 4.69 and 4.70. These figures show the stress of nodes 3

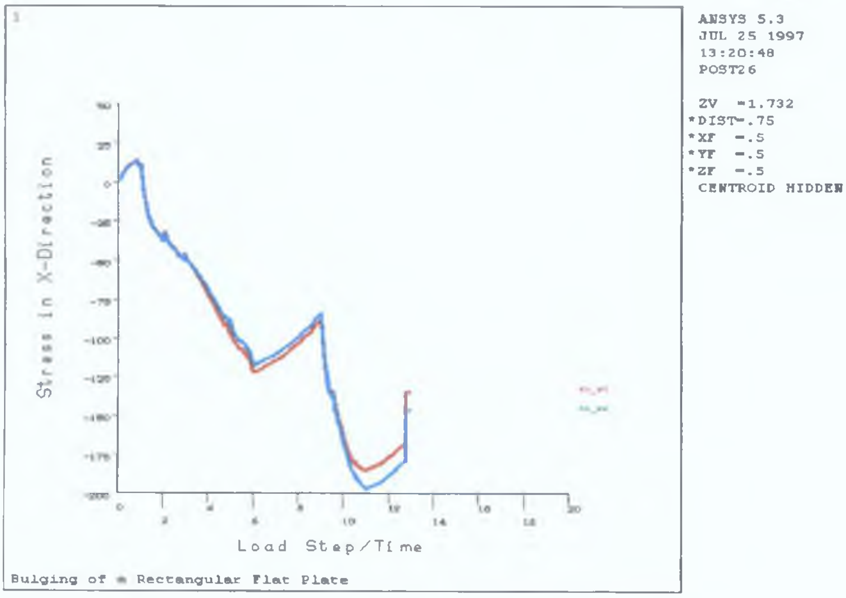

Figure 4.69: Development of stress in nodes 3 and 4 in X-direction over the load steps by loading profile I.

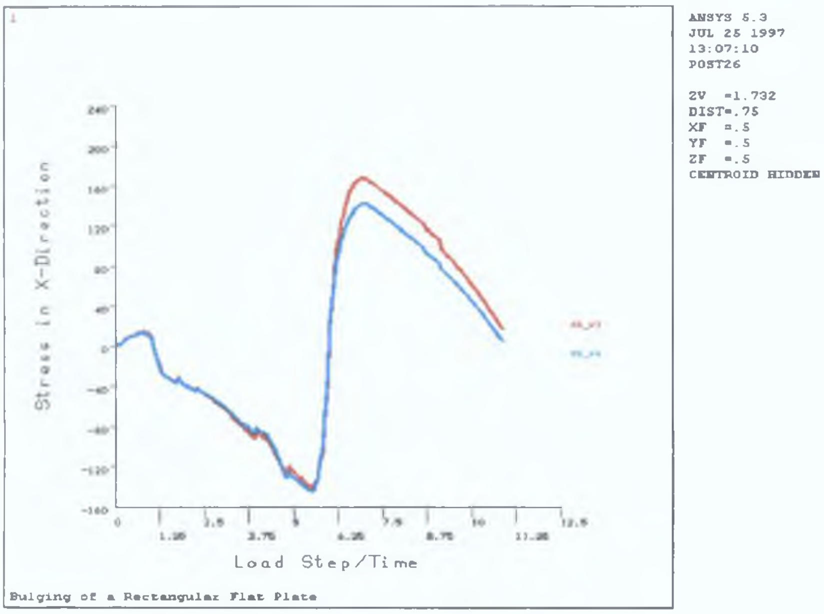

Figure 4.70: Development of stress in nodes 3 and 4 in X-direction over the load steps by loading profile II.

and 4 in X-direction developed due to loading profiles I and II respectively. It can be seen from these figures vis-à-vis Figure 4.55 that whenever there was rise in pressure, the stress had a positive turn. Figures 4.71 and 4.72 show the strain in X-direction of nodes 3 and 4 for loading profiles I and II respectively. It may be mentioned here that X-direction is the direction of compressive load in this model. Nodes 3 and 4 were

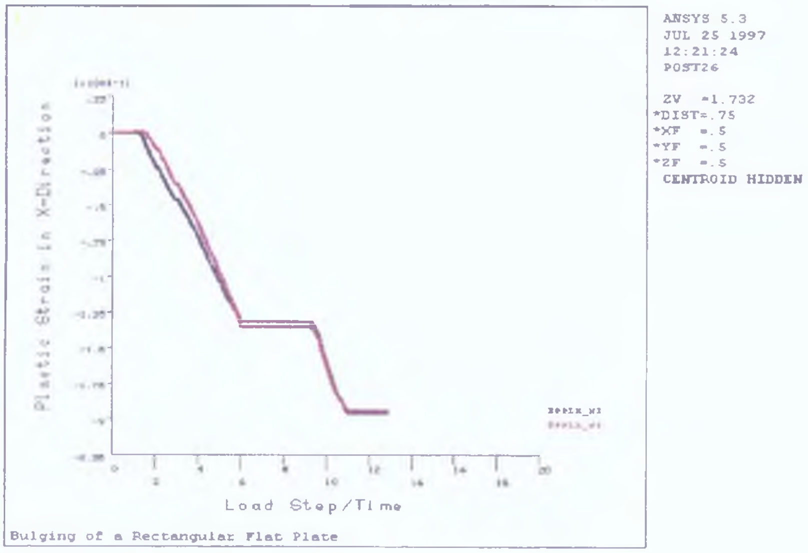

Figure 4.71: Development of strain in nodes 3 and 4 in X-direction over the load steps by loading profile I.

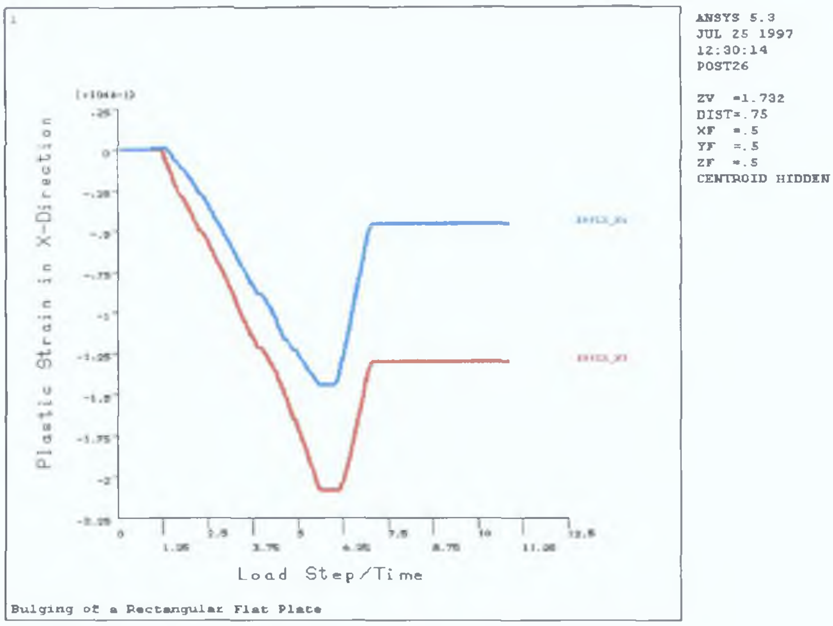

Figure 4.72: Development of strain in nodes 3 and 4 in X-direction over the load steps by loading profile II.

chosen as these nodes depressed down due to buckling by loading profile II. Looking at Figures 4.70 and 4.72 for loading profile II it can seen that at one point in time, node 3 had peak negative stress and strain in X-direction. This is exactly the time when node 3 was depressing down leading to the buckling. The stress and strain of node 3 in X-direction at that time were about -150 MPa and -2.1 respectively. The ratio of stress to strain at that time was 71.42. Comparatively, in loading profile I, node 3 also had a peak of negative stress and strain but at different point in time but there was no buckling. The stress and strain of node 3 at that instant by loading profile I were about -195 MPa and -1.97 respectively. The ratio of stress and strain in this case was about 99. From the above it seems that by studying the stress and strain in the direction of compression it would be possible to figure out a load profile that would not give rise to any buckling before the pressure reaches its critical value. A likely loading profile is given in Figure 4.73 along with the tried profiles. The predicted profile was not tried because of unusually long computer time required for the simulation of each run. It may be mentioned here that the computer time for simulation of this model was about 20 days for each profile.

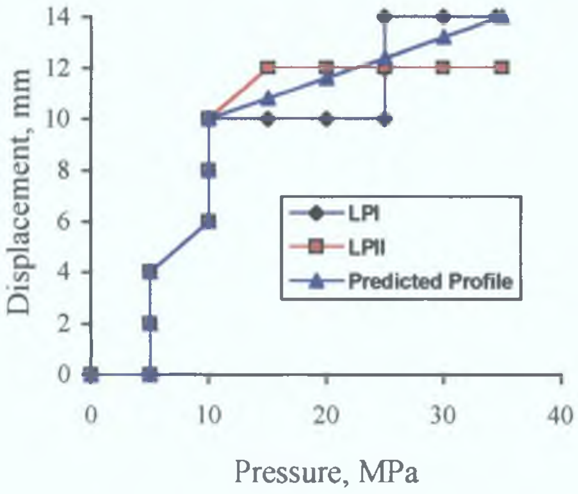

Figure 4.73: A possible profile of loading that would give better bulging.

The development of stress or strain in the model were smooth and conforming to loading as was seen in different figures showing variation over the load steps or time. The contact between the plate and die was also satisfactory. Maximum of about one tenth of a millimetre penetration was reported in only three contact elements for both loading profile. This much penetration is not expected to affect the stress or strain results at the interfaces where these contact elements are located.

4.3 Axisymmetric Bulging of Tubes

Analysis of axisymmetric bulging of tubes could be done in two-dimension by taking advantage of the axisymmetry However, in two-dimensional analysis certain aspect of forming like wrinkling or any unusual deformation due to buckling can not be detected Therefore a three dimensional analysis was aimed LS-DYNA 3D explicit solver was used for the three dimensional analysis ANSYS pre-processor was used for finite element model development After reviewing the results from three dimensional analysis a two dimensional analysis was taken up for optimisation with respect to strain in the bulge

4 3.1 Three Dimensional Analysis

Modelling

A 12 7 mm outer diameter tube of 50 mm length was adopted for bulging in the middle The span of the middle section that would be bulged was 20 5 mm The bulging surface was free at the top The die surrounded the tube where there was no bulging The die recess had a fillet radius of 2 mm Initially a 15^0 sector of one half of the full problem was modelled in cylindrical co-ordinate system using 8- node brick elements for explicit solution However, after obtaining the solution it was found that the elements are compressed to one edge of the model It seemed that the pressure was acting on the wrong face of the elements It was later discovered that the particular type of element does not work in models developed in cylindrical co-ordinate system Since this was the only elements available in the element library for this kind of analysis, the model was developed afresh in Cartesian co-ordinate system This time a quadrant of the full problem was modelled in order that the symmetry edges can be constrained in circumferential direction properly The die was modelled in three volumes One along the tube wall, one perpendicular to the tube wall(die recess wall) and the volume joining the two The last one comprises of double curvatured patches modelled by coon patches All the volumes were developed from bottom up The tube was modelled in single volume by extruding the cross-sectional area in the first attempt But it worked out to be problematic to assign the pressure load in proper face of the element. Later the tube was developed from bottom up from key points to lines, area and volume. The tube was discretised by 20 element divisions along its modelled length and circumference and 2 element divisions across the thickness. The die was discretised relatively coarsely but in reasonable proportion to tube element lengths. Figure 4.74 shows the discretised die and tube. A total of 950 elements describe the model of which 800 elements are in the tube and the rest are in the die. Some node numbers are labelled in the figure for discussion of results later.

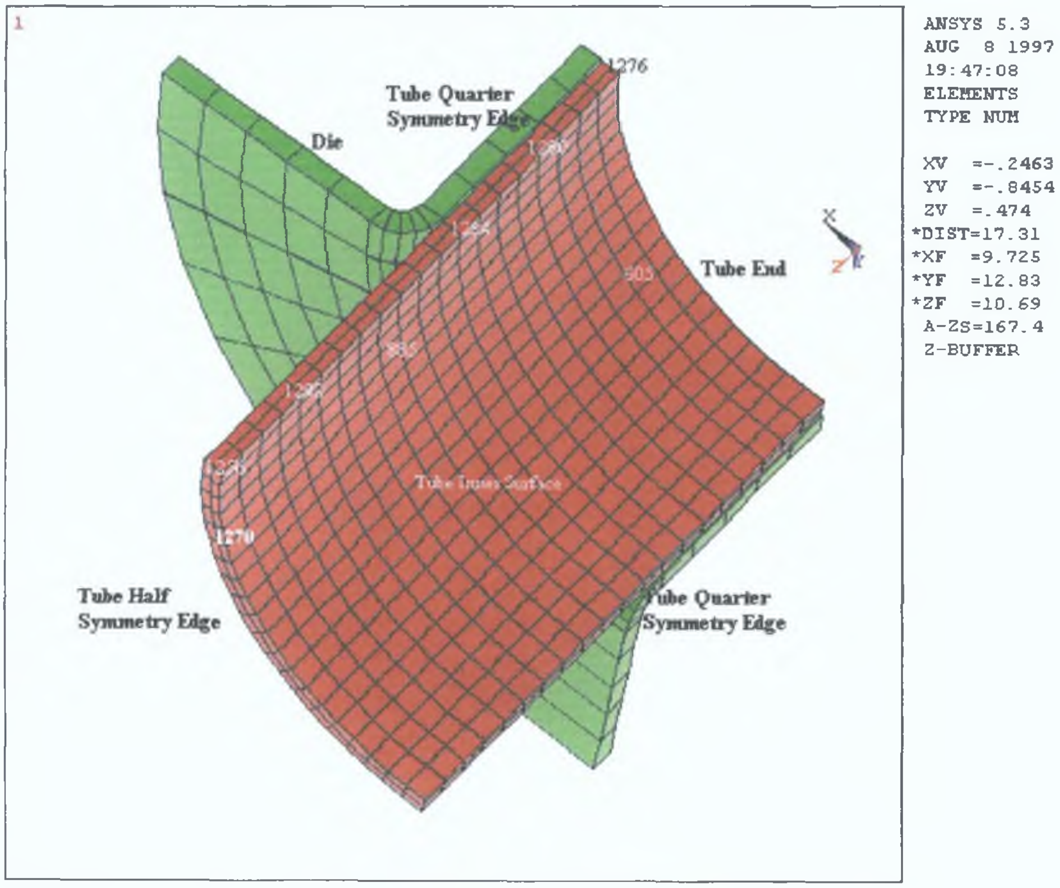

Figure 4.74: Finite element model of axisymmetric bulging of tube.

A bi-linear isotropic material model was assumed for the tube. The material parameters approximately represent Aluminium (Al 5052-0). Different parameters of the material are:

Young`s Modulus = 69.3x10 ^{3} MPa, Yield strength = 90 MPa,

Poisson`s ratio = 0.33, Density = 2.68x10^{-6} kg/mm ^{3},

Tangent Modulus = 475 MPa,

The approximate strain hardening exponent of the material is 0.223. The die was assigned an elastic material model and standard parameter values of mild steel was given. The die was modelled as a rigid body.

A surface to surface contact algorithm was chosen for interface modelling. Elastic Coulomb friction law was assumed and the coefficient of friction was 0.15. This solution process has an in-built algorithm to calculate the stiffness of the contact elements. The algorithm uses material properties of both the contacting surfaces.

Loading and Solution

The pressure load was applied at the inner surface of the tube and the inner layer of the elements were assigned for pressure loading. Pressure load was applied to the inner surface of the elements. The node connectivity of some of the elements of the tube inner layer was checked to find out the face of the element that would take the pressure load. It was thought that all the inner layer elements would have the same face to take the pressure load. But after the simulation it was apparent that all elements did not have the same face notation for the inner surface. As a result the pressure load was on proper face of some element and was on the wrong face for some other elements. Figure 4.75 shows an example of deformation that occurred due to the wrongly placed pressure loading.

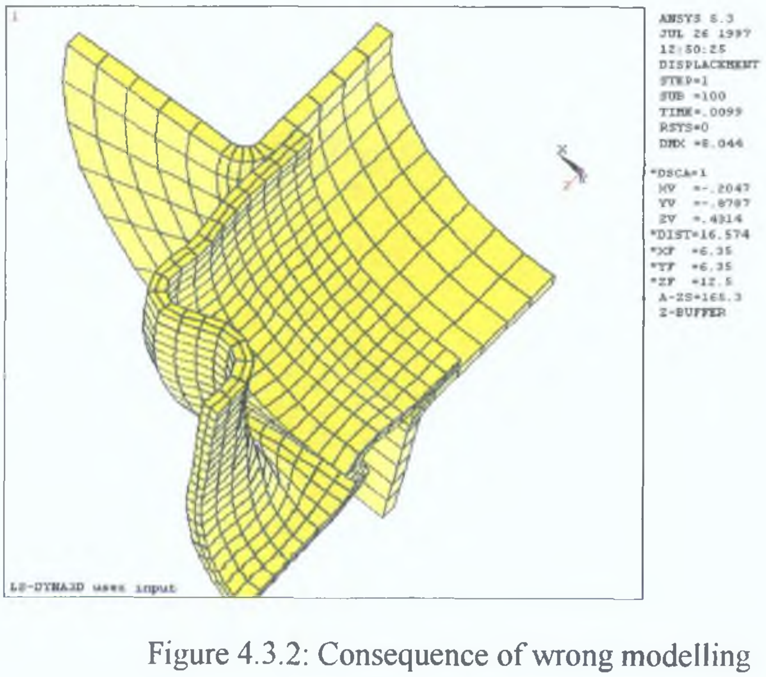

```
ANSYS 5.3
JUL 26 1997
12:50:25
DISPLACEMENT
STEP=1
SUB =100
TIME=.0099
RSYS=0
DMX =8.044

*DSCA=1
 XV  =-.2047
 YV  =-.8707
 ZV  =.4314
*DIST=16.574
*XF  =6.35
*YF  =6.35
*ZF  =12.5
 A-ZS=166.3
 Z-BUFFER
```

Figure 4.3.2: Consequence of wrong modelling

After checking element by element it was found that there were few different element connectivity pattern. Then it was decided to build the tube volume from bottom up where the modeller can develop lines and areas in a consistent manner. This way all the inner layer elements had consistent connectivity and same surface notation of the elements could identify the tube inner surface.

After that, considerable difficulty was faced with contact condition at the quarter symmetry edges of the model. The edge nodes deformed in a very unusual manner. Initially it was thought that hourglass type deformation is taking place. As explained in section 3.3, hourglass type deformation is a zero energy mode deformation which is in fact a spurious deformation. But checking the tube surface removing the die, it was found that the deformation problem is limited to the symmetry edges. All possible contact parameters were changed but the behaviour remain unchanged. Then it was thought that at the edges there was no die node to harbour tube nodes to form a contacting pair. Subscribing to that idea, the die edges were extended a little further from the tube edges which can be seen in the finite element model in Figure 4.74. After that there was no problem of deformation at the edges.

After sorting out these problems, the first model was run with relatively high pressure so that an idea of the critical pressure could be obtained. From earlier simulation on bulge forming it was found that the pressure to rupture the bulge is same irrespective of the way the displacement loading is applied. Once the critical pressure is established then the pressure can be manipulated within that limit to suit the displacement loading. Accordingly subsequent models were run within that pressure limit. Two different loading patterns were tried as shown in Figures 4.76 and 4.77.

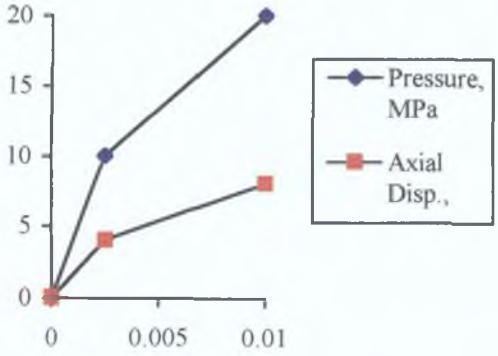

Figure 4.76: Loading pattern I

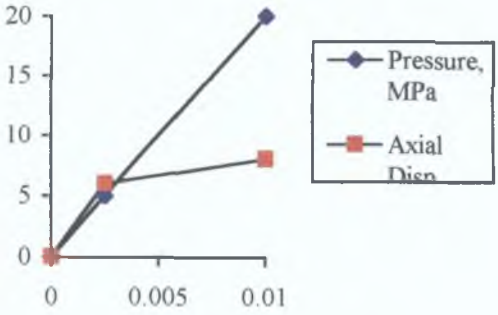

Figure 4.77: Loading Pattern II

In the first loading pattern, half of the pressure and axial displacement load was applied within the quarter of the simulation period In the second pattern the axial load is enhanced and the pressure load is delayed Three quarter of the axial load was applied within the first quarter of the simulation period while only one fourth of the pressure load was applied during the same period in the second loading pattern

The simulation time for the model was 0 01 seconds which is much shorter than the real time of the process This was necessary to reduce the computer time to solve the problem One possible outcome of shortening the time scale would be that the kinetic energy in the process might become unacceptably high This would be unrealistic from practical manufacturing point of view Therefore, it is always important to check the development of kinetic energy in the process Usually the kinetic energy should be very negligible compared to the internal energy of the system

The brick elements used in the model was opted for reduced integration Reduced integrated elements are prone to hourglass type deformation as explained in section 3 3 However, they are computer time efficient and generally give better results for metal forming provided the energy due to hourglass deformation mode is not high LS-DYNA developers[103] suggests that hourglass energy within 10% of internal energy is acceptable All the simulation models were checked for hourglass energy One particular model was run with full integration option for the elements mainly to compare with reduced integration results and thereby confirm the results from reduced integration options

Results and Discussion

As mentioned earlier, the model was initially subjected to high pressure to determine the pressure at which the bulge ruptures The point of rupture is assumed when a node in the highly stressed area is steeply stressed or strained Figure 4 78 shows a deformed state of the tube It can be seen that the tube has been expanded quite considerably in circumferential direction The maximum diameter in the expanded area is about 40 mm The original tube diameter (mid-plane) is 24 5 mm Therefore, the ratio of expansion is about 1 63 mm The thickness of the tube in the expanded zone has gone down to about 28% of the original thickness

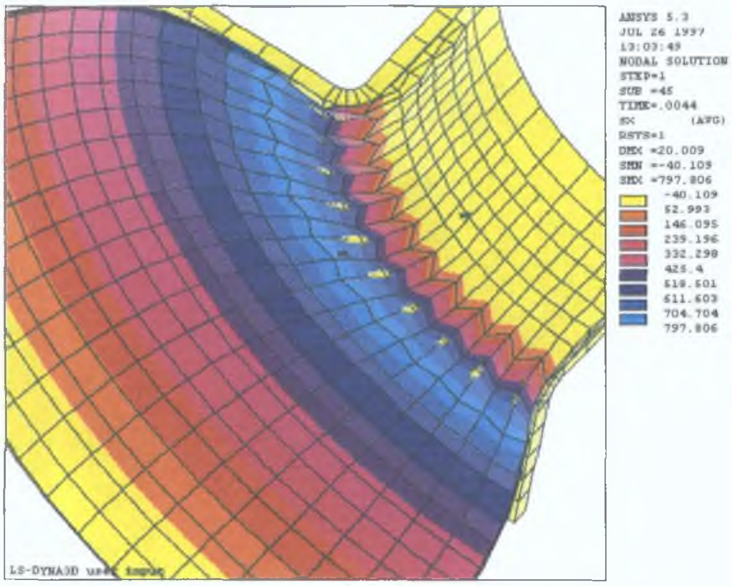

Figure 4.78: Excessively deformed bulge due very high internal pressure.

Figure 4.79 shows the development of principal strains in the node 1270 (location identified in Figure 4.74). It can be seen from the figure that at about 0.0043 seconds in the simulation time, the node started straining at a faster rate, which indicates the onset of necking. At the same time, the total internal and kinetic energy of the system also took an up turn and soon reached infinite values as can be seen from Figure 4.80.

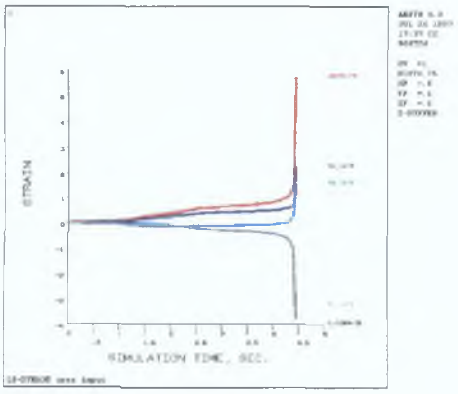

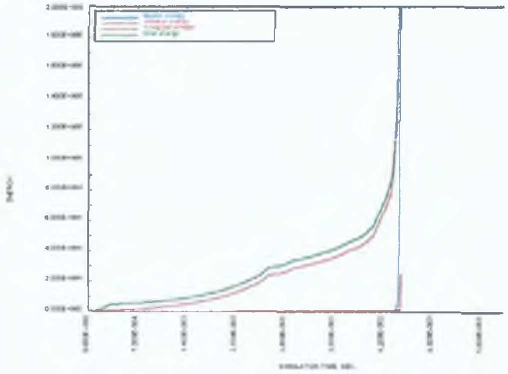

Figure 4.79: Principal strains of node 1270. Figure 4.80: Development of energy

The loading situation at this point in time can be seen from Figure 4.81. It is seen that a pressure of about 25.0 MPa was active at that time of simulation. The end displacement was about 3.72 mm. From Figure 4.80 it is also evident that hourglass energy of the system also picked up around the same time. Severe hourglass deformation is also evident in Figure 4.78. Almost all elements in the main branch and around the die bend have hourglass mode of deformation. This state of deformation is not reliable. Therefore, it may be concluded that the critical pressure identified earlier is expected to give rise to hourglass deformation. Accordingly a lower pressure of 20 MPa was administered in the subsequent trials of the model.

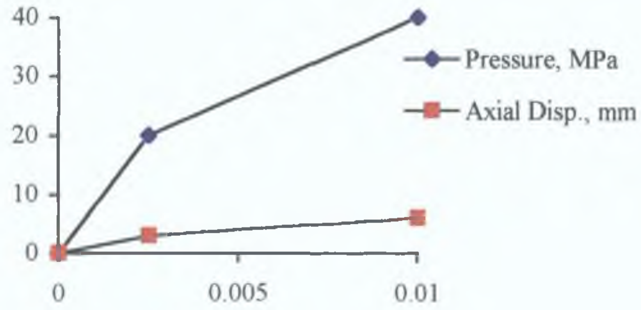

Figure 4.81: *Loading pattern of the highly pressure loading simulation.*

Figure 4.82 shows the deformed shape of the bulge formed at 20 MPa pressure and 8 mm end displacement by following loading pattern I in Figure 4.76. The figure also plots the distribution of displacement of nodes in radial direction. It can be seen from the displacement plot that a good length of the bulge has expanded parallel to the axis.

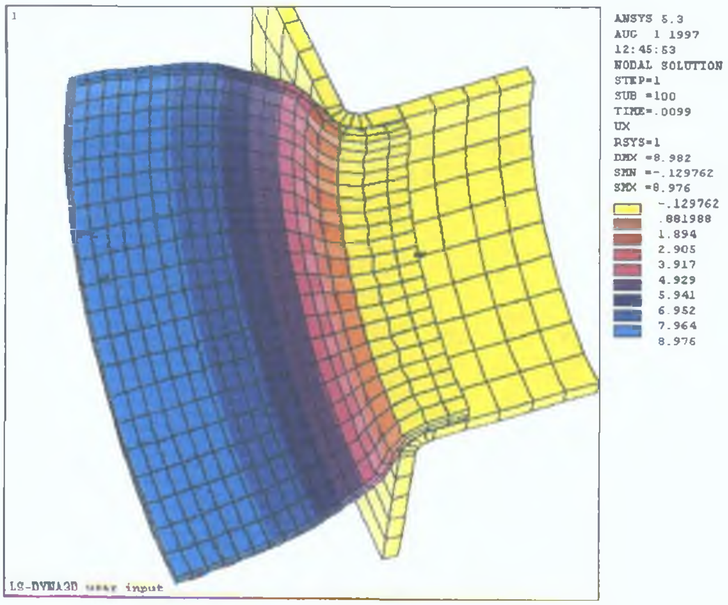

Figure 4.82: Deformed shape of the bulge by loading pattern I.

The bulge actually has taken different shapes before it took the final shape shown in Figure 4.82. Figures 4.83 and 4.84 show the deformed shapes at quarter way and half way through the simulation. It can be seen that the bulge initially started like a hump near the die recess and then gradually the whole bulging zone inflated.

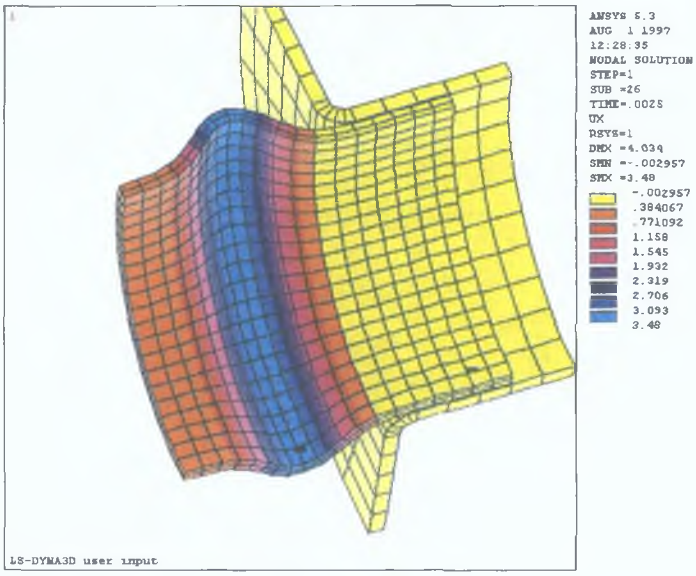

Figure 4.83 : Intermediate shape taken by the bulge at 0.0025 seconds in the simulation by loading pattern I.

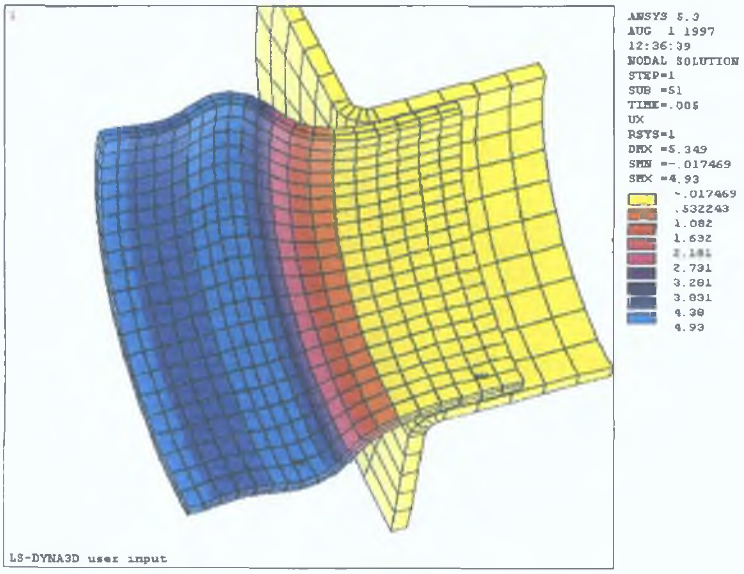

Figure 4.84 : Intermediate shape taken by the bulge at 0.005 seconds in the simulation by loading pattern I.

Also, the elements in these figures have maintained regular shape meaning no hourglassing. This fact is more evident in Figure 4.85 where the ratio of hourglass energy to internal energy is plotted over the simulation time. The ratio is more or less steady over the period maintaining a value within 0.005 which is almost negligible. The ratio of kinetic energy to internal energy is also plotted in the figure. After a initial kick which is quite plausible due to the movement of material from stationery condition, the kinetic energy has almost become negligible. Figure 4.86 shows the development of internal energy and total energy of the system over the simulation period. It is seen that the energy development in the process was steady.

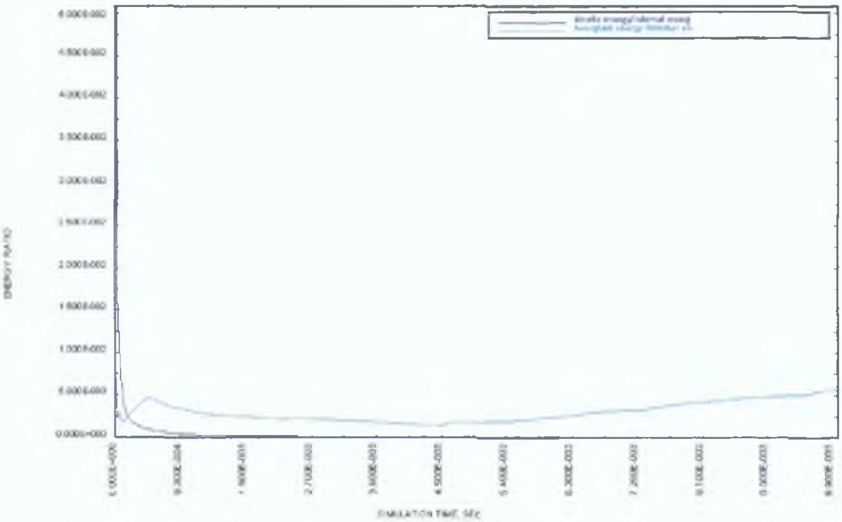

Figure 4.85: Ratio of hourglass energy and kinetic energy to internal energy by loading pattern I.

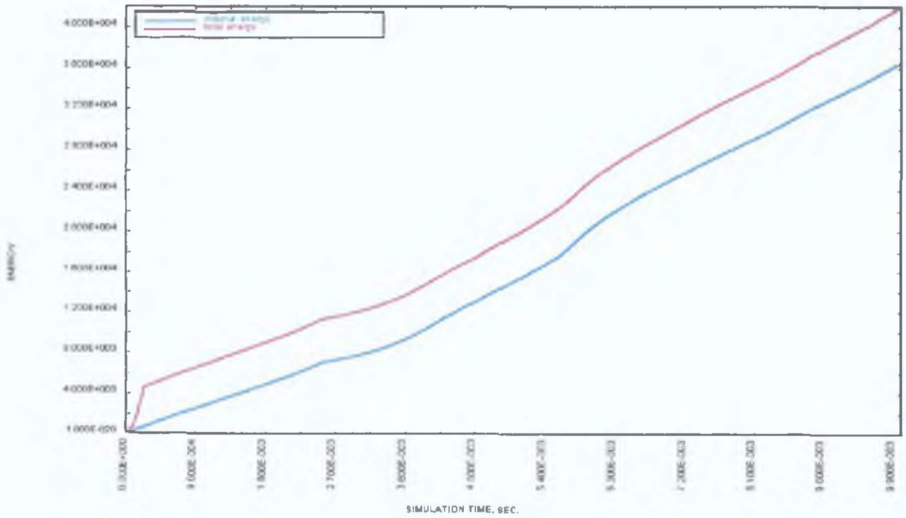

Figure 4.86: Development of internal energy and total energy in the deformation process by loading pattern I.

Figure 4.87 shows the distribution of von-Mises stress in the bulged tube. The tube has more or less equally stressed at the cylindrical portion of the bulge. A stress gradient is observed at the die bend and at the main body of the tube. However a good part of this region has developed lower stress compared to the main bulge. This is a sign that this region which had undergone appreciable compression from the end was simultaneously relieved by the pull due to the pressure.

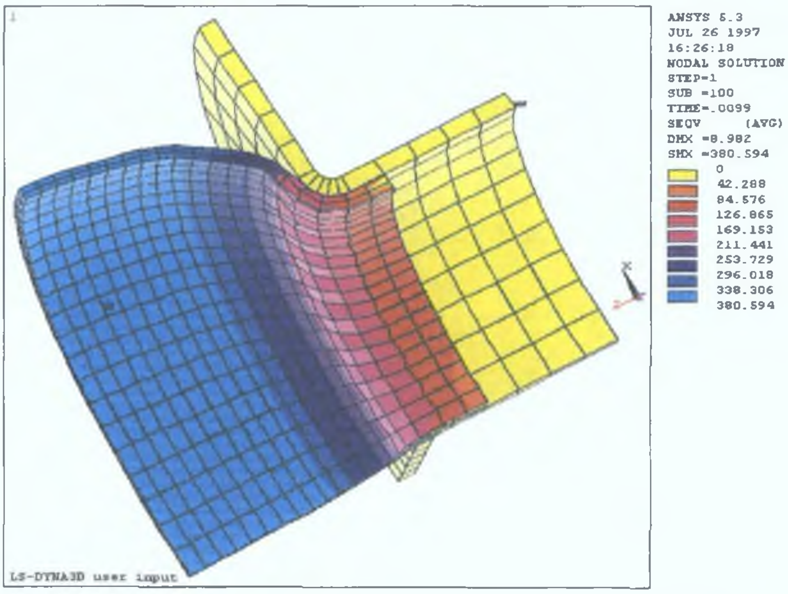

Figure 4.87: von-Mises stress in the deformed bulge by loading pattern I.

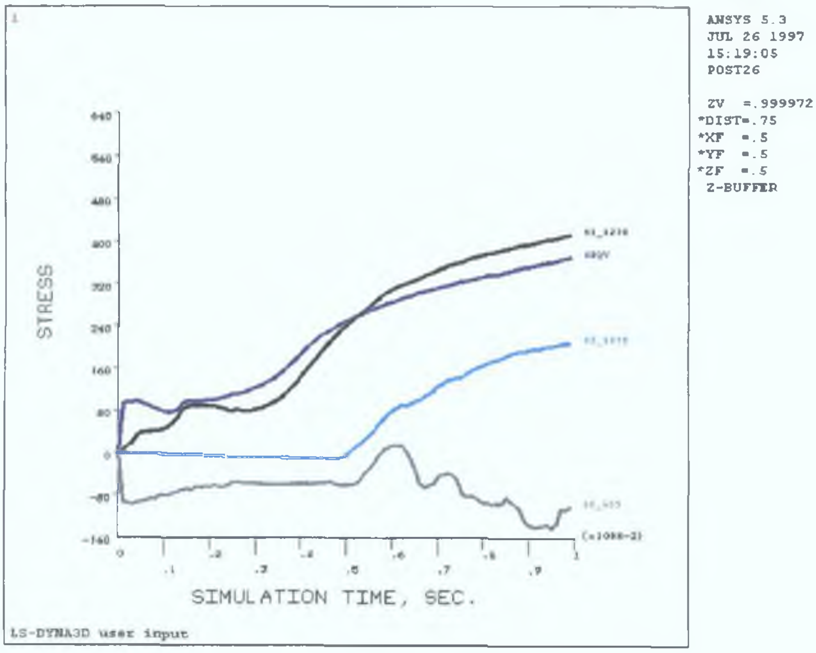

Figure 4.88: Development of stresses in node 1270 and node 605.

The above observation may be confirmed by looking at the stress development of a node in that region Node 605 is a node in the region whose location was indicated in Figure 4 74 This node is in the above mentioned region after the deformation Figure 4 88 shows the development of stress in the node in the axial direction (bottom most curve) It can be seen from the figure that the stress in the node maintained a steady negative value almost half way through the simulation period although there was continuous end displacement loading during the period Subsequently the stress in the node seems to be going negative with a stick-slip effect which implies a push-pull situation At the end of the simulation period it seems that the node is experiencing a pull due to the pressure

The von-Miss stress and two principal stresses of node 1270 (a node at the half symmetry of the bulge) are also plotted in Figure 4 88 The stress in the node shows a steady and stable growth Looking at the state of stress development it appears that the bulge could continue to expand a little further However, since both the circumferential and the meridional stress are positive and increasing, the rupture instability would not be late According to theoretical works on axisymmetric bulging of tubes[40,56] the instability strain is given as,

$$\bar{\varepsilon} = \frac{2n\sqrt{(1-\alpha+\alpha^2)}}{(1+\alpha)} \quad \text{where, } \alpha = \sigma_1/\sigma_2 \text{ and } n \text{ is the strain hardening exponent}$$

σ_1 = the first principal stress and σ_2 = the second principal stress

The above relation implies that a negative stress ratio ≥ -1 would raise the instability strain to even infinity In other words, it would be always desirable to maintain the stress ratio α such that

$-1 \leq \alpha < 0$

From Figure 4 88 it can be seen that the ratio was negative until about half way through the simulation Then the ratio was positive as the second principal stress turned tensile from compressive Theoretically it would had been better if the second principal stress could be maintained compressive That could have been done by giving higher level of axial loading But since the tube length in the model was limited, a higher ratio of axial loading to pressure loading was not possible for all over the simulation period Also a larger model was not an option because of the computer limitation However, a higher ratio of displacement loading was tried for a limited period of simulation which is discussed later.

The thickness strain distribution in the final shape of the bulge is shown in the Figure 4.89. From the figure it seems that strain distribution pattern is rather unexpected in the sense that the bulge is likely to thin uniformly over a length as in the stress pattern in Figure 4.87. This could be due to the movement of nodes from their angular position while the bulge was expanding. For a perfect bulging, the nodes should move radially keeping the same angular position as shown in Figure 4.90. Point A should maintain the same radial position by moving along the line of expansion.

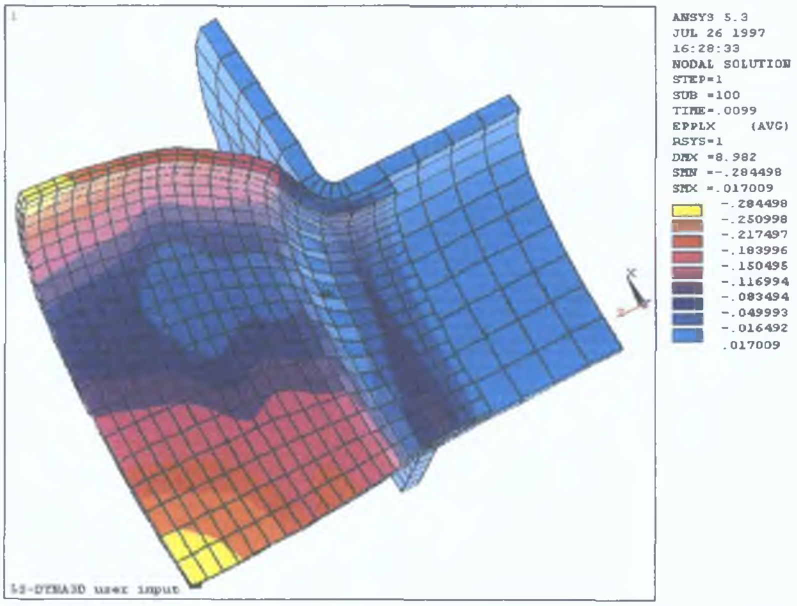

Figure 4.89: Distribution of thickness strain of the bulge by loading pattern I

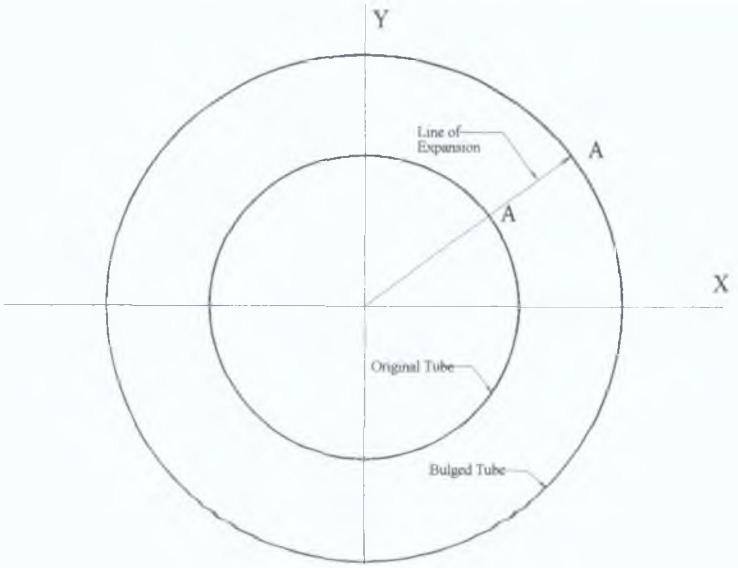

Figure 4.90: Ideal mode of expansion of a point in tube bulging.

But from Figure 4.91, where the distribution of displacement of nodes in circumferential direction was plotted it can be seen that the nodes have slightly deviated from their theoretical path. Theoretically they should have zero displacement in this direction. From the contour labels in the figure it can be seen that the magnitude of the deviation is at the most 0.038 mm. Still, this has resulted in variation of strain in the mid-region of the bulge in Figure 4.89. The quarter symmetry edge nodes were all constrained circumferentially. Therefore the edge nodes have not moved circumferentially. It can be seen in Figure 4.89 that the pattern at both edges of the model is same and, therefore, can be taken as what the actual pattern should be. In fact similar pattern is evident in the distribution of stress in the thickness direction of the bulge as illustrated in Figure 4.92. Accordingly, the bulge has thinned most about the middle section and very negligible thinning in the bend area. There is almost no thickening in the main tube part despite axial compression.

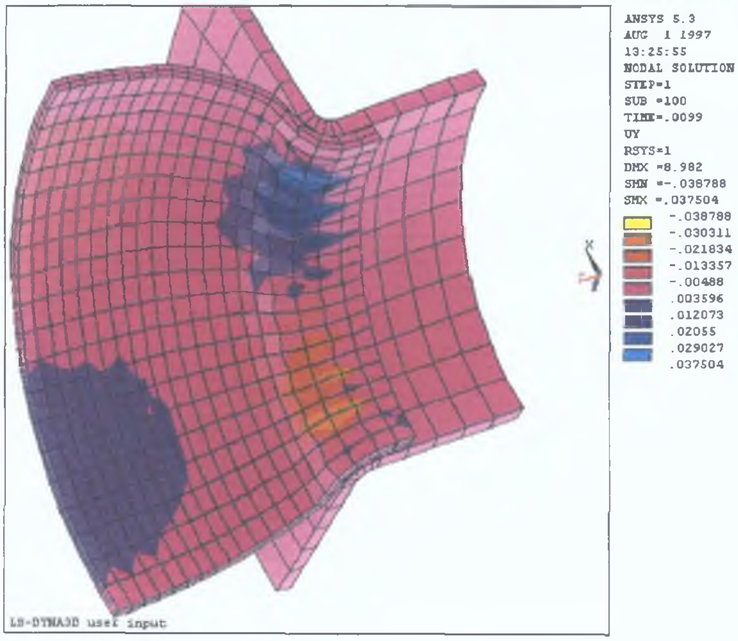

Figure 4.91: Displacement of nodes in the circumferential direction of the bulge by loading pattern I.

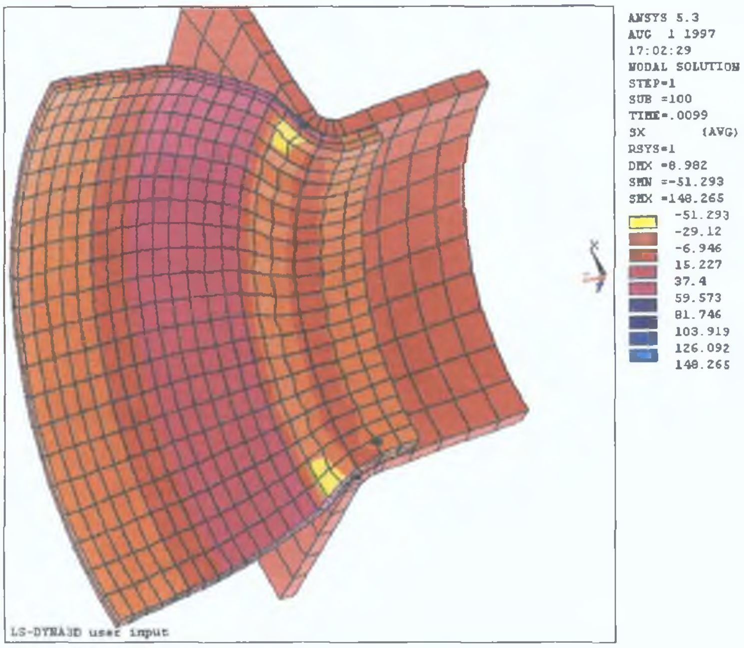

Figure 4.92: Distribution of stress in thickness direction of bulge by loading pattern I.

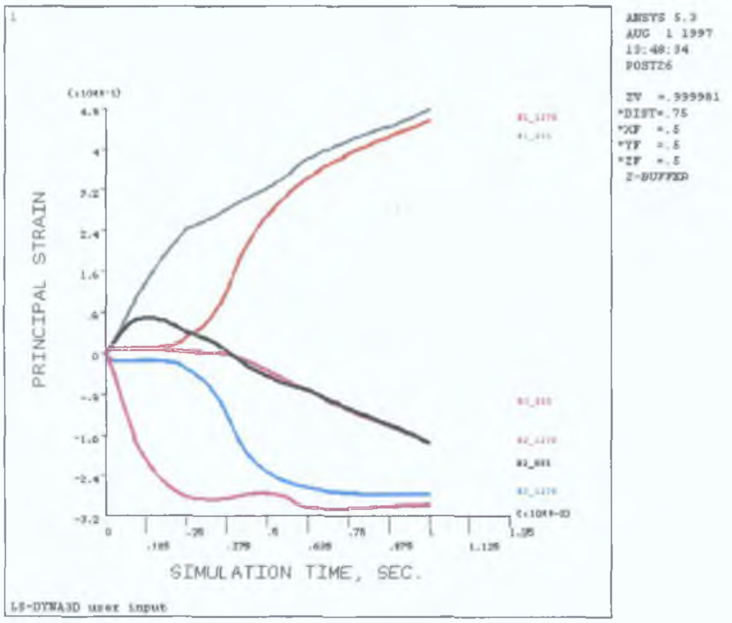

Figure 4.93: Development of principal strains in nodes 1270 and 885.

Figure 4.93 shows the plot of principal strains of nodes 1270 and 885. The former is at the half symmetry edge of the bulge and the latter is somewhere about the middle of the modelled bulged part. Both nodes show similar history of straining. From the figure it can be seen that the strain in the axial direction is maintaining a steady compressive value while the strain in the hoop direction is increasing in tensile mode. This state of straining implies fast thinning of the bulge. If the loading pattern were continued the bulge would have ruptured. Theoretically [56] it is said that when the strain in thickness direction reaches the magnitude of strain hardening exponent of the material, the bulge will rupture. From the figure it can be seen that the strain in both nodes is close to the strain hardening value which is about 0.223 for the material.

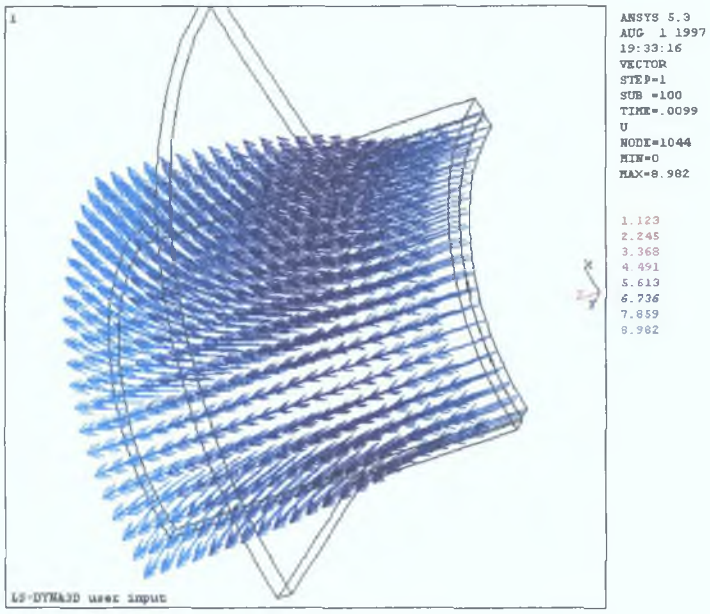

Figure 4.94: Vector plot of total displacement of nodes of the tube.

Figure 4.94 shows the vector plot of the total displacement of nodes. This illustrates the material movement in the deformation. It can be seen from the figure that the nodes even close to the half symmetry edge have moved axially towards the symmetry edge bringing the material in the central region of the bulge.

Although the hourglass energy of the simulation was observed to be very low (Figure 4.85), a simulation was run with fully integrated elements where there could be no hourglass mode of deformation. The result is almost identical in all aspects. Figure 4.95 shows the deformed shape of the bulge with contour plotting of displacement of the nodes in radial direction. It can be seen that the shape of the bulge is almost the same and the maximum radial displacement is 8.524 mm as against 8.982 mm obtained by reduced integrated elements. Table 4.19 shows the summary of main results of the two simulations for comparison. Slight difference in displacement, stress and thinning is quite reasonable as the relatively stiffer fully integrated elements allow less deformation compared to the reduced integration elements.

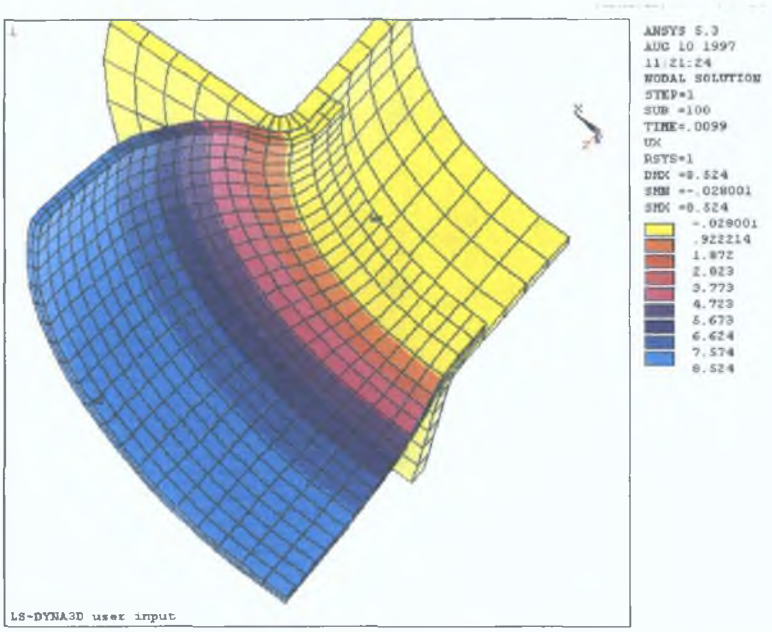

Figure 4.95: Deformed shape of the bulge simulated using fully integrated brick elements.

Table 4.19: Comparison of results between simulations with fully integrated and reduced integration brick elements.

Simulation	Max^{m} radial displacement (mm)	Max^{m} von-Mises stress (MPa)		Max^{m} thinning (% of original thickness)		Total energy after the end of simulation
		Value	Location	Value	Location	
Fully integrated elements	8.524	377.74	bulge mid-section	78	bulge mid-section	≅ 40,000
Reduced integration elements	8.982	380.59	bulge mid-section	75	bulge mid-section	≅ 40,000

History of development of stress and energy in the bulge is also nearly the same for both the cases. Figure 4.96 shows the stress development in nodes 1270 and 605 for fully integrated element simulation. Figure 4.97 shows the development of energy in the process for the same case. Comparing these two figures with Figures 4.88 and 4.86 respectively it can be seen that pattern of development of stress and energy is very much similar although the rate of change at any instant could be little different. But the values at the end of the simulation are almost equal.

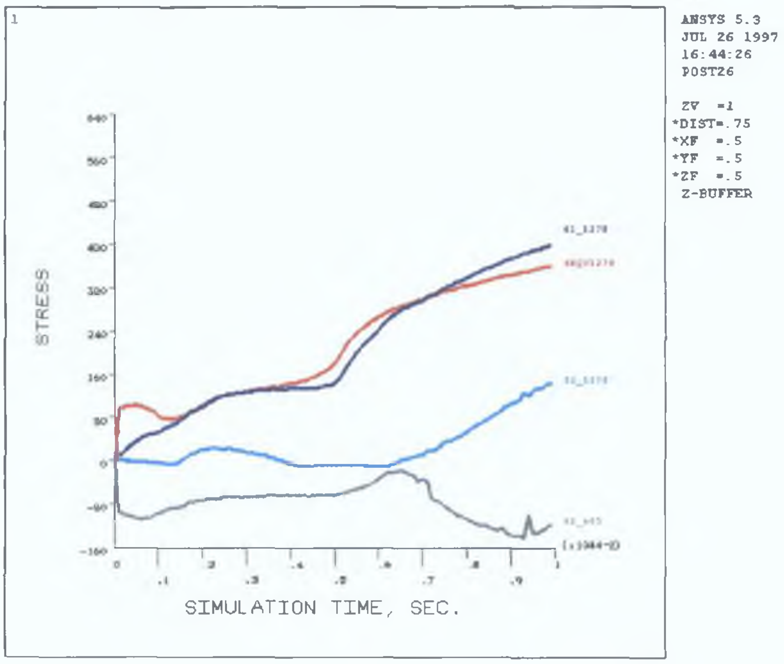

Figure 4.96: Development of stress in nodes 1270 and 605 in simulation using fully integrated brick elements.

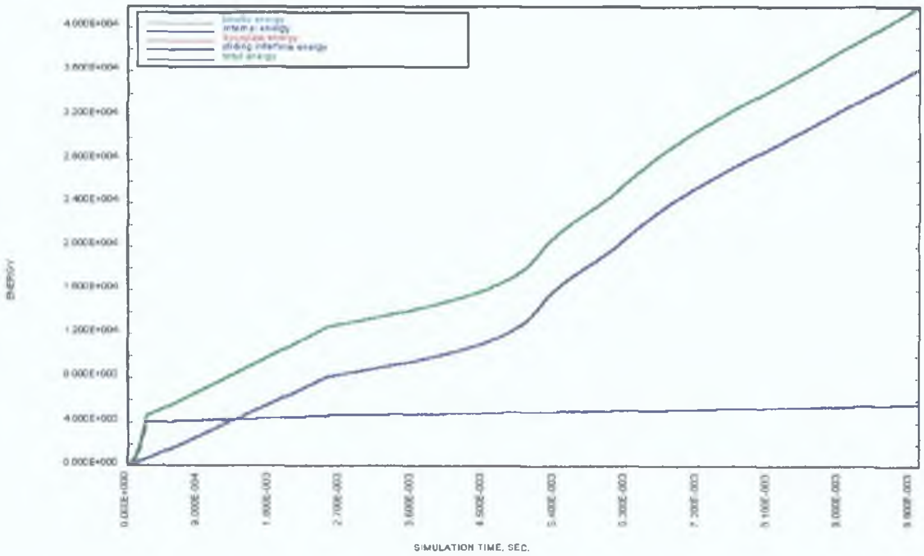

Figure 4.97: Energy development in the simulation using fully integrated brick elements.

Considering the above comparative results for fully integrated elements and reduced integration elements it was found that both of them give almost the same result. But the simulation with fully integrated elements take more than 3 times computer time than that taken by reduced integration elements. Therefore, it was decided that subsequent simulations of this forming process would be done using reduced integration elements.

As mentioned, the same model was run for a different loading pattern called pattern II as was shown in Figure 4.77. This loading imposes a higher ratio of axial loading to pressure loading in the first quarter of the simulation period as compared to the loading in previous simulations. This enhanced axial loading has induced different forming situation. Figure 4.98 shows the deformed shape of the bulge with contours of the radial displacement of the nodes. It can be seen from the figure that the shape is quite different to that developed by previous simulations in which the bulge had taken a smooth change of shape from the main tube to the fully developed bulge. But in this case the shape is rather irregular. The transition region from the main tube to the full blown bulge has two humps. One is just near the recess and the other slightly away from the recess.

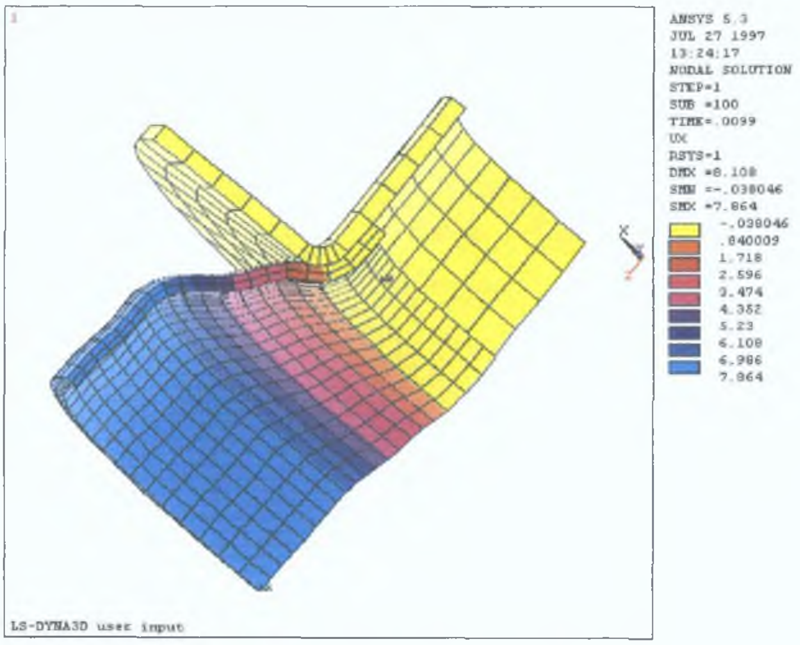

Figure 4.98: Deformed shape of the bulge by loading pattern II.

The reason for this state of deformation is related to the deformation shapes the bulge had taken at earlier stages of the simulation period. Figures 4.99 and 4.100 respectively show the shapes of the bulge when the simulation was one fourth and one half way through the period. Comparing these two figures with Figure 4.83 and 4.84 respectively it can be seen that bulge development was quite different in this case. In this case the initial hump was more prominent and continued to maintain the at half way through the simulation. In earlier simulation the hump had inflated and lost its shape when the simulation was half way. Though the hump went on inflating in the earlier simulation and eventually disappeared fully at the end of the simulation period, the hump in this case, in contrast, continued to maintain its shape until about three quarters way through the simulation period. After that the hump end near the die recess started inflating and continued and about 0.009 seconds through the simulation period the other end of the hump started inflating very fast. However, the ultimate bulge shown in Figure 4.98 could not eliminate the impression of the hump. The maximum radial displacement of the bulge was about 7.864 mm which is about 1.12 mm less than that obtained by previous loading pattern.

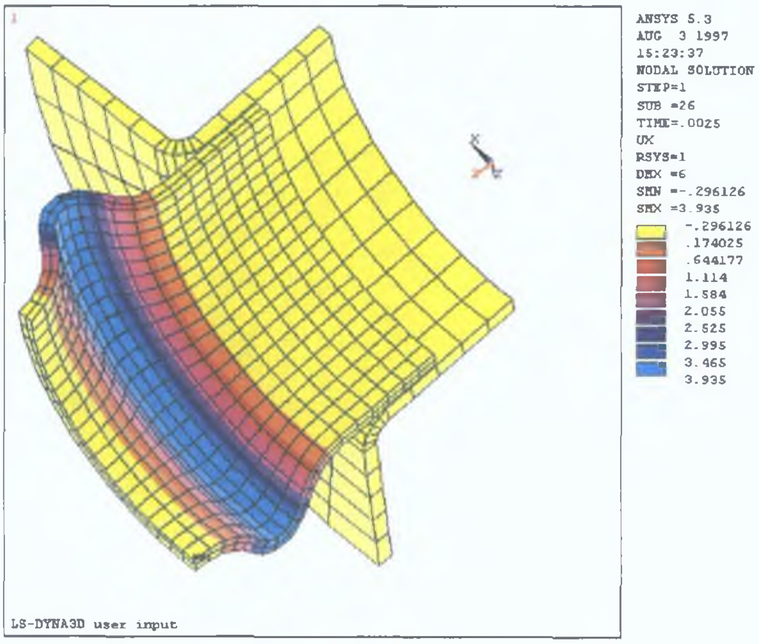

Figure 4.99: Bulge shape by loading pattern II after simulation time of 0.0025 seconds.

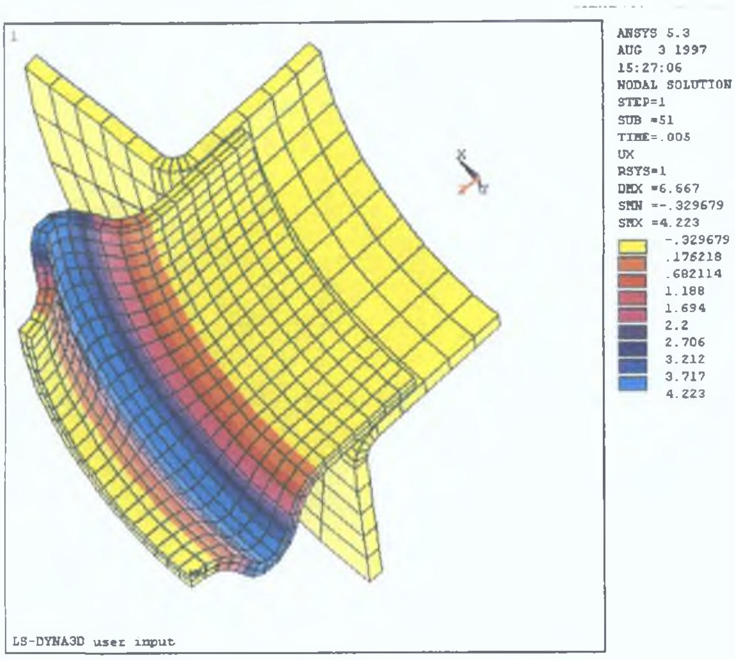

Figure 4.100: Bulge shape by loading pattern II after simulation time of 0.005 seconds.

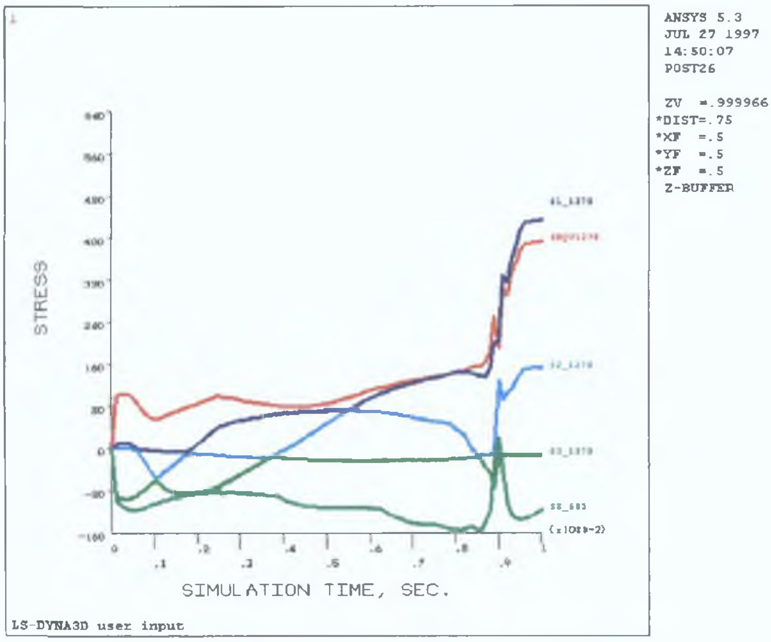

Figure 4.101: History of stress development in nodes 1270 and 605 by loading pattern II.

The different history of deformation due to different loading can be seen more clearly by observing the development of stress at some nodes in the tube. Figure 4.101 shows the history of stress development in node 1270 and 605 for the present loading. It can be seen that the nodes did not pick up much stress until about 0.008 seconds in the simulation. This is the time about when the hump end started inflating as described before. In contrast, these nodes developed stress right from 0.005 seconds through the simulation as was shown in Figure 4.88. It is interesting to note the development of stress of node 605 in Figure 4.101 which is near the die bend after full loading. Unlike Figure 4.88 where the node had a stick-slip deformation, the node here continued to be in compressive stress state until about 0.0088 seconds in the simulation. After that the node suddenly came under tensile stress state when the far end of the hump started inflating exerting a pull at the tube end. At this point in simulation time, stresses in other nodes also started picking up very fast. The stress history indicates that the bulge was more or less in a balance between circumferential tensile stress and axial compressive stress that kept the stress in bulge steady. Towards the end the influence of pressure load started dominating the deformation over the axial load. Although there was no sudden change in either the pressure or the axial load, the deformation in the bulge took a sudden change in mode from predominant compression mode to predominant expansion mode. This change has caused sudden change in the kinetic energy of the process. Figure 4.102 show the ratio of kinetic energy to internal energy over the simulation period. It can be seen that after the initial kick the kinetic energy in the process built up suddenly at 0.009 seconds in the simulation. This is also the time that the bulge started expanding very fast as noted earlier. The increase in the kinetic energy was only about 2 percent of the internal energy. It can also be seen from the figure that the bulge became stable immediately after it switched its mode and continued expanding.

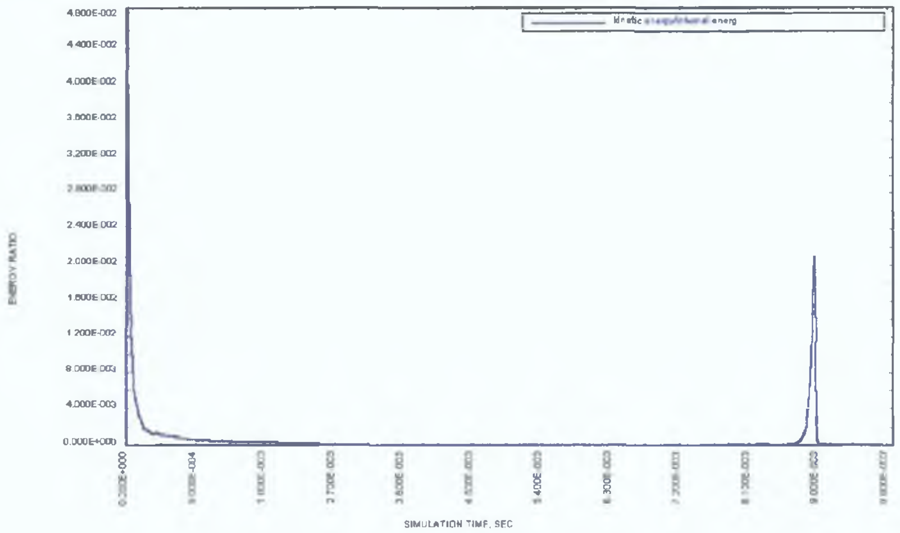

Figure 4.102: Ratio of kinetic energy to internal energy over the simulation period.

The deformation process described above suggests that if the loading in axisymmetric bulging is predominantly compressive due to higher level of axial loading, then the bulge will have a mode shape change as soon as the pressure loading takes over. In explicit dynamic solution process this type of situation is handled by system damping techniques within the solution process. However, it is always better to avoid this kind of temporary instabilities which might yield unreliable result specially if the system is not damped down soon. Observations from trial solutions would help the designer to avoid loading conditions that give rise to situations like this. It was observed in Figure 4.88 that the stress in node 605 suggested a stick-slip situation which indicates that the bulge is alternately under compression and expansion. But in Figure 4.101 it was found that node 605 was consistently developing compressive stress meaning that the expansion in the bulging region is not strong enough to pull the nodes towards the bulging region. This is a situation for potential mode change.

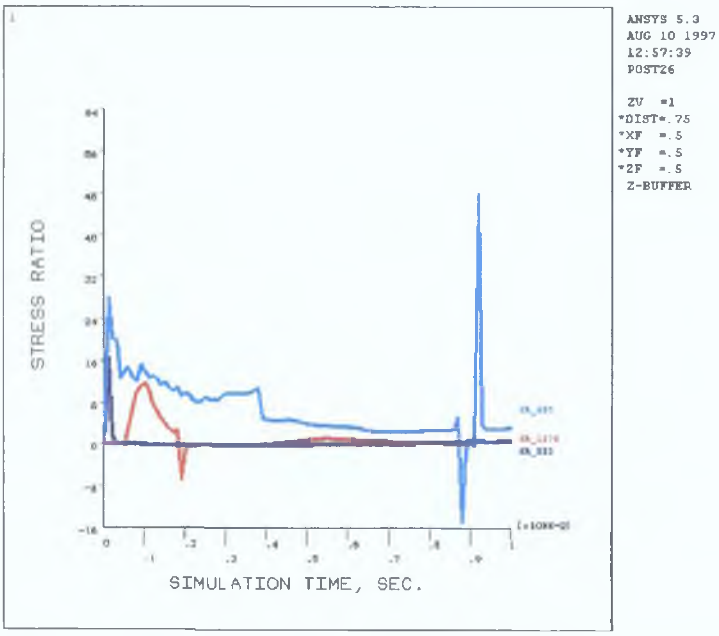

Figure 4.103: Ratio of principal stresses of node 1270, 885 and 605 as developed due to loading pattern II.

Figure 4.103 shows of principal stress ratio of nodes 1270, 885 and 605. These nodes are respectively at the bulge mid-section, at the hump developed during the process and at the main tube which eventually ended up at the die bend. The stress ratio indicates the ratio of axial stress to hoop stress in the nodes. It can be seen that the effect of enhanced axial displacement has reflected in the stress ratio of nodes 1270 and

885 during the first quarter of the simulation period. After that these nodes have steady and stable ratio of axial stress to hoop stress even when the temporary instability was set in the structure. But the ratio of node 605 was decreasing all along and eventually with a sudden sign of relief in axial stress the temporary instability was set in the bulge.

This kind of instability does not result in sound deformation behaviour. It was already found that this simulation has resulted in a bulge with smaller radial expansion. In this kind of deformation the stress and strain in the bulge is expected to be higher and uneven than a smooth forming situation. Figure 4.104 shows the von-Mises stress in the bulge. The maximum stress in the bulge is in the cylindrical part as was the case with loading pattern I. But the magnitude of the stress is about 1.13 times higher than that developed by loading pattern I in the previous simulation. Figure 6.105 shows the distribution of strain in the bulge in thickness direction. Taking the strains at the quarter symmetry edge as representative pattern, as reasoned out earlier, it can be seen that the bulge has thinned out at two locations along the length. For full model this would be at four locations. The extent of thinning is about 80% of the original thickness. Unlike previous simulation, this simulation has resulted in slight thickening at the main tube.

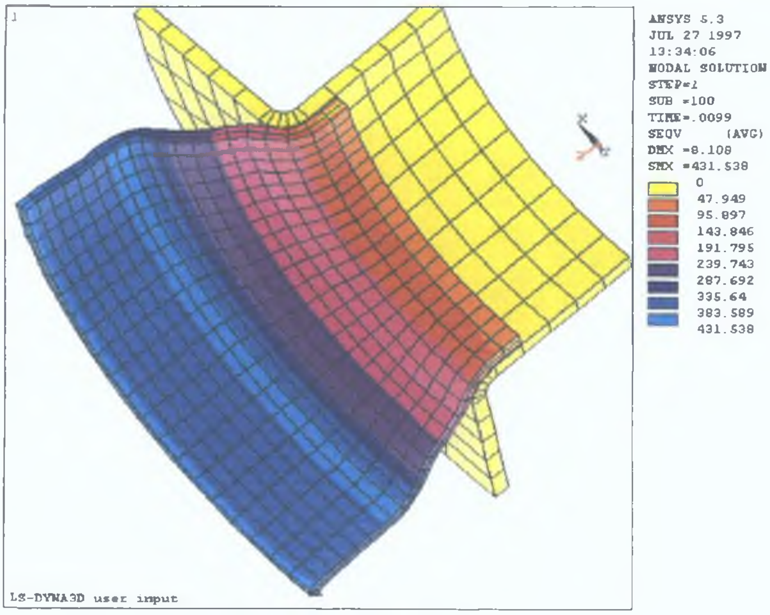

Figure 4.104: von-Mises stress in the bulge by loading pattern II.

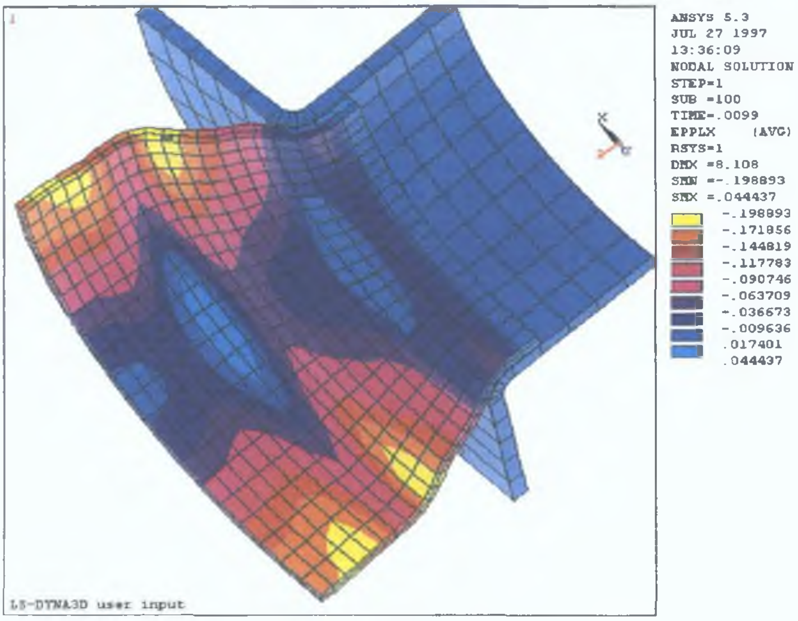

Figure 4.105: Distribution of strain in the thickness direction of the bulge by loading pattern II.

Figures 4.106 and 4.107 show the axial displacement of some nodes along the length of the tube for loading pattern I and II respectively over the simulation period. It can be seen from Figure 4.106 that all nodes along the length except 1282 to 1286 have steadily moved in axial direction towards the bulge mid-section. Nodes 1282 to 1286 have reversed their movement in axial direction at about half-way through the simulation. These nodes were pushed back to the die recess at that time and then again started moving towards the bulge centre. The situation due to loading pattern II is sharply different as can be seen in Figure 4.107. In this case almost all nodes except those very near the tube end and bulge mid-section have moved back sharply in the axial direction at about 0.0088 seconds in the simulation after a steady movement towards the bulge centre. At about 0.009 seconds in the simulation these nodes either stabilised or continued to move back but at a much slower rate.

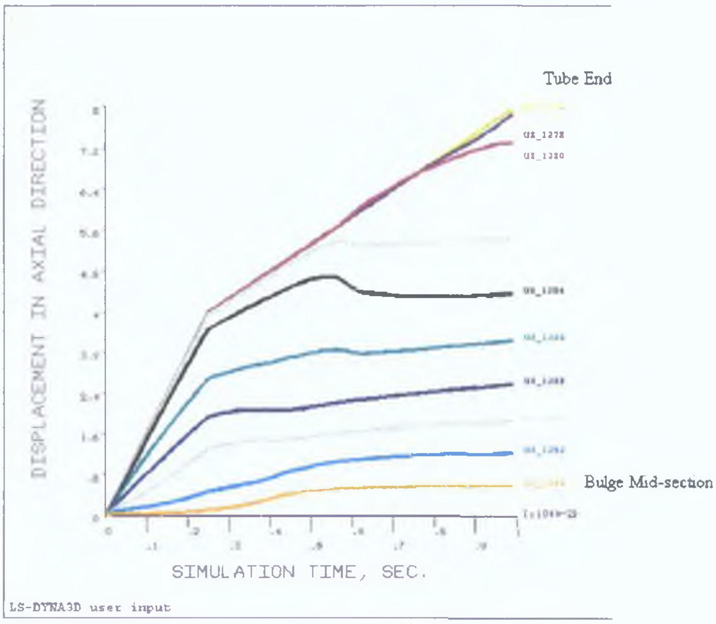

Figure 4.106: Axial movement of some nodes along the tube length due to loading pattern I.

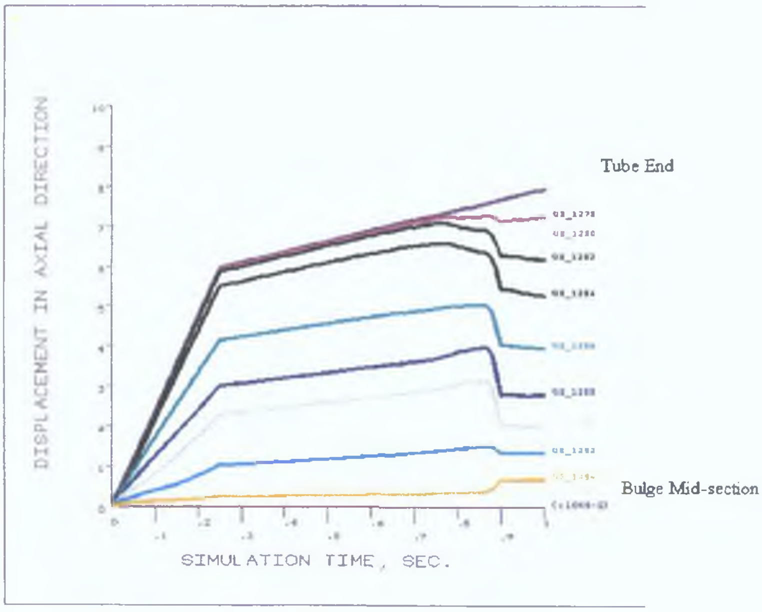

Figure 4.107: Axial movement of some nodes along the tube length due to loading pattern II.

Figures 4.108 and 4.109 show the strain path followed by nodes 1280, 1284, 1292 and 1256 in the principal strain planes due to loading patterns I and II respectively. Finite element model in Figure 4.74 shows the positions of the nodes in the tube. In general, under loading pattern I, the tube initially deformed under bi-axial tension in the first quadrant and then quickly moved on to the second quadrant where the bulge experienced tension in the hoop direction and compression in the axial direction. Under loading pattern II, the initial and final forming condition are nearly the same but differences are observed during the intermediate period of deformation. Most striking difference is observed in the strain path of nodes 1256 and 1284 in Figure 4.109 than that in Figure 4.108. The strain path of node 1256 by loading pattern II suggests that the bulge middle section experienced tension followed by compression and then again tension followed by compression in axial direction. Node 1284 which was initially under the die and ended up in the conical portion of the bulge experienced very weak compression until towards the end of the simulation.

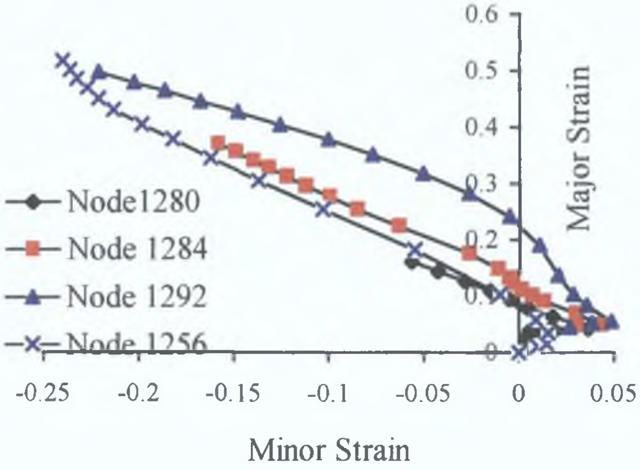

Figure 4.108: Strain path of some nodes due to loading pattern I.

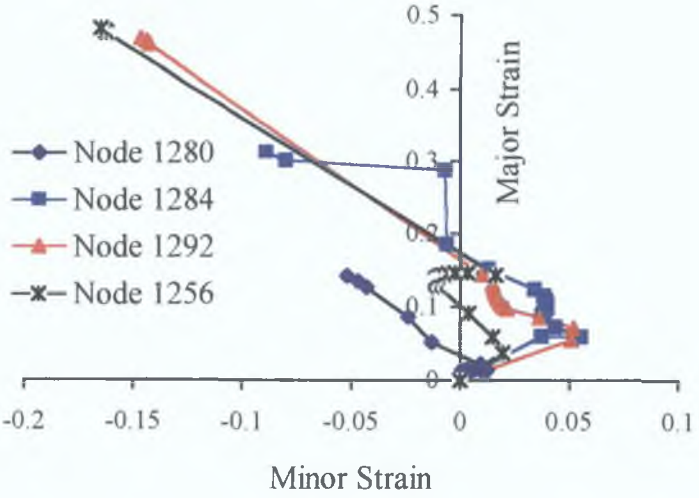

Figure 4.109: Strain path of some nodes due to loading pattern II.

Although it was not possible to identify a best loading pattern from the limited simulations, it can be said with certainty that the loading pattern I was better than the loading pattern II for the simulation problem Effort to identify an optimum loading pattern for the axisymmetric bulging of tubes is discussed in the next sub-section

4.3.2. Optimisation of Axisymmetric Bulging

It was illustrated in the previous section that the loading pattern has profound effect on the deformation of axisymmetric bulging process It would, therefore, require large number of trial runs to establish a loading pattern that would result in desirable deformation behaviour during the bulging process With the present computer resources of the project it was a question of weeks to have good number of trials to determine an effective loading pattern In the three dimensional analysis it was found that within the prescribed load limits there was no unusual deformation like wrinkles or buckling beyond recoverable limit Therefore, it was thought that the axisymmetric two dimensional analysis of the process could be possible to undertake Accordingly a two dimensional analysis of the problem was tried and it was found that the solution converges within about 50% of the time for three dimensional analysis The results were also close to the three dimensional analysis It was, therefore, decided that an optimisation exercise will be carried out to determine a better loading pattern

Finite Element Model

Figure 4 110 shows half of the axisymmetric two dimensional model of the problem The geometrical dimensions of the tube and die are the same However, the tube here is modelled in two parts for the convenience of defining the optimisation problem and for the generation of contact elements Also, the discretisation of the tube is done slightly differently Part one of the tube is likely to undergo compression at the tube end and expansion at the other end Therefore, mesh size at the tube end are coarser than the other end The second part of the tube is meshed uniformly Contact elements were generated selectively by considering the likely surface of interaction Outside surface of the first part of the tube has contact elements with all of the inner

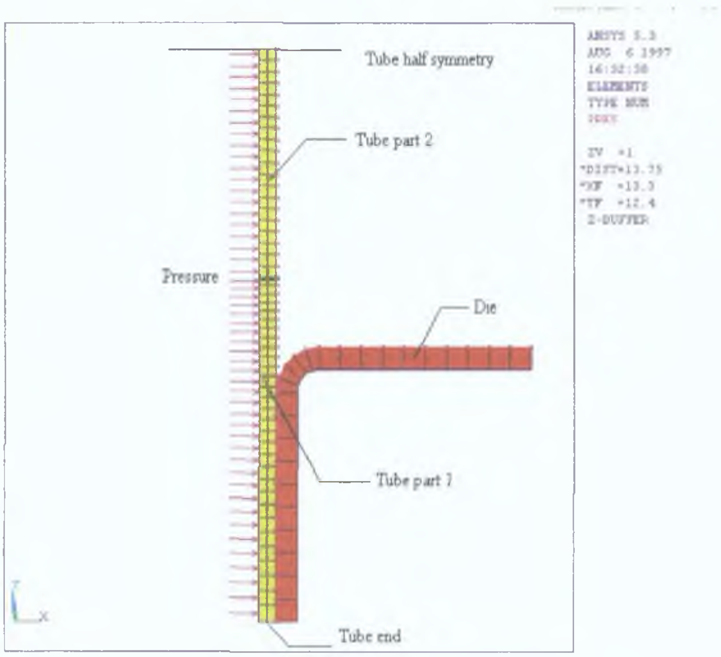

Figure 4.110: Finite element model of the optimisation exercise

surface of the die. Since the outside surface of the second part of the tube would only come in contact with the die recess, the contact elements there were generated accordingly. The stiffness of the contact elements were determined by several trial runs. After each trial run the contact gaps were checked and the stiffness value was changed to suitable value until a negligible contact penetration was achieved. The final stiffness value assigned to the contact elements was 138.6 kN/mm. An elastic Coulomb friction model was assumed the friction factor was 0.15. Figure 4.110 also shows the pressure loading at the inner surface of the tube and displacement loading at the tube end. Y- axis is the axis of symmetry. All die nodes are totally fixed. Tube nodes at the half symmetry are fixed in Y-direction. The tube and die material are the same as in three dimensional analysis.

Optimisation Problem

The optimisation problem was set up based on the results from three dimensional analysis. In three dimensional analysis it was found that the deformation starts as a little hump somewhere in-between the die recess and the symmetry plane of the model. Depending on the loading pattern the ends of the hump either inflate or do not The ends can also behave independently It was, therefore, observed that the deformation behaviour on both sides of the initial hump could be different Accordingly, the tube in the finite element model was built in two parts The initial hump is expected to build up within the second part of the tube near the interface of the two parts Therefore, the maximum stress is expected to develop in the second part of the tube and eventual rupture there In the optimisation problem, one of the state variable was defined to keep the stress in that part limited within the instability stress In three dimensional analysis it was found that the maximum equivalent stress in that region was around 400 MPa Accordingly the limit of the maximum equivalent stress in the nodes in the second part was defined as,

$$380 \le \text{A2NSMAX} \le 400$$

One of the objective of tube expansion is to obtain a certain minimum extent of radial expansion of the tube within the bulging region The conical part of the bulge (from main tube to full blown bulge) is expected to be formed from the first part of the tube Therefore, the nodes here will have widely different amount of radial displacement All of the second part, on the other hand, is expected to be the part of the full blown bulge The radial displacement of the nodes here should be as maximum as possible From the observations in three dimensional analysis the minimum radial displacement of the nodes in part two of the tube was defined as,

$$7 \le \text{A2NUXMIN} \le 10$$

As in 3D analysis, the full pressure load applied was 20 MPa and the full axial displacement was 8 mm However, the load is applied in two load steps At the first load step a fraction of the full load was applied This fractions were considered as design variables For the pressure load, the factor was named PRESFACT and the limit was set as,

$$0\ 2 \le \text{PRESFACT} \le 0\ 8$$

The displacement load factor was named as DISPFACT and the limit was set as,

$$0 \le \text{DISPFACT} \le 0\ 5$$

The limits were set based on the simulation experience in three dimensional analysis The limit of DISFPACT was explicitly kept within 50% of the full load to avoid instability The rest of the load after first load step was applied in the second and final load step

An ideal condition of bulging any blank into a shape by internal pressure and in-plane compressive load would be pushing the material of the blank in the bulging region without any folding or wrinkling at the constrained region and without any buckling or rupture at the bulging region The state variables A2NSMAX and A2NUXMIN would take care of the latter criteria The former criteria of no folding or wrinkling could be attained if the constrained part could be just displaced without much straining Thus the strain in the constrained region could be kept at a minimum The first part of the tube model is in the the constrained region Therefore, it was thought that minimising the maximum strain in this part of the tube would provide the optimum loading pattern Accordingly, minimisation of the maximum equivalent strain in the node of the constrained part of the tube, A1NEPMAX, was set as the objective function of the optimisation problem The optimisation problem can be summarised as

Minimise $\quad \text{A1NEPMAX} = f(\text{PRESFACT}, \text{DISPFACT})$

Subject to

$380 \le \text{A2NSMAX}(\text{PRESFACT}, \text{DISPFACT}) \le 400$

$7 \le \text{A2NUXMIN}(\text{PRESFACT}, \text{DISPFACT}) \le 10$

and

0 2 ≤ PRESFACT ≤ 0 8

0 0 ≤ DISFACT ≤ 0 5

After necessary post-processing the results of the initial trial run to define the optimisation problem, the optimisation solution process was started With the results from few more random trial runs within the limit of design variables, the solution progressed as dictated by regression curve of the objective criterion as a function of design variables A quadratic plus cross term fit was requested for the regression analysis for objective and state variable functions

Results and Discussion

The optimisation solution converged after 7 optimisation iterations after about 58 hours of computation time Solution converged to possible optimum based on design variable tolerances between the best and final designs This means that the design variable values of the final design set are within the tolerance limit of the design variable values of the last best design Although the solution did not find an explicit optimum of the objective variables, it points to the fact that the optimum solution is hovering around a certain set of design variable values The design sets obtained from the optimisation exercise are presented in Table 4 20

Table 4 20 Different design sets obtained from the optimisation run

Variable	Set 1	Set 2	Set 3	Set 4	Set 5	Set 6	Set 7
A1NEPMAX (obj)	0 79096	0 74124	0 85917	0 79245	0 74152	0 74244	0 77580
DISPFACT (DV)	0 20	0 42366	0 1943	0 26901	0 41385	0 42656	0 23764
PRESFACT (DV)	0 50	0 47431	0 61592	0 57075	0 48678	0 51888	0 50086
A2NSMAX (SV)	392 36	405 55	419 70	394 10	402 67	400 71	386 67
A2NUXMIN (SV)	8 0984	7 2743	8 8253	8 1240	7 3136	7 3535	7 9160

Figure 4 111 shows the variation of objective function and design variables over various design sets produced during the solution process The graph shows 8 design sets although the optimum solution produced 7 sets with seventh one being the optimum The 8th set is a repeat of set 5 to restore results for analysis and presentation Actually the design set 5 gave the minimum objective figure of merit (strain in the first part of the tube) but discarded by the algorithm because the state variable A2NSMAX, the maximum equivalent stress in the second part of the tube, was slightly more than the set limit of 400 MPa This limit violation caused the solution set to be infeasible It may be mentioned here that the limits set on state variables are based on trial solutions and are approximate values It may be seen from Table 4 3 2 that A2NSMAX in set 5 is 402 67 MPa which is very close to the limit value Therefore, design set 5 could be taken as the best available solution set

This design set suggests that 0 48678 part of the total pressure load of 20 MPa be applied along with 0 41385 part of the total axial displacement load of 8 mm at the first load step The ratio obtained from the optimisation exercise are close to the ratio of maximum available axial displacement to critical pressure which is approximately 0 40 in this case It was also the experience from simulation of circular and rectangular plates that a ratio like this gives better results

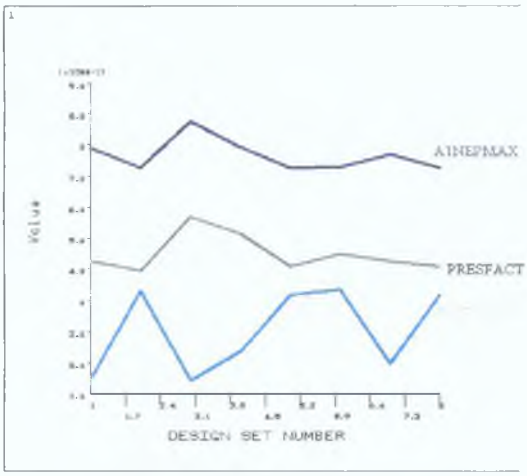

Figure 4.111: Variation of objective function and design variables over the design sets.

Figure 4.112 shows the deformed shape of the bulge due to this optimum loading. It can be seen that the bulge has a maximum radial displacement of 8.95 mm at the mid-symmetry plane. Unlike the 3D analysis, the bulge here does not have a good cylindrical portion at the middle. However, the difference in radial displacement is only 1 mm for a good portion of the bulge.

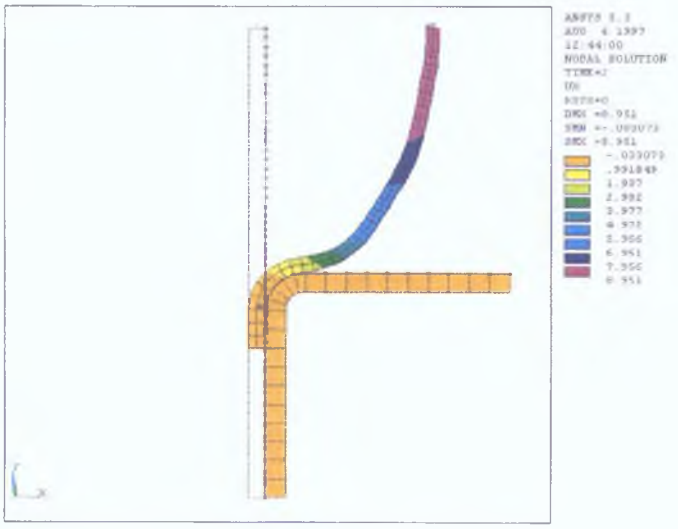

Figure 4.112: Deformed shape of the optimised bulge.

Figure 4.113 shows the bulge shape after the first load step. The shape is pretty much the same taken by the three dimensional analysis after the first quarter of simulation period by when an equivalent part of the full load was administered.

Figure 4.114 shows the thickness strain in the bulge. Maximum thinning is observed at the middle of the full bulge. The thickness there has reduced to about 75%

of the original thickness. In three dimensional analysis similar thinning was also observed

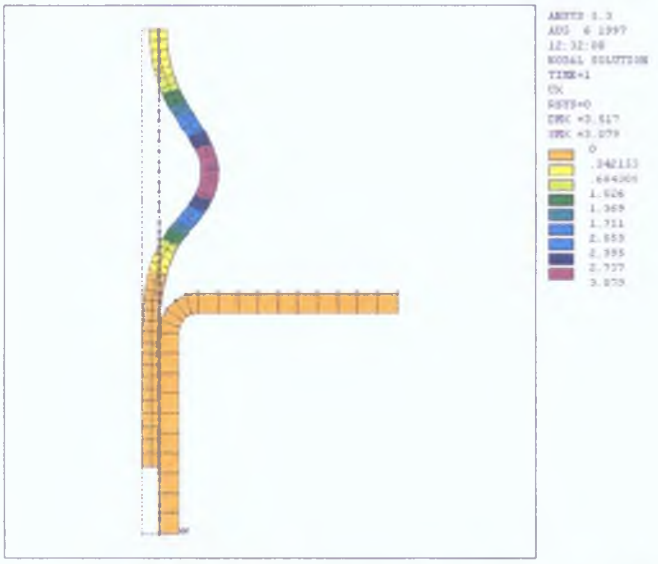

Figure 4.113: Bulge shape after the first load step.

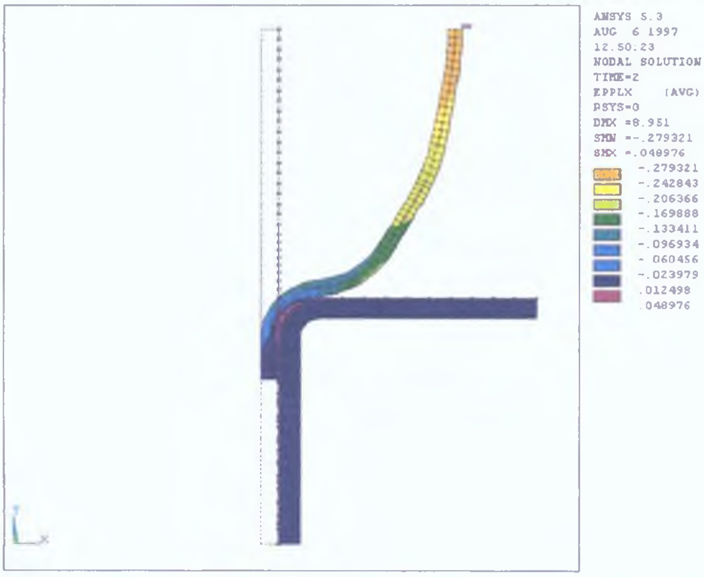

Figure 4.114: Distribution of strain in the thickness direction of the optimised bulge.

The load ratio suggested by the optimum solution is due to a particular way of defining the problem. Keeping the basic reasoning same, the problem could be defined in some other ways. Also the problem could be broadened by inducing more variables. But that kind of trial would warrant very long computation time for the computer resources used in this work. However, such exercise is worth exploring if faster computer resources are available.

4.4 Asymmetric Bulging of Tubes

It was stated in the introduction that asymmetric bulging of tubes is a very complex forming process Yet there are many different types of products made by this process This work involved simulation of the deformation of two types of products One is the forming of T- branch and the other is the forming of L-bend The former involved application of both the internal pressure and the axial compressive load while the later was formed with internal pressure only

Modelling and simulation of T-branch forming started with the limited ANSYS package The models developed with this package were somewhat restricted in number of elements However, good insight into the problem could be achieved from these simulations Later more satisfactory models were developed and simulated by acquiring LS-DYNA3D package Results from both analysis packages are presented Some simulations were done to analyse the failure mode of T-branch forming These were also done in LS-DYNA3D but with a different pre and post processor Forming of L-bend was also simulated with the latter package

4 4 1 ANSYS Simulation of T-branch Forming from a Tube

Modelling

For asymmetric forming specially T-branch forming, the die is a complicated part to model Serious difficulties arise to describe or develop the blending region between the die main body and the die recess Figure 4 115 shows a rendered solid model of one quarter of the die which would be required to model for finite element analysis Apart from the blending region, the die had to be extended from its symmetry planes to address the problem of contact pairing mentioned earlier in section 4 3 This was particularly important for LS-DYNA3D model For ANSYS model extension of die was not required as its contact algorithm has some tolerance mechanism to extend symmetry surfaces

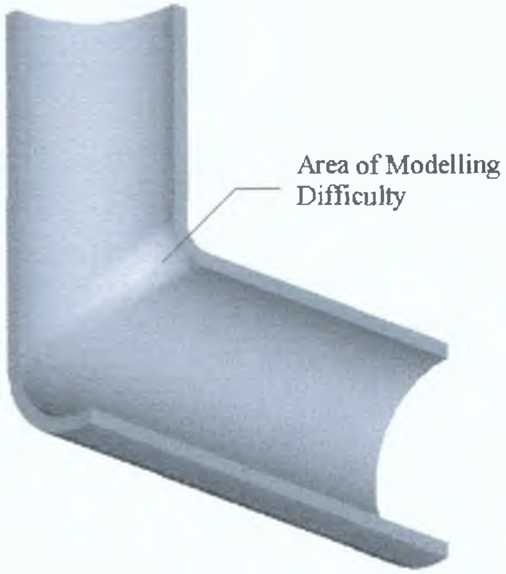

Figure 4.115: Cut-away view of one quarter of the die.

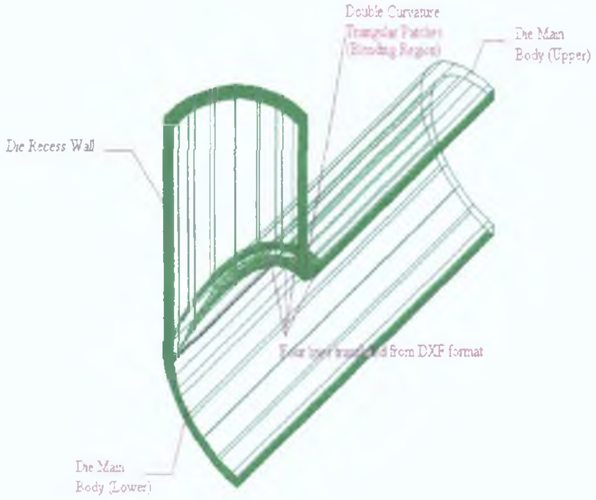

Figure 4.116: Wireframe model of the die quarter.

Figure 4.116 shows a wireframe model of the die quarter. From the figure it can be seen that the blending region is at the junction of two double curvatured volumes. Therefore the surfaces to be blended are doubly curved. In addition, the blending radius is varying; at one end it has some radius but at the other end the radius is infinity. Also the surfaces at this end meet at a point which eventually may result in bad shaped element at that location unless very fine sized mesh is generated.

The ANSYS pre-processor can not develop such surfaces. It also does not have a translator to import CAD files in DXF format. It has an IGES translator but the CAD software available for the project did not have IGES translator. Although it was not difficult to develop the geometrical model in AutoCAD, the difficulty was to transfer it to ANSYS solid modeller. The other CAD models supported by ANSYS are Pro-Engineer, Unigraphics and SAT. None of them were available for the project. However, the difficulty were resolved in a different manner.

The ANSYS modeller can generate splines or B-splines with maximum of six points. It was decided that the four curves in Figure 4.116 describing the blending region will be generated by B-splines. Accordingly the data points for these four lines were extracted from the DXF files of the wireframe model developed by AutoCAD. Seventy two data points describe each curve. Out of them only six could be picked up for ANSYS modeller. Looking at the nature of the curves data points for six locations were chosen so that the curvature is well represented. The top two lines were to remove the degeneracy point (sharp prismatic corner of the solid model) by shifting them little upwards.

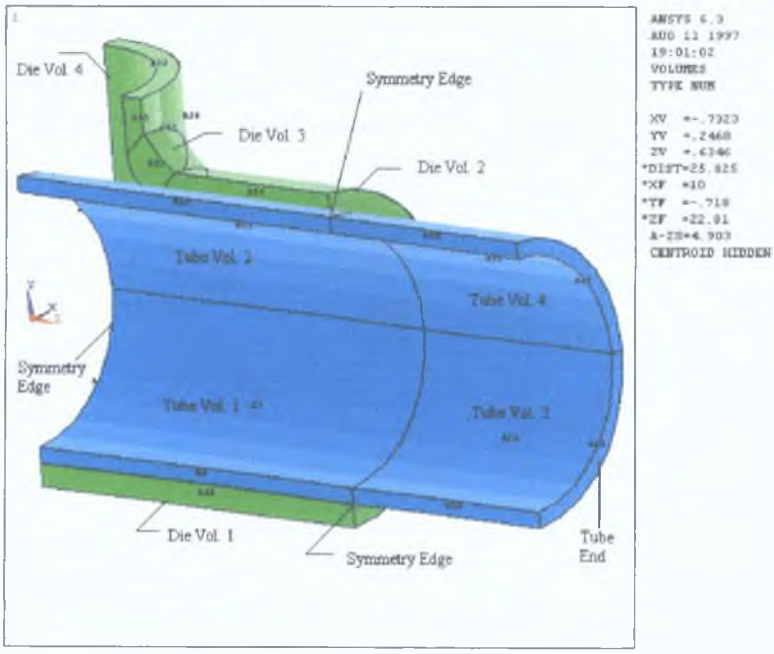

Figure 4.117: Solid model of the die and the tube.

The die was then built up in four volumes. One volume described the lower half of the die main body; one described the upper half of the die main body which had the approximate curves at its one edge; the third volume is the blending region itself and the last part was the die recess. To keep the number of elements in the model minimum the die main body did not cover all of the tube surface.

The tube was modelled into four volumes to facilitate limited contact modelling. Figure 4.117 shows the solid model of the die and tube. Volumes 3 and 4 of the tube were kept out of the die and treated as rigid body between the die and the punch (please refer to Figure 1.2). The internal diameter of the die body and the recess was 12.06 mm. The length of the modelled part of the tube was 53.5 mm. The length of the tube covered by the punch was 20 mm. The thickness of the tube was 1.37 mm.

The die was discretised into 56 brick elements. The die thickness was covered by one element height. The tube was discretised with two layers of elements across its thickness. The total number of elements in the tube was 390. Figure 4.118 shows the discretised the die-tube model. Some of the die elements (green) or part of them are visible through the tube elements. This is due to the fact that when there is graphics on the same display area the computer displays the latest pixels of the graphics. In this particular picture some die elements' graphic information was displayed after the tube elements resulting in the anomaly.

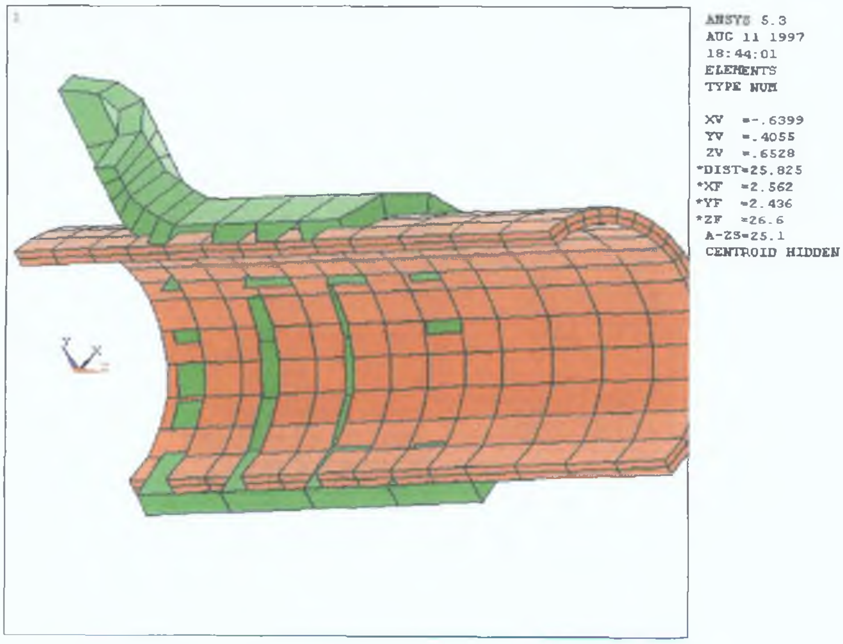

Figure 4.4.4: Finite element model of the die and the tube

Point to surface general contact elements were generated in different ways to see that the model size was within the limit After several trials contact elements were generated as below

- i tube volume 3 and 4 were treated as rigid body and thereby not included in contact pairing
- ii inner surface of die volume 1 and outer surface of tube volume 1 had 5 contact elements closest to the centroid of each target element face Both tube and die surfaces were alternately contact and target surfaces
- iii outer surfaces of the tube volume 1 and inner surfaces of die volume 2 and 3 had contact elements within 8 mm radius of each element face
- iv outer surfaces of the die volume 2 and inner surfaces of die volume 2 and 3 had contact elements within 8 mm radius of each element face
- v outer surfaces of tube volume 2 and inner surfaces of die volume 4 had contact elements within 8 mm radius of each element face

The tube was assigned a piecewise linear plastic material model The material data are

Young s Modulus = 3 66x10^{3} MPa Density = 8 9x10^{6} kg/mm^{3}

Poission s Ratio=0 3

strain	stress(MPa)
0 005	18 3
0 500	220 0
2 000	465 0

The die was assigned elastic material model and was treated as rigid body by fixing all its degree of freedom

Boundary Conditions, Loading and Solution

Since a quarter of the model was developed by taking advantage of symmetry, the tube nodes at the symmetry edges were restrained in appropriate directions Tube volumes 3 and 4 inner and outer surface nodes were restricted in X and Y directions restricting them to move radially and circumferentially but free to move axially The interior nodes in these tube volumes, however, were left free to move at any direction

The pressure load was applied as surface load at the inner surface of tube volumes 1 and 2. The axial compressive load was applied as prescribed displacement of nodes at the edge of the tube end. First three simulations were done with pressure loading only. The tube ends were kept either fixed or free in these models. In subsequent simulations both pressure and axial loads were applied. In all cases the loads were ramped linearly. The maximum pressure load applied in the former simulations was 30 MPa. For the later cases it was 15 MPa and the axial displacement was 6 mm. The loading pattern is shown in Figure 4.119.

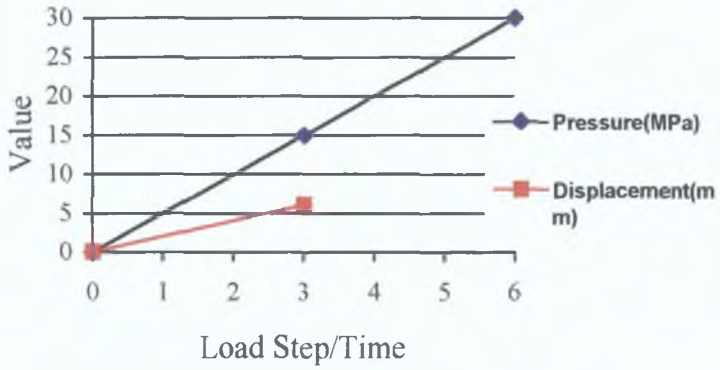

Figure 4.119: Loading pattern of the simulation models.

Preconditioned conjugate gradient solver was used for the solution of the problems instead of wavefront solvers used in other previous solutions by ANSYS. This solver is faster and appropriate for large wavefront problems. This solver also requires less disk space than frontal solver as triangulation matrix by frontal solver is not needed. However, this solver uses more memory. In spite of all these, solution for each simulation was obtained after about 8 days of computation.

Results and Discussion

As mentioned, first three simulations of the forming process were done with pressure loading only. In the first case, the tube ends were kept fixed and in the second, they were left free to move. The friction factor assigned for the two simulations was 0.3. In the third simulation, the friction factor was reduced to 0.15 and the ends were kept free.

Table 4.21 presents the comparative results of these three simulations. It can be seen from the table that there are not much difference between the simulations although the forming conditions were different. This is largely due to the high friction between the die-tube interface that prevents the tube to move towards the bulging region. It was found in the second simulation that the tube ends even moved in the other direction by a few hundredths of a millimetre. The effect of friction was slightly visible in the third simulation where friction was halved to 0.15. Here, the branch height is slightly high, the stress in the branch top is less and has thinned less. Very low friction is expected to improve above results but such simulation was not attempted because of very long computation time.

Table 4.21: Summary of results from simulations of T-branch forming by keeping tube blank ends fixed or free

Simulation	End Condition	Friction	Max^{m} branch height (mm)	Max^{m} eqv. stress (MPa)		Thickness at branch top (% of original thickness)
				Value	Location	
I	fixed	0.3	8.255	221.0	branch top	65.0
II	free	0.3	8.266	221.8	branch top	66.3
III	free	0.15	8.426	215.0	branch top	66.7

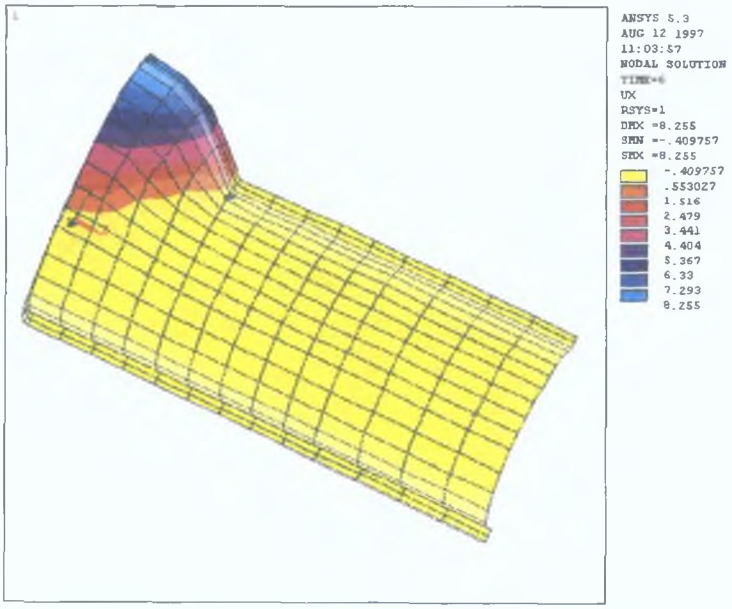

Figure 4.120: Deformed shape of the tube with radial displacement contoured.

Figure 4.120 shows the deformed shape of the tube for the first simulation. It also displays the radial movement of nodes in the tubes. Results for other simulations are very much the same. Figure 4.121 shows the absolute movement of the nodes in the tube. It can be seen that the nodes originally at the bulge region moved radially. There is no sign of any movement of the nodes in the constrained regions. Also the nodes directly under the bulging region have not moved. For the other simulations the condition was very much the same. Results presented in the following are from the simulation where the friction factor was 0.3 and the tube ends were kept fixed.

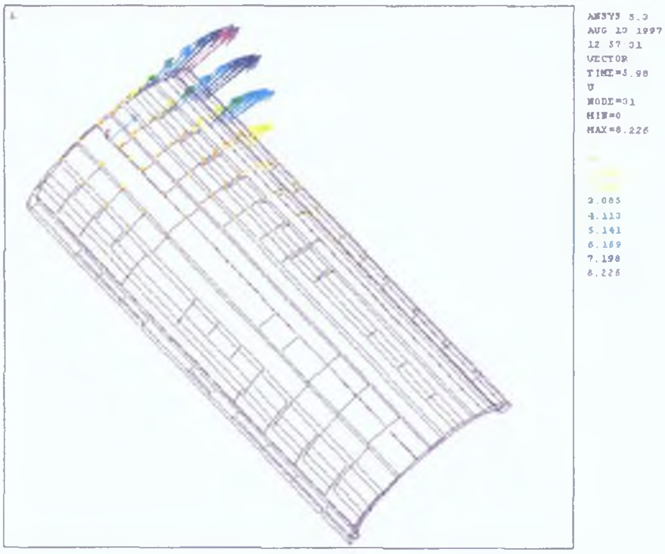

Figure 4.121: Absolute displacement of the tube nodes.

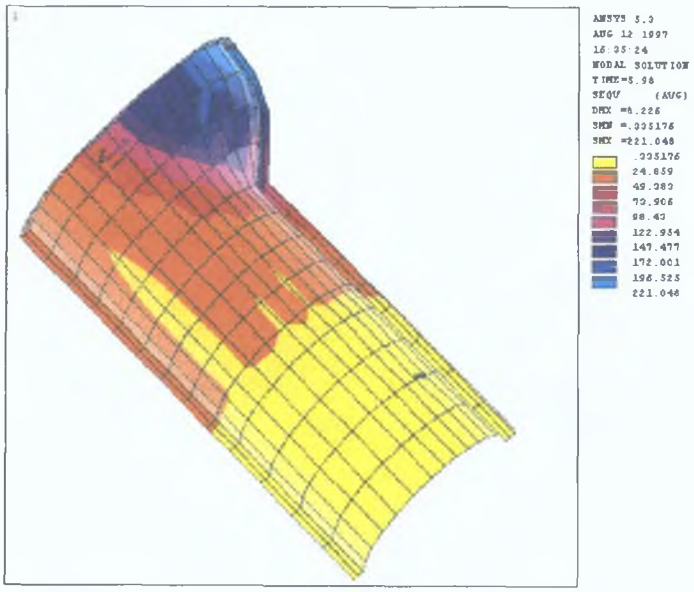

Figure 4.122: Distribution of von-Mises stress in the tube(ends were kept fixed).

Figure 4.122 shows the von-Mises stress distribution in the deformed tube. The stress developed is maximum at the branch top gradually decreasing towards the bulge base. The main tube (excluding the location under the punch), has stressed the least. There are some pockets of low stress at the main tube. This is thought to be due to the coarse meshing. Due to coarse meshing the contact elements between the interfaces are also sparse. As a result, interfacing forces act at the locations of contact elements. It is as if the surfaces have asperities which come in contact first resulting in areas of higher and lower stress. The distribution of stress in other simulation was very similar.

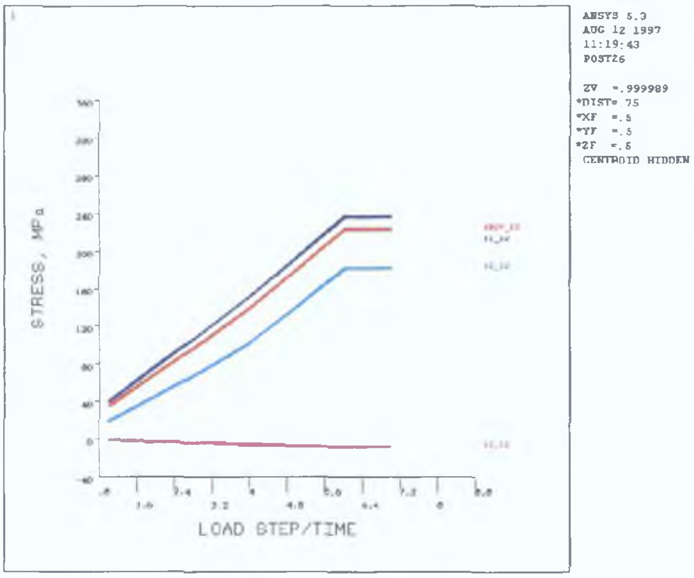

Figure 4.123: Development of stress at the central node of the branch (ends fixed).

Figure 4.123 shows the development of equivalent stress and principal stress of a central node at the branch top. It can be seen that up to load step 7 when a pressure load of 30 MPa was applied, the stress development was steady. There were some undulations after that due to which results beyond 30 MPa were not accepted. All the results presented above, were up to load step 7. It can also be seen that the ratio of the first and the second principal stress were never constant although the pressure load was raised uniformly throughout the simulation.

Subsequent three simulations were done with pressure load and axial displacement for the same model. The only difference between these simulations was friction factor. The first one was for a friction factor of 0.3, the second one for 0.15 and the third one was for frictionless condition. The maximum pressure load applied in these simulations was 15 MPa. Further pressure load was not possible as contact elements were generated in a restricted manner Further loading actually resulted in loss of contact

Table 4 22 presents the summary of results from the above three simulations As can be seen from the table that the simulations have resulted in different branch height, stress and strain As expected, the frictionless forming condition has allowed more material movement in bulging region allowing more deformation and stress but less thinning Comparing to the deformation by only pressure load it can be said that a comparable length of branch can be formed at much low internal pressure and the stress and thinning in the branch would be relatively less

Table 4 22 Summary of results from simulations of T-branch forming by pressure and axial compressive load

Simulation	Friction	Max^{m} branch height (mm)	Max^{m} eqv stress (MPa)		Thickness at branch top (% of original thickness)
			Value	Location	
I	0 3	7 418	185 71	at the middle region around Z-symmetry	87 0
II	0 15	8 279	203 76	at the middle region around Z-symmetry	88 0
III	0 0	9 374	225 65	at the middle region around Z-symmetry	90

The only commonality in the results of these simulations is the location of maximum stressing and thinning In all simulations the maximum stress occurred where the tube upper half meets the lower half near the Z-symmetry of the tube The location can be seen in Figure 4 124 which shows the distribution of von-Mises stress in the deformed tube according to the first simulation Apart from the region under the punch, the minimum stress has developed at the bend around the die which may be slightly inaccurate as this part has undergone some bending deformation which is not well accounted for by solid elements Prominent stress gradient is observed at the main branch which is due to different contact modelling at the upper and lower half and also due to the coarse element mesh resulting in different normal and frictional contact forces This phenomenon in this region has also affected the stress distribution in the punched region The situation was not much different in the second simulation where the friction factor was 0.15. The absence of frictional force in the third simulation has largely smoothened the stress distribution as can be seen in Figure 4.125.

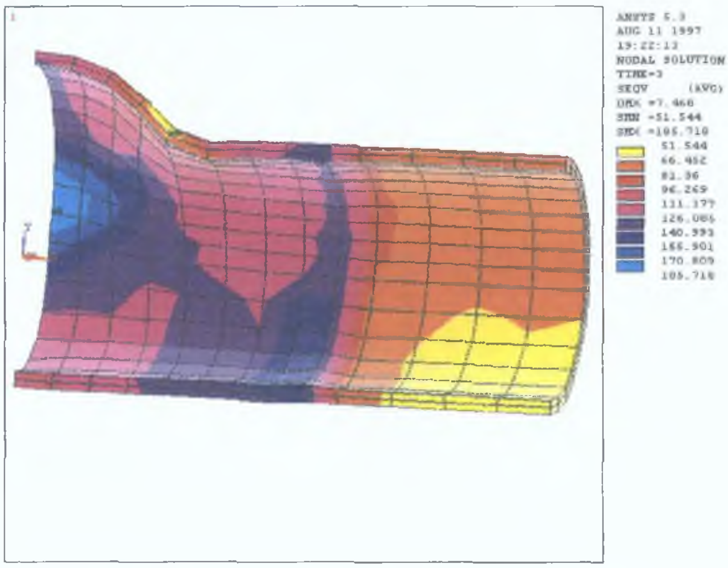

Figure 4.124: von-Mises stress distribution in the tube formed at higher friction

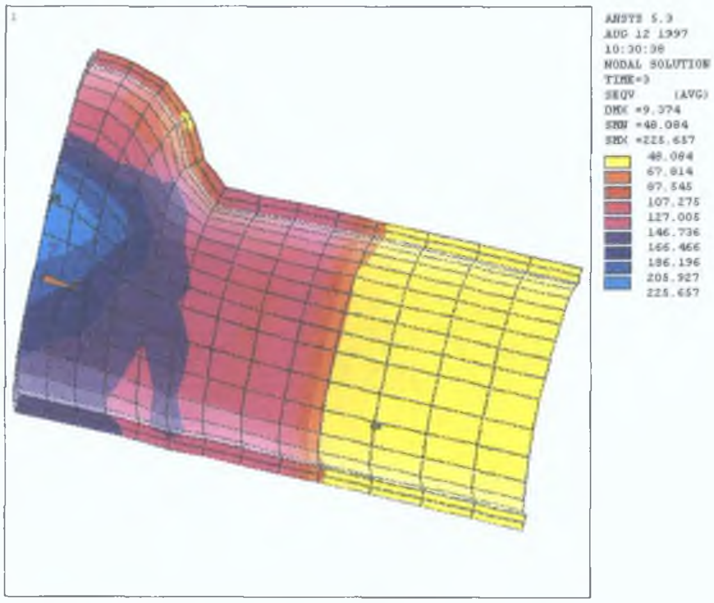

Figure 4.125: von-Mises stress distribution in the tube formed at frictionless condition.

Figure 4.126 presents the distribution of strain in the radial direction which shows the amount of thinning or thickening in the deformed tube. This figure illustrates the case for the frictionless forming condition. The pattern is more or less same for other friction condition although the magnitudes varied. Most thinning has occurred in the T-branch top. The main tube has thickened everywhere and most thickening is observed right opposite the T-branch at the lower half of the tube. Materials moved into this part due to the end push has not moved upwards causing most thickening there.

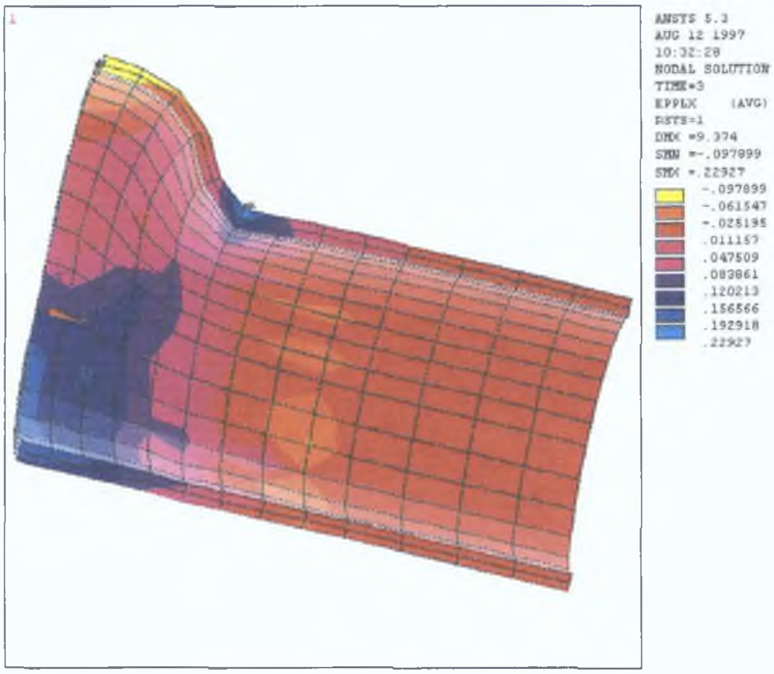

Figure 4.126: Distribution of strain in thickness direction of the tube formed at frictionless condition.

Figures 4.127 and 4.128 show the absolute displacement of nodes in the tube for the first and third simulation respectively. There is considerable material movement due to the push at the end. The total displacement is more in frictionless forming as depicted in Figure 4.128 compared to that in Figure 4.127 where considerable friction is present. In both conditions there is some material movement from the lower half of the tube in the proximity of the bulging zone towards the bulge. Movement is more for frictionless condition. It may be mentioned here that there was no movement of material from the lower half of the tube in the case of bulging by pressure loading only although the pressure applied was double. It points to the fact that push from the end compelled material to move from the lower half of the tube to the bulging zone. However, the influence of bulging zone is only in the immediate vicinity.

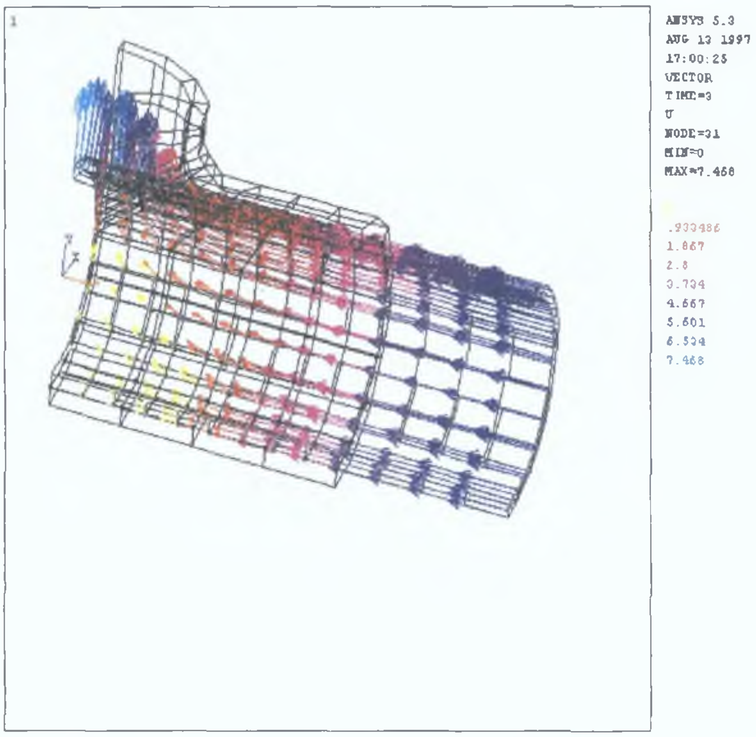

Figure 4.127: Absolute displacement of tube nodes in the case of higher friction.

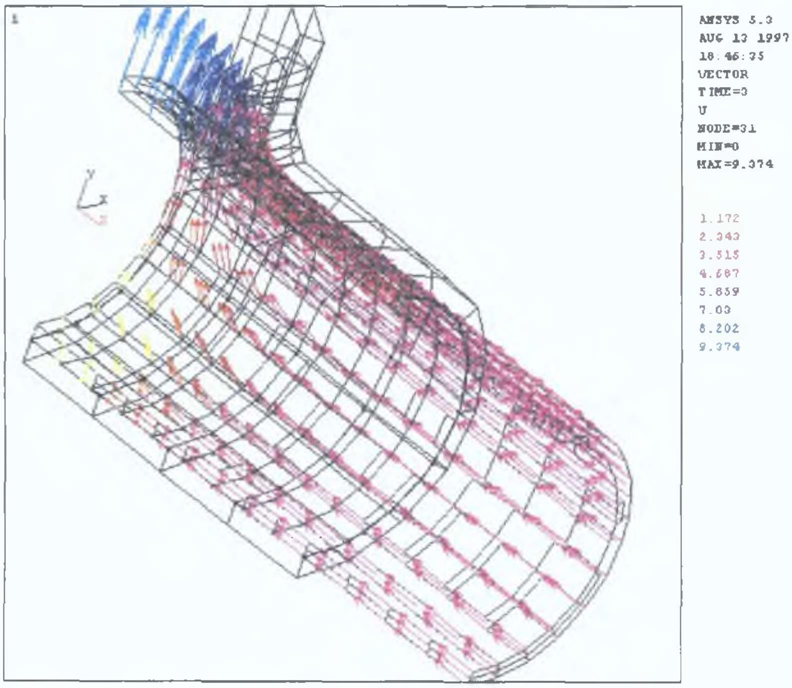

Figure 4.128: Absolute displacement of tube nodes in the frictionless forming case.

Finally, Figure 4.129 shows the development of stress over time in a central node at the T-branch top in frictionless forming condition. It is evident from the figure that the stress development pattern over the simulation period closely resembles the multilinear stress-strain relationship of the material indicating a good reliable solution.

The stress ratio in the T-branch top seems to have varied while the deformation was in progress. Despite the axial compressive load and frictionless interface between the tube and the die, the axial stress in the bulge (third from top) has never been compressive. The pressure load was dominating the forming condition in the bulge.

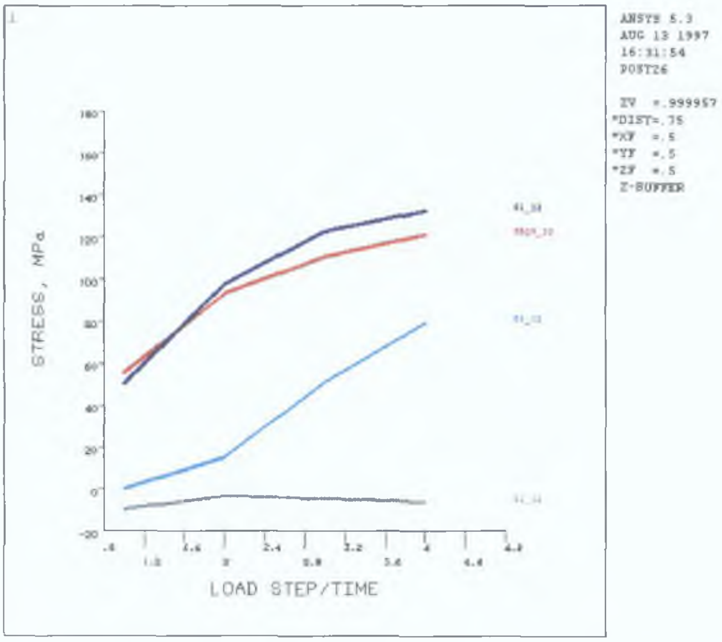

Figure 4.129: History of stress development at the central node of the T-branch over the simulation period in frictionless forming condition.

4.4.2 LS-DYNA 3D Simulation of T-branch Forming from a Tube

Modelling

The pre-processor used to develop the model for LS-DYNA 3D was the same as for ANSYS. Therefore, the same technique was used to develop the solid model of the die. However, the finite element model was different. Since LS-DYNA3D solver was free from any model size limitation except the computation time for the particular computer resources of the project, the solid model of the die was developed covering all of the tube. Also as LS-DYNA3D has different contact searching technique, there was no need to develop the tube in parts. Accordingly the tube was build in one volume. Figure 4.130 shows the solid model of a quarter of the die-tube assembly.

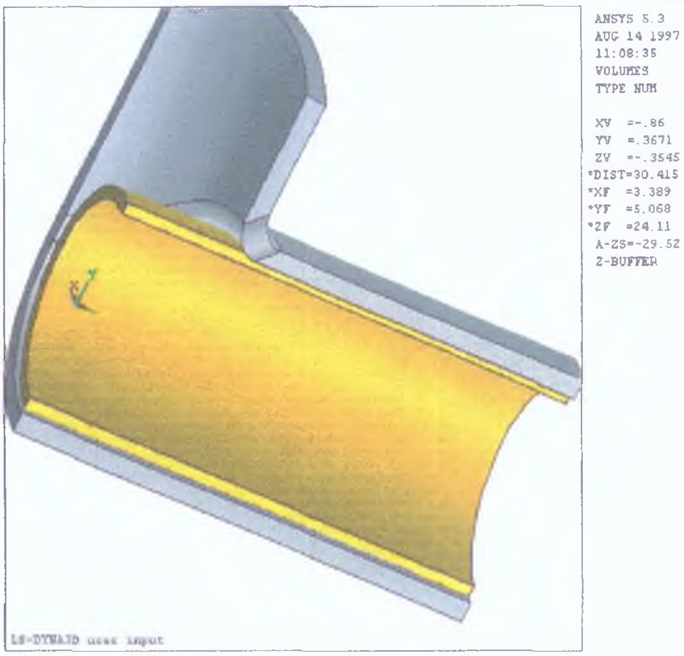

Figure 4.130: Solid model of the die and tube for LS-DYNA3D analysis.

This time the solid model could be discretised into more fine meshes. Figure 4.131 shows the discretised finite element model of the problem. A total of 2565 brick elements describe the model out of which the tube comprises of 1900 elements. Total nodes in the model is 4537. The brick elements describing the model had one integration point at their centroid.

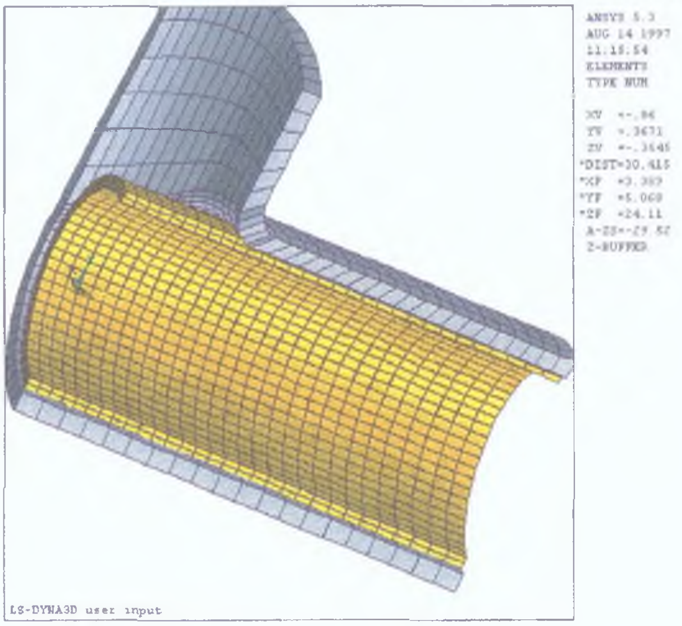

Figure 4.131: Finite element model for LS-DYNA3D analysis.

The same soft material was used as in the previous section. Surface to surface contact elements were generated for all interfaces. Elastic Coulomb friction law was assumed for interface friction. Three simulations were carried out for two friction conditions. The friction factors were 0.0 and 0.3. The two loading conditions differing mainly in the rate of application of pressure load were simulated. The rate of axial displacement was same for all models. Each simulation took about 4 hours of computation time.

The deformation was given a quasi-static treatment in simulation as LS-DYNA3D is basically a explicit dynamic solver. For this purpose, the simulation period was made much shorter than the actual deformation time would be. However, the kinetic energy of deformation was kept on check so that the dynamic effect in the simulation is negligible.

Results and Discussion

First two models were run with same loading pattern as shown in Figure 4.132. They differed in friction conditions. The first one was run at frictionless condition while the second was run for a friction factor of 0.3. Figure 4.133 shows the deformed condition of the tube after application of full 30 MPa pressure at the inner surface of the tube and 20 mm axial displacement of the tube end. It can be seen that the elements are severely distorted. Hourglass mode of deformation is evident all over the deformed tube.

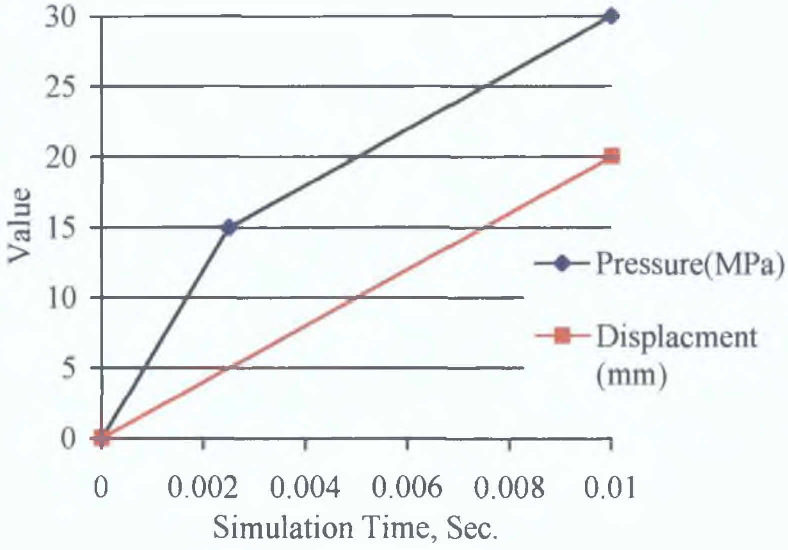

Figure 4.132: Loading pattern for the first and the second simulation

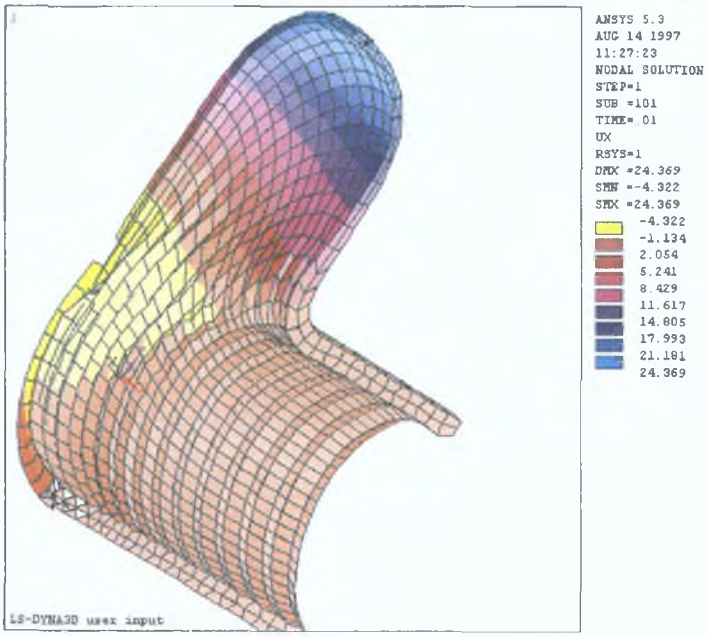

Figure 4.133: Deformed shape of the tube after full time of simulation.

A check of the development of hourglass energy during the deformation in Figure 4.134 reveals that the energy started picking up at about 0.0090 seconds in the simulation period. Towards the end of the simulation period the hourglass energy suddenly shot up. Looking at the figure it is expected that deformation at 0.0085 seconds in the simulation would have acceptable level of hourglass type of deformation. Figure

4.135 shows the deformed shape of the tube at this time. The pressure and axial displacement at this stage was 27.0 MPa and 17 mm respectively. The branch height attained by this load was about 20.6 mm.

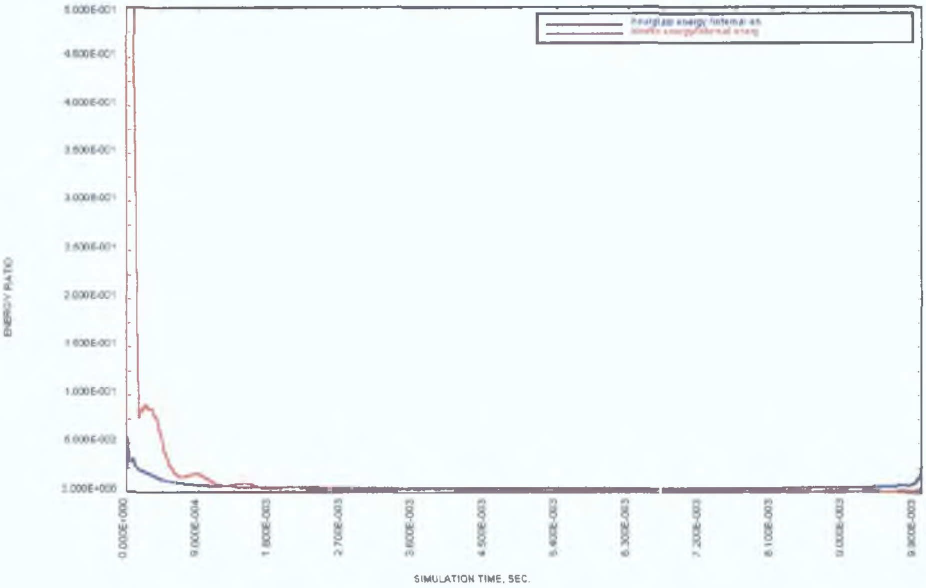

Figure 4.134: Ratio of hourglass energy and kinetic energy to internal energy of deformation over the simulation period.

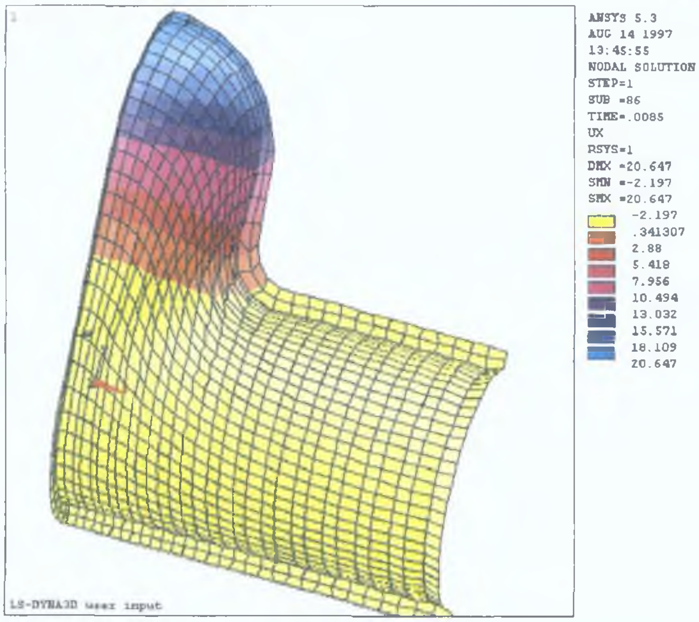

Figure 4.135: Deformed shape of the tube after 0.0085 seconds in the simulation.

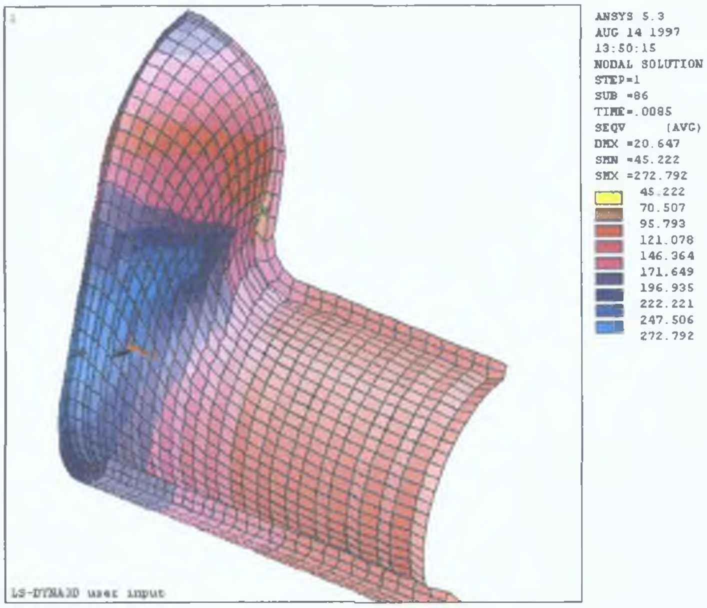

Figure 4.136: Distribution of von-Mises stress in the deformed tube at 0.0085 seconds in the simulation.

The state of the equivalent stress in the deformed tube is shown in Figure 4.136. It can be seen that the region in the main tube right below the T-branch base has stressed most. The location of the maximum stress in this region is where the upper and lower half of the tube meets near the Z-symmetry plane of the model. This was also the location obtained in the simulations by ANSYS in the previous section. The magnitude of the maximum stress was about 272.8 MPa. The minimum stress in the deformed tube happened to be around the die bend. The deformation in this region is translational and bending. The brick elements do not have any rotational degree of freedom and thereby no stiffness in bending. Only the translational movement is accounted for in the solution. Likely bending in this region has not been taken care of resulting in relatively less stress. The branch top also has stressed to a high level compared to its base or trunk region. The main tube not under the T-branch has stressed uniformly.

Most thinning has occurred at the top of the T-branch as shown in Figure 4.137. The thinning there is about 77% to 64% of the original thickness of 1.37 mm. Thinning is observed until the base of the branch whereupon thickening started . All of the main tube including the part directly under the branch has thickened. The thickening in this areas is about 133% to 146% of the original thickness. The thinning at a particular axial position of the main tube is observed to be varying along the circumference. The top part of the tube that meets the die at its higher bend radius seems to have thickened more than the part immediately below. The thickening has increased at the lower part of the tube. This was a direct consequence of the material movement towards the bulging region form the main tube. The areas that thickened more faced more obstacles or resistance to movement.

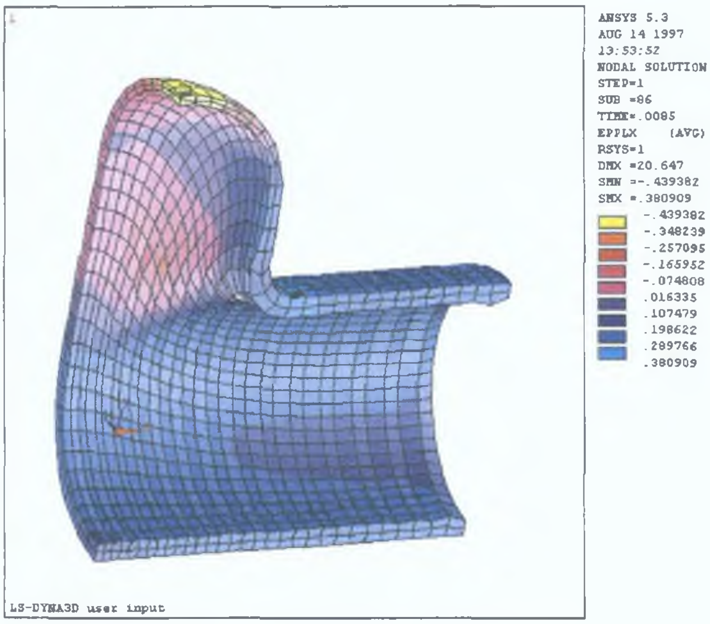

Figure 4.137: Distribution of strain in the thickness direction of the tube.

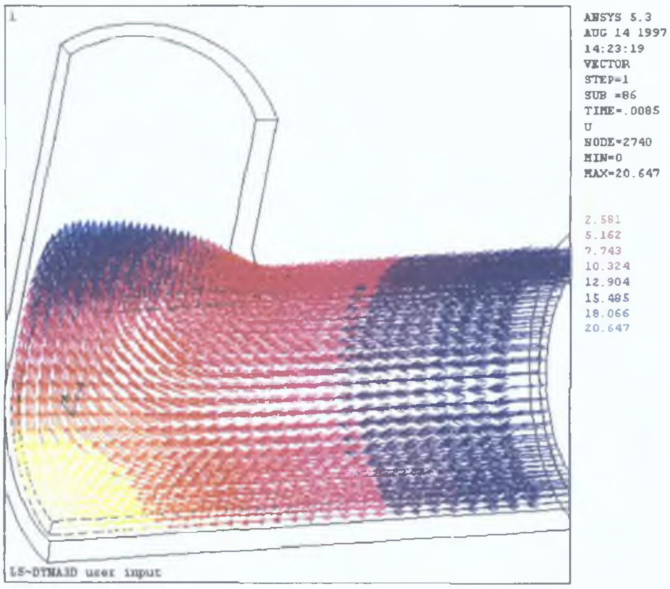

Figure 4.138: Absolute displacement of the nodes in the tube.

Figure 4.138 shows the absolute movement of the nodes in the tube indicating the material flow pattern in the deformation. Material once entered in the bulging region from the ends moved towards the bulge developing at the top. Materials from a good part of the lower half of the tube under the T-branch moved upwards with this forming condition. However, there was different degree of movement along the circumference which is not very clear from the figure as there is overlapping due to the bent. Viewing the situation in virtual reality could clearly reveal the phenomenon. A zone at lower left corner exists where material has either not moved or moved only slightly in the axial direction and very little in the circumferential direction.

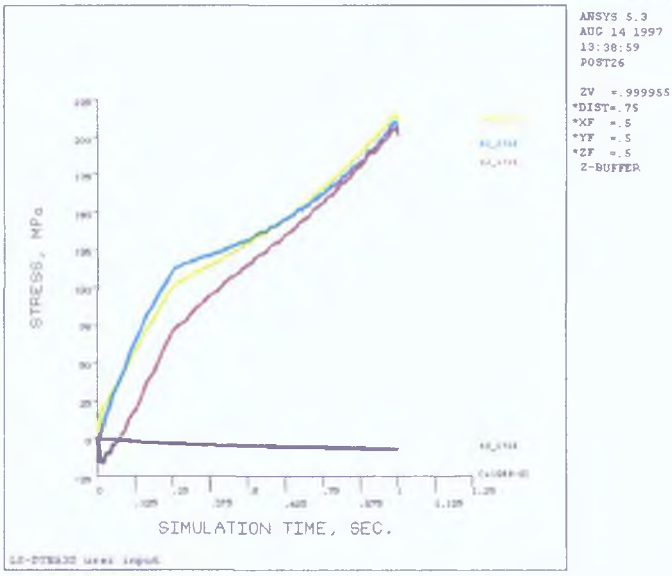

Figure 4.139: Development of stress in the top central node of the T-branch.

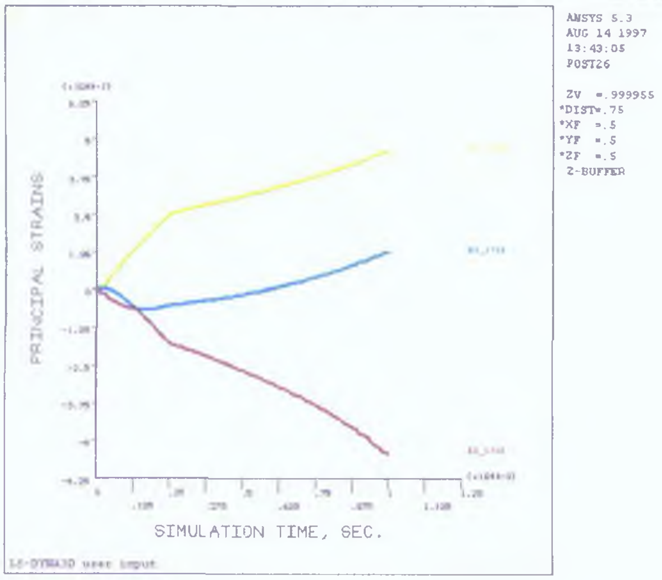

Figure 4.140: Development of strain in the top central node of the T-branch

Figures 4.139 and 4.140 respectively shows the development of principal stress and principal strains of a node at the top central point in the formed T-branch. Figure

4.139 also shows the equivalent stress in the node which has developed more or less steadily over the simulation period. The hoop stress was always tensile while the axial stress was compressive for a brief period and then switched to tensile state. Axial strain in the branch top was negative until about 0.005 seconds in the simulation and then turned positive maintaining an almost constant ratio with the hoop strain. Plotting the two principal strains in more popular form in Figure 4.141 it can be seen that the deformation at the top of the forming T-branch was continuing in the second quadrant with a gradient of almost -0.5 for a short period and then there was no straining in axial direction but strain in the hoop direction was growing. Eventually the deformation at the top ended up at the first quadrant with a gradient of almost 0.5. This means the T-branch top was elongating at a faster rate in the hoop direction than in the axial direction towards the end of the loading.

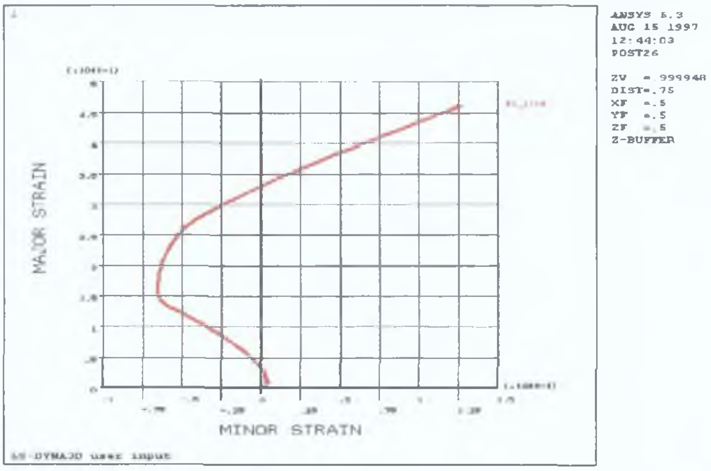

Figure 4.141: Strain path of the top central node of the T-branch.

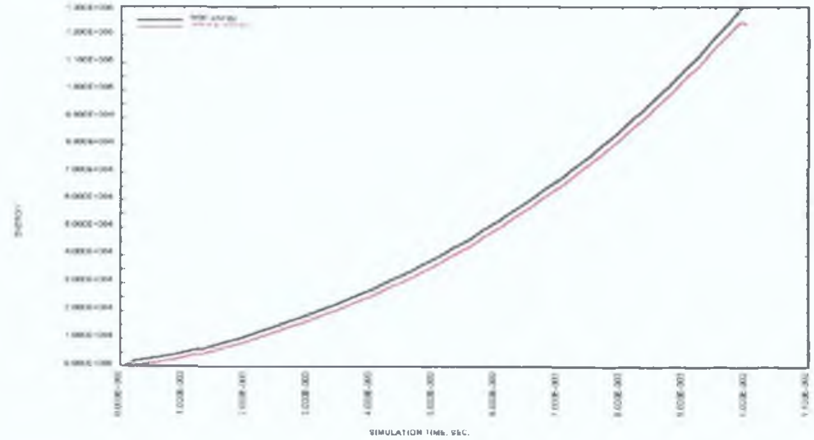

Figure 4.142: Development of internal and total energy of deformation.

The internal energy and the total energy in the deformation process shows a steady growth as shown in Figure 4.142. This implies a good and reliable simulation. Also the kinetic energy in the deformation was between 2 and 10% of the internal energy within 0.0010 seconds in the simulation time as can be seen in Figure 4.134 presented earlier. The kinetic energy was almost negligible after this initial period.

The second simulation in this series was done for a high friction condition but with the same loading pattern as in Figure 4.132. The friction factor was 0.3 for this simulation. Figure 4.143 shows the state of deformation of the tube at 0.0085 seconds in the simulation when deformation was at an acceptable stage in frictionless forming. It can be seen that the tube end has almost collapsed mainly because of hourglass mode of deformation there. Because of high friction the material could not move axially despite the pull from the bulging region and push from the end. The deformation was limited to the bulge where it was free to expand and at the end because of prescribed displacement.

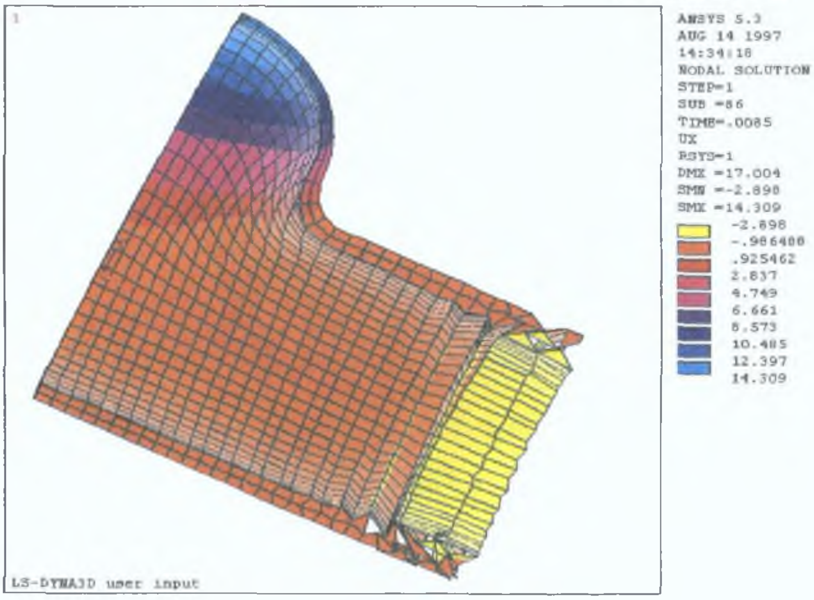

Figure 4.143: Deformed shape of the tube at 0.0085 seconds in the simulation.

Looking at Figure 4.144 which shows the development the hourglass energy and the kinetic energy as a ratio of internal energy it may be seen that the hourglass energy in the system started building up at around 0.007 seconds in the simulation. The deformation before that period is expected to be free of hourglass type of deformation . Figure 4.145 shows the deformed shape of the tube at 0.0065 seconds of simulation. The pressure and axial displacement applied up to that period was 23 MPa and 13 mm respectively; considerably lower than what could be applied in frictionless condition. Some hourglass mode of deformation is visible at the tube ends. The figure also illustrates the contour of radial displacement of the tube nodes. The maximum branch height obtained at this forming condition was about 11.8 mm; slightly more than half of that attained by frictionless condition.

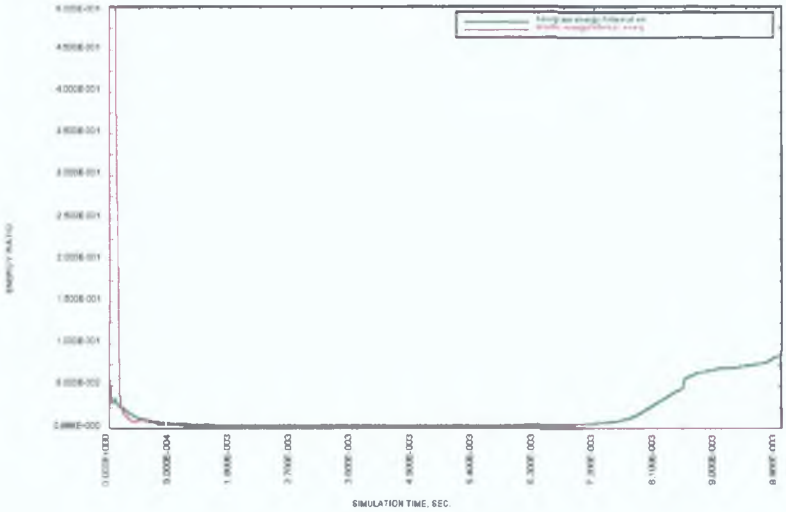

Figure 4.144: Ratio of hourglass and kinetic energy to internal energy during the simulation period.

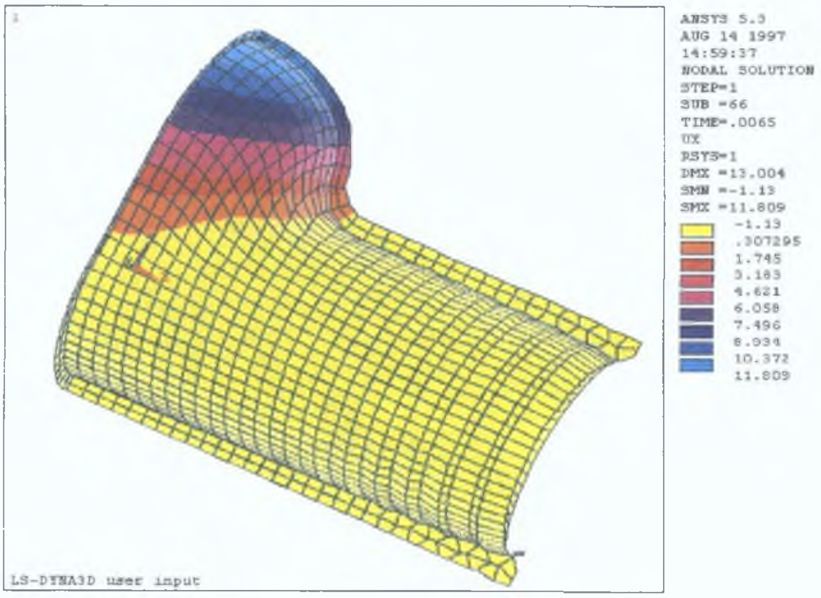

Figure 4.145: Deformed shape of the tube at 0.0065 seconds in the simulation.

Figure 4.146 shows the state of the equivalent stress in the deformed tube. Most stress has developed at the bulge region and at the tube end. The area in-between these two regions has stressed moderately. The magnitude of maximum stress developed in this simulation was about 191 MPa. In the bulging region the maximum stress has occurred at the T-branch top and at the region where the bulge base meets the main tube at the Z-symmetry of the model. The latter location is similar to what happened in frictionless forming but at a slightly upper location. Understandably the magnitude of the stress in this forming condition is less than that in frictionless forming due to lower level of loading and thereby deformation.

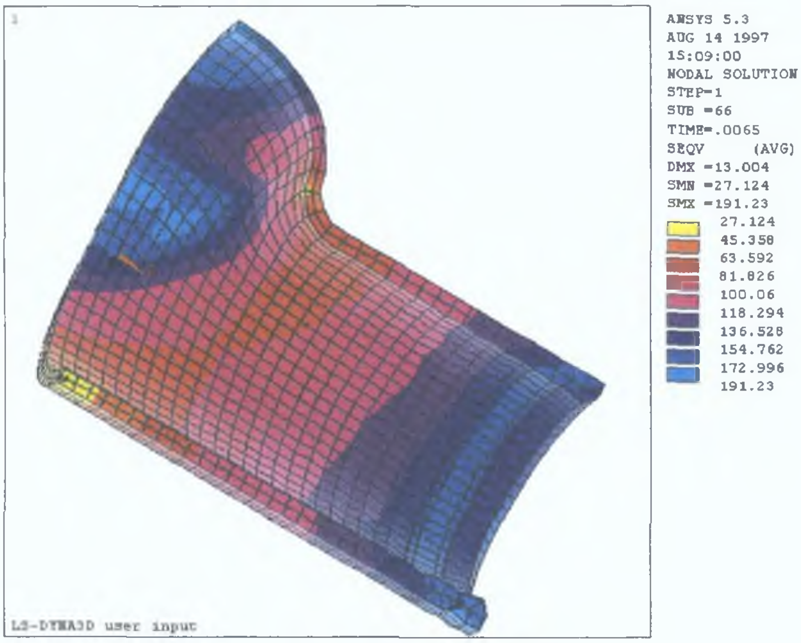

Figure 4.146: Distribution of von-Mises stress in the deformed tube.

Figure 4.147 shows the distribution of strain in thickness direction of the tube for this high friction forming. The location of maximum thinning is at the top surface of the formed T-branch as in the case of frictionless forming. The thickness at the top has reduced to about 65% of the original thickness; almost equal thinning as in frictionless condition. However, much less thinning was observed at the trunk and the base of the T-branch. The lower part of the tube under the T-branch have almost retained the original thickness of the tube. Thickness has gradually increased in the main branch towards the tube end in a zigzag pattern. This was due to varying degree of material movement at different circumferential position of the tube. Although the push at the end was equal, it seems that the pull due to the bulging has not affected the nodes equally because of friction. Figure 4.148 shows the total movement of the nodes in the tube. It can be seen, although not very clearly, that the nodes in the middle have moved less axially than the nodes at upper or lower locations to them in the figure. Also, the nodes with no or little movement occupy a bigger area at the lower left corner than that in frictionless condition.

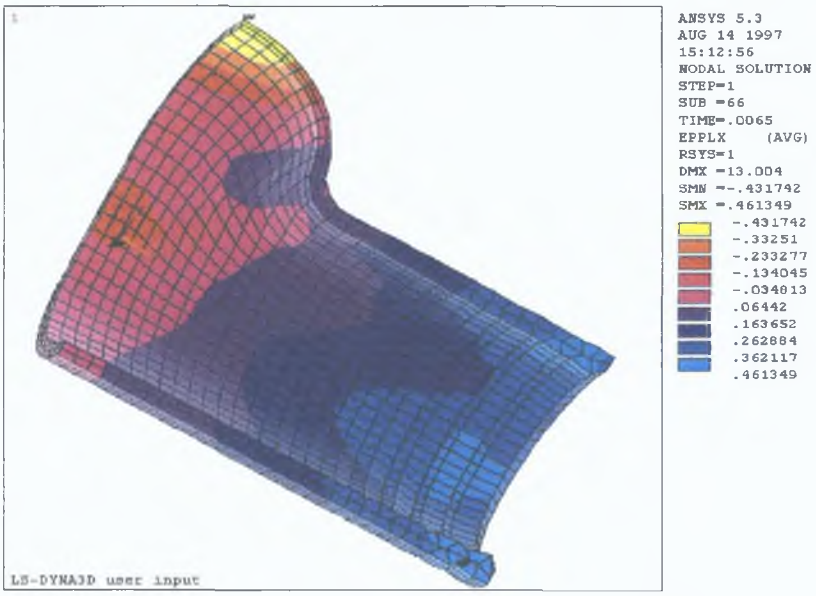

Figure 4.147: Distribution of strain in the thickness direction of the tube.

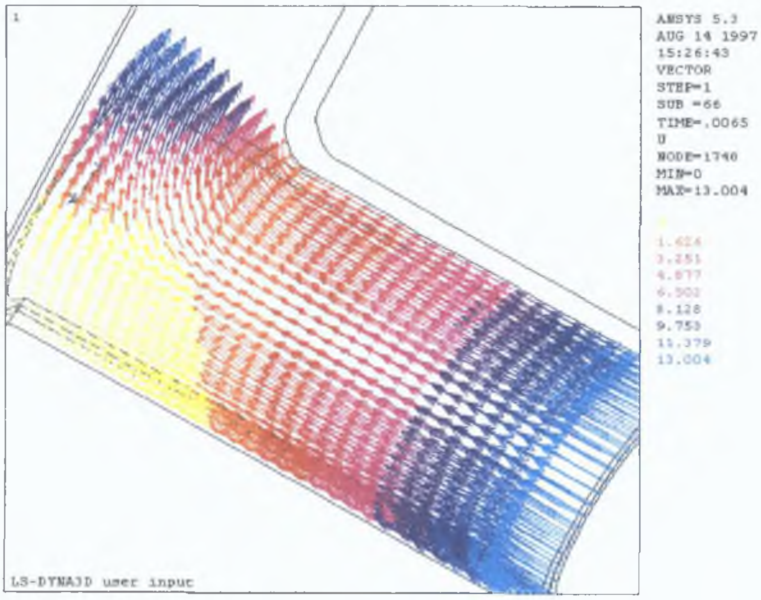

Figure 4.148: Absolute displacement of nodes in the tube.

Figure 4.149 shows the development history of equivalent stress and principal stress in a node at the centre of the top surface of the T-branch. Again the development was steady and smooth. The hoop stress was tensile all along and the axial stress was compressive for a very brief period at the beginning and then turned tensile. The ratio between these two stresses was always varying. Figure 4.150 shows the strain path in principal planes. It can be seen that the deformation was at the second quadrant for a very brief period at the beginning and then turned back to the first quadrant and then the gradient there indicates a faster growth in the tensile hoop strain than the axial strain.

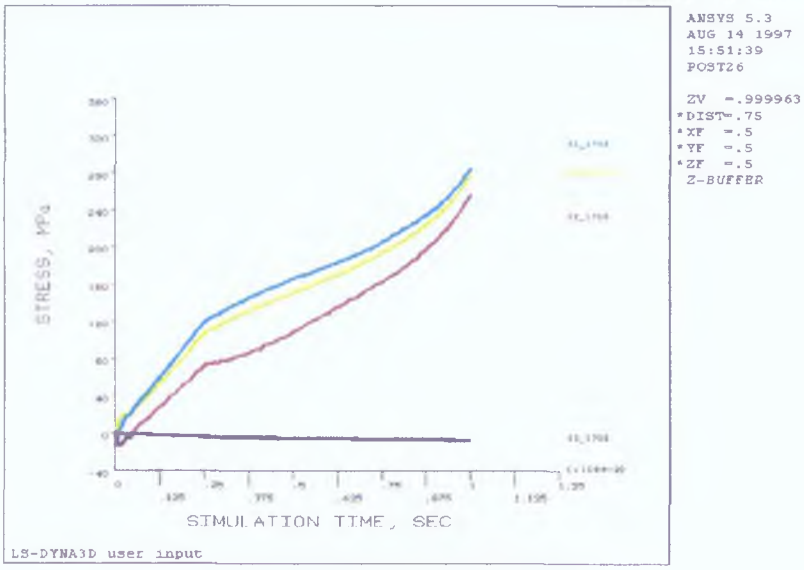

Figure 4.149: Development of stress in the top central node of the T-branch.

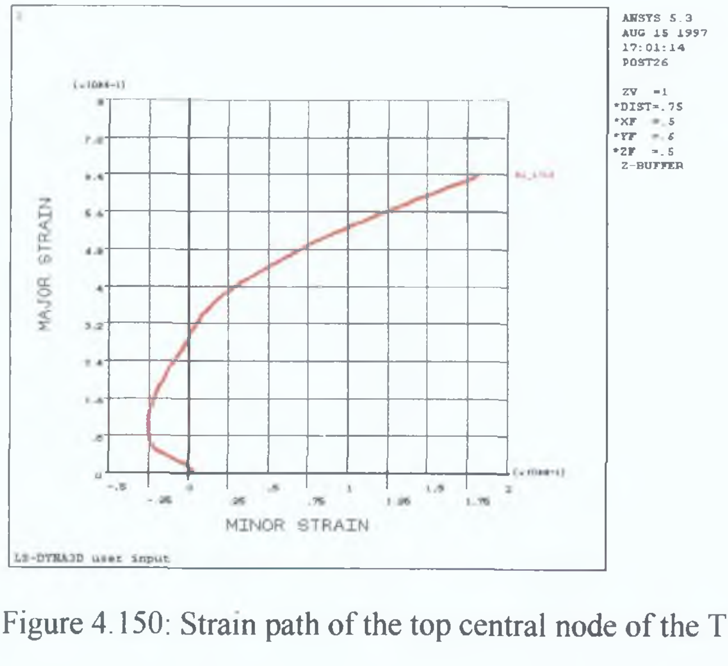

Figure 4.150: Strain path of the top central node of the T-branch.

The development of internal energy and total energy in the deformation is presented in Figure 4.151. The development was gradual until about 0.0085 seconds in the simulation. The kinetic energy was very negligible as can be seen as a ratio of internal energy in Figure 4.144 earlier.

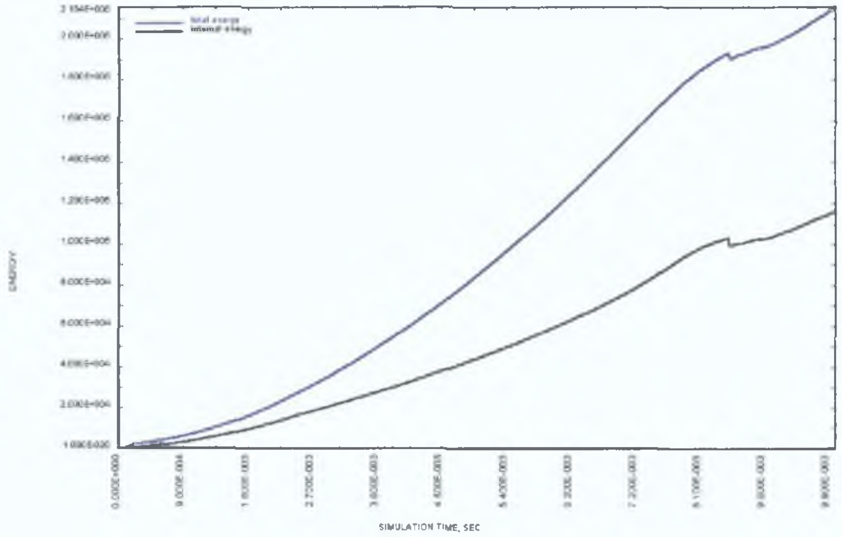

Figure 4.151: Development of internal and total energy of deformation over the simulation period.

One of the main reasons for different deformation behaviour in the second simulation was high friction. In practical application the friction may not be as high as this but at the same time a frictionless forming condition is next to impossible. Higher friction causes higher resistance to movement of material in the axial direction. The resisting frictional force is proportional to the normal force at the interface. High internal pressure at the inner surface of the tube results in high normal pressure at the die-tube interface. The third simulation in this series was done keeping the same high friction condition but reducing the internal pressure during the initial period of simulation and keeping the previous rate of pushing the tube end. The idea is to push more material towards the bulging zone at lower pressure-lower frictional resistance regime. Figure 4.152 shows the loading pattern for this simulation.

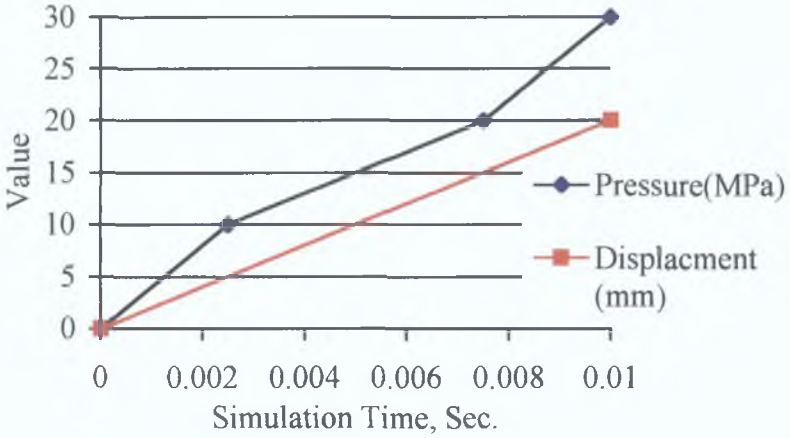

Figure 4.152: Loading pattern for the third simulation

This loading pattern could not continue the simulation any longer than the previous simulation. Hourglass deformation was prominent at the tube end after 0.0065 seconds in the simulation as in the previous simulation. The pressure and axial displacement load at this time was 18 MPa and 13 mm respectively. The T-branch height developed by this loading was about 10 mm; lower than that developed by the previous loading. The pattern of equivalent stress distribution and thickness strain in the deformed tube is pretty much the same as in the previous loading. Figures 4.153 and 4.154 show the von-Mises stress and thickness strain distribution of the deformed tube for this loading. Maximum thinning has occurred in the T-branch top and the thickness was reduced to about 76% of the original thickness.

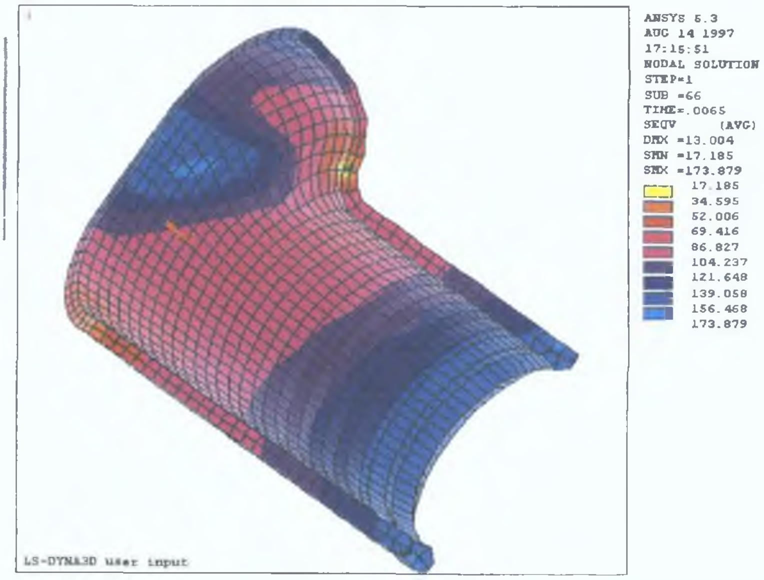

Figure 4.153: Distribution of von-Mises stress in the deformed tube.

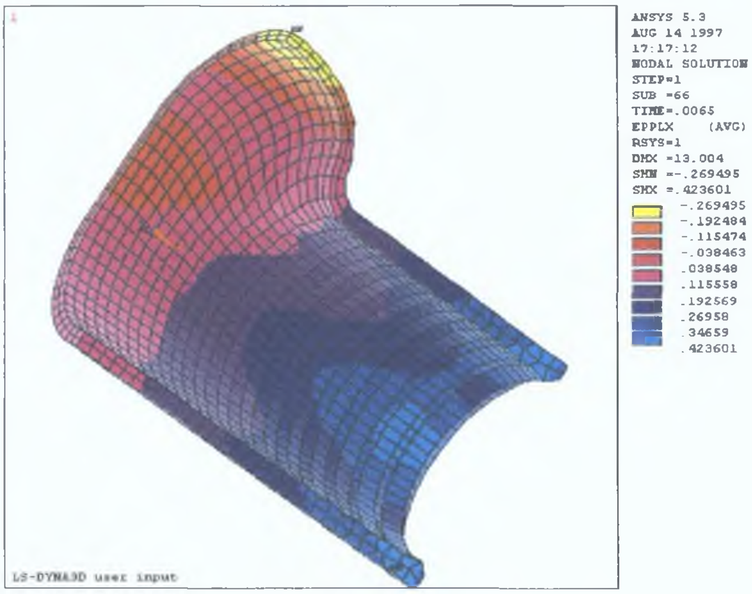

Figure 4.154: Distribution of thickness strain in the deformed tube.

The only visible difference due to the two loading pattern was observed in the strain path of the central node of the T-branch top surface. Figure 4.155 shows the strain path in principal strain plane for this loading. The deformation continued much longer in the second quadrant although most of it was growth of tensile hoop strain while axial strain was maintaining the same compressive state. The axial strain then turned tensile but the hoop strain was still dominating in terms of rate of increment.

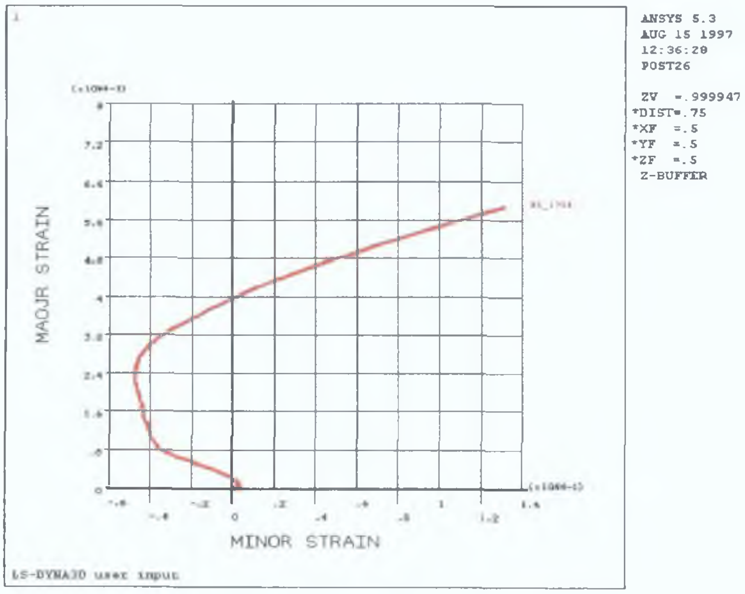

Figure 4.155: Strain path of the top central node of the T-branch.

The main idea behind the lower rate of pressure loading was to keep the interface frictional force low so that material can move axially But this seemed to have not happened as can be seen in Figure 4 156 where the total energy and the internal energy of deformation is shown over the simulation period The difference between the total and internal energy which largely comprises of interface sliding energy appears to be the same as for enhanced pressure loading in Figure 4 151 shown before

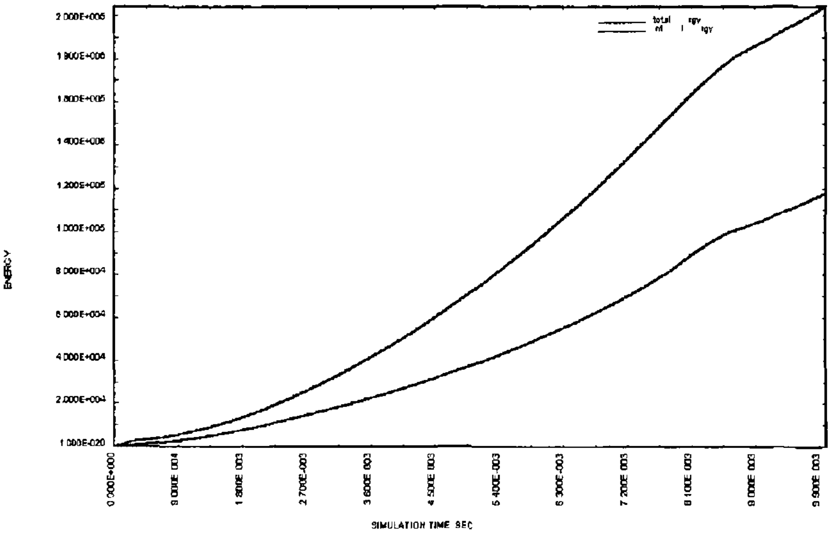

Figure 4 156 Development of internal and total energy of deformation

Table 4 23 Summary of the three simulations

Simulation	Loading pattern	Final acceptable load		T-branch height	Maxm eqv stress (MPa)		Thickness at the T-branch
		press (MPa)	disp (mm)	(mm)	value	location	(% of original)
I	enhanced press initially, uniform axial disp	27 0	17 0	20 64	272 79	middle region of the Z-symmetry	64 0
II	enhanced press initially, uniform axial disp	23 0	13 0	11 80	191 23	same as above plus T-branch top	65 0
III	lower press initially, uniform axial disp	18 0	13 0	10 04	173 88	same as II	76 0

Table 4 23 shows the summary of results of the three simulations of this section Clearly, the frictionless forming condition provides the best result out of these three conditions It is better to lower the friction than to try different loading keeping the friction high Low friction gives better stress and strain distribution in the deformed product The gradient of thickness of the main tube is also expected to be lower for low friction forming

4 4.3 LS-DYNA3D Simulation of T-branch Forming from Copper Tube

In the previous section the tube material was chosen arbitrarily Simulations in this series were done for copper tube The material parameters for the tube were taken from a compression test done by Hutchinson[104] for experimenting T-branch forming Three simulations were done The first two simulations had the same geometry and material but formed at different load The third one was done for a thinner tube but material remained the same

Modelling

The die and the tube solid model was the same as in the previous section for the first two simulations This time, however, the tube ends are put under a punch The punch was not modelled Instead, the nodes of the tube under the punch were restrained in radial and circumferential direction which would be equivalent to the punch in position This markedly reduced the model size Figure 4 157 shows the finite element model of the problem with boundary condition symbols The red arrow-heads at the right of the figure shows the length of the tube covered by the punch The length of the tube covered by the punch varied from model to model depending on the axial displacement value The model consisted of 765 die elements and 1800 tube elements

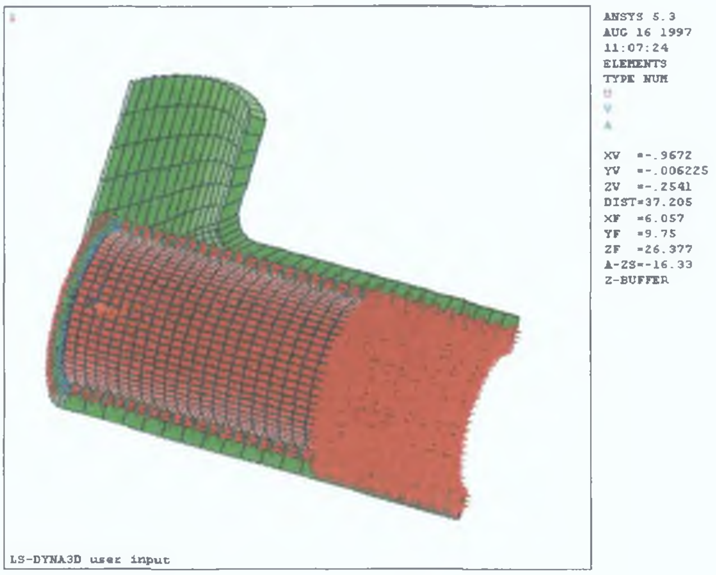

Figure 4.157: Finite element model for the first two simulations

The third simulation of forming a thinner tube was done by using a different model of the die. This model was developed from a solid model by AutoCAD R13C-4. Using an IGES translator which was available late in the project period, the model was transferred to ANSYS solid modeller. IGES stands for Initial Graphics Exchange Specification which is an ANSI standard that defines a neutral format for the exchange of information between dissimilar CAD and CAM system. The version of IGES used by AutoCAD R-13 C4 was 5.2.

In the translation from AutoCAD solid model to IGES format a total of 4 transformation matrices, 125 rational B-spline curves, 17 rational B-spline surfaces and 17 boundary entities were exchanged. The version of IGES translator in ANSYS pre-processor was 5.1. All the entities transferred from AutoCAD model are supported by the IGES translator in ANSYS. However, the solid model reconstructed by ANSYS pre-processor had many unwanted lines and surfaces which posed a problem for mapped meshing of the die volume. It was difficult to identify these entities. Therefore, all the surfaces were first deleted. Then the lines were checked one by one and the unnecessary lines were detected. Many duplicate lines and keypoints were found most of which were due to very small default tolerance (0.0001). All of them were merged within a tolerance of 0.005 mm. However, the basic outline of the model was satisfactory. After necessary cleaning operations some lines were added to the model and then areas and volumes were built in them. The model of the die consists of 6 volumes as shown in Figure 4.4.44. It may be seen in the figure that the blending region meets here at a line.

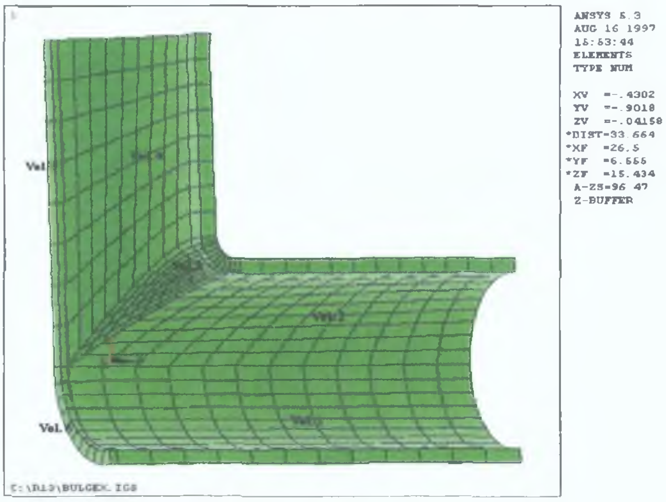

Figure 4.158: Discretised solid model of the die for the third simulation.

The die had to be extended little further in the axial direction to take care of contact problems referred earlier. Volumes 5 and 6 define this extra thin strip of material. The die also had to be extended at the diametrical faces which is visible from the complete die-tube finite element model in Figure 4.159. The die was discretised into 413 solid elements and tube into 800 solid elements. The die had one layer of elements while the tube had two layers.

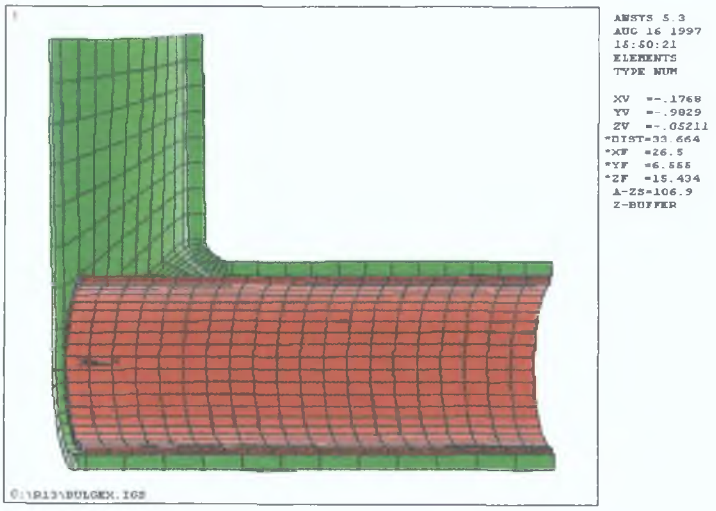

Figure 4.159: Discretised finite element model for the third simulation.

In all models automatic surface to surface contact elements were generated during the solution process by special search techniques described in theoretical chapter Elastic Coulomb friction law was assumed in all models with a friction factor of 0 15

The material properties of the tube were taken from Hutchinson[104] working on bulging of copper tubes as mentioned before The material data available there were generated by compression test Material parameter applied in these simulations were approximated from the available data The approximate data for a bi-linear material model were as below

Young's Modulus = $124X10^3$ MPa   Yield strength = 160 MPa

Tangent Modulus = 925 MPa   Poisson s ratio = 0 3

Density = $8\ 9X10^{-6}$ kg/mm^3

The die and tube dimension for the first two models were same as in the models in previous section In the third model, the tube thickness was changed to 1 03 mm from 1 37 mm in earlier models The tube diameter and the die size remained the same The die and the tube dimensions were actually chosen from Hutchinson's experimental studies[104] The die was considered as a rigid body The tube nodes at the symmetry edges were restrained in appropriate directions

Results and Discussion

The model for the first simulation was discretised with reduced integration point brick elements The loading values and patterns were adopted from Hutchinson s experiment [104] The loading pattern for the first simulation is shown in Figure 4 160

Figure 4 161 shows the deformed shape of the tube after the full load The displacement contour of the nodes in the radial direction is also illustrated in the figure The maximum height of the T-branch was 9 747 mm The top is almost flat In fact much of the branch was formed right at 0 0025 seconds in the simulation when full axial load was already on The branch height was 9 374 mm at that stage Figure 4 162 shows the deformed tube at that stage It may be seen that the T-branch is off the die wall at this stage Subsequent pressure load actually pushed back the branch to the die wall to some extent. The elements are reasonably well shaped. Slight hourglass type deformation is visible at the edge of the punched part.

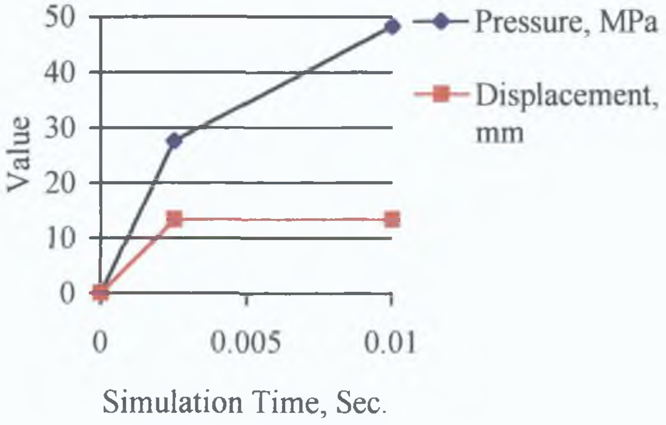

Figure 4.160: Loading pattern for the first simulation.

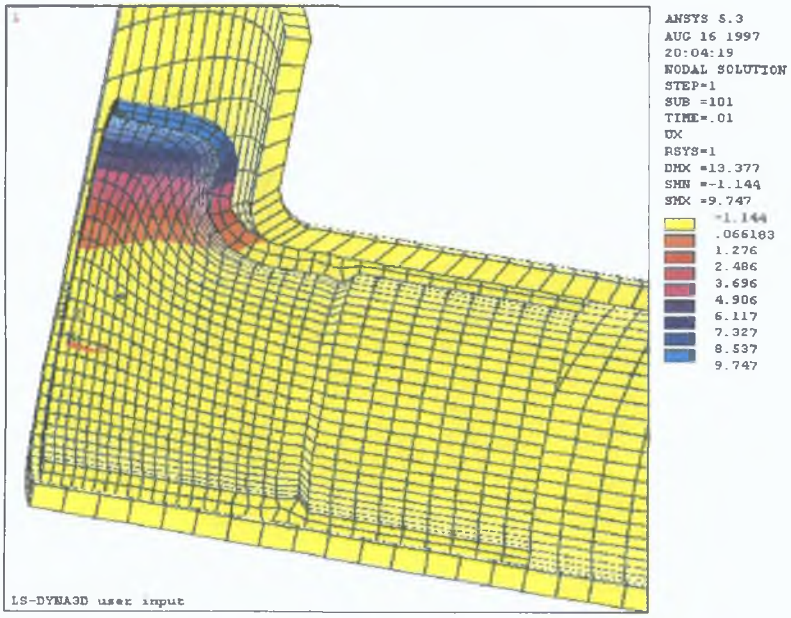

Figure 4.161: Deformed shape of the tube at full load by first simulation.

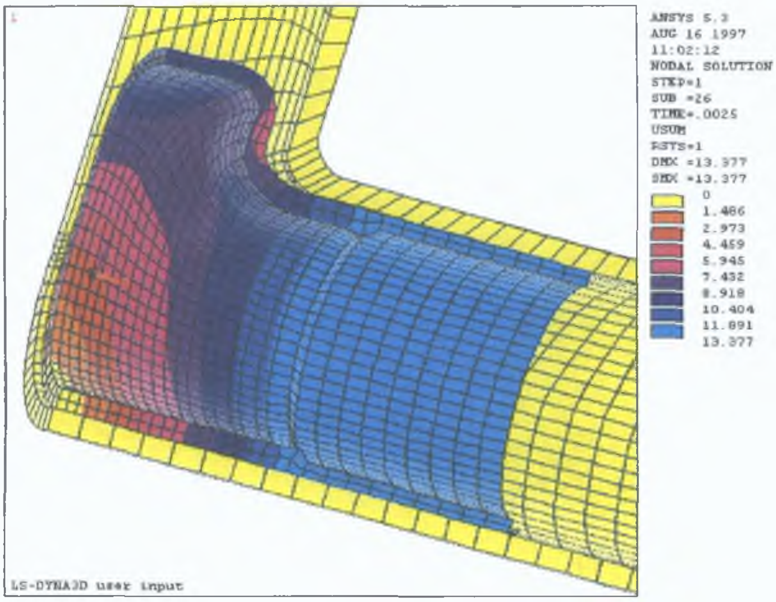

Figure 4.162: Deformed shape of the tube at 0.0025 seconds in the first simulation.

A check of the hourglass energy in Figure 4.163 shows very negligible hourglass energy; to the tune of about 0.8 percent of the internal energy. The kinetic energy of deformation was also negligible. The internal energy and the total energy of deformation developed mostly within the first quarter period of simulation time as shown in Figure 4.164. The energy development was smooth and was conforming to the loading pattern.

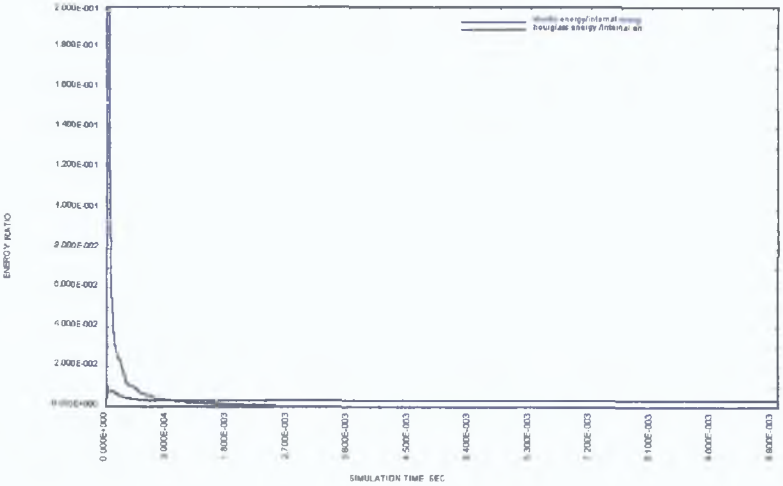

Figure 4.163: Ratio of hourglass energy and kinetic energy to internal energy in the first simulation.

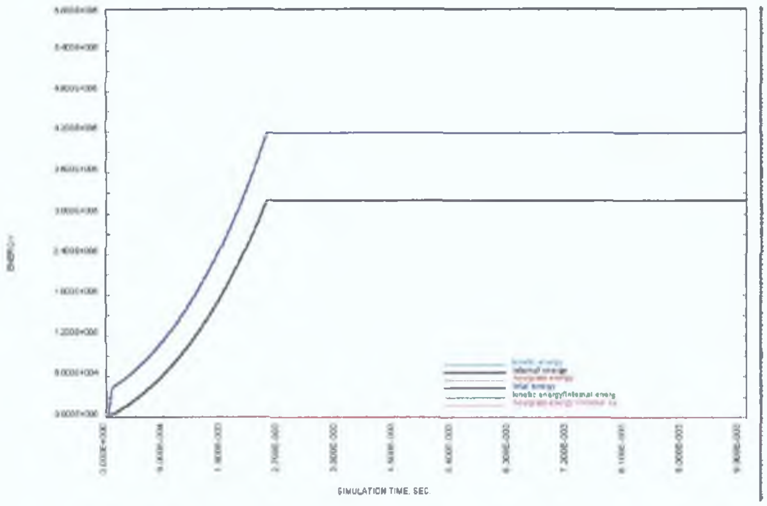

Figure 4.164: Development of internal and total energy of deformation over the first simulation period.

The equivalent stress in the tube after full load is shown in Figure 4.165. The T-branch is relatively less stressed compared to the main tube. The most stressed area is in the Z-symmetry region of the main tube. This pattern is also observed in similar earlier simulations. The maximum stress developed in the region is about 745 MPa. In comparison the T-branch has stressed at most half of that value.

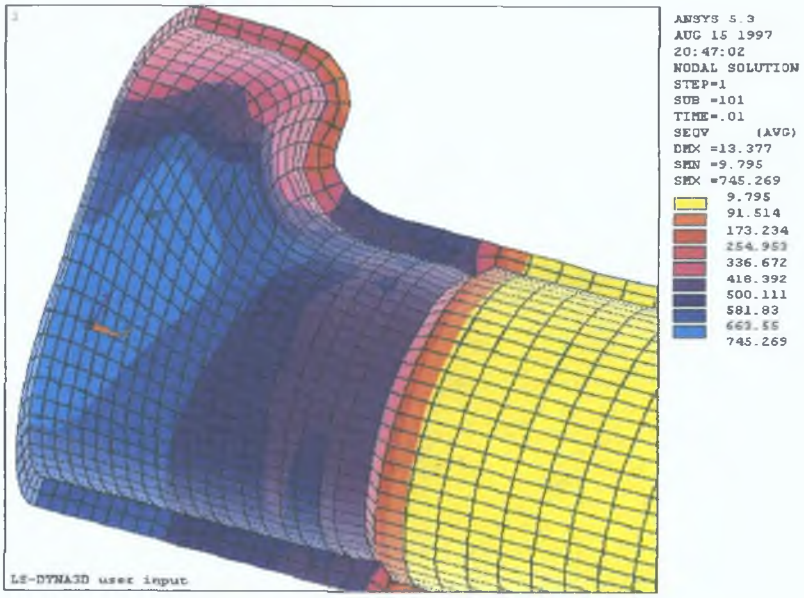

Figure 4.165: Distribution of von-Mises stress in the deformed tube by the first simulation.

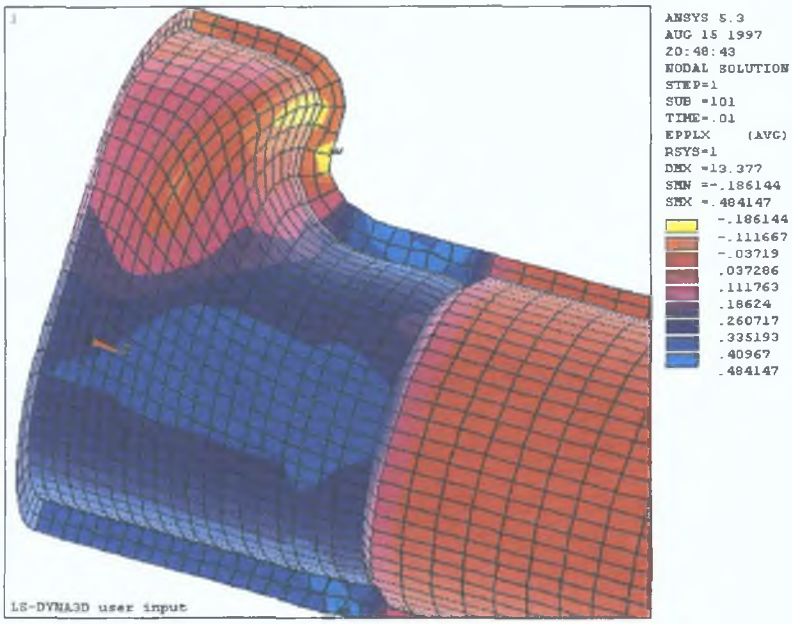

Figure 4.166: Distribution of thickness strain in the deformed tube by the first simulation.

At full load the branch has hardly thinned. Figure 4.166 shows the strain in the thickness direction of the tube. The minimum strain (negative) seen in the contour is surface contour as the contour is not visible across the thickness. Also the location of minimum strain is the location where the deformation is likely to be bending and translational. As such the strain shown here could be little inaccurate. The main tube has thickened quite a lot. The average thickening in the main tube was about 150% of the original thickness. There is variation of thickening along the circumferential length of the tube. This was due to the difference in material movement. Materials at different circumferential position has moved differently towards the bulging region. Similar phenomenon was also observed in earlier simulations. Figure 4.167 shows the absolute movement of the nodes in the tube. The above mentioned difference in movement is somewhat evident from the figure. But since the figure depicts a cylindrical surface in two dimensions, much of the detail is blurred as stated earlier.

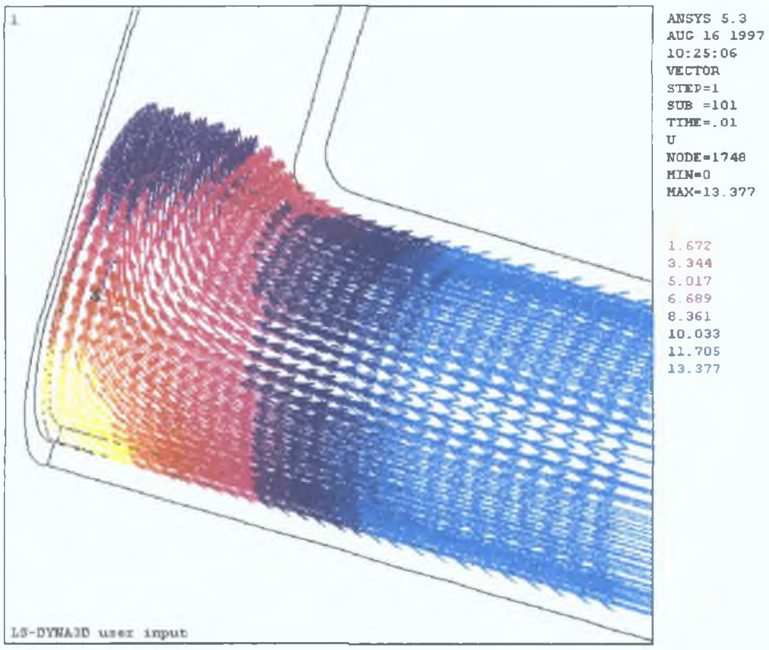

Figure 4.167: Absolute displacement of tube nodes by the first simulation.

Figure 4.168 shows the development of equivalent stress and principal stress in the central node of the T-branch top surface. The stress development was erratic indicating a stick-slip type of deformation at the main tube. Although all of axial displacement was provided within the first quarter of deformation period, it seems the tube surface beyond the punch was sticking and slipping with the die due to pressure in the bulge. The ratio of the hoop stress and the axial stress was naturally very variable.

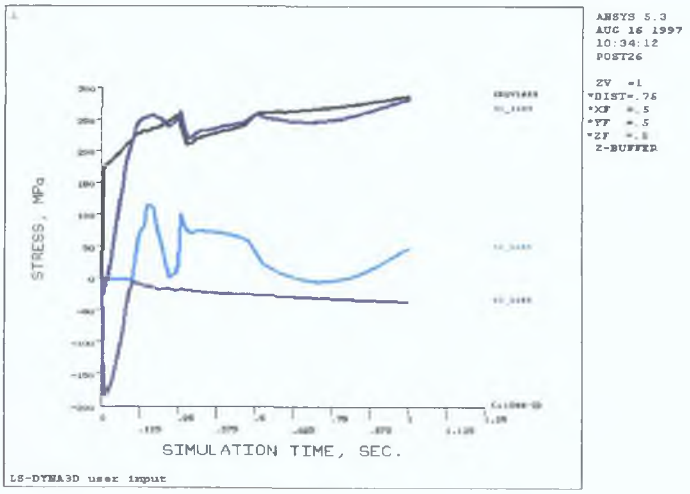

Figure 4.168: Development of stress in the top central node of the T-branch over the first simulation.

The principal strains in the central node of the T-branch top surface is shown in Figure 4 169 It can be seen from the figure that although the bulge started in biaxial tensile state the compressive axial load soon changed the state by pushing the state of deformation to the second quadrant The compression remained there in the bulge even at the end of the simulation period it seems that the hoop tension is dominant and further loading in the same manner would rupture the branch in axial direction of the tube This mode of rupture was evident in experiments [104]

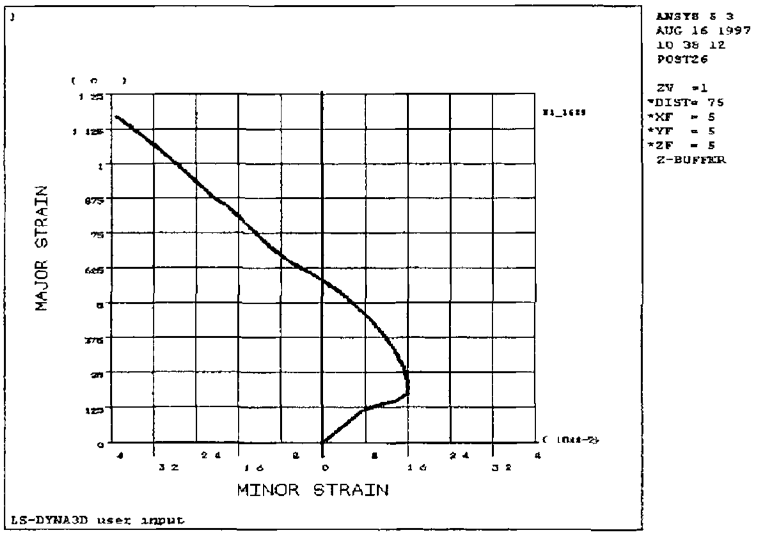

Figure 4 169 Strain path of the top central node of the T-branch by the first simulation

Hutchinson in his experiment[104] measured the thickness at different heights of the T-branch The thickness was measured along the plane of axial symmetry of tube exactly the symmetry plane of the FE model His experimental findings along with findings from the simulation is presented in Figure 4 170 The simulation results are from the average of thickness strains of three nodes across the tube thickness It can be seen from the figure that T-branch height obtained by simulation is nearly the same as that from experiment The thickness at the root of the T-branch and at the top area are very close Some difference is observed at the trunk part of the branch Thickness at this part obtained by simulation is lower than that from the experiment It was already pointed out that the simulation at this particular location is not truly representative due to the use of solid elements where some bending deformation actually takes place However, at the same time, it may be mentioned here that the die bend at that location has the smallest radius and gradually changes to higher radius along the circumference thereby keeping the bending mode of deformation to a very small area.

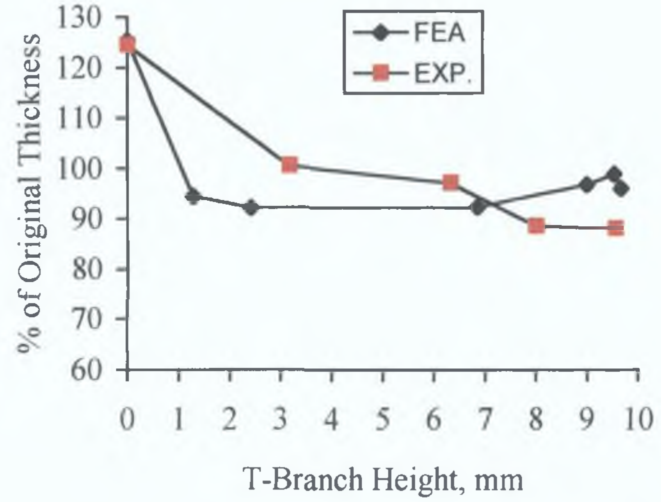

Figure 4.170: Comparison of simulation results with experimental results of Hutchinson [104].

The second simulation was done on the same finite element model but for a different load condition. Figure 4.171 shows the loads and their pattern of application. Both the pressure and the axial compressive load are high. This time the axial load is applied at a slower rate. The punch length was reduced to accommodate more axial load in this simulation.

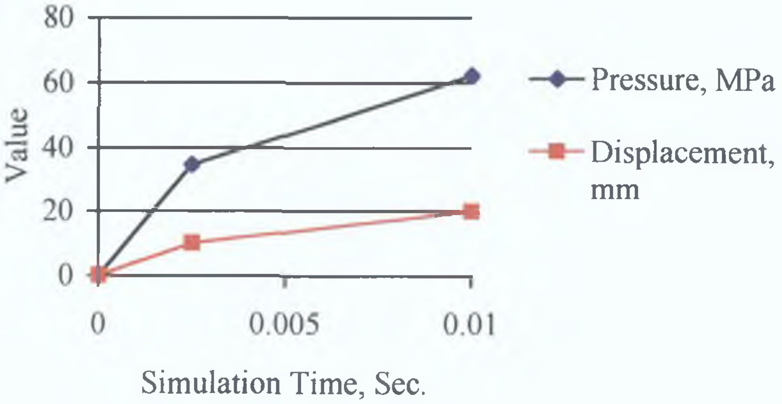

Figure 4.171: Loading pattern for the second simulation.

Initially the simulation was tried with brick elements with reduced integration point. But severe hourglass deformation is observed at full load deformation. Figure

4.172 shows the deformed state of the tube. The hourglass energy was also high. The deformed state of the elements at the edges does not suggest any strong shear stress due to frictional resistance. This was also checked by looking at the shear stress distribution at the circumferential plane. Few other options were tried but were of no good. So, the tube element properties were changed to fully integrated brick elements although they would be much stiffer in deformation.

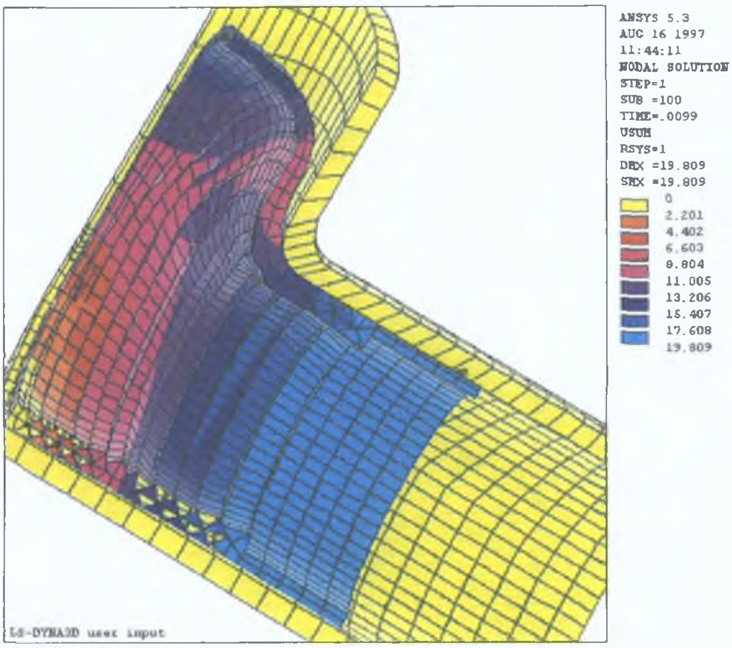

Figure 4.172. Deformed shape of the tube in the second simulation by reduced integration elements.

Figure 4.173 shows the deformed tube at full load with fully integrated element properties. The elements at the deformed state are well shaped. The radial displacement of the nodes are also contoured in the figure. The maximum height of the T-branch was 14.71 mm. The branch top is almost flat.

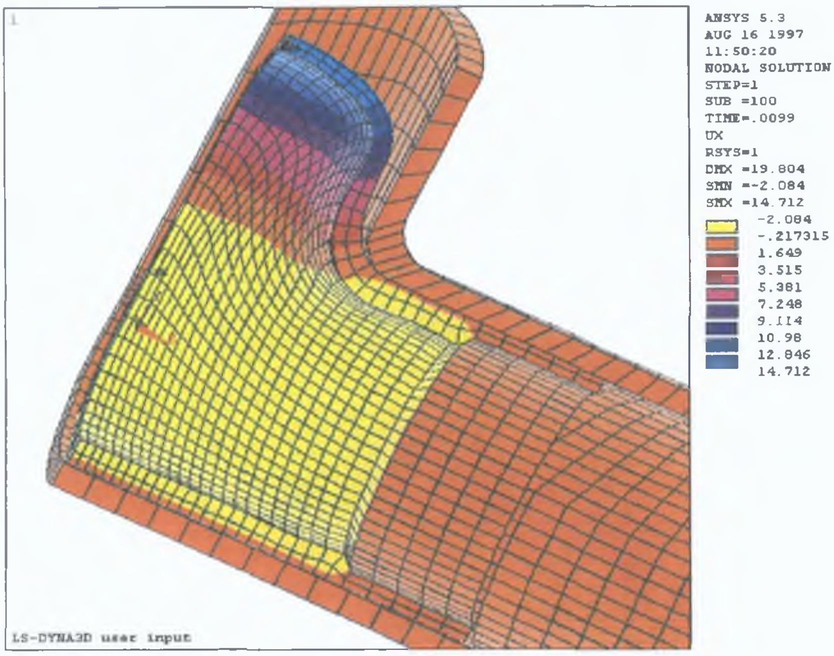

Figure 4.173: Deformed shape of the tube in the second simulation.

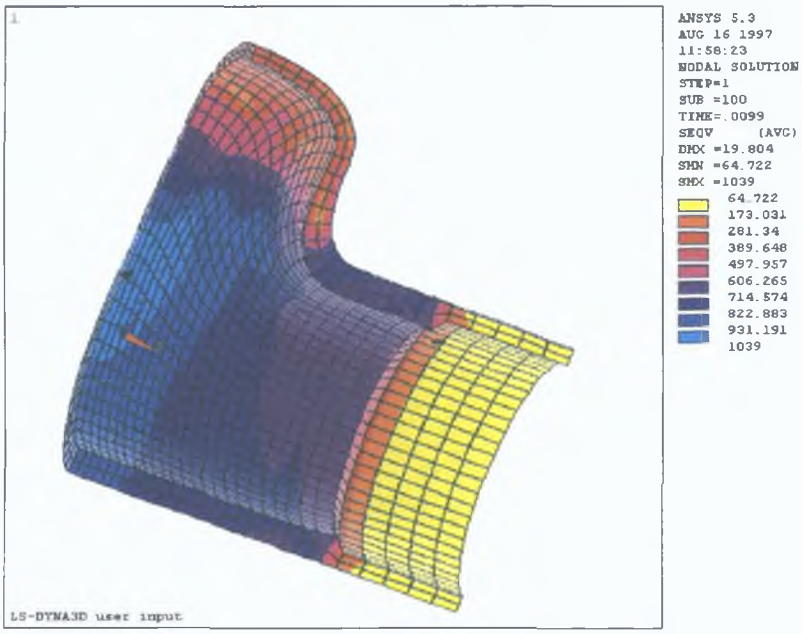

Figure 4.174: Distribution of von-Mises stress in the deformed tube by the second simulation.

The equivalent stress in the deformed tube is illustrated in Figure 4.174. Most of the main tube except the position under the punch has stressed considerably. The distribution is relatively uniform. The maximum stress was 1039 MPa. The T-branch proper has stressed less than half of that in the main tube.

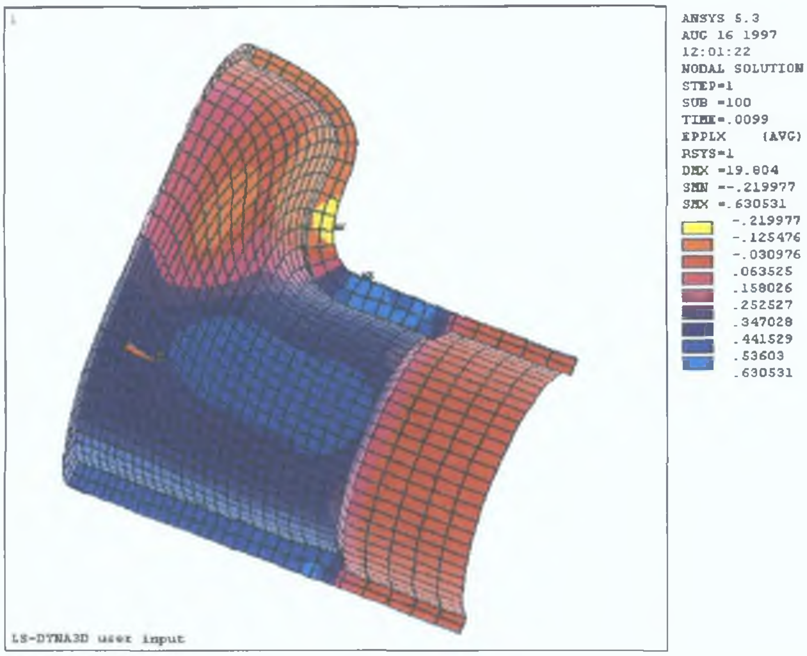

Figure 4.175: Distribution of thickness strain in the deformed tube by the second simulation.

The main tube has thickened considerably as shown in Figure 4.175. The range of thickening in the main tube except the portion under the punch was 141% to 188% of the original thickness. There was some variation of thickness at different circumferential position of the main tube as was observed earlier. The T-branch has slightly thinned at the top. The trunk area near the Z-symmetry has more or less maintained the original thickness while it has thinned near the die bend area. The thinning at this location is misleading because elements at this area has undergone large rotation deformation which is not well simulated by solid elements. The top has thinned at most to 88% of the original thickness. Figure 4.176 shows the thickness at different heights of the T-branch by the simulation and from experiment by Hutchinson[104]. The branch height obtained by the simulation was about 14.7 mm while that found in the experiment was about 18.0 mm. This suggests that there is less deformation in the simulation. The stiffer behaviour of the fully integrated brick elements could be one of the reason for less deformation. This less deformation has also affected the thickness at the branch top. However, the thickness at the root matches quite well with the experimental finding.

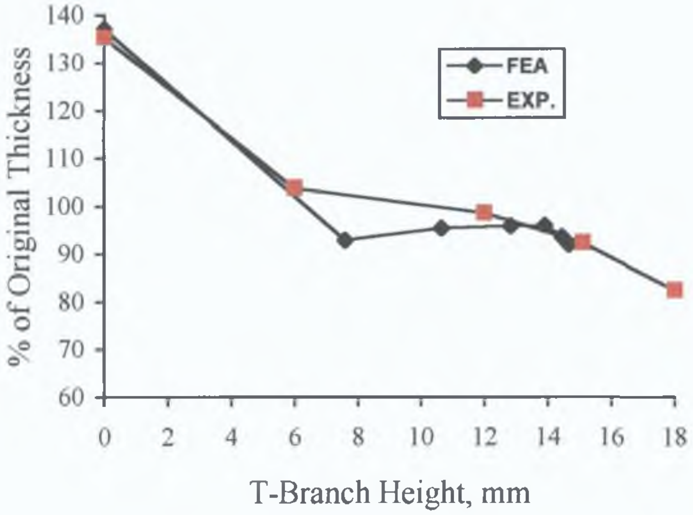

Figure 4.176: Comparison of simulated result with experimental result from Hutchinson[104].

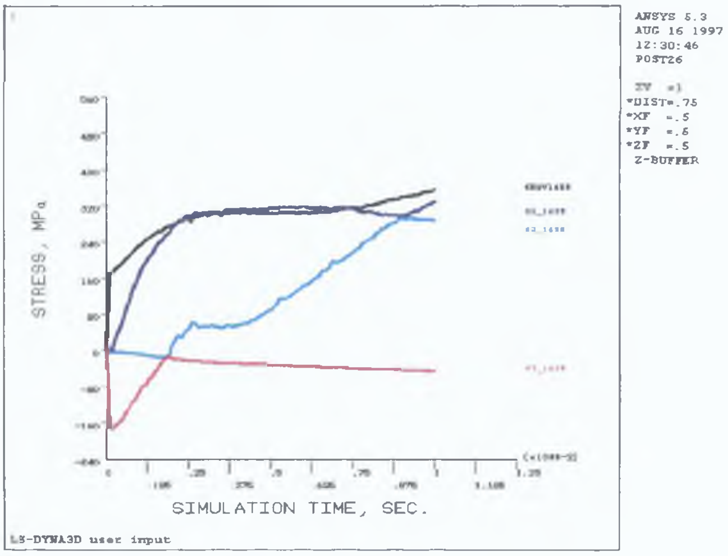

Figure 4.177: Development of stresses at the top central node of the T-branch.

The development of equivalent stress and principal stresses in the central node of the T-branch top shown in Figure 4.177 indicates a more or less smooth growth unlike the previous simulation. This was probably due to the slower rate of axial compressive load. Stick-slip phenomenon is there but not as prominent as was for the case in the previous simulation. The ratio of the hoop stress to axial stress was always variable throughout the simulation.

The strain path plot of the same central node of the T-branch top shown in Figure 4.178 indicates a brief biaxial tension followed by tension in hoop direction and compression in the axial direction. This continued in the T-branch top until the end of simulation. The slope there at the end suggests that the elements there are elongating faster in the hoop direction than they are compressing in axial direction. If the loading is continued in the similar manner the T-branch would rupture in axial direction of the tube. As mentioned, in practical tests this kind of rupture was observed [104].

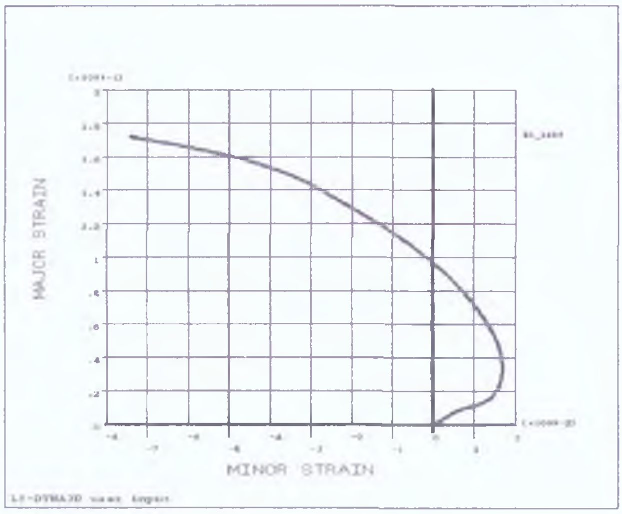

Figure 4.178: Strain path of the top central node of the T-branch.

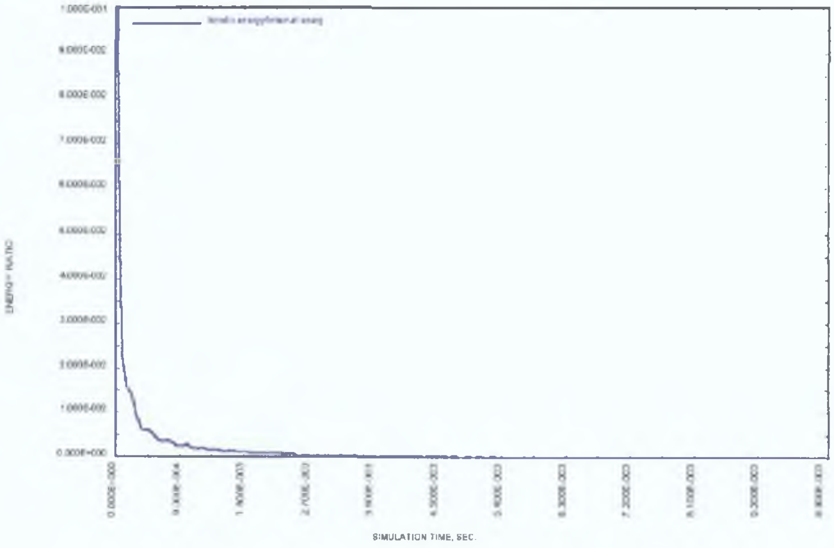

Figure 4.179: Ratio of kinetic energy to internal energy in the simulation.

The kinetic energy of deformation was very low at the initial period. It was about 0.5% of the internal energy initially up to 0.0009 seconds of the simulation and then decreased even further as seen in Figure 4.179. The development of internal energy and total energy of deformation was smooth and was conforming to the pattern of loading as presented in Figure 4.180.

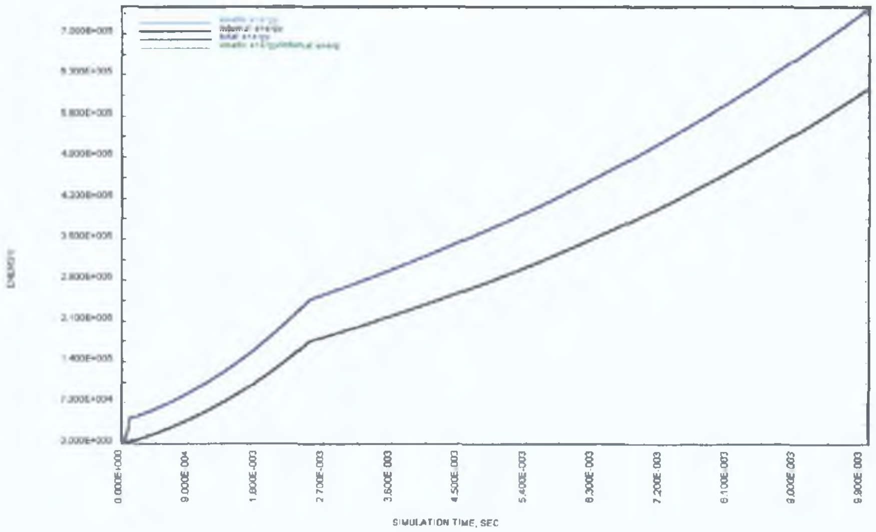

Figure 4.180: Development of internal and total energy of deformation in the simulation.

The third simulation in this series was done for the forming of a thinner tube of 1.03 mm thickness. The load values and their pattern of application is shown in Figure 4.181. The brick elements discretising the tube had fully integrated properties in this simulation. The die elements had reduced integration properties.

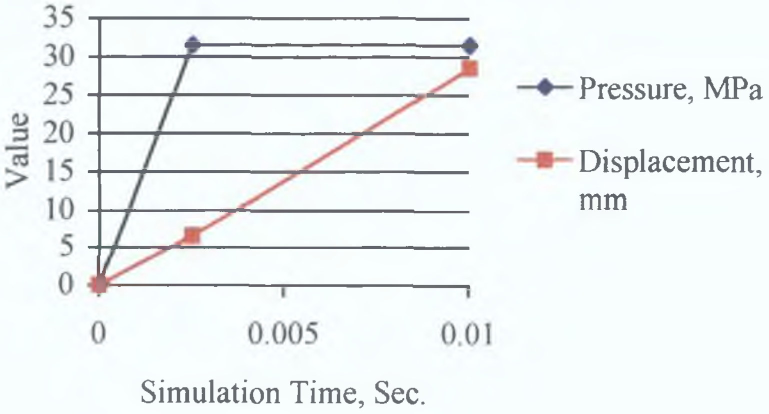

Figure 4.181: Loading pattern for the third simulation.

The deformed shape of the tube at full load is shown in Figure 4.182. The elements were in well shape. The T-branch top had taken a torospherical shape. The branch trunk this time has conformed more to the die bend. The maximum height attained was 21.987 mm.

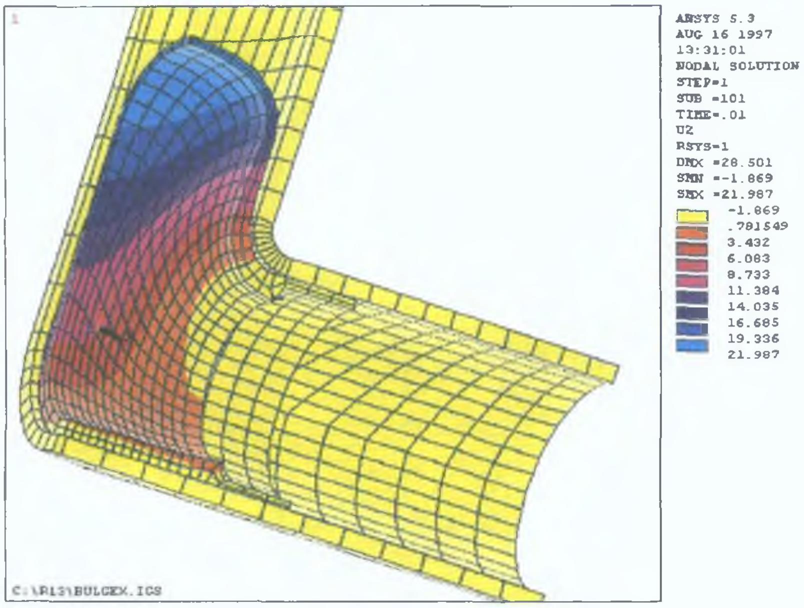

Figure 4.182: Deformed shape of the tube at full load.

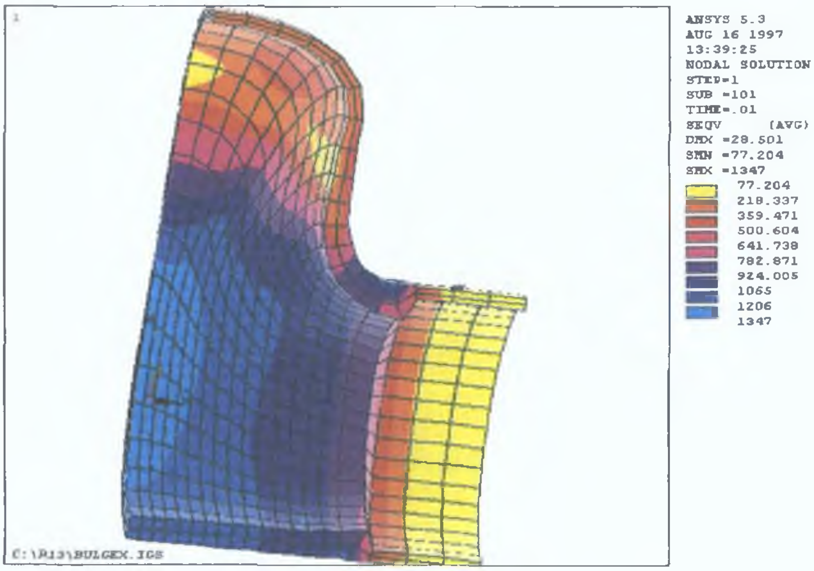

Figure 4.183: Distribution of von-Mises stress in the deformed tube.

The main tube under the T-branch has stressed most as can be seen from Figure 4.183. The maximum stress was about 1347 MPa located around the Z-symmetry edge. In comparison the T-branch has stressed much less; less than half of the stress in the main tube. Stress differential in the T-branch is considerably steep. But stress in the main tube is relatively uniform.

The main tube directly under the T-branch and near the die bend has thickened to about 198% to 270% of the original thickness as indicated by Figure 4.184 illustrating the strain in the thickness direction of the tube. The side wall of the main tube near the punch edge did not thicken significantly. Much material has been drawn into the bulge region due to higher pressure load relative to tube thickness. The T-branch top has also thinned down to 80% of the original thickness. Again the high negative strain at the bend is not a proper representation. As reasoned earlier the elements at this area has undergone rotational deformation which was counted as displacement thereby increasing the compressive strain.

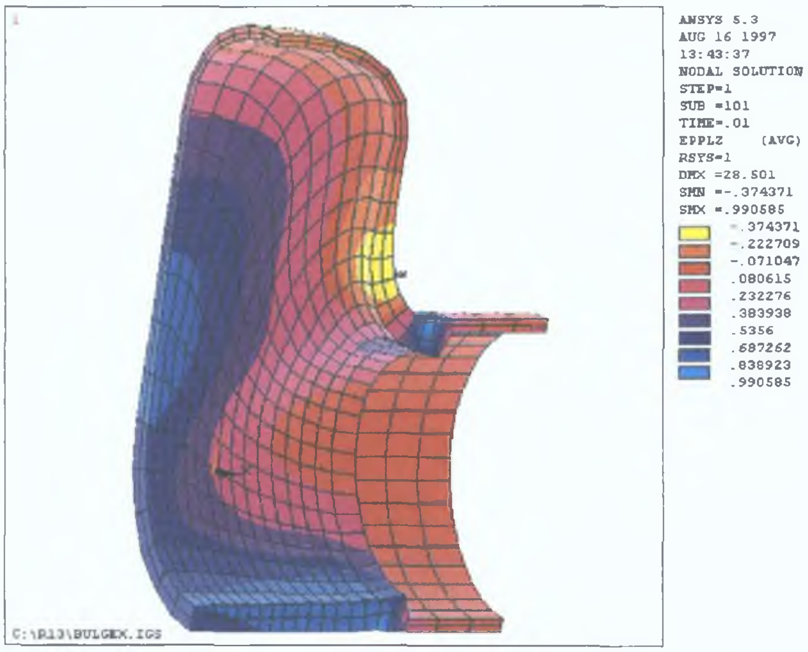

Figure 4.184: Distribution of thickness strain in the deformed tube.

The development of equivalent stress and principal stresses in the central node of the T-branch top shown in Figure 4.185 indicates stick slip behaviour of deformation. The full pressure applied within the first quarter of the simulation time has increased the stress and subsequent axial compressive load has eased the tension in the bulge. The strain path followed by the node is shown in Figure 4.186. The compression from the tube end is still acting but the hoop strain is also developing. The elements at the branch top are elongating in the hoop direction and compressing in the axial direction. The rate of elongation is higher than the rate of compression. In the case of further loading the branch top is expected to rupture in the axial direction of the tube which is the usual experience from practice.

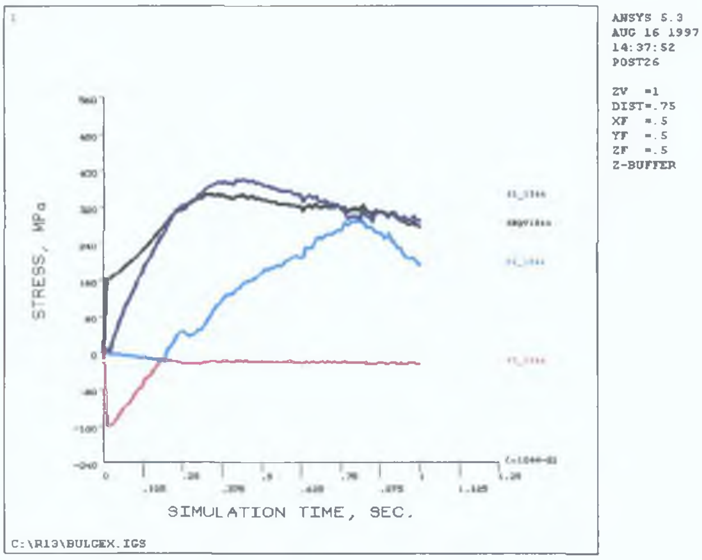

Figure 4.185: Development of stresses in the top central node of the T-branch over the simulation period.

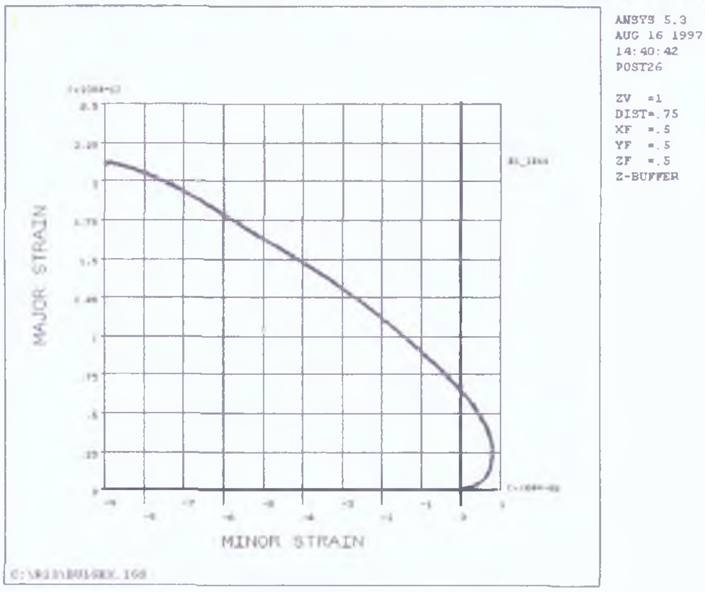

Figure 4.186: Strain path of the top central node of the T-branch.

The kinetic energy of deformation was very low; about 0.3% of the internal energy at the initial period and eventually became negligible as can be seen from Figure 4.187. Figure 4.180 shows the development of internal and total energy of deformation. This shows a smooth gain in energy.

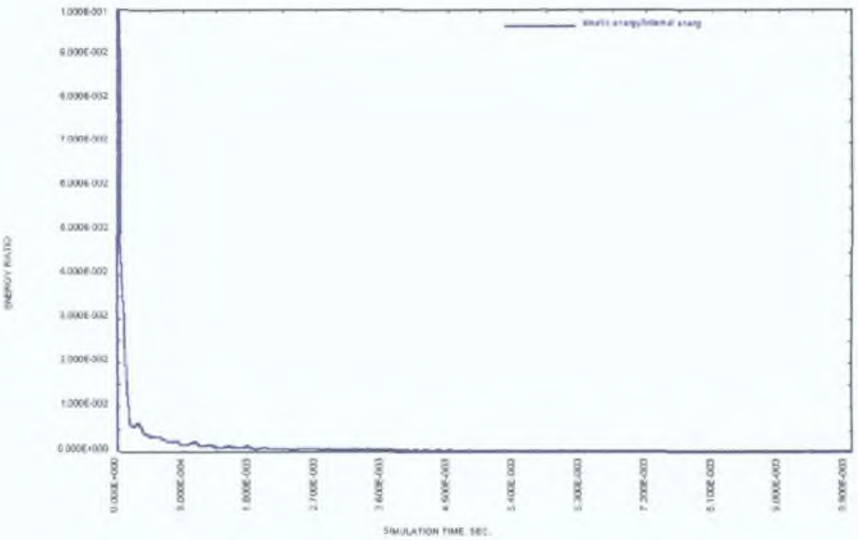

Figure 4.187: Ratio of kinetic energy to internal energy of deformation.

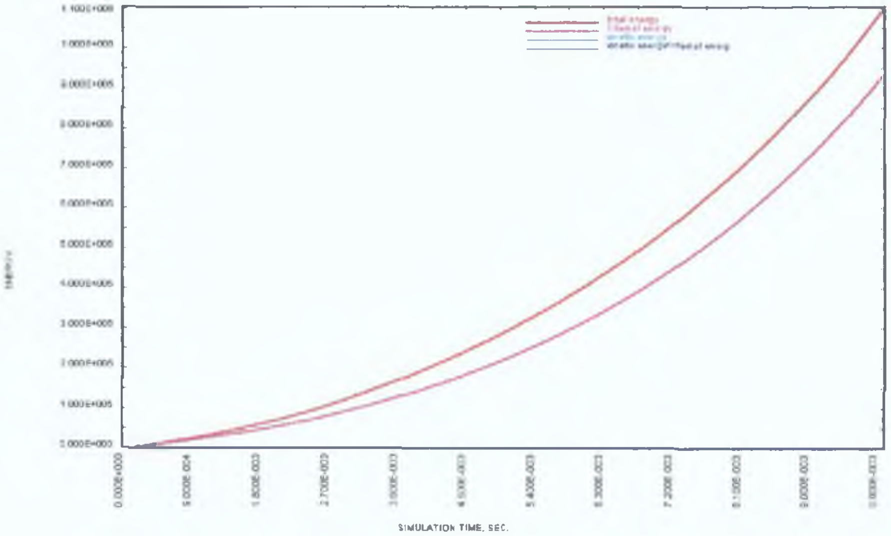

Figure 4.188: Development of internal and total energy of deformation in the third simulation.

Figure 4.189 shows the T-branch thickness against height as found in simulation and in experiment by Hutchinson[104]. The height obtained in the simulation is slightly higher than that obtained by experiment. On average the simulated T-branch has higher thickness than that in the experimental one.

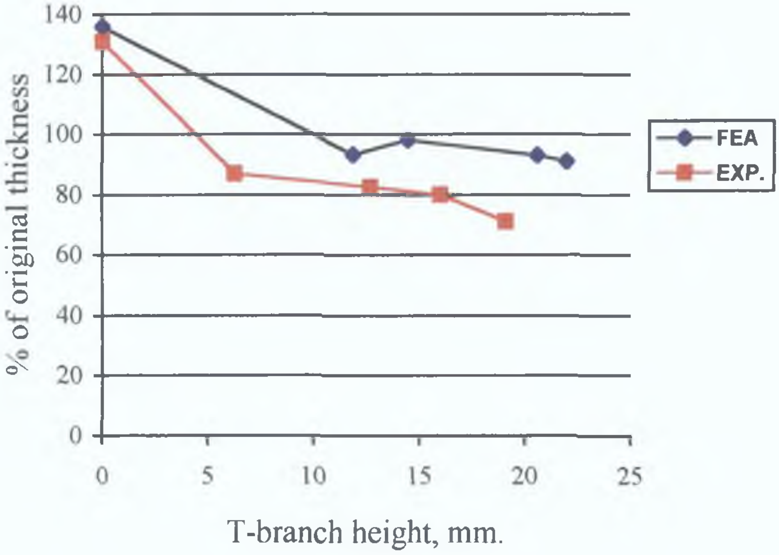

Figure 4.189: Comparison of simulation result with the experimental results of Hutchinson [104].

4.4.4 Simulation of Failure in T-branch Forming

In the simulation of T-branch forming it was observed that the relative pattern of the pressure load and axial compressive load has great influence on the formability of a good T-branch. A critical balance of these loading is essential for a stable process. Prominence of any one type of loading would lead to failure of the process. Two modes of failure are rupture and buckling. Rupture occurs when the pressure load is high compared to the axial compressive load. Buckling on the other hand, develops when the axial compressive load is dominant over the pressure loading.

In this series two simulations were done for a tube of particular material and thickness basically to find the situation at which these failure occurs. A third simulation was done applying a loading pattern determined from the experience of the simulation of the two failure modes.

Modelling

The simulation in this series were done using LS DYNA3D package as before. But the finite element model was developed in a different pre and post processor. Half of the component was modelled. The die was built using the same technique as described in section 4.4.1. A CAD solid model was developed, and from that model the points on the line defining the blending region between the die proper and the die recess were extracted. The co-ordinates of these points were used in this pre-processor to develop the die surface.

The tube diameter was 24.12 mm and the length was 107 mm. The thickness of the tube was 1.37 mm. The tube was modelled in one surface. Figure 4.190 shows half of the discretised die and tube. Both the die and the tube was modelled with shell element. Belytschko-Wang-Chiang[105, 106] model of the shell element was assumed. Five integration points across the thickness of the tube was assumed. For die elements the number of integration points were three. A total of 3000 elements describe the whole model out of which 1200 elements are for the tube. The tube ends were restrained to simulate the effect of a punch over the ends.

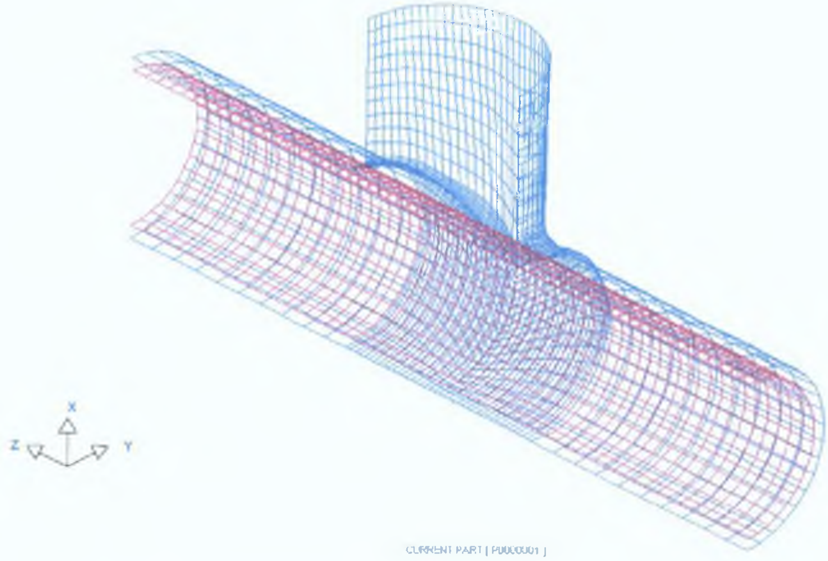

Figure 4.190: Finite element model of the failure simulation of T-branch forming.

A piecewise linear plastic material model was assumed for the tube. Different properties of the material are;

Young's Modulus = 3.66X10^3 MPa   Yield stress = 18.3 MPa

Density = 8.9 X10^{-9} tonne/mm^3 Poisson's ratio = 0.3

Strain	Stress(MPa)
0.005	18.3
0.50	220.0
2.0	465.0

A failure strain of 1.0 was input in the material model which implies that when the logarithmic plastic strain in an element reaches that strain value then that element is assumed to have failed. The die was modelled with elastic materials and was given rigid body constraints.

A surface to surface contact algorithm was employed. The algorithm takes care of the shell thickness of both the die and the tube. It may be noted here that the die and the tube surfaces developed in the model represent their mid-surfaces. The thickness values supplied in the shell element property take care of the thickness of the actual bodies.

Results and Discussion

The first simulation was done with a loading pattern shown in Figure 4.191. A pressure load of 30 MPa was applied at the inner surface of the tube and the axial displacement of 29 mm was applied at both tube ends. The axial displacement was intentionally enhanced to permit creation of a buckling situation.

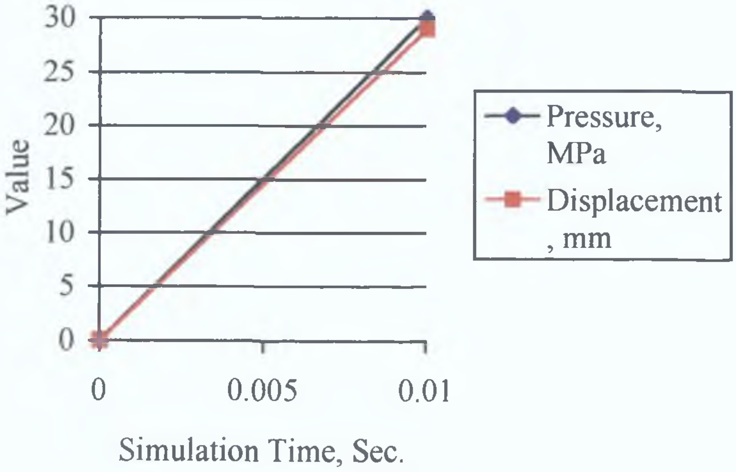

Figure 4.191: Loading pattern for the first simulation.

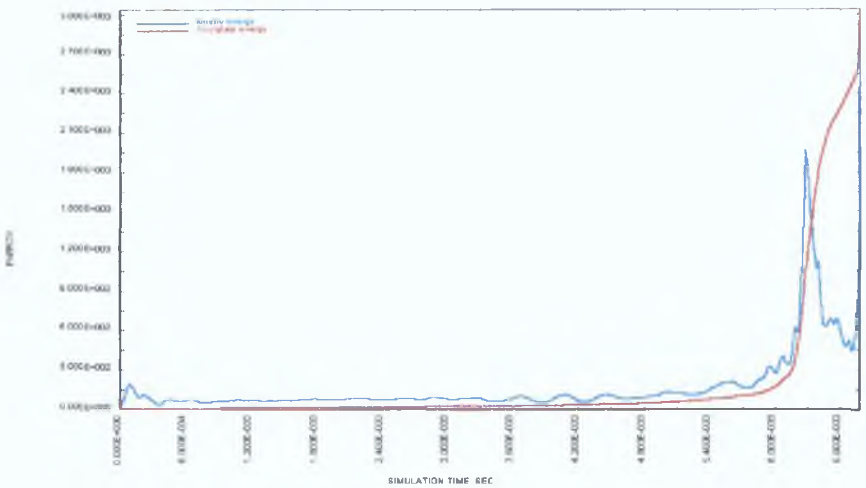

Figure 4.192: Development of kinetic energy and hourglass energy of deformation.

Figure 4.192 shows the development of the kinetic energy and hourglass energy of deformation. It can be seen from the figure that about 0.005 seconds in the simulation the kinetic energy started picking up and around 0.006 seconds both the kinetic energy and the hourglass energy was building very fast. This indicated a sudden change in the deformation mode.

Figures 4.193 and 4.194 shows the state of the deformed tube at 0.005 seconds and 0.006 seconds of simulation respectively. In Figure 4.193 there is some sign of buckling in the middle while the Figure 4.194 a prominent buckle has developed at that location. By 0.005 seconds about 15 MPa of pressure and 14.5 mm of end displacement were applied. The T-branch formed to a height of about 8.0 mm.

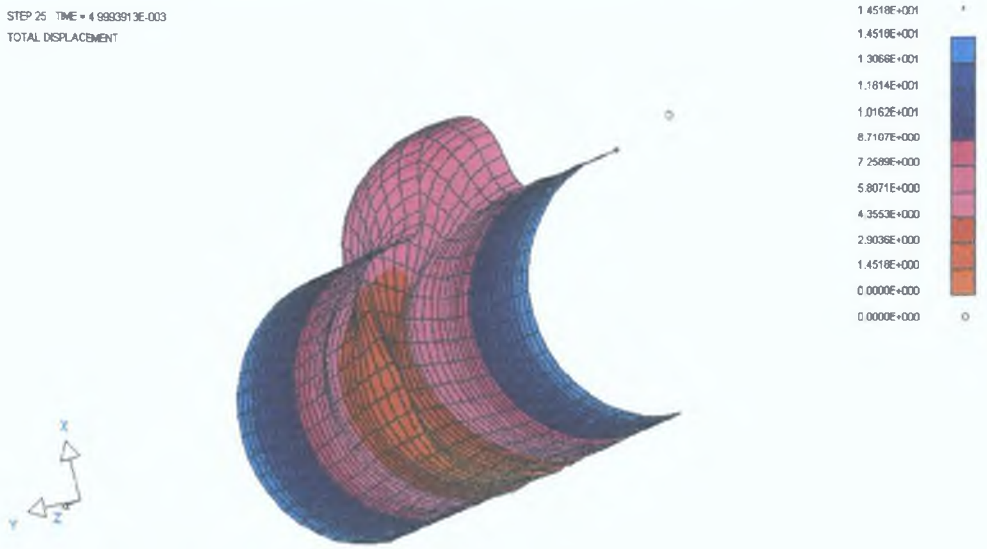

Figure 4.193: State of deformation at 0.005 seconds in the simulation.

Figure 4.194: State of deformation at 0.006 seconds in the simulation.

The available post-processor can not process the stress and strains for principal directions. As a result the stress or strain paths followed by the nodes at the region of buckling could not presented. However, the stress in co-ordinate directions can be listed. But while doing so the computer crashes after one data collection because of the low memory of the computer. It is not possible to present all the graphical plotting of stress at different time. Table 4.24 shows the stress values of element 3310 at 0.005 seconds and at 0.006 seconds. This element is at the middle of the buckling region. It can be seen from the table that the stress in Y-direction has changed quite sharply compared to the changes in other directions. The Y-direction for the element is nearly the radial direction. Suddenly the element has gone to strong compression in radial direction from almost no compression. Also the axial compression in the element was easing although compression at the tube end was on.

Table 4.24: Stresses of an element at the buckling zone before and after the onset of buckling

Stress designation	Stress (MPa) at the simulation time of 0.005 sec.	0.006 sec.
S_x	57.26	42.6
S_y	-4.83	-46.35
S_z	-143.42	-131.03

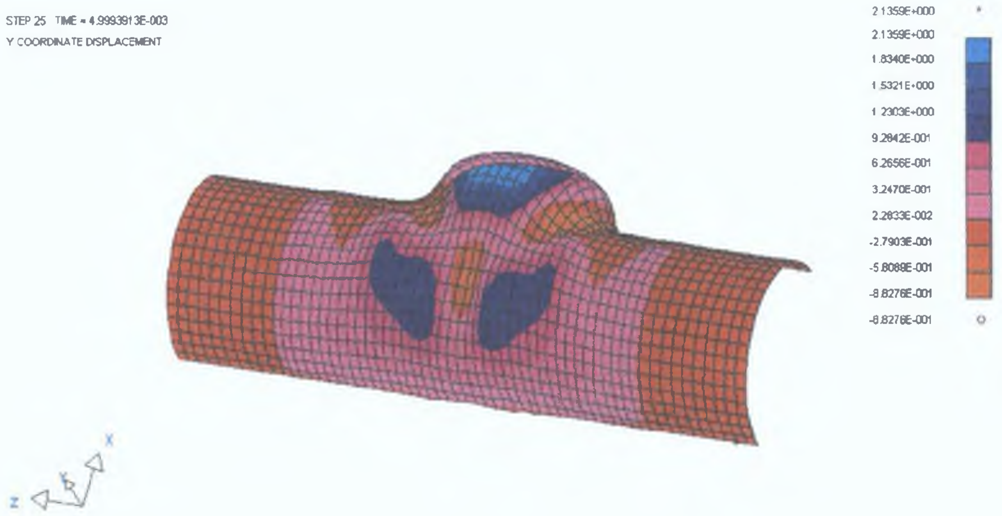

Figure 4.195: Plotting of displacement of the nodes in Y-direction at 0.005 seconds of simulation.

The plotting of the displacement of nodes in Y-direction is shown in Figure 4.195 at time 0.005 seconds in simulation. It can be seen from the figure that a portion in the middle has negative displacement(red) of about -0.6 mm while the neighbouring region has positive displacement of about 1.23 mm (purple). This is a condition where buckling is obvious as the tube at that region is deforming at two different radial planes under an axial compressive load. Figure 4.196 shows the buckled tube at 0.006 seconds in the simulation.

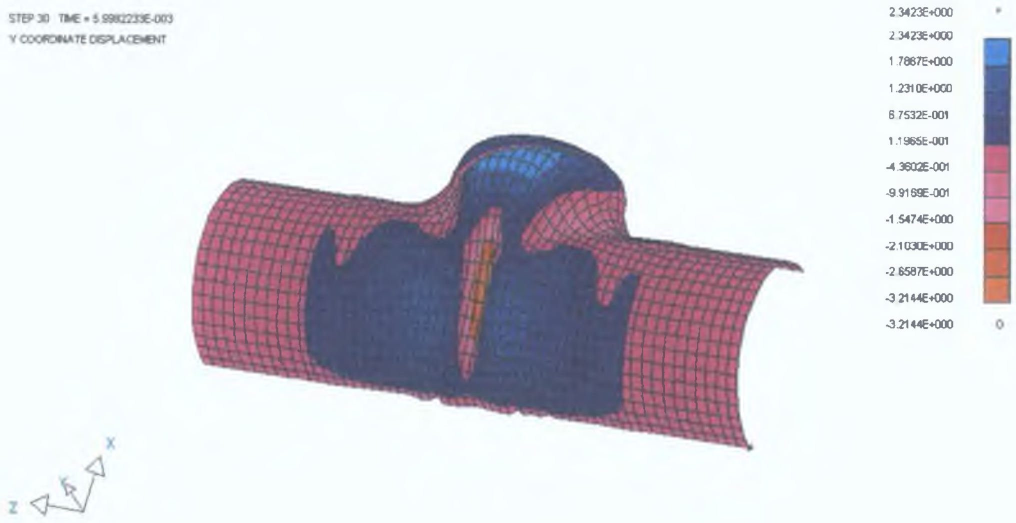

Figure 4.196: Plotting of displacement of the nodes in Y-direction at 0.006 seconds of simulation.

Figure 4.197 shows the development of equivalent strain in a node of element at the buckling region over the simulation. It is seen that the strain has gone up quite sharply after 0.005 seconds when buckling started. The strain in the node has reached close to the failure strain of 1.0 from the material model. The element must have been stretched due to buckling which is reflected in the upturn in its plastic strain.

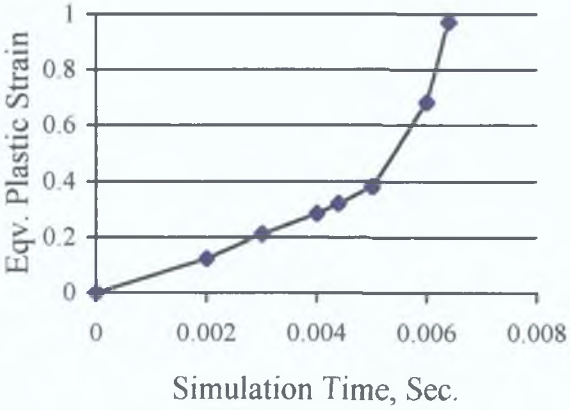

Figure 4.197: Development of plastic strain of a node in the buckling region.

The next simulation was carried out for the same model applying the load in a pattern shown in Figure 4.198. Obviously the pressure load was hyped while the end displacement was suppressed to cause a rupture in deformation.

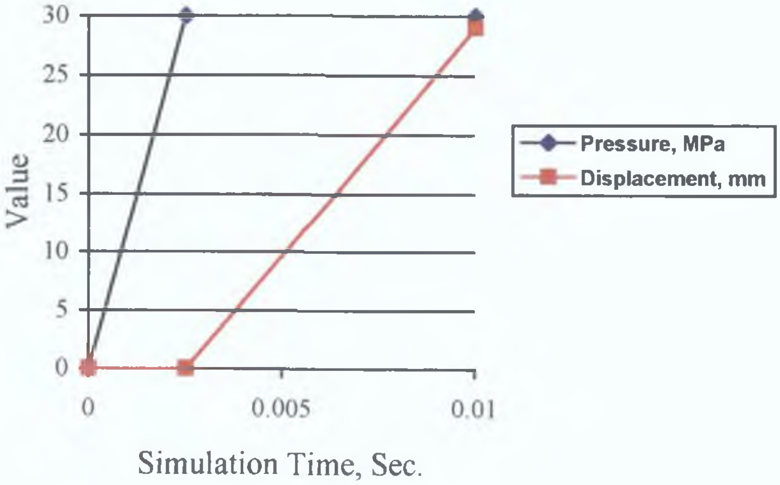

Figure 4.198: Loading pattern for the second simulation.

Figure 4.199 shows the development of the kinetic energy and the hourglass energy of deformation. A kick around 0.0025 seconds was due to the start of the end displacement which subsided immediately. Around 0.0038 seconds time the kinetic energy shot up and the process became unstable.

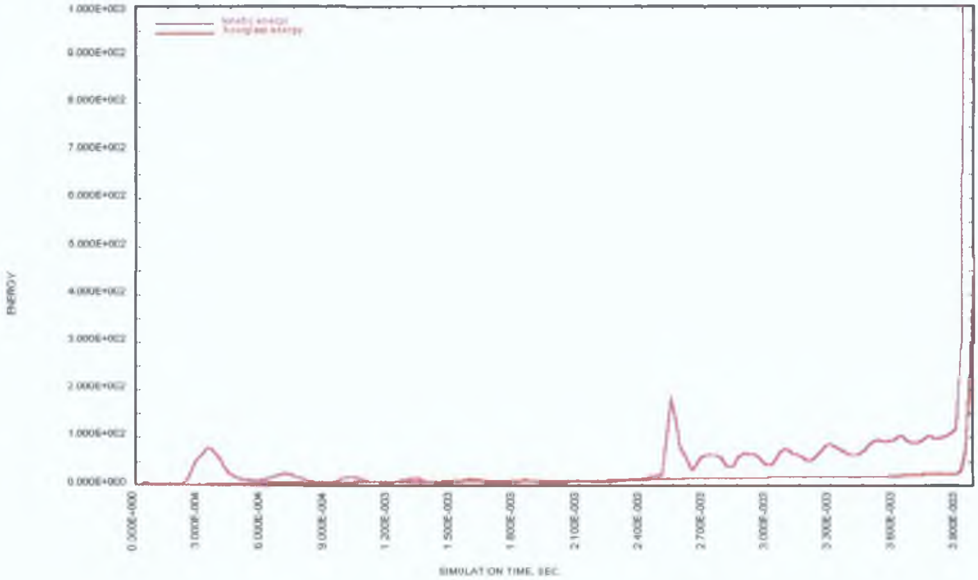

Figure 4.199: Development of kinetic energy and hourglass energy of deformation in the simulation.

Figure 4.200 shows the mid-plane plastic strain in the deformed shape just before rupture. It can be seen that the strain in the bulge has reached about 0.842. Figure 4.201 shows the development of this strain in a node at the bulge over the simulation period. It can be seen that the strain in the node had one sharper rise at 0.0025 seconds when the end displacement started. The strain was maintained at nearly a constant value until about 0.0036 seconds and then started rising again leading to rupture.

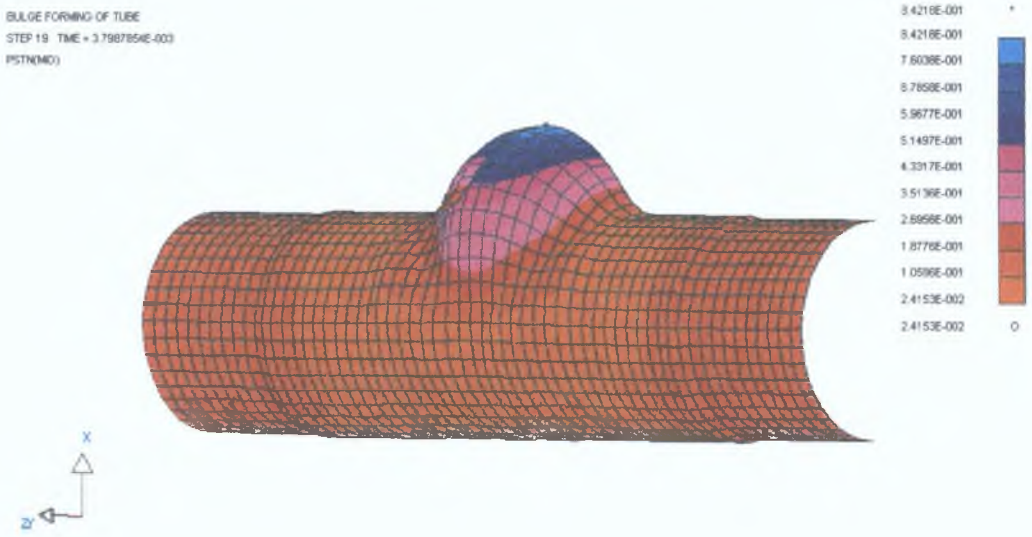

Figure 4.200: Mid-plane plastic strain in the tube just before rupture.

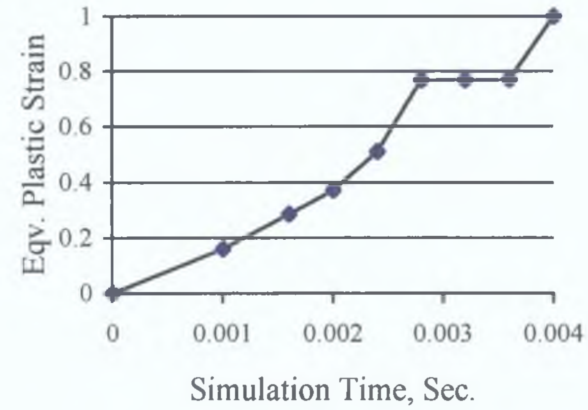

Figure 4.201: Development of plastic strain at a node in the rupture zone.

Figure 4.202 shows the ruptured tube at 0.004 seconds time. The mid-plane plastic strain is also plotted in the figure. It can be seen from the legend that the plastic strain in the tube has reached the value of unity. Quite a few number of elements have failed by this time.

The tube has experienced a pressure of 30 MPa and an end displacement of about 5.0 mm. The height of the T-branch developed at this load was about 9.0 mm.

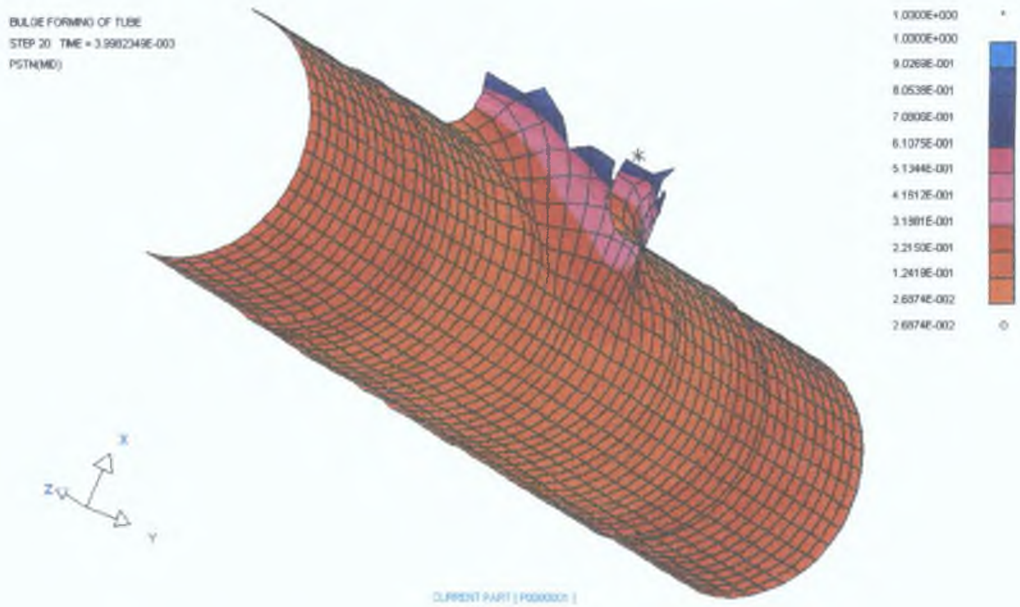

Figure 4.202: Equivalent plastic strain in the ruptured tube.

The third simulation in the series was carried out with a loading pattern which applied the pressure load in a pattern same as in the 2nd simulation and the axial displacement load in a manner same as the first simulation with the hope that the deformation would continue for a longer time without any failure. Figure 4.203 shows the loading pattern for this simulation.

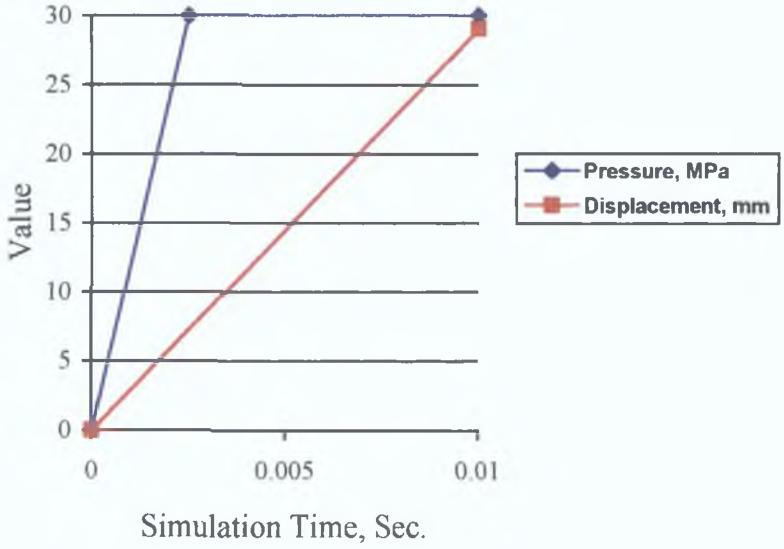

Figure 4.203: Loading pattern for the third simulation.

The simulation indeed continued for a longer time. Figure 4.204 shows the development of the kinetic energy and the hourglass energy of deformation. It can be seen that after 0.0074 seconds both the energies built up fast. A pressure load of 30 MPa is already applied by this time. The T-branch has formed to the height of about 17.0 mm.

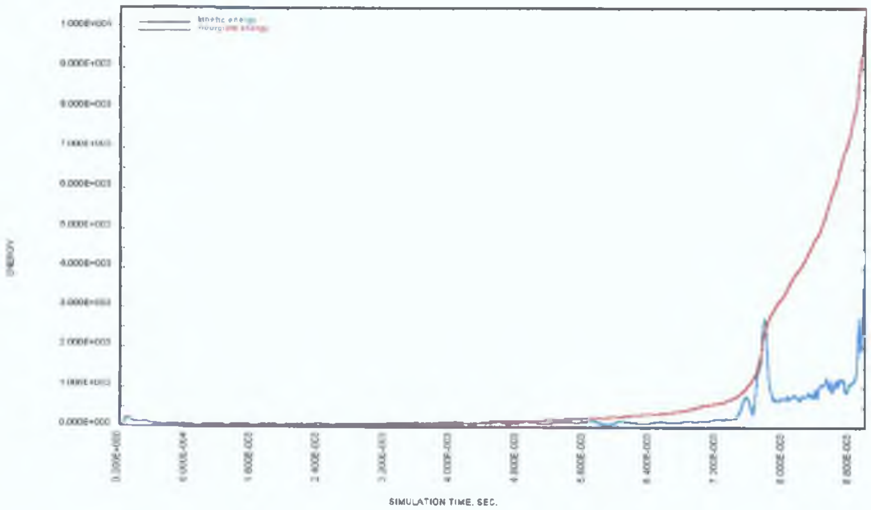

Figure 4.204: Development of kinetic energy and hourglass energy in the simulation.

Buckling seems to have started which is evident in Figure 4.205 where the Y-displacement of the nodes is plotted. Again a negative displacement of about -0.6 mm at the middle and positive displacement of about 1.3 mm in the neighbouring region indicates that the tube at the location is deforming at two different radial planes separated by a distance of about -2.0 mm.

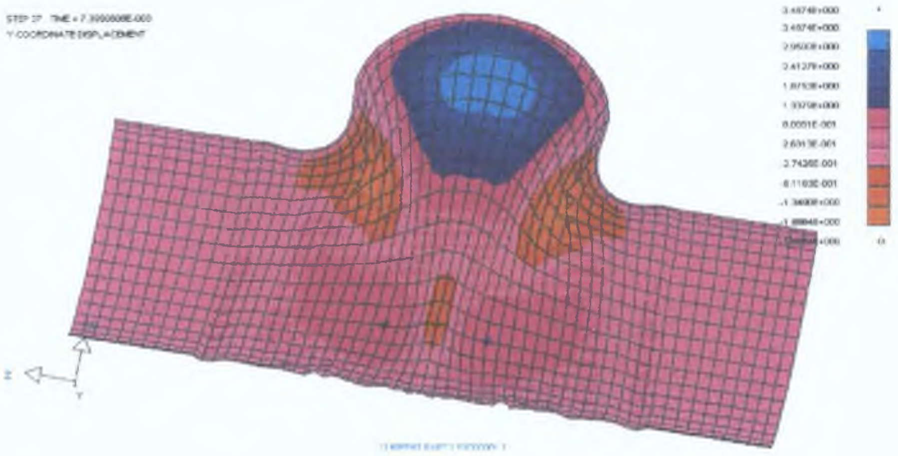

Figure 4.205: Contour of displacement of nodes in Y-direction at 0.0074 seconds of simulation.

The consequence is evident in Figure 4.206 plotting the Y-displacements of nodes at 0.0076 seconds of simulation time. The buckle is now well in the process and the contour shows more to follow.

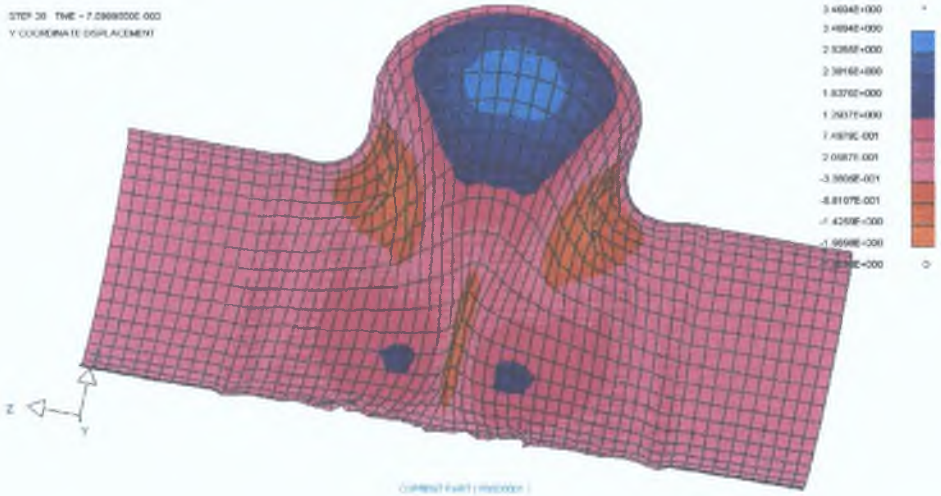

Figure 4.206: Contour of displacement of nodes in Y-direction at 0.0076 seconds of simulation.

Figure 4.207 shows the development of plastic strain in a node in the buckling region. It can be seen that the strain in the node was maintaining a value of about 0.5 for a long time starting from 0.0025 seconds to 0.0070 seconds. It seems that around that time further pressure load could have suppressed the buckling.

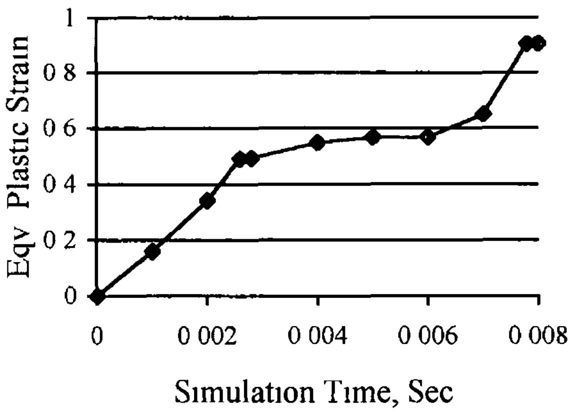

Figure 4 207 Development of plastic strain in a node in the buckling region

4.4 5 Bulge forming of box sectioned elbow from circular tube

Apart from typical asymetrical tubular components, hollow structural components of different cross-sectional shape are manufactured from circular tubes by bulge forming process Structural components of automobile chassis or differential gear are examples of products that can be manufactured using bulge forming process In this process the tube blanks are usually bent to the desired shape of the structure before it is bulged to the cross-sectional shape of the component This section presents the simulation of the bulge forming of such products All the modelling and analyses presented in this section were done using LS-DYNA3D package

Modelling

Studying the process of manufacturing structural components of automobile chassis [69] it was apparent that unlike the manufacture of tubular components discussed earlier the tube blank here is not given any axial displacement loading while bulging Therefore, the deformation behaviour of a component at different locations along its length is supposed to be independent It was observed in earlier analyses that in the presence of friction at the die-tube interface there was almost no axial movement of tube along the die by bulging pressure As such, the forming of the component may be analysed by sectioning it to different parts For example, if a component has an L-bend followed by a 45^0-bend, then the deformation at the L-bend can be simulated independent of the deformation at the 45^0-bend since there will be no movement of material along the length of the component.

Accordingly, simulation in this section deals with bulging of an L-bend circular tube to a square-sectioned elbow which could be a section of a structural component. Figure 4.208 shows the finite element model of the half section of the die and the tube. Advantage of half symmetry was availed. Both the die and the tube were given a bend radius of 5 mm and 3 mm respectively at the outer and inner edges of the 90^o bend. But the box corners of the die had sharp bend of zero radius. Each arm of the elbow was 100 mm long. The cross section of the die was 22 mm square and the diameter of the tube was 20 mm. The thickness of the tube was 1 mm.

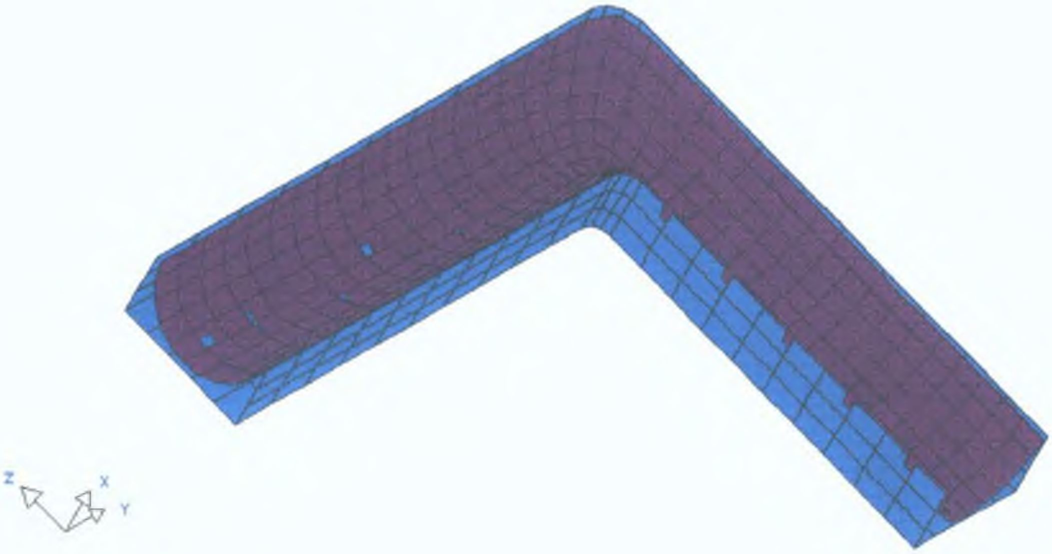

Figure 4.208: Finite element model of the half section of the die and tube

The die half is discretised into 253 elements and the tube half into 380 elements. Belytschko-Tsay [107] shell element properties were assigned to the elements. The tube elements have 5 integration points along the through-thickness direction. The die was treated as a rigid body. An automatic single surface contact algorithm [108] was employed. Two friction conditions were tried. One with a friction co-efficient of 0.15 and the other with a friction coefficient of 0.05.

The die material was assigned the properties of mild steel The material assigned to the tube closely conform to annealed aluminium alloy 2014 with the following properties

Elastic Modulus	72 4 GPa
Yield Strength	97 0 MPa
Tangent Modulus	278 MPa
Poisson's Ratio	0 33
Density	2800Kg/m^3

A maximum of 50 MPa or 100 MPa pressure load was applied at the inner surface of the tube and then it was brought down to zero Figure 4 209 shows the loading pattern against simulation time The ends of the elbow arms were left free to move along the die in one simulation case, while in the other case they were restricted

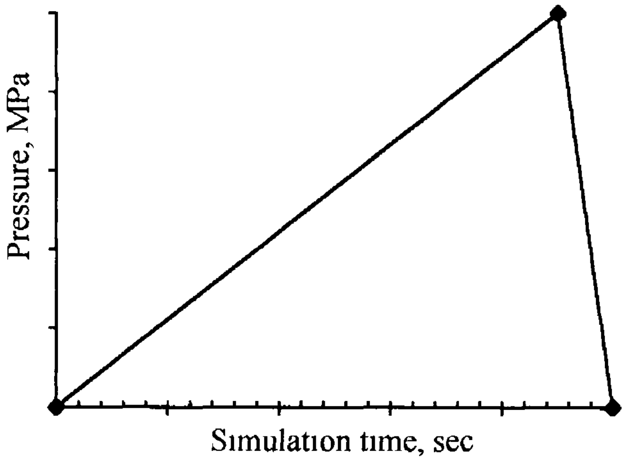

Figure 4 209 Load curve

LS-DYNA3D is an explicit dynamic solver by which dynamic forming situation may be simulated But the forming situation taken up here does not require dynamic treatment Therefore, a quasi-static analysis was done for both simulation cases by carrying out the simulation within a time period much smaller than the actual time would be However, the system was checked to ensure that any dynamic effect was not active

Results and Discussion

As mentioned earlier, the simulation of two forming conditions viz. ends free and ends fixed were done. The results are presented in parallel for both cases for comparison. The results presented next are for a applied pressure load of 50 MPa which was subsequently brought down to zero. The coefficient of friction was 0.15.

Figures 4.210 and 4.211 respectively show the deformed state of the elbows formed keeping the ends free and ends fixed. Figure 4.120 shows both the die and the deformed tube. Some of the die pixels have surfaced up because of the way computer displays the graphics as explained before. These die patches may be ignored and considered as the tube surface. One clear difference between the two forming conditions is evident at the inner edge bend. The elbow with ends free has a sharp dent which can be seen in Figure 4.212 which is presented without the die. It may be seen in the figures that for both the forming conditions, the deformed tube has not conformed to the die configuration at the sharp corners.

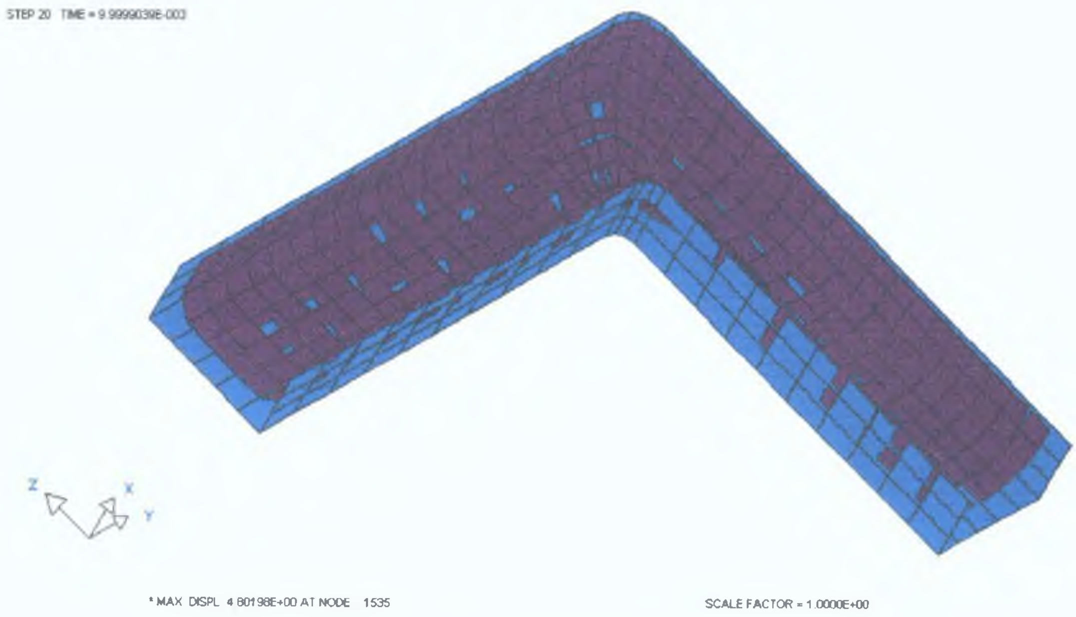

Figure 4.210: Deformed shape of the elbow formed with ends free

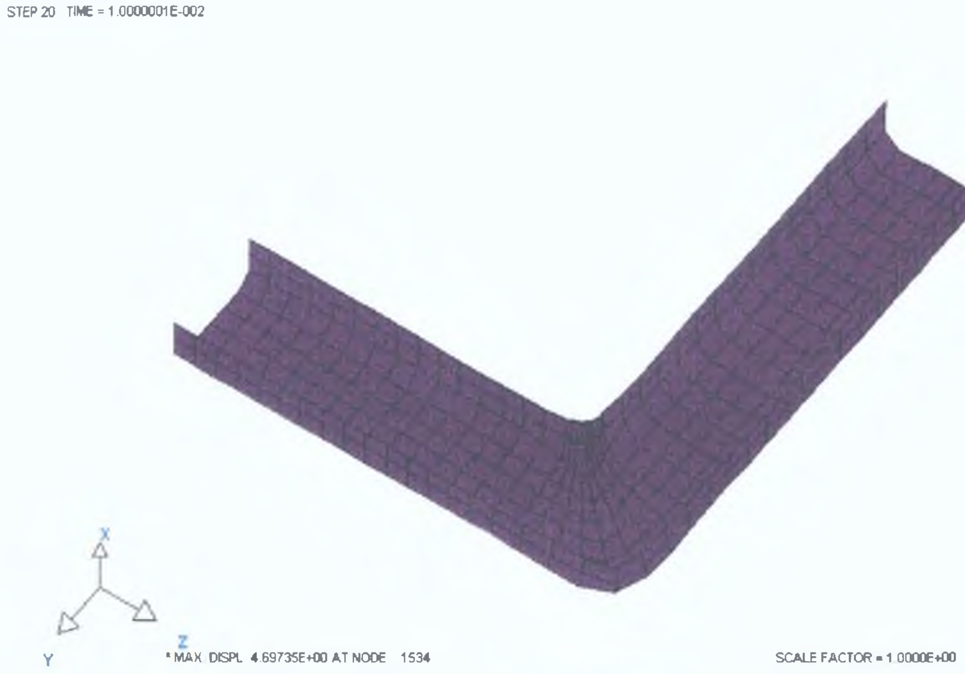

Figure 4.211: Deformed shape of the elbow formed with ends fixed

From Figure 4.210 it is apparent that the nodes at the ends of the elbow formed with free ends have moved along the die. The movement is between 3-4 mm in the respective axial direction.

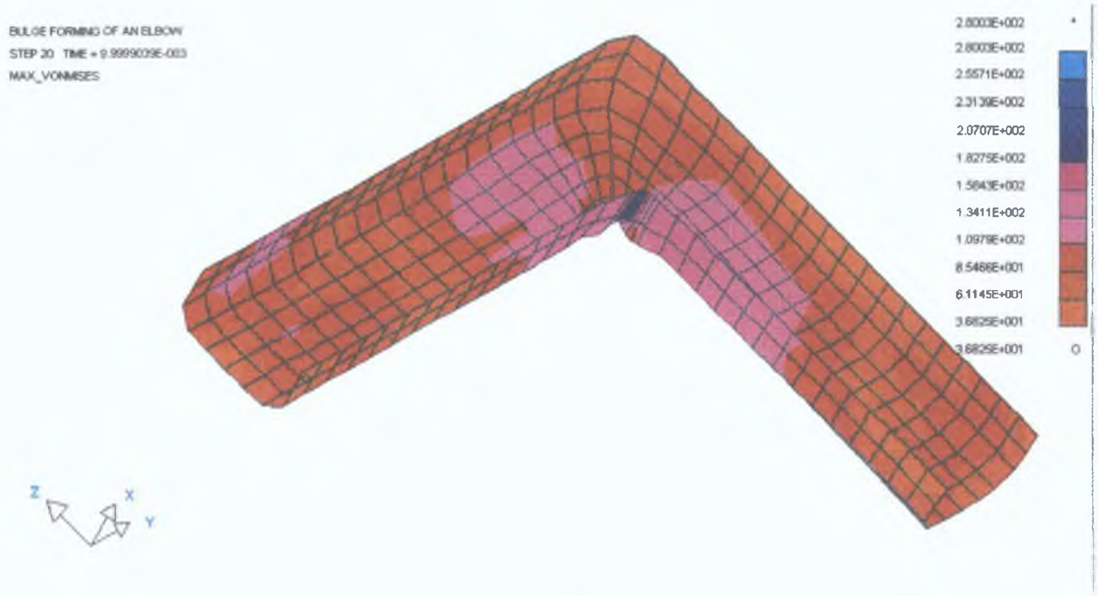

Figure 4.212: Distribution of von-Mises stress in the elbow formed with ends free

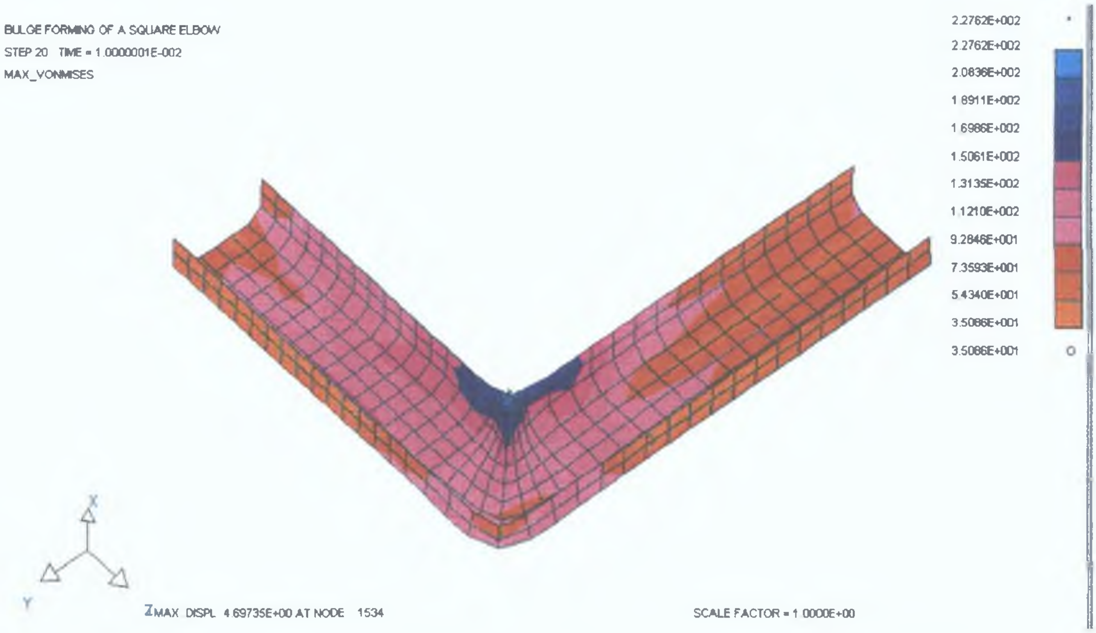

Figure 4.213: Distribution of von-Mises stress in the elbow formed with ends fixed

Figures 4.212 and 4.213 present the distribution of von-Mises stresses in the formed elbow for ends free and ends fixed forming conditions respectively. It can be seen that the maximum stress developed in the elbow formed with ends free is higher than that developed in the elbow formed with ends constrained although the location of the maximum stress is the same i.e. at the inner edge bend. Also, the elbow formed with fixed ends has more even distribution of stress compared to the other one. From Figure 4.212 it can be seen that the elbow formed with ends free has a sharp dent at the inner edge of the bend which resulted in its higher stress even though the arms of the elbow are not as stretched as the elbow with constrained ends. It is apparent from the above that the elbow formed with ends fixed has better stress properties.

Figures 4.214 and 4.215 display the mid-surface plastic strain distribution for ends free and ends fixed forming conditions respectively. As expected, the strain gradient is much better in the elbow formed with ends restricted than the other one formed with free ends. Also, the latter elbow has strained more.

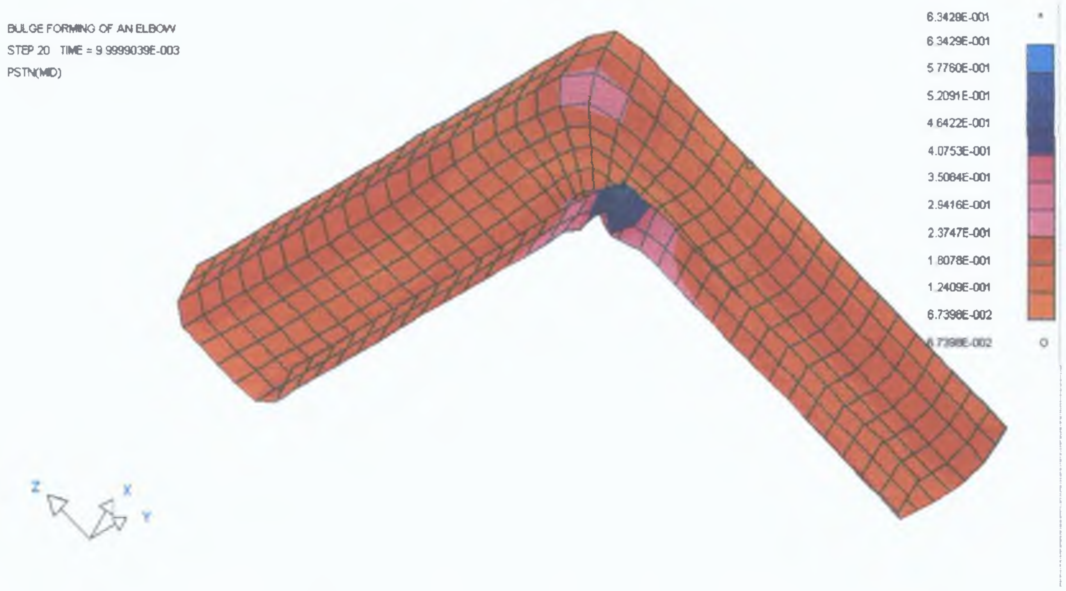

Figure 4.214: Distribution of plastic strain in the mid-plane of the elbow formed keeping the ends free

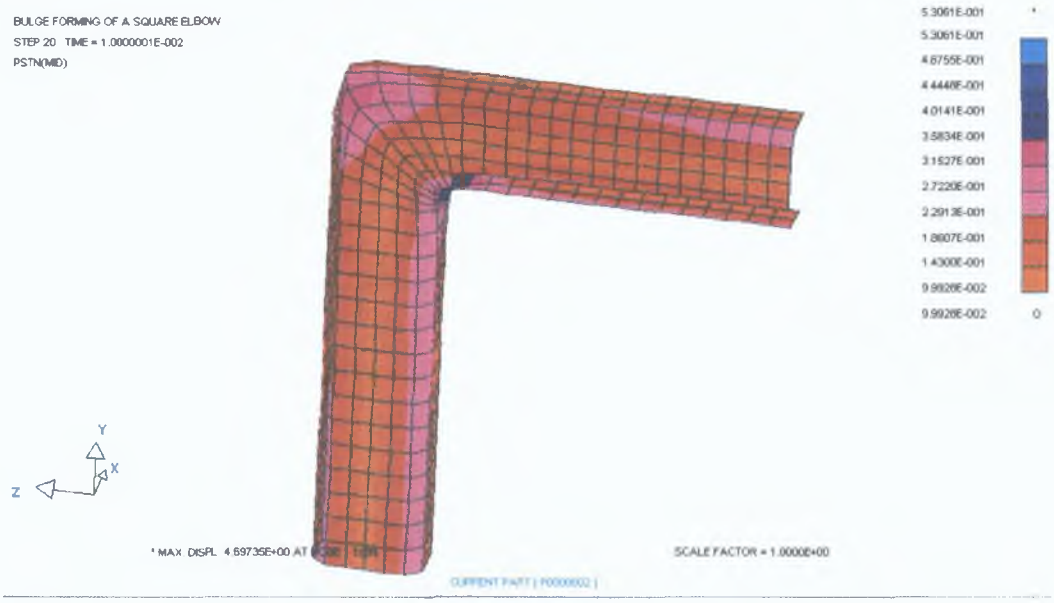

Figure 4.215: Distribution of plastic strain in the mid-plane of the elbow formed keeping the ends fixed

Figures 4.216 and 4.217 respectively show the thinning pattern in the elbows formed with ends free and ends fixed. The elbow formed with free ends has thickness ranging from 76% to 97% of the original thickness. In comparison, the elbow formed with ends fixed has thinned more. Its thickness range is form 70% to 91% of the original thickness. However, the location of maximum thinning for both elbows is the same i.e. at the elbow junction.

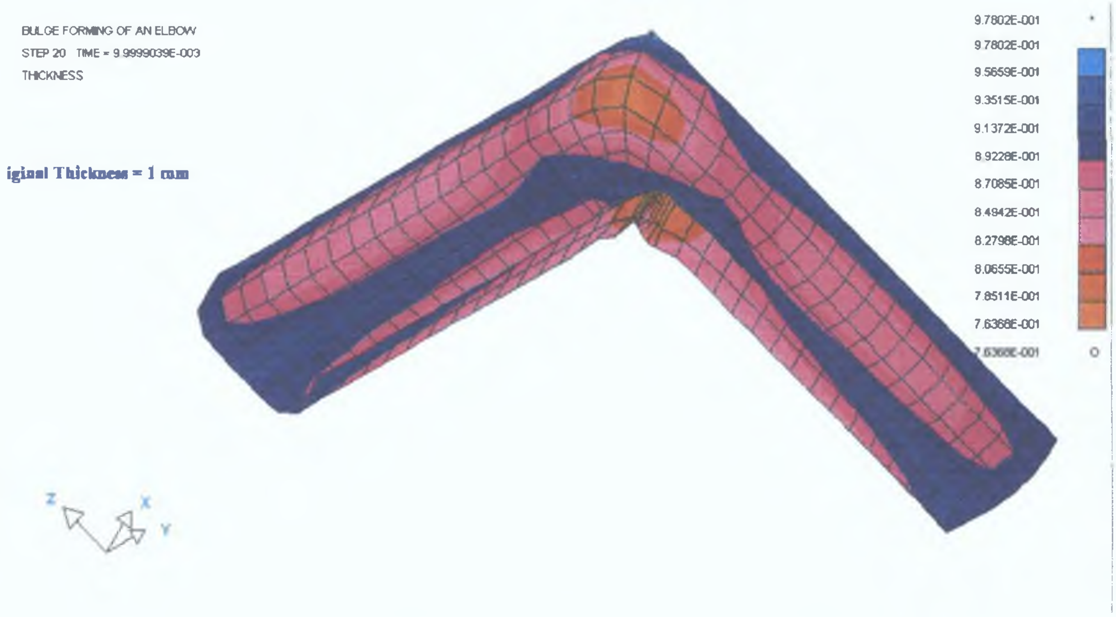

Figure 4.216: Distribution of thickness in the elbow formed with ends free

Figure 4.217: Distribution of thickness in the elbow formed with ends fixed

As mentioned, another simulation of the forming case with ends fixed was done at a lower friction condition. The friction factor employed in this case was 0.05. Figures 4.218 and 4.219 show the distribution of total displacement of the nodes for high(0.15) and low (0.05) friction conditions respectively. It can be seen that the distribution is almost identical. The nodes have not moved much due to lower friction. The difference in the maximum total displacement values for the two friction conditions is only about 0.27 mm.

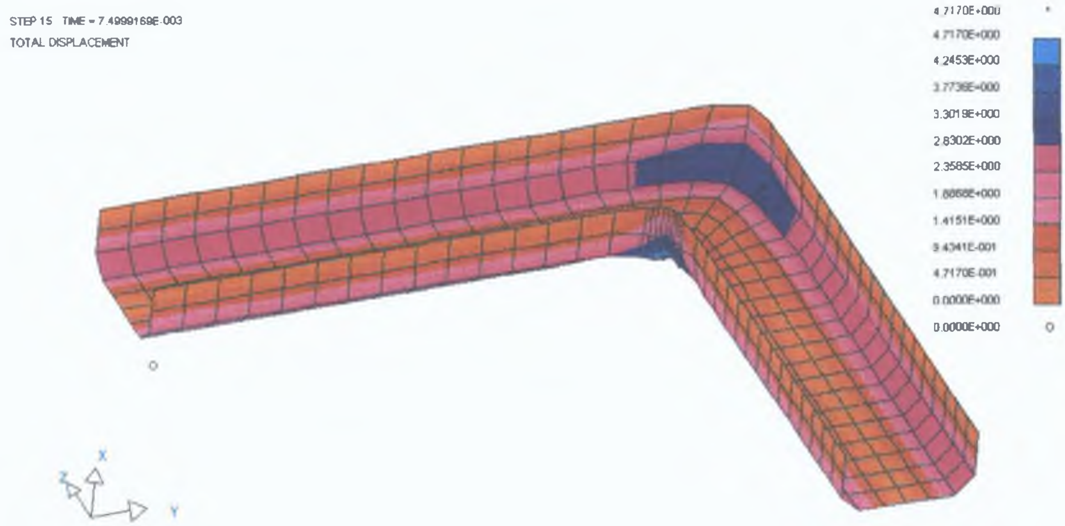

Figure 4.218: Distribution of total nodal displacement of elbow formed at friction factor of 0.15

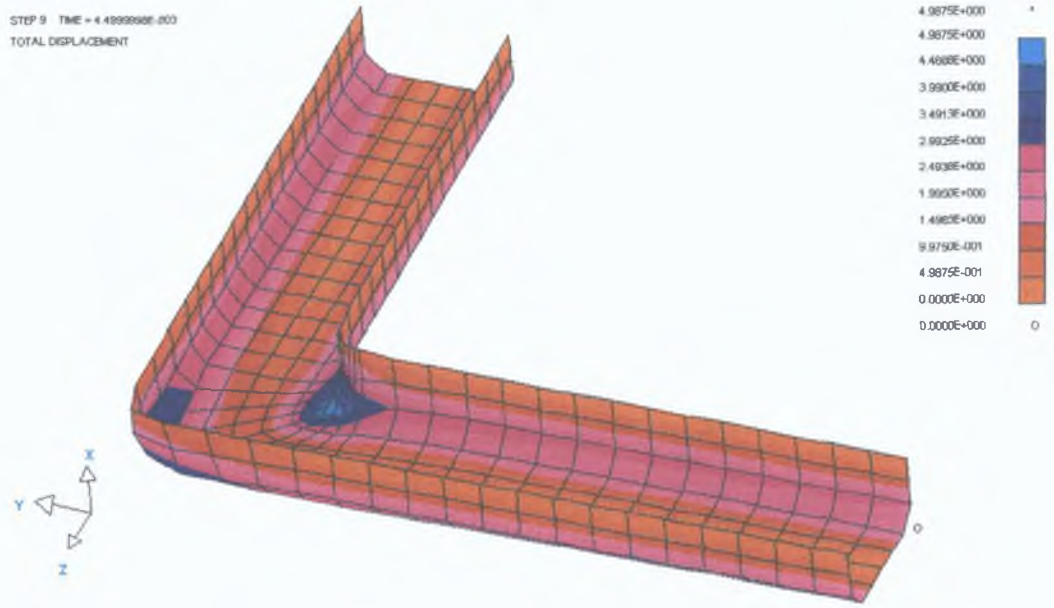

Figure 4.219: Distribution of total nodal displacement of elbow formed at friction factor of 0.05

Figures 4.220 and 4.221 show the distribution of von-Mises stress and plastic strain respectively in the bulge formed at lower friction condition. Comparing these figures with Figures 4.213 and 4.215 respectively it can be observed that there is more stress and strain localisation in the elbow formed with lower friction. Because of lower friction the elbow has strained slightly more thereby inducing little more stress compared to that formed at the higher friction condition. Higher stress and strain coupled with the stress and strain localisation phenomenon in low friction forming it appears that it is better to form at a moderate friction condition. Since the forming condition does not involve much movement of the tube along the die, the higher friction will not affect the forming load much differently.

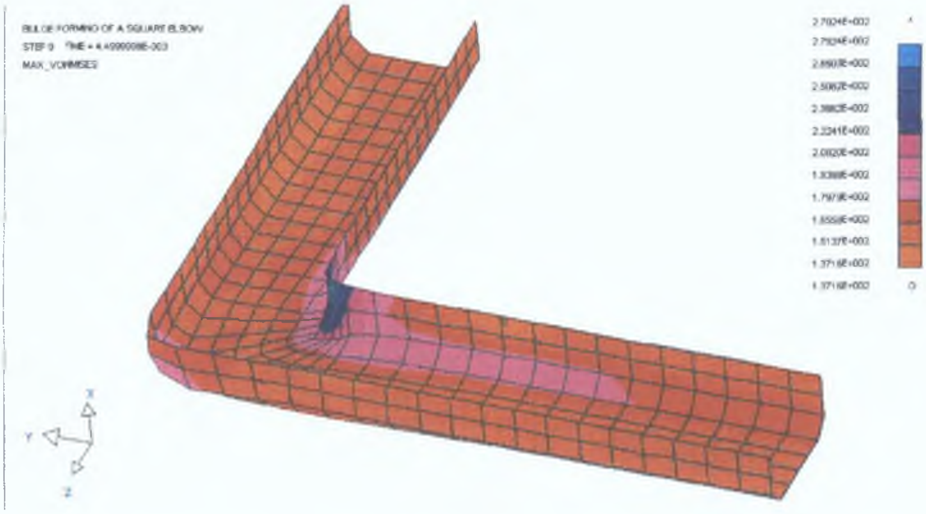

Figure 4.220: von-Mises stress in the elbow formed at friction of 0.05

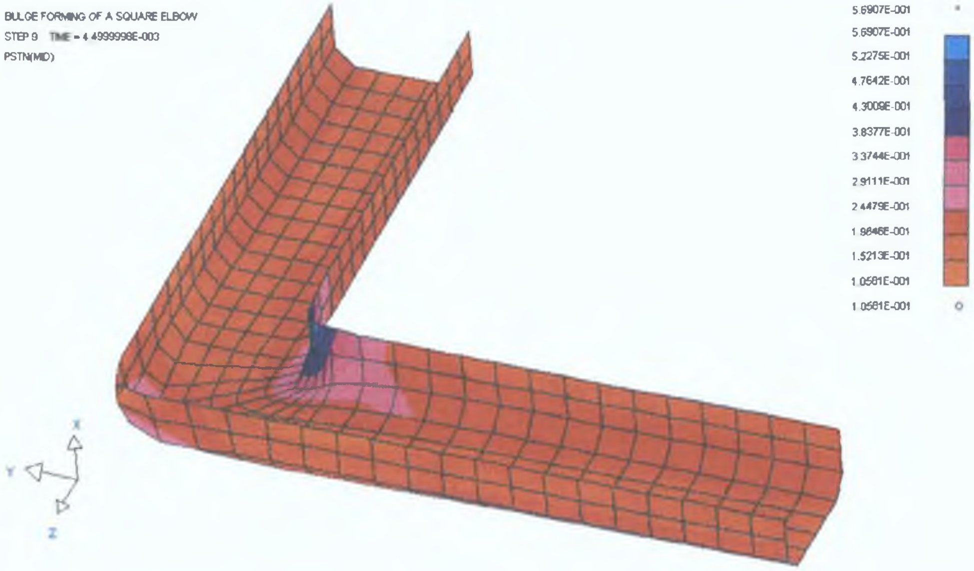

Figure 4.221: Distribution of plastic strain in the elbow formed at friction of 0.05

The thinning pattern in the elbow for low friction forming condition is shown in Figure 4.222. It is very much similar to that formed with higher friction condition shown in Figure 4.217. Most thinning is at the bends and at the corners. The magnitude of thinning is also very close for both forming conditions.

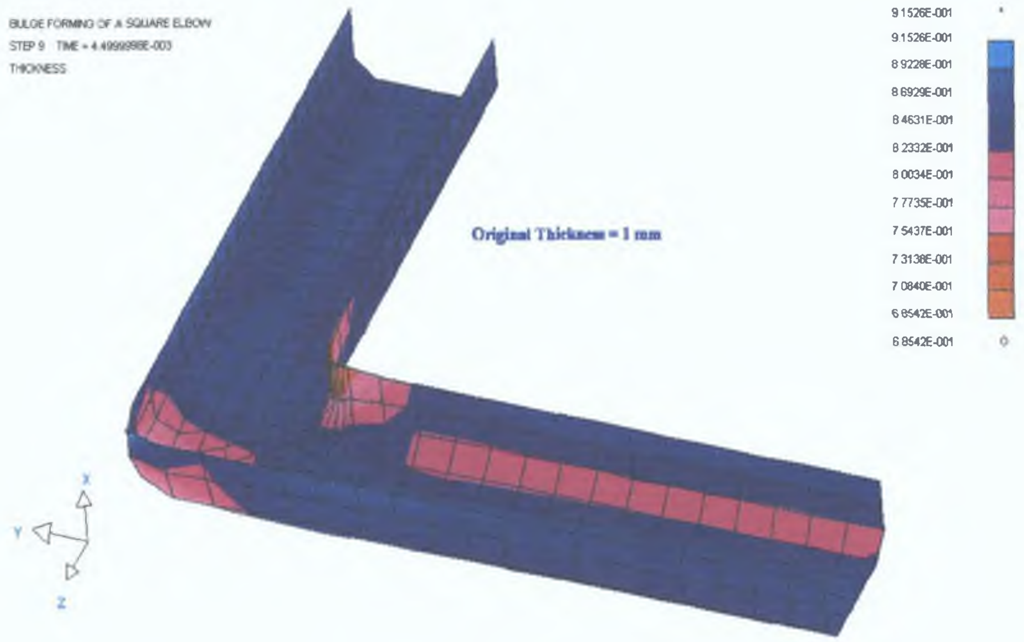

Figure 4.222: Thinning in the elbow formed at lower friction

In this kind of forming the springback is usually a concern for the designers. In this particular forming condition the nodes at the bends and corners are more likely to show springback. Figures 4.223 and 4.224 respectively show the total displacement pattern of the nodes when the full load (50 MPa) was applied and when the load was completely withdrawn for ends fixed forming condition. It can be seen from the contour level values in the legend presented in the figures that there is little change in the magnitude of displacement. A more objective picture of springback may be obtained from the displacement values of certain nodes indicated in Figure 4.223. Table 4.25 presents the displacement values of those nodes. It can be seen from the table that the nodes have moved very little. The retraction of the nodes in percentage of total displacement at full load is between 0.4 to 1.2 which may considered to be negligible.

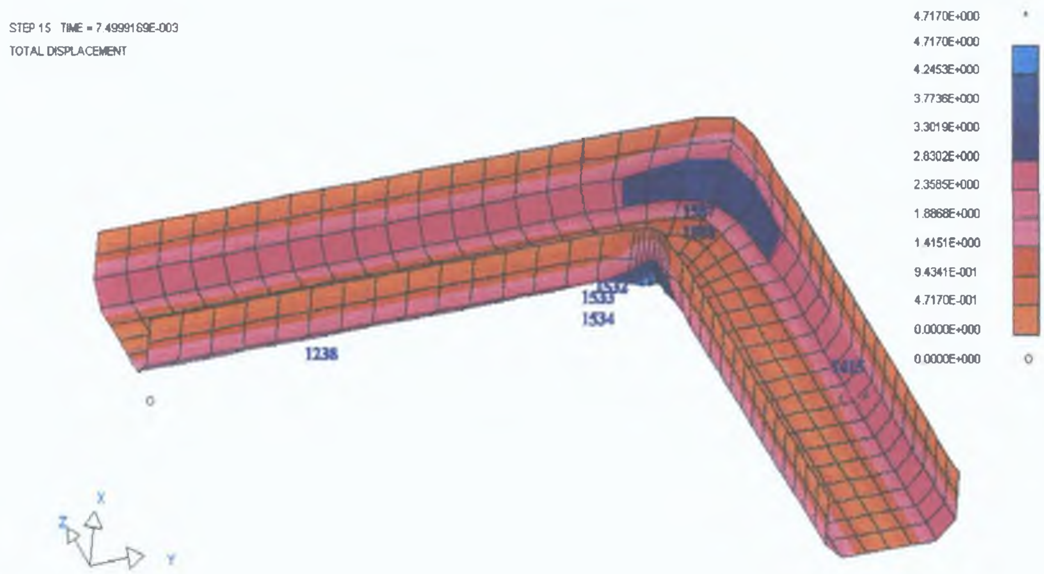

Figure 4.223: Total nodal displacements at full applied pressure of 50 MPa.

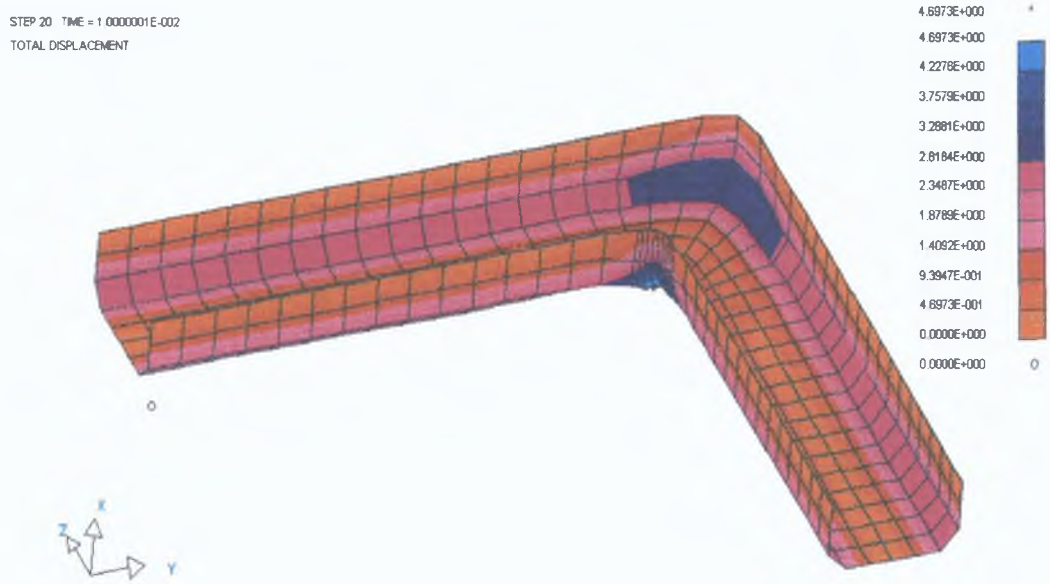

Figure 4.224: Total nodal displacements after complete withdrawal of the pressure

Table 4.25: Displacement values of certain nodes at full load and after load removal

Node No.	Location in the elbow	Total displacement at full load (mm)	Total displacement after load removal (mm)	Difference (mm)	percentage of total displacement at full load
1532	inner bend	4.67	4.6515	0.0185	0.396
1533	inner bend	4.6373	4.6149	0.0224	0.483
1534	inner bend	4.717	4.6973	0.0197	0.417
1587	outer bend	3.385	3.3569	0.0281	0.83
1588	outer bend	3.5912	3.5523	0.0389	1.083
1238	midway along arm	2.5251	2.4958	0.0293	1.16
1415	midway along arm	2.6102	2.5791	0.0311	1.191

In the above elbow forming simulations it was seen that the tube did not deform to the fullest extent at the box corners. It was not expected also mainly because of two reasons. Firstly, the die was modelled with zero corner radius which would theoretically require infinite straining of the tube material points meeting the die corner which is impractical. Secondly, the tube was discretised with elements having linear shape functions. This means that the element sides would not take any curvilinear shape on deformation. To conform to sharp die contour it is necessary either to use more number of elements at such critical locations or use higher order elements. The first choice is computer costly and the second choice was not there in the finite element package that was used for the simulation. Apart from the above two modelling constraint, a third possibility due to which the tube may not deform to the fullest extent is the insufficient pressure. Figures 4.225 and 4.226 show the total displacement of the elbow at an applied pressure of 50 MPa and 100 MPa respectively. The friction factor was 0.05 and the ends were fixed. It can be seen from the contour level values in the figures that the increase in maximum displacement was only 0.252 mm.

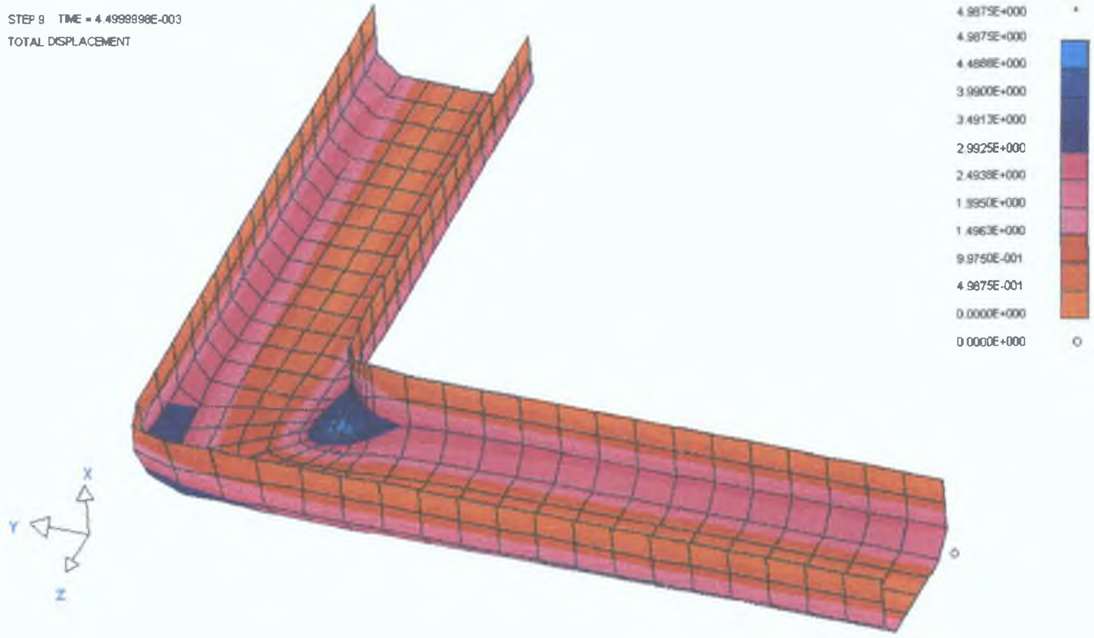

Figure 4.225: Total displacement of nodes at 50 MPa pressure.

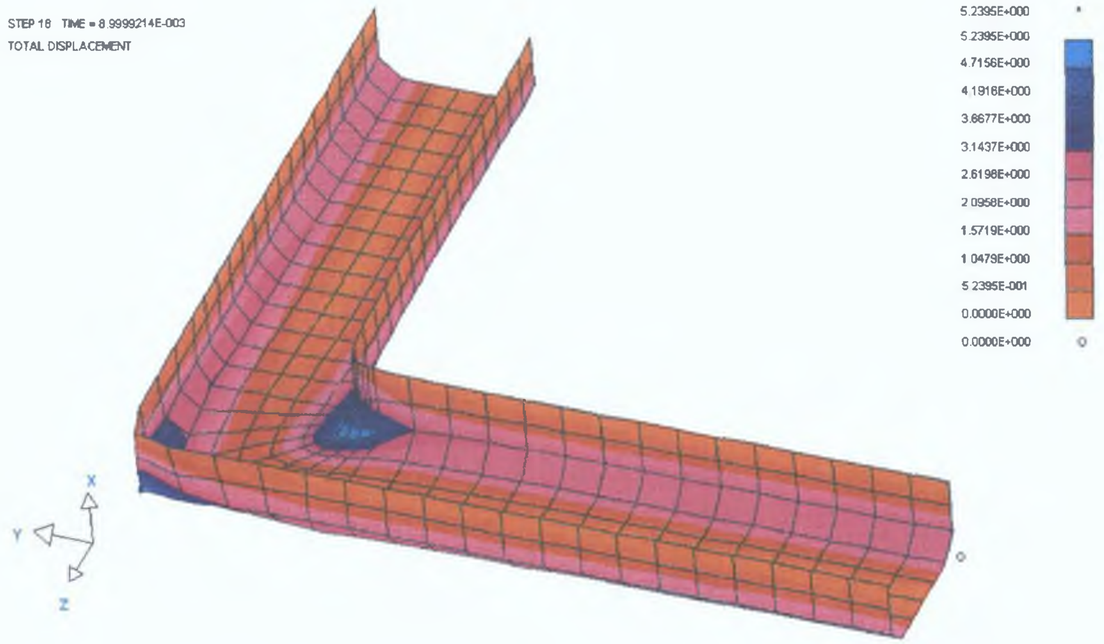

Figure 4.226: Total displacement of nodes at 100 MPa pressure.

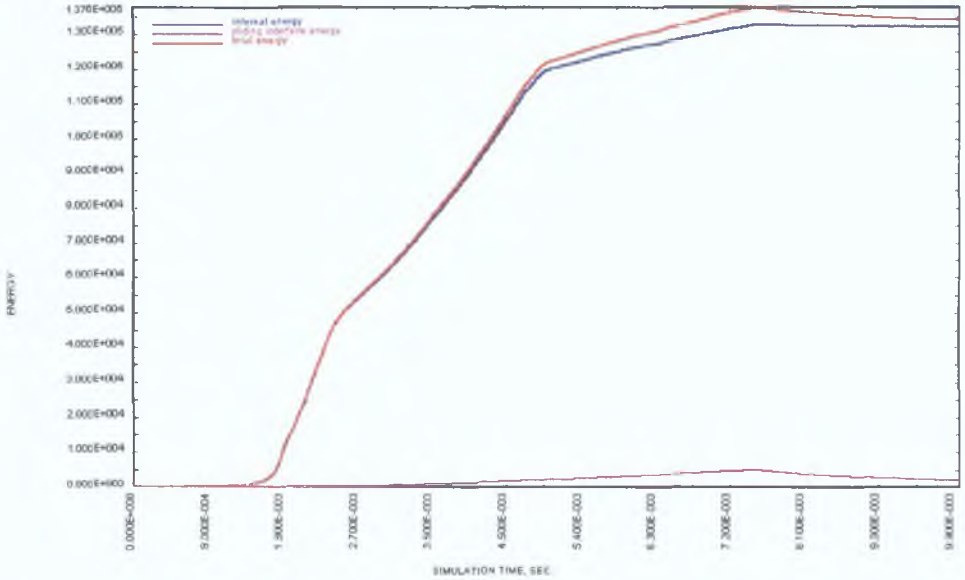

Figure 4.227: Development of internal energy, total energy and sliding interface energy of deformation during simulation.

Finally, it was stated before that a quasi-static analysis was done for the forming problem by using a duration of forming much smaller than the actual duration would be. In such analysis it is essential that the kinetic energy during the deformation remains low compared to the internal energy or total energy of

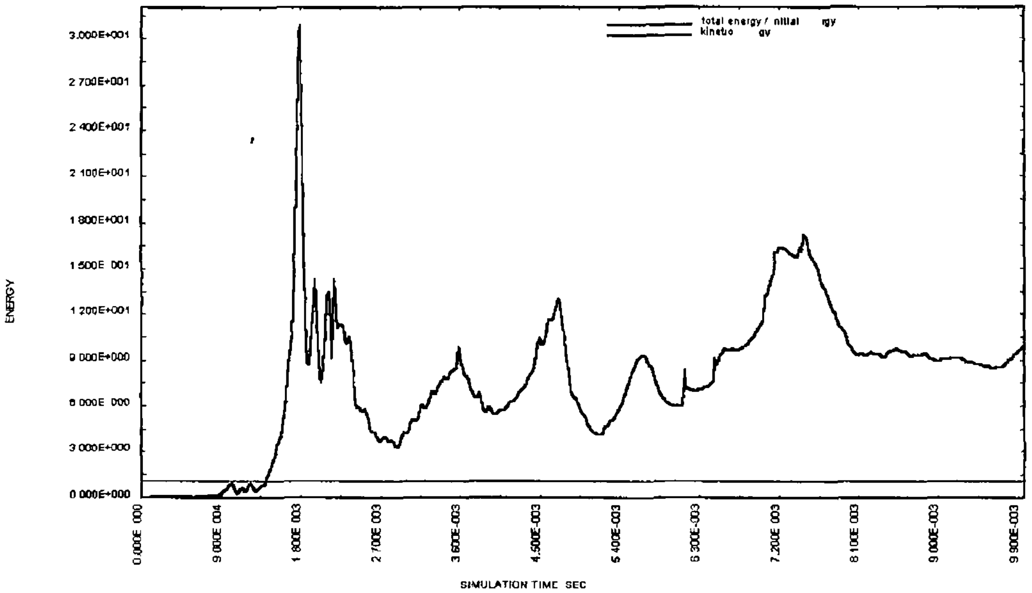

Figure 4 228 Development of kinetic energy of deformation during the simulation

deformation Figure 4 227 shows the total energy, internal energy and sliding interface energy of deformation Figure 4 228 shows the kinetic energy of the system during deformation of a particular simulation The state of energy for the other simulation cases was similar It can be seen that the system has smoothly gained energy The kinetic energy was negligible compared to the internal energy or total energy

Chapter 5

CONCLUSIONS AND RECOMMENDATIONS

Finite element modelling and simulation of bulge forming of different blank shape and size, friction conditions and loading patterns were carried out in this work Three blank shapes viz , plane circular sheet, plane rectangular plate and straight cylindrical tubes were considered for simulation In all cases the pressure and in-plane compressive load were applied for forming Simulations of forming from plane circular sheet were done in axisymmetric two dimensions Simulations of forming from all other blank shapes were done in three dimensions Two stand-alone pentium PCs with 32 MB and 64 MB memory were used in the project ANSYS and LS-DYNA3D finite element packages were used for the simulation works

The main list of simulations in this work are

i bulge forming of plane circular sheets in the middle at different loading conditions and optimisation of the process,

ii bulge forming of plane rectangular plate at the middle at different loading conditions,

iii axisymmetric bulge forming of straight cylindrical tube at different loading conditions and optimisation of the process,

iv asymmetric bulge forming of straight cylindrical tubes to T-branches and simulation of the failures of the process,

v asymmetric bulge forming of an initially bent cylindrical tube to an L-bend at different loading and friction condition

Summary findings from each of these simulation categories are presented in the following under separate headings Any conclusion or recommendation from these findings is also presented

5 1 Simulation of Bulge Forming of Plane Circular Sheets

Main Findings

In this axisymmetric 2D simulation the effects of the in-plane compressive load, blank thickness, friction, blank diameter and loading pattern were observed The main observations were

i Bulge forming by simultaneous application of pressure and in-plane compressive load produces more height, less stress and strain, and the bulge crest thins less compared to the one formed by pressure load only

ii Thinner sheets may be formed to comparable height with less pressure load But for the same blank size, and bulge diameter, thicker sheets can be bulged to more height before instability is reached

iii Bulging of same blank size and same bulge diameter by same loading pattern but different friction conditions (frictionless and with friction) gives comparable bulge height and gives rise to comparable stress But strains in the bulges are different for changes in friction conditions

iv Bulging from a sheet of larger blank diameter but same thickness allows more bulging as more peripheral displacement is available It is seen that the gain in the bulge height is nearly equal to the additional peripheral displacement This also gives a thicker bulge

v The ratio of the pressure load to displacement load has marked influence on the bulge forming process Enhanced peripheral displacement without sufficient pressure pushes the bulge root away from the die rather than material to the bulge centre

vi The sheet undergoes considerable circumferential compressive strain at the bulge root and base area At the same time these regions of the bulge have also thickened The net effect of straining in these regions is difficult to predict without simulating the problem in three dimensions

vii The instability in the bulge occurs at different state of strain for different loading conditions It is seen that bulges that are formed with more peripheral displacement fails at lower state of biaxial strain viii Restrained forming by putting flexible load of up to 25% of the applied pressure load on the top of the forming bulge does not result in appreciable difference with respect to bulge shape and the stress and strain state compared to free forming However, rigid restraint on the forming bulge produce significantly different shape of bulge The pattern of stress and strain distribution also changes The onset of instability is delayed and moves to locations where the bulge is not supported

ix In the maximisation of bulge height in free forming, the process optimises when variables viz , pressure, peripheral displacement and die fillet radius are maximum within their specified range In the stress differential minimisation of the same forming problem, the pressure and the displacement loads settled to values near the upper range while the fillet radius of the die settled to the specified maximum value

Conclusions and Recommendations

From the simulations of the bulge forming of a circular sheet it is apparent that sheets of higher thickness, larger diameter at lower friction condition and a balanced pressure to peripheral displacement ratio would result in a stable process The 2D simulations show considerable circumferential strain but can not show whether there is wrinkling at the bulge base A 3D simulation would be more appropriate to reveal that deformation phenomenon

5 2 Bulge forming of Plane Rectangular Plates

Main Findings

The simulations in this forming case were done in 3D for two loading conditions In one loading condition the pressure load was kept dominant over the axial compressive load over certain period of loading, while in the other, the axial compressive load was kept dominant over the pressure load until certain point of loading The model was very limited in terms of element numbers and consequently in loading The main observations from the simulations of this forming situation were i The dominant pressure loading produced a smooth bulge while the other loading condition resulted in buckling at the base of the bulge which could not be recovered by the subsequent pressure loading although the magnitude of the pressure load was same for both the loading conditions

ii The stress state in the bulge was nearly the same for both the loading conditions but the dominant displacement loading has caused more stress gradient at the unbulged flat part

iii From the simulations it appeared that the ratio of stress and strain in the direction of axial compression was a determinant factor for the onset of buckling at the flat part of the plate For the pressure dominant loading where there was no incident of buckling, the ratio was 99 and for the displacement dominant loading the corresponding value was 71 5 which resulted in the buckling

iv In spite of the buckling which acted as a barrier for the movement of material in the bulging zone, the displacement dominated loading produced a higher bulge

Conclusions and Recommendations

The simulations revealed that the in-plane compression is desirable to get a higher bulge at the same time it should not produce any buckling in the process which impedes material movement in the bulge region A desirable balance between the pressure load and the displacement load would be the one which does not produce buckling It was seen that the in-plane compressive stress to in-plane compressive strain ratio of 99 does not produce buckling while a ratio of 71 5 produced buckling Because of very long computation time it was not possible to try other loading patterns However, based on the two simulations, a loading pattern was suggested which was expected to result in higher bulge without buckling in the process In forming problems like this, more powerful computers and solvers are essential where more trials could be done to determine the desirable loading pattern

5.3 Axisymmetric Bulge Forming of Straight Cylindrical Tubes

Main Findings

In this 3D simulation of tube expansion two loading patterns were tried In the first loading pattern the pressure loading was initially high compared to the axial displacement loading In the second loading pattern relatively intense axial displacement loading was tried during the initial period of simulation The main observations from the simulations were

i In both simulations the bulging started as a hump somewhere between the die recess and the Z-symmetry line With the first loading pattern the hump gradually inflated evenly at its both ends and eventually spread all over the bulging region In contrast, the hump continued to maintain the shape in the second loading pattern and at one stage the die end of the hump started inflating and the whole bulging region suddenly changed from compressive mode to tensile mode of deformation

ii Because the deformation progressed in two different modes due to the two loading conditions, the deformed shape of the bulges were different For the first loading the bulge took a regular barrel shape for most of its length The bulge by the other loading had a rather irregular shaped barrel The impression of the initial hump could not be eliminated although at the end of the simulation the pressure load was equal

iii The bulge produced by the second loading pattern was more stressed than that by the first loading pattern although the latter induced more deformation and thereby more bulge diameter The principal stresses in the bulge indicated agreement with the relevant theory regarding instability in the bulge

iv The bulge by the first loading pattern was thinned at most to 75% of the original thickness of the tube and almost no thickening in the main tube while the bulge by the second loading thinned at most to 82% of the original tube thickness and thickened to 104% at the main tube v The principal strains in the bulges by both the loading pattern showed intense straining in hoop direction at the end of the loading This indicated that the bulge would eventually rupture along its length as is the experience from practical tube expansion

vi The axial movement of the nodes in the bulge over the loading period by the second pattern indicated a jolt in the bulge which settled down quickly But if the loading intensity were high at that moment, then the process may become unstable

vii The optimisation exercise of the process showed that about 50% of the pressure load and about 40% of the displacement load applied at the first quarter of the simulation period would result in minimising strain in the likely region of buckling which would ensure smooth development of the bulge

Conclusions and Recommendation

The simulations of axisymmetric tube expansion showed that the stress and strain development in the bulge agree well with the theoretical understanding of the process as well as with the practical experience The simulations revealed that depending on the loading pattern a mode shape change in the deformation process is likely and might lead to instability Since axisymmetric bulging as a structure is more flexible compared to other type of bulge forming, it is better to do a mode shape analysis to identify the critical loads so that in real forming such loads can be avoided

In the simulations of the axisymmetric bulge forming the nodes in the bulge except those at the symmetry planes moved slightly in the circumferential direction which should not be the case This has resulted in a different strain distribution inside the bulge than that at the symmetry edges This problem can be addressed by fixing all the nodes in the circumferential direction In cylindrical co-ordinate system this could be achieved easily But in Cartesian co-ordinate system the movements of hundreds of nodes have to be restricted by coupling the movements by equations which is quite time consuming Alternately, the tube can be given the effect of some stiffeners along its length at some circumferential location fixing the circumferential freedom of the nodes at those locations

The optimisation problem was described in a particular way The problem may be described in some other way and more effective optimum solution could be possible

5 4 Bulge Forming of T-branches from Straight Cylindrical Tube

Main Findings

This forming process was initially simulated by a limited finite element model Then simulations of forming of T-branches from tubes were done with satisfactory finite element model Some simulation results were compared with available test results Simulation of the failure of the T-branch forming process were carried out The main observations from these simulations are listed bellow

i ANSYS static simulation of forming T-branches by pressure load only and keeping the tube end either fixed or free revealed that at high friction the deformation behaviour is hardly different This is because the high friction resists the material in the main tube to move in the bulge region The T-branch formed are of almost equal height and the magnitude of stress and strain and their distribution pattern in the deformed tube are almost same The maximum stress and strain occurred at the branch top

ii Simulation of T-branch forming by both the pressure load and axial displacement of the end at different friction condition yielded different results In frictionless forming condition the tube deformed most This condition produced maximum branch height and the thinning at the branch top was least However, the stress state in the deformed tube was highest for the frictionless forming The more the friction the less is the branch height, the less is the state of stressing and higher is the intensity of thinning at the branch top In all the friction conditions the maximum stress in the deformed bulge developed at the middle region around the Z-symmetry of the model although the magnitude were different for different friction iii In LS-DYNA explicit dynamic solution of the same forming situation as described in the previous point but at higher pressure and end displacement showed similar findings Because of the higher pressure and axial displacement more deformation of the tube could be obtained resulting in longer T-branch with more stress and strain in the bulge The top of the T-branch experienced compressive meridional stress for a short period and quickly turned to tensile The development of tensile hoop stress in the branch top was always at a faster pace than the meridional stress indicating a possible rupture in the axial direction of the tube In practice the rupture failure of T-branches also occur in the same mode

iv The effect of friction was observed by simulating the process at a friction of 0 3 and at frictionless condition In the simulation with friction, a much lower forming load could be applied as further loading caused wrinkling at the ends This resulted in a T-branch which is only 57% of the height of the T-branch formed in frictionless condition The T-branch top thinned almost equally for both the friction conditions, but the main tube thickened differently In frictionless forming the main tube thickened uniformly to 133% of its original thickness while in the forming with friction the main tube developed considerable strain gradient and thickened to a maximum of 158% of its original thickness

v The simulation of T-branch forming from copper tubes were done for the same loading conditions as was done in the experiments by Hutchinson[104] The simulation results agreed reasonably well with the experimental results

vi The T-branch formed from thicker tubes had almost flat top while that formed from relatively thinner tube produced T-branch with torospherical shaped top

vii The stress and strain distribution in the T-branches formed from thicker and thinner tubes also differed The stress gradient at the T-branch formed from a thinner tube is more prominent than that formed from a thicker tube This has happened as the thinner tube has deformed more compared to the thicker tube At equal state of deformation this difference is likely to disappear

viii The thicker tube was formed at 48 3 MPa pressure and 13 4 mm axial displacement as well as 62 1 MPa and 20 mm axial displacement These two forming load conditions naturally produced T-branch of different heights with different stress and strain But the pattern of distribution of the stress and strain in the deformed tube was quite similar The history of stress and strain development at the branch top during the simulation were different mainly because of the difference in the loading pattern

ix The simulation of the failure of the T-branch forming process by bulging showed that the rupture failure occurs at the top of the forming T-branch when the pressure load dominates the forming process The buckling failure occurs at the main tube directly under the forming T-branch The buckling at the main tube starts when two neighbouring region move axially at two different radial position of the tube High axial load and low internal pressure creates a loading situation comparable to compression of an imperfect slender column This kind of loading situation would naturally lead to buckling

Conclusions and Recommendation

The simulation of T-branch forming revealed the pattern of stress and strain in the formed component at different forming conditions The simulation showed that the lower the friction the better it is to overcome the problem of thickening in the main tube Also the stress and strain distribution in the formed component is more even for low friction forming

The simulation compared quite well with the experimental results This provides the necessary evidence that the results from the FEM simulation of this complex process can be accepted as nearly the realistic state of deformation of the process

It was found in the results that the distribution of stress and strain at a smaller part of the deformed component near the die bend was slightly erroneous It was also reasoned that the solid elements are not very suitable for the kind of deformation that takes place in this small region However, it can be taken care of by modelling this small region by thick shell elements in association with solid elements for the other part of the model

The bulge forming of T-branch by hydraulic pressure was simulated in this work T-branches can also be formed by using solid medium instead of liquid Simulation of such cases would make the model even larger as the solid medium has also to be modelled and consequent solution time would be longer However, such modelling and simulation can be taken up with powerful computers Also, due to the computer resource constraint forming of long T-branches could not be taken up which can be tried with more powerful computers

5.5 Bulge Forming of Box-Sectioned Elbow from Cylindrical Tube

Main Findings

In this simulation a cylindrical L-bend was bulged to a box-sectioned bend by applying pressure load only but at different forming conditions Simulations were carried out for different end conditions and friction conditions The main observations from the simulation results are listed bellow

i The simulation where the elbow ends were kept free developed a sharp dent at the L-bend and the length of the arms reduced by few millimetres In the case where the ends were kept fixed these deformation phenomena were not observed rather the L-bend was smooth Also, in the latter case the stress and strain distribution was more even compared to the former case In both cases the thinning pattern was similar although the case with ends fixed has thinned slightly more all over Also, springback was negligible for both the cases

ii Simulations were carried out at friction factor values of 0 15 and 0 05 keeping the ends fixed It was observed that there was more stress and strain localisation in the elbow formed with lower friction

It was apparent from the simulations that in forming cases like this it is better to keep the ends fixed It was also apparent that because of low friction more straining takes place in the bends and corners when the ends are kept fixed This results in higher stress and strain localisation Therefore, it is better to have moderate friction at the interface for such forming processes

The number of elements in the model were not sufficient specially at the corners Thus the deformation at the corners were not well represented The model can be developed with more elements at the corners to have more representative results

The simulation in this work started with an initially bent blank Simulation can be attempted to include the initial bending process or simultaneous bending and bulging process

5 6 Thesis Contribution

Bulge forming of tubular components is a relatively new forming process which is increasingly getting widespread application in industry The understanding of the process made so far has been limited to some aspects of the process In the case of complex forming of asymmetric components it is even poor The important aspects like flow pattern in the process for different forming condition, stress and strain conditions in the formed components, thinning and thickening behaviour within the component etc are largely unknown to the researchers as well as to the practitioners As a result the defects and failures in the process is a major concern for the industry Also, the design of machine tools for the process lacked sufficient knowledge and understanding of the process The simulations in this work will contribute some knowledge in this largely unknown area of bulge forming In particular, the simulations in this work provided

i the state of stress and strain in the formed bulge from plane circular sheet formed by pressure and in-plane compressive load Also, the pattern of metal flow in such forming has been identified An optimum set of process variables were identified to minimise the stress differential in the bulge while developing the bulge to a certain minimum height ii identified the pattern of stress and strain, thinning or thickening and metal flow in the bulge forming of rectangular plates at the middle by pressure and in-plane compressive load on the shorter side of the plate Also, a possible loading pattern was suggested that would avoid any buckling in the flat part of the plate during forming

iii the pattern of stress and strain, thinning or thickening and flow of metal in the tube expansion process by bulge forming has been identified Some observations were made as to the instability of the process due to the mode shape change during the forming process Also, an optimum loading pattern was identified that would eliminate buckling in the main part of the tube

iv the pattern of stress and strain, thinning and thickening and metal flow in the complex bulge forming process of T-branches has been identified in the simulations The simulations also identified the effects of friction, blank material and blank thickness on the forming process Also, the locations and reasons for failure of the T-branch forming process have been found from the simulations

v the state of stress and strain and the pattern of thinning or thickening in the bulge formed elbow have been revealed in the simulations The springback behaviour of the elbow has also been identified

REFERENCES

1 N Brannberg and J Mackerle, "Finite element methods and material processing technology", Engineering Computations, Vol 11, pp 413-455 , 1994

2 E Chater and K W Neale, "Finite plastic deformation of a circular membrane under hydrostatic pressure-1 rate independent behaviour", Int J Mech Sci , Vol 25 No 4 pp 219-233, 1983

3 W Brown and G Sachs " Strength and failure characteristics of thin circular membranes", Trans ASME, Vol 70, pp 241-251, 1948

4 A Gleyzal, "Plastic deformation of a circular diaphragm under pressure", J Appl Mech, Vol 15, pp 288-296 , 1948

5 W Brown and F Thompson " Strength and failure characteristics of metal membranes in circular bulging", Trans ASME, Vol 71, pp 575-585 ,1949

6 R Hill, "A theory of the plastic bulging of a metal diaphragm by lateral pressure", Phil Mag(sec 7), Vol 41, pp 1133-1142 , 1950

7 H W Swift, "Plastic flow under plane stress", J Mech Phys Solids, Vol 1, pp 1-18, 1952

8 P B Mellor, " Strength forming under fluid pressure", J Mech and Phy of Solids, Vol 5, pp 41-56, 1956

9 D Rees, "Plastic flow in the elliptical bulge test", Int J Mech Sci , Vol 37 No 4, pp 373-389, 1995

10 M Atkinson, "Accurate determination of biaxial stress-strain relationship from hydraulic bulging tests and sheet metals", Int J Mech Sci , Vol 39 No 7, pp 761-769, 1997

11 M F Ilahi and T K Paul, "Hydrostatic bulging of a circular soft brass diaphragm", Int J Mech Sci , Vol 27 No 5, pp 275-280, 1985

12 D Rees, " Instability limits to the forming of sheet metals", J Mat Proc Tech , Vol 55, pp 146-153, 1995

13 M Atkinson, "Hydraulic bulging of near isotropic sheet metal through an elliptical aperture", Int J Mech Sci, Vol 36, 1994

14 D M Woo, "The analysis of axisymmetric forming of sheet metal and the hydrostatic bulging process" Int J Mech Sci , Vol 6, pp 303-317, 1964

15 Y Yamada and Y Yokouchi, Seisan kenku (in Japanese), Vol 21 No 11, pp 636, 1969

16 N M Wang and M R Shammamy, "On plastic bulging of a circular diaphragm by hydraulic pressure" , J Mech Phys and Solid, Vol 17, pp 43-61, 1969

17 M F Ilahi, A Parmar and P B Mellor, "Hydrostatic bulging of a circular aluminium diaphragm", Int J Mech, Sci , Vol 23 , pp 221-227, 1981

18 H Iseki, T Jimma and T Murota, " Finite element method of analysis of the hydrostatic bulging of sheet metal(part 1)", Bulletin of the JSME, Vol 17 No 112, pp 1240-1246, 1974

19 H Iseki, T Murota and T Jimma, "Finite element method in the analysis of hydrostatic bulging of sheet metal (part 2)", Bulletin of JSME, Vol 20 No 141, pp 285-291, 1977

20 S Kobayashi and J H Kim, "Deformation analysis of axisymmetric sheet metal forming process by the rigid plastic FEM", Proc of Symp in Mechanics of sheet metal forming ed D P Koisten and N M Wang , pp 341-363, 1978

21 Y J Kim and D Y Yang, " A rigid-plastic finite element formulation considering the effect of geometric change and its application to hydrostatic bulging", Int J Mech Sci , Vol 27 No 7/8, pp 453-463, 1985

22 A S Wifi, " FE correction matrices in metal forming analysis with application to hydrostatic bulging of a circular sheet", IJMS, Vol 24, No 7, pp 393-406(1982)

23 P Keck, M Wilhelm, K Lange and M Herrmann, "Comparision of different finite element methods for the simulation of sheet metal forming", Proc of Numiform 89, pp 481-488, Balkema, Rotterdam, 1989

24 K Lange, M Herrmann, P Keck and M Wilhelm, "Application of an elasto-plastic finite element code to the simulation of metal forming process", JMPT , Vol 27, pp 239-261, 1991

25 Y Li, P Hu and J Lian, "Numerical study for influences of material parameters on hydrostatic bulging of metal sheet", Acta Mechanica Solida Sinica (English), Vol 6 No 2, pp 133-144, 1993

26 R J Cronin, J Y Xia and D T Llewellyu, "Finite element modelling of hydraulic bulging during sheet metal forming", Ironmaking and steelmaking, Vol 21 No 1, pp 32-36, 1994

27 W B Lee and Z R Ma, "Prediction of the limiting shape of a die height in the hydraulic bulge forming of a circular cup", JMPT, Vol 51, pp 309-320, 1995

28 J Grey, A D Devereaux and W Parker, Apparatus for making wrought metal Ts", USA Patent office, Filed June 1939, Patent no 2203868

29 R Crawford, "Solder fitting" Industrial progress, pp 33-36, 1948

30 J Stalter, "Method of forming complex tubing shapes" UK Patent office, Filed March 1968, Patent no 1181611

31 J Remmerswaal and A Verkaik, "Use of compensation forces and stress in difficult metal forming operations", Int Conf on Manufacturing Technology, ASME, pp 1171-1180, 1967

32 T Ogura and T Ueda, "Liquid bulge forming", Metalworking Production, pp 73-81, 1968

33 H A Al-Qureshi, P B Millor and S Garber, "Application of Polyurethane to the bulging and piercing of thin-walled tubes", Advances in Mach Tool Des Res 318-338, Pergamon Press, 1969

34 H A Al-Qureshi, "Comparison between the bulging of thin walled tubes using rubber forming technique and hydraulic forming process", Sheet Metal Industry, Vol 47, pp 607-612, 1970

35 D M Woo, "Tube bulging under internal pressure and axial force", J of Engineering Materials and Technology, pp 421-425, 1978

36 Limb, J Chakrabarty, S Garber and P B Millor, "The forming of axisymmetric and asymmetric component from tube", Proc 14th Int MTDR conf, PP 799(1973)

37 Limb, J Chakrabarty, S Garber and W T Roberts, "Hydraulic forming of tubes"Sheet Metal Industries, PP 418-424(1976)

38 M Limb, J Chakrabarty and S Garber, "The axisymmetric tube forming process", Int Inst for Prod Eng Research Conf ,Tokyo, pp 280-283, 1974

39 S Kandil, "Hydrostatic metal tube bulging as a basic process", Metallurgia and Metal forming, pp 152-155 , 1976

40 W J Sauer, A Goetra, F Robb and P Huang, "Free bulge forming of tubes under internal pressure and axial compression", Trans of NAMRC VI, SME, pp 228-235, 1978

41 D M Woo and A C Lua, "Plastic deformation of anisotropic tubes in hydraulic bulging" , Journal of Engineering Materials and Technology, pp 421-425, 1978

42 D M Woo, "Development of a bulge forming process", Sheet Metal Industries, pp 623-624 and 628, 1978

43 V L Lukanov, V V Klechkov, V P Shateev and L V Orlov, "Hydromechanical stamping of tees with regulated liquid pressure", Forging and Stamping Industry, Vol 3, pp 5-7 , 1980

44 A R Ragab, "Producing superplastic tubular tee joints by thermoforming", Proc Int MTDR Conf , pp 223- , 1980

45 M S J Hashmi, “Radial thickness distribution around a hydraulically bulge formed annealed copper T-joint experiments and theoretical predictions”, Proc of 22nd Int MTDR Conf, pp 507-516, 1981

46 M S J Hashmi, “Forming of tubular components from straight tubings using combined axial load and internal pressure theory and experiment”, Proc of Int Conf of Dev of Drawing of Metals, Metals Society, pp 146-155, 1983

47 M S J Hashmi and R Crampton, “Hydraulic bulge forming of axisymmetric and asymmetric components comparison of experimental results and theoretical predictions” Proc 25th Int MTDR Conf, pp 541-549, Birmingham, 1985

48 M I Hutchinson R Crampton, W Rushton and M S J Hashmi, “The hydraulic bulge forming of tubular components - the effect of altering the plungers applying compressive axial load”, Proc 6th Irish Manu Committe Conf, pp 248-254, Dublin, 1989

49 M I Hutchinson, R Crampton, M S Ali and M S J Hashmi,“The hydraulic bulge forming of tubular components - the effect of changing the tube blank material”, Proc 4th Nat Conf in Prod Res, pp 439-444, Sheffield, 1988

50 T Ueda, “Differential gear casing for automobiles by liquid bulge forming processes-part 1”, Sheet Metal Industries, Vol 60 part 3/4, pp 181-185, 1983

51 T Ueda, “Differential gear casings for automobiles by liquid bulge forming processes- part 2” Sheet Metal Industries, Vol 60 part 4, pp 220-224, 1983

52 L A M Filho and H A Al-Qureshi, “Unconventional tee forming on metal tubes”, Trans ASME, J Eng Ind, Vol 107, pp 392-396, 1985

53 F Dohmann and F Klass, “Liquid bulge forming of tubular workpieces”, Strips Sheets Tubes, Vol 4(1), pp 7-10, 1987

54 M Murata, Y Yokouchi, K Onodera and H Suzuki,“The hydraulic tube bulging of a tube-attached lining rubber membrane with axial compressive force”, JSME Int J, Series III, Vol 32 No 1, pp 118-123, 1989

55 S Thiruvarudchelvan and F W Travis, “Tube bulging with a Urethane rod”, JMPT, Vol 23, pp 195-209, 1990

56 S Thiruvarudchelvan and A C Lua, “Bulge forming of tubes with axial compressive force proportional to the hydraulic pressure”, J Mat, Shaping Tech, Vol 9, pp 133-142, 1991

57 F Dohmann and C Hartl, “Liquid bulge forming as a flexible production method”, JMPT, Vol 45, pp 377-382, 1994

58 F Dohmann and C Hartl, “Hydroforming - a method to manufacture light weight parts”, JMPT, Vol 60, pp 669-676, 1996

59 L A M Filho, J Menezes and H A Al-Qureshi, "Analysis of unconventional Tee forming on metal tubes" JMPT vol 45, pp 383-388, 1994

60 S Thiruvarudchelvan, "A theory for initial yield condition in tube bulging with urethane rod", JMPT, Vol 42, pp 61-74, 1994

61 S Thiruvarudchelvan, "A theory for the bulging of aluminium tube using urethane rod", JMPT, Vol 41, pp 311-330, 1994

62 S Sheng and W Tonghai, "Research into the bulge forming of a tube under axial -radial compound forces and its application", JMPT, Vol 51, pp 346-357, 1995

63 J Tirosh, A Neuberger and A Shirizly, "On tube expansion by internal fluid pressure with additional compressive stress", Int J Mech Sci , Vol 38 No 8, pp 839-851, 1996

64 P B Mellor, "Tensile instability in thin-walled tubes", J Mech Eng Sci , Vol 4 No 3, pp 251-256, 1962

65 B H Jones and P B Mellor, "Plastic flow and instability behaviour of thin-walled cylinders subjected to constant ratio tensile stress", J Strain Analysis, Vol 2, pp 62-72, 1967

66 R P Felgar, "Plastic analysis of the instability of pressure vessels subjected to internal pressure and axial load", Transec ASME, J Basic Eng , Vol 84, pp 279-286, 1962

67 N A Weil, "Tensile instability of thin-walled cylinders of finite length", Int J Mech Sci , Vol 5, pp 487-506, 1963

68 K Manabe, K Suzuki, S Mori and H Nishimura, "Bulge forming of thin-walled tubes by micro-computer controlled hydraulic press", Proc of Adv Tech Plasticity, Vol 1, pp 279- , 1984

69 A D Eldred, R F Malkin and T Barringer, "Variform - a hydroforming technique for manufacturing complex tubular components", Technische Mitteilungen Krupp (English), Vol 1, pp 45-50, 1994

70 J Hashemi, J Rasty, S D Li and A A Tseng, "Integral hydro-bulge forming of single and multi-layered spherical pressure vessels" ASME Journals of Pressure Vessels Technology, 1992

71 Z R Wang, T Wang, D C Kang, S H Zhang and Y Fang, "The technology of the hydrobulging of whole spherical vessels and experimental analysis", Journal of Mech Work Technol , Vol 18, pp 85-94, 1989

72 K Lange, M Herrmann, P Keck and M Willhelm, "Application of an elasto-plastic finite element code to the simulation of metal forming processes" JMPT, vol 27, pp 239-261, 1991

73 H Bauer, "FE simulation of the production process of builded camshaft", Numerical Methods in Industrial Forming Processes, pp 595-600, Balkema, Rotterdam, 1992

74 M Michino, M Tanaka, M Koike, M Watanbe, K Sano and M Norita, "Forming of elbows with zero bending radius", In Concurrent Engineering Approach to Materials Processing , Ed Suren N Dwivedi, J Paul and F Robert Dax, The Minerals, Metals and Material Society, pp 291-303, 1992

75 S Zhang and Z R Wang, "FEM simulation of the hydrobulging process for a 32 petal spherical vessel", IJMS, Vol 36, No 1, pp 13-22, 1994

76 J Hashemi and Q Zheng, " A three dimensional FEA of hydrostatic bulging of an integral polyhedron into a spherical vessel", Recent Advances in Structural Mechanics, ASME Winter Annual Meeting Proc , Vol 13, pp 113-117, 1993

77 A Honecker and K Mattiasson, "Finite element procedures for 3D sheet forming simulation", Proc NUMIFORM '89, pp 457-463, Balkema, Rotterdam, 1989

78 K Mattiasson, L Bernspang, A Samuelson, T Hamman, E Schedin and A Melander, "Evaluation of dynamic approach using explicit integration in 3-D sheet forming simulation", Numerical Methods in Industrial Forming Processes, pp 55-67, Balkema, Rotterdam, 1992

79 N Rebelo, J Nagtegaal, L M Taylor and R Passman, "Comparison of implicit and explicit FEM in the simulation of metal forming processes", Numerical Methods in Industrial Forming Processes, pp 99-108, Balkema, Rotterdam, 1992

80 D Yoo, I Song, D Yang and J Lee, "Rigid-plastic FEA of sheet metal forming process using continuous contact treatment and membrane elements incorporating bonding effects", Int J Mech Sc , Vol 36, pp 513-546, 1994

81 C Teodosin, D Daniel, H-L Cao and J-L Duval, "Modelling and simulation of the can-making process using solid finite elements", JMPT, Vol 50, pp 133-143, 1995

82 J S Arora, "Computational Design Optimisation a review and future directions", Structural Safety, Vol 7, pp 131-148, 1990

83 M Z Cohn and A S Dinovitzer, "Application of structural optimisation", J Struc Eng , Vol 120(2), pp 617-650, 1994

84 J Kusiak and E Q Thompson, "Optimisation techniques for extrusion die shape design", Numiform 89, pp 569-574, Balkema, Rotterdam, 1989

85 M Becker and R Kopp "A new approach to optimisation of metal forming processes", Numiform'89, pp 107-113, Balkema, Rotterdam, 1989

86 M S Joun and S M Hwang, "Optimal process design in steady-state metal forming by finite element method-1 theoretical considerations", Int J Mach Tools Manu Vol 33, No 1, pp 51-61, 1993

87 M S Joun and S M Hwang, "Optimal process design in steady-state metal forming by finite element method-2 application to die profile design", Int J Mach Tools Manu , Vol 33, No 1, pp 63-70, 1993

88 M S Joun and S M Hwang, "Application of FEM to process optimal design in metal extrusion", Numerical Methods in Industrial Forming Processes, pp 619-624, Balkema, Rotterdam, 1992

89 C S Han, R V Grandhi and R Srinivasen, "Optimum design of forging die shapes using non-linear FEA", AIAA Journal, Vol 31 No 4, pp 774-781, 1993

90 J Shu and C Hung, "Finite element analysis and optimisation of springback reduction the double-bend technique", Int J Mach Tools Manu Vol 36, No 4, pp 423-434, 1996

91 J Kusiak, "A technique of tool shape optimisation in large scale problems of metal forming", JMPT, Vol 57, pp 79-84, 1996

92 L Fourmant and J L Chenot, "Optimal design for non-steady state metal forming processes-I shape optimisation method", Int J Num Meth Eng , Vol 39, pp 33-50, 1996

93 L Fourmant and J L Chenot, "Optimal design for non-steady state metal forming processes-II application of shape optimisation in forging", Int J Num Meth Eng , Vol 39, pp 51-65, 1996

94 S Roy, S Ghosh and R Shivpuri, "Optimal design of process variables in multipass wire drawing by genetic algorithm", J Manu Sci Eng , Vol 118, pp 244-251, 1996

95 S Roy, S Ghosh and R Shivpuri, "A new approach to optimal design of multistage metal forming processes with micro-genetic algorithms", Int J Mach Tool Manu , Vol 37 No 1, pp 29-44, 1997

96 G Park, W Hwang and W Lee, "Structural optimisation post -process using Taguchi method", JSME Int Journal, Series A, Vol 37 No 2, 1994

97 G Beer and J O Watson, "Introduction to finite element and boundary element methods for engineers" John Wiley and Sons, 1992

98 K-J Bathe, "Finite element procedures in engineering analysis", Prentice Hall, 1982

99 P Kohnke (ed), "ANSYS User's Manual, Rev 5 1, Vol 4, theory, Swanson Analysis Systems Inc , Houston, 1994

100 J O Hallquist, "LS-DYNA3D Theoretical Manual", Livermore Software Technology Corporation, California, USA, 1993

101 J O Hallquist and D J Benson, "Explicit finite element methods for impact engineering", Proceedings of the first Australasian Congress on Applied Mechanics, pp 11-16, Melbourne, 1996

102 Y Wu and S Taguchi, "Orthogonal Arrays and Linear Graphs", American Supplier Institute Press, 1987

103 ANSYS, "ANSYS-LSDYNA Users' Guide, 1st ed , ANSYS Inc , Houston, 1996

104 M I Hutchinson, "Bulge Forming of Tubular Components" , PhD Thesis, Sheffield City Polytechnique, Sheffield, 1988

105 T Belytschko, B L Wong and H Y Chiang, "Improvement in low order shell elements for explicit transient analysis", Analytical and Computational Models of Shells, A K Noor, T Belytschko and J Simo (ed), ASME, CED -Vol 3, pp 383-398, 1989

106 T Belytschko, B L Wong and H Y Chiang, "Advances in one point quadrature shell elements", Computer Methods in Applied Mechanics and Engineering, Vol 96, pp 93-107, 1992

107 T Belytschko, J Lin and C S Tsay, "Explicit algorithms on non-linear dynamics of shells", Computer Methods in Applied Mechanics and Engineering, Vol 42, pp 225-251, 1984

108 D J Benson and J O Hallquist, "A single surface contact algorithm for the post buckling analysis of shell structures", Computer Methods in Applied Mechanics and Engineering, Vol 78 pp 141-163, 1990

APPENDIX

Taguchi Parameter Design Method

Taguchi has developed an experimental method for determining the optimum values of product and process parameters called design variables which will minimise variation while keeping the mean value of the output parameter called the objective figure of merit on target In this method two category of design variables viz control factors and noise factors are identified by the designers either out of their experience or from brain storming sessions Control factors are those factors of the product or process which can easily be controlled Noise factors, on the other hand, are those variables of the product or process which are either difficult, or impossible, or expensive to control Each variable is assigned certain discrete values Number discrete values of a variable determines its levels Depending on the number of factors and number of levels of the factors an orthogonal array is chosen to conduct experiments The orthogonal array determines the factor-level combinations to be tried on the process A particular ~~figure of merit decided~~ by the designer is recorded for each trial of the process determined by the orthogonal array The figure of merit responses from the trials are then analysed to find the optimum factor-level combination

The principle of analysis is to determine the average response of the figure of merit and the average signal to noise (S/N) ratio at each level of the design variables and then check the trend of the average response and/or average S/N ratio for changes in the factor levels Depending on the problem type the level of a factor that give the maximum or minimum average response or minimum S/N ratio is the desired level for that particular factor There are some standard S/N ratio expressions The expressions for S/N ratio that are used widely are given bellow

A) for problem types where nominal value of the response is better

$$S/N = 10 \log [(S_m - V_e)/ n V_e] \qquad \text{(A-1)}$$

where, $S_m = (\Sigma Y_i)^2 / n$ and $V_e = [\Sigma Y_i^2 - (\Sigma Y_i)^2 / n] / (n-1)$,

Y_i is an observation of the output characteristic and n is the number of observations

B) for problem types where smaller is the better response

$$S/N = 10 \log [(\sum Y_i)^2 / n] \tag{A-2}$$

C) for problem types, where bigger is the better response

$$S/N = 10 \log [(\sum 1/Y_i^2) / n] \tag{A-3}$$

Taguchi method used in this project identified the optimum level of design variables that give minimal variation to the objective function value Each design variable was given two different desirable values around the optimum solution obtained by the non-linear optimisation A three factor-two level orthogonal array was chosen for trial runs Equations A-2 and A-3 were used for S/N ratio calculation

List of Publications

1 Ahmed, M and Hashmi, M S J "Finite element simulation of bulge forming of an elbow of box section from circular tube" in the proceedings of the international conference on materials and processing technology '97 (AMPT97), pp 785-792, University of Minho, Portugal, July, 1997

2 Ahmed, M and Hashmi, M S J " Defects in hydraulic bulge forming of tubular components and their implication for design and control of the process" in Advanced Methods in Materials Processing Defects, M Predeleanu and P Gilormini (ed), Elsevier, pp 197-204,1997

3 Ahmed, M and Hashmi, M S J "Comparison of free and restrained bulge forming by finite element method simulation" Journal of Materials Processing Technology , Vol 63, pp 651-654, 1997

4 Ahmed, M and Hashmi, M S J " Estimation of machine parameters for hydraulic bulge forming of tubular components" Journal of Materials Processing Technology, Vol 64, pp 9-23 , 1997

5 Ahmed, M and Hashmi, M S J "Optimisation of bulge forming of a circular plate applying pressure and in-plane compressive load", in "Mechanics in Design", Proceedings of the Symposium on Mechanics in Design, Toronto, Canada , May 6-9, pp 427-436, 1996

6 Ahmed, M and Hashmi, M S J "Transforming an optimised design to a practical application by Taguchi parameter design method" Proceedings of the13th Conference of the Irish Manufacturing Committee, Limerick, Ireland , September 4-6, pp 935-944, 1996

7 Ahmed, M and Hashmi, M S J "Finite element analysis of bulge forming applying pressure and in-plane compressive load", Proceedings of the International Conference on Advances in Materials and Processing Technologies, Dublin, Ireland , August 8-12, 1995 (also accepted for publication in Journal of Materials Processing Technology)

8 Ahmed, M and Hashmi, M S J "Aspects of tooling and machine design for hydraulic bulge forming of tubular components", Proceedings of the International Conference on Advances in Materials and Processing Technologies, Dublin, Ireland, August 8-12, 1995

9 Ahmed, M and Hashmi, M S J " Design optimisation of metal forming using finite element simulation - an overview" Proceedings of the 12th conference of the Irish Manufacturing Committee, Cork, Ireland , September 6-8, 1995